2010

Deformation State of Aluminum-6% Silicon Alloy (319 Al) Subjected to Orthogonal Cutting at Different Speeds and Feed Rates

Shilpi Pratibha
University of Windsor

Deformation State of Aluminum-6% Silicon Alloy (319 Al) Subjected to Orthogonal Cutting at Different Speeds and Feed Rates

by

Shilpi Pratibha

A Thesis

Submitted to the Faculty of Graduate Studies

through Engineering Materials

in Partial Fulfillment of the Requirements for

the Degree of Master of Applied Science at the

University of Windsor

Windsor, Ontario, Canada

2009

Deformation State of Aluminum-6% Silicon Alloy (319 Al) Subjected to Orthogonal Cutting at Different Speeds and Feed Rates

by

Shilpi Pratibha

APPROVED BY:

_____

Dr. N. Zamani
Department of Mechanical, Automotive, and Materials Engineering

_____

Dr. V. Stoilov
Department of Mechanical, Automotive, and Materials Engineering

_____

Dr. A. T. Alpas, Co-Advisor
Department of Mechanical, Automotive, and Materials Engineering

_____

Dr. W. J. Altenhof, Co-Advisor
Department of Mechanical, Automotive, and Materials Engineering

_____

Dr. H. Hu, Chair of Defense
Department of Mechanical, Automotive, and Materials Engineering

21 September 2009

Author's Declaration of Originality

I hereby certify that I am the sole author of this thesis and that no part of this thesis has been published or submitted for publication.

I certify that, to the best of my knowledge, my thesis does not infringe upon anyone's copyright nor violate any proprietary rights and that any ideas, techniques, quotations, or any other material from the work of other people included in my thesis, published or otherwise, are fully acknowledged in accordance with the standard referencing practices. Furthermore, to the extent that I have included copyrighted material that surpasses the bounds of fair dealing within the meaning of the Canada Copyright Act, I certify that I have obtained a written permission from the copyright owner(s) to include such material(s) in my thesis and have included copies of such copyright clearances to my appendix.

I declare that this is a true copy of my thesis, including any final revisions, as approved by my thesis committee and the Graduate Studies office, and that this thesis has not been submitted for a higher degree to any other University or Institution.

ABSTRACT

Dry machining of cast aluminum 6%-Si alloy 319 Al was studied. Investigations were carried out to understand deformation mechanisms leading to discontinuous chip formation during the process. A force transducer was constructed for measuring cutting and thrust forces which increased with an increase in feed and with a decrease in cutting speed. Surface roughness increased with an increase in feed. Plastic strain and flow stress estimations in region ahead of tool-tip indicated high strains (1.8) and stresses (369MPa) in shear zone. Optical investigations showed that zone of silicon particle damage below machined surface increased with feed. Theoretically estimated specific energy for cutting correlated well with values obtained from force measurement results. Experimental observations indicated that 319 Al alloy possesses a good degree of machinability under dry conditions.

To my ma and baba

for standing beside me, always.

And to my brother

for pushing me to run that extra mile.

ACKNOWLEDGEMENTS

I would like to express my sincere gratitude to my advisor Dr. A. T. Alpas for his constant supervision, encouragement, support and patience during my graduate studies. I also wish to extend my heartfelt thanks to my co-advisor, Dr. W. J. Altenhof for his invaluable comments, suggestions and guidance during my research. Working under their expert guidance has been a great learning experience.

I also wish to thank my committee members: Dr. V. Stoilov and Dr. N. Zamani for their invaluable discussions, suggestions and time. Special thanks to the Technical Assistance Shop crew for providing assistance with the set-up, for their invaluable suggestions and for coordinating the tests. Sincere thanks to Mr. P. Seguin for his invaluable help with the designing, construction and calibration of the force measurement system. Mr. P. Chen's help with the calibration of the force measurement system is greatly appreciated. Sincere thanks to Mr. Robinson for his constant help and the training related to SEM. I would also like to thank Engineering Materials Department secretary Ms. Denomey for her continued help and understanding.

Special thanks to my fellow researchers Ms. S Das, Mr. S Dey, Mr. S. Bhowmick, Mr. F. Sen, Dr. M. Safiei, Mr. S. Bhattacharya, Mr. Abougharam, Mr. Slattery, Ms. K. Farrokhzadeh and Mr. O. Gali for their support and friendship.

Financial support provided by NSERC (Nature Science and Engineering Research Council of Canada), General Motors of Canada Limited through an Industrial Research Chair Program under Dr. A. T. Alpas is greatly appreciated.

I would also like to thank my parents, Mr. D. N. Rout and Mrs. R. Rout and my brother, Niraj for their constant help, support, and understanding and for having so much faith in me.

TABLE OF CONTENTS

LIST OF ABBREVIATIONS

PDZ	Primary Deformation Zone
SDZ	Secondary Deformation Zone
TDZ	Tertiary Deformation Zone
BUE	Built-Up Edge
PCD	Poly Crystalline Diamond
SEM	Secondary Electron Microscope
TEM	Transmission Electron Microscope
EDS	Electron Dispersive Spectroscopy
COF	Coefficient of Friction
MQL	Minimum Quantity Lubrication
UTS	Ultimate Tensile Strength
YS	Yield Strength
ECM	Electrochemical Machining
EDM	Electrodischarge Machining
UM	Ultrasonic Machining
SADS	Secondary Dendritic Arm Spacing
SHPB	Split Hopkinson Pressure Bar
JC	Johnson Cook
EPH	Elastic Plastic Hydrodynamic

NOMENCLATURE

α	Rake angle
β	Friction angle between chip and tool
V_c	Cutting speed
f	Feed per revolution or feed rate
t_c	Chip thickness
D	Depth of cut
w	Width of chip
ϕ	Shear angle
μ_e	Coefficient of friction
$F_{friction}$	Friction force between rake face of tool and chip
F_r	Force exerted by the tool on the workpiece
F_c	Cutting force
F_t	Thrust force
F_s	Shear force along shear plane
N_s	Normal force acting perpendicular to shear plane
F_p	Force parallel to rake face of tool
N_p	Force perpendicular to rake face
N_f	Normal force acting perpendicular to rake face
r	Cutting ratio: defined as ratio of feed to chip thickness
τ_s	Shear stress on the shear plane
σ_s	Normal stress on the shear plane
τ_f	Shear stress on the chip in contact with the rake face
w	Width of chip

γ	Shear strain in cutting
$\dot{\gamma}$	Strain rate in cutting
d_s	Thickness of shear band
γ_s	Shear displacement in shear band
$\bar{\varepsilon}$	Equivalent Plastic strain
θ	Deformation angle
d_s	Displacement between the shear bands formed
t_s	Thickness of shear bands
H	Vickers Hardness
σ	Flow stress
C	Material constant, equal to 3
Q	Volume removed per revolution of workpiece
u_s	Specific cutting power
W	Work of plastic deformation per unit volume of material
ρ	Density
C_p	Specific heat capacity of material
K	Thermal diffusivity of the material
T_{amb}	Ambient temperature
F_{sys}	Force on force measurement system
M	Total mass of weights
m	Mass of weight hanger pan
g	Acceleration due to gravity
σ	Flow stress
σ_f	Normal stress on the rake face
σ_s	Saturation stress or stress at which work hardening becomes zero
σ_0	Yield stress
$P_{cutting}$	Power expended by cutting force
P_{feed}	Power expended by thrust force
R	Material removal rate during cutting
U	Power consumed per unit time during cutting

$U_{friction}$	Power consumed in overcoming rake-chip friction, per unit time
$u_{friction}$	Specific power consumed in overcoming rake-chip friction, per unit time

CHAPTER 1

INTRODUCTION

1.1 Outline of the Studied Problem

Metal cutting operations are manufacturing processes, which are undertaken to shape metal components by removal of excess material. Turning, boring, drilling and milling are among many types of metal cutting or machining processes where the excess material removal takes place in the form of chips. The outcome of a given machining operation is affected by a large number of factors. Variation of parameters like cutting tool material and geometry, workpiece properties etc bring about significant changes in the results and efficiency of the process. This allows only a few of the output parameters of practical machining operations, like the cutting force and power consumption, being quantitatively predicted.

The use of cutting fluids and lubricants during cutting is an important factor which affects the efficiency of machining process. A large percentage of industrial machining is lubricated machining, and thus subjected to huge expenses towards the cost of cutting fluids. Maintenance and disposal of these fluids lead to further concerns. The use of cutting fluids also leads to health hazards for the workers involved and their disposal leads to contamination of the environment in general. These have resulted in an increase

in effort towards minimizing the use of cutting fluids, thus brining into focus dry metal cutting.

Research into the field of machining started as early as the 19th century and since then many important models attempting to explain the basic mechanisms involved in shearing of metal have been proposed, which include models by Merchant [1,2] and Piispanen [3]. Metallographic analyses of the machined samples and sections have also been carried out extensively in an attempt to better understand the plastic deformation behaviour of various work-pieces subjected to machining [1- 5].

The chips produced during machining can be classified mainly into two categories, continuous chips marked by an almost continuous flow of material with long ribbon-like geometry and discontinuous chips formed due to cyclic cracking and fragmentation of material. An extensive amount of research has been conducted in an attempt to understand the reason and mechanism leading to the production of these chips and factors which favour the generation of one type over the other. Various theories regarding the generation of continuous chips have been proposed and although none of them has yet been shown to be able to accurately predict the outcome of the process, some have been relatively successful and are widely used [1,2,14]. However, the same theories do not apply to the generation of discontinuous chip formation. Different theories explaining discontinuous chips formation have been suggested, which attribute the formation of saw-tooth like segments to factors like adiabatic shear [32], cyclic cracking

[6,23,47] and presence of second phase particles [60]. These have been examined in details in Section 2.8.

Aluminum, one of the most heavily consumed non-ferrous metal with current consumptions of over 24 million tons annually, is extensively used for manufacturing engineering components for industries which include aerospace and automobile sectors [56]. Also, according to an industry estimate, nearly ninety percent of all components manufactured have one or more machined part [6]. This makes study of machinability of aluminum and its alloys an important filed of investigation. Apart from the sheer volume of production, another factor that makes study of Al-Si alloys important is that depending on the alloying elements, and more specifically the percentage of silicon present, Al-Si alloys display wide ranging machinability performances. An extensive amount of work has been done in the field of continuous chip generation in Al-Si alloys, including work by Balaji et al [82,] Jeelani et al [78], Elmadagli et al [4,5]. Song[20] has also carried out investigations into generation of discontinuous chips in Al 380. Section 2.7 takes an in-depth look at machinability of these alloys. However, the complex nature of the process and large variations in machining performance due to differences in factors like composition, heat treatment, etc, a greater amount of studies into the area is required to further develop an understanding of discontinuous chip formation.

In the light of the above issues, this work aims at understanding the dry machinability of hypoeutectic aluminum alloy 319 Al by carrying out dry turning

experiments on it and subsequently analyzing the machinability of the alloy, which is a combination of the force and power requirements of the process, the surface finish of the machined product and the form and geometry of the chip produced. Beside this, the work aims at analyzing the deformation zones produced during the process by estimating the stress and strains in the workpiece. The work also investigates the fracture behaviour of silicon particles in workpiece as it gets subjected to high deformation during machining. Generation and recording of data pertaining to the machinability of the alloy, which can be used as input for and validation of a numerical model which can predict the results of machining of 319 Al and hence do away with the need for prototype testing of the process, also served as an important motivation behind this study.

1.2 Thesis Objective

The objective of this work was to conduct dry orthogonal cutting experiments on Aluminum 319 under different cutting conditions, followed by a detailed analysis of the process. Dry machinability of the alloy, which is judged by analysis of factors such as forces generated during the process and the power expended during machining, quality of surface generated and the geometry of chip produced was studied. Understanding of the deformation structures generated during dry turning of 319 Al by estimation of stress and strain distribution in the workpiece was the main motivation behind this research. This study was also aimed at analyzing the fracture of silicon particles present in the alloy in

order to understand their behaviour during machining. Another prime driver was accumulation of data for being used for the purpose of construction and validation of a numerical model which can effectively simulate the discontinuous chip formation during orthogonal machining process.

CHAPTER 2

LITERATURE REVIEW

Machining is a process of the removal of excess material from a component in order to impart it the required dimension and finish. Importance of the machining process can be appreciated by the fact that nearly every device produced today has one or more machined surface or holes [6]. Research into this field is mainly driven by the need to improve cutting techniques which may further ramify into improvements in the productivity, greater precision of finished product and longevity of the same, as well as advancement in the rate and efficiency of production. This section outlines the previous work done towards better understanding of the machining process as well as the influence of various cutting parameters on the process.

2.1 An Introduction to Material Removal Processes

Material removal processes are designed to shape a component by removal of excess and unwanted material thus imparting it the desired shape, dimension and surface roughness. Such processes generally remove the excess material in the form of chips. These processes can be broadly classified into cutting or machining processes, grinding processes and other special techniques [6,43]. Cutting produces macroscopic chips which are generally shaped as long ribbons in case of ductile workpieces or as small fragmented

chips in case of brittle samples. Chip thicknesses produced during cutting range from approximately 0.025 mm to 2.5 mm [6]. Grinding leads to material removal in as chips which are much smaller in dimension than cutting, with chip thicknesses ranging from 2.5 μm to 0.25 mm. Other special techniques include electrochemical machining (ECM), electrodischarge (EDM), ultrasonic machining (UM) etc. which produce chips of atomic or submicroscopic dimensions [6].

2.1.1 Turning: A Type of Cutting Process

Three most commonly used types of cutting or machining operations are:

i) Turning;

ii) Milling;

iii) Drilling.

Fig.2.1 shows schematic diagrams of these three basic types of machining operations. Beside these most popular types, i.e. reaming, tapping, planning, shaping, sawing, abrasive machining, broaching etc. also constitute types of machining processes [7].

Turning is a process where a single point tool is employed for removing the unwanted material from the component being machined. Such processes are generally carried out on lathes and the important process variables which are changed to manipulate the process are the cutting speed (generally expressed in units of meters per minute), feed per revolution or feed (generally expressed in units of mm per revolution or mm) and the

depth of cut (mm). However, generally, the depth of cut is much larger in comparison to the feed, thus essentially reducing the problem to a plane strain situation where the width of the chip can be approximated to be equal to that of the uncut chip for all practical purposes [6].

2.1.2 Orthogonal Cutting

Orthogonal cutting derives its name from the orientation of the tool's cutting edge with respect to the sample being machined. Here the cutting tool generates a plane surface parallel to an original plane surface of the material being cut. Also, here the tool is set with its cutting edge perpendicular to the direction of relative motion of tool and workpiece [1], as is shown in Fig.2.2.

2.2 Machining Performance Measures

Machinability as a term has traditionally been used to define some level of machining performance, with most of its focus on the workpiece [56]. However, with time, the term has come to involve performance level factors associated with cutting tool and machine tool as well. For aluminum alloys, the machining performance can be categorized into five classes on the basis of chip length and surface characteristics of the final product, namely A, B, C, D and E, in increasing order of chip length and decreasing order of surface finish produced [12,56]. The factors which generally are taken into

consideration in order to determine the machinability performance [56] of a given machining process are as follows:

2.2.1 Cutting Force or Power Requirements

Cutting forces generated or power expended during the process gives important insight into the energy required to be spent for machining the material, hence, into the economics of the process. Also, higher cutting forces show that the material is difficult to machine and vice versa, which has a direct influence on longevity of the tool and surface of the finished product.

2.2.2 Geometry and Chip Breakability

These two factors are the most obvious pointers to the machining performance and give a direct insight into the ease or difficulty of machining a given material. However, the cutting tool and lubrication used during the process should be taken into account before arriving at any conclusive theory about machinability on the basis of chip geometry.

2.2.3 Surface Roughness and Integrity

Surface quality of the machined surface is one of the most important concerns in a machining operation. Surface roughness measurements and optically observed features on the finished surface given important information about the quality of the surface produced and hence about the machinability of the given alloy under the conditions used for the process.

2.2.4 Tool-Wear

Since tool-wear leads to detrimental effects being seen in terms of surface finish and cutting forces, apart from adversely affecting the economics of the process, damage done to the tool being used for machining is another factor that must be taken into account to estimate the machinability performance of an alloy-tool combination.

2.3 Important Machining Process Variables

The outcome of a given machining process depends on a number of parameters. The properties of the workpiece, tool and the machine, all influence the process in different ways. The following section takes a look at some such parameters:

2.3.1 Workpiece Properties

The workpiece or component being machined affects the results of the machining process in several ways. Its geometry and material properties dictate the kind of machining conditions that should be used to obtain the desired shape and finish, and have an effect on results of the operation. Also, the material properties of the component determine the ease of machinability, the power consumed during the process and the efficiency of the process. Ductile materials like pure Aluminum, 6061 Al, copper etc are easier to machine as compared to materials like Titanium and Steel.

2.3.2 Cutting tool properties

The geometry, design and the material properties of the cutting tool has a very significant impact on the performance of a given machining operation. Tools with proper design lead to production of machined parts of consistent geometry, quality and lead to greater efficiency in production due to their longevity. Tools are generally classified on the basis of the cutting edge material and the geometry which includes rake angle (Fig.2.3), clearance angle, and tool tip radius, and the clamping methods. The tool selection for a given machining operation should be on the basis of volume of material required to be removed, the properties of the workpiece material, the required degree of accuracy in geometry and the surface finish for the finished product. An ideal tool must be able to withstand the high stresses and the high temperatures generated during machining and should possess high hardness at high temperatures, high resistance to deformation, high fracture toughness, chemical inertness, high thermal conductivity, high fatigue resistance, high thermal shock resistance, high stiffness for higher accuracy and low friction [8].

Tools most frequently employed include tools made up of High speed steel (HSS) Cobalt enriched high speed steels (HSS-Co) and sintered tungsten carbide (WC), Polycrystalline Cubic Boron Nitride (PCBN), polycrystalline diamond (PCD), and single-crystal natural diamond [8].

2.3.3 Cutting Speed and Feed per Revolution:

Cutting speed (V) is defined as the speed of the lathe rotation in a turning operation and feed (*f*) is defined as the distance, perpendicular to the cutting direction, between the surface machined in the previous tool pass and the surface exposed in the current tool pass Fig 2.4. Both of these factors affect a machining process drastically, and should be selected so to maximize the efficiency of the process.

2.4 Classification of Chips

The unwanted material removed during orthogonal cutting is in form of chips or swarf. Although these are not of any commercial value, the mechanism of chip formation is crucial in determining the force and power and tool-workpiece temperature. Fig.2.5 shows the various kinds of chips produced during orthogonal cutting of metals. The chips produced during orthogonal cutting can be classified into the following main classes:

2.4.1 Continuous Chips

Continuous chips are long, ribbon-like chips generally produced during machining of soft, ductile material such as 6061 Al and copper (Fig.2.5a) These long chips may lead to operational hazards as they may wrap around a tool or workpiece. High speeds and small feeds and small depths of cut are conditions that favour generation of continuous chips.

2.4.2 Discontinuous Chips

Discontinuous chips are fragmented chips characterized by the chip breaking into small segments due to cyclic fracturing (Fig.2.5b), generally encountered during machining of brittle materials such as cast iron. Low cutting speed or at high tool-chip friction and large feed and depth of cut are factors that favour the formation of such chips.

2.4.3 Chip with Built-up Edge

During machining, sometimes the excess material being sheared off is deposited on the rake face of the tool, close to the cutting edge, thus leading to the formation of a built-up edge (BUE) (Fig 2.5c). BUE formation leads to modification of effective tool geometry, thus leading to irregularities in the machined surface. A BUE, once formed, grows until it reaches a critical size and then passes off with the chip. This behaviour leads to a cyclic variation in the surface finish and depth of cut [6] and hence making BUE formation undesirable in a machining operation. This can be achieved by reducing the depth of the cut, increasing the cutting speed, using positive rake tools, or by application of a coolant.

2.4.4 Serrated Chips

Serrated chips are a type of discontinuous chips where partial penetration of the crack into the chips leads to discontinuities in the chip (Fig 2.5d). Shear localization resulting from thermal softening exhaustion of strain hardening mechanisms in the

primary shear zone is sometimes responsible for the generation of serrated chips [9]. Inability of the material being cut to quickly dissipate the heat produced during cutting leads to adiabatic shear and formation of shear bands. Other theories for explaining the formation of serrated chips claim that cyclic cracking of material in front to tool tip and not adiabatic shearing is responsible for the serrated morphology [6, 47]. Also, high hardness of the workpiece, such as in the case of titanium alloys, leads to serrations in chips. Other alloys showing serrated chip formations include A380 [20], AISI 1045[47], etc.

2.5 Deformation Mechanisms and Deformation Zones

During orthogonal cutting, as the metal is sheared by the tool-tip, it undergoes a huge amount of deformation. The deformation has been seen to be concentrated primarily in certain zones in the material in front of the tool tip. These regions are classified as the Primary Deformation Zone (PDZ), the Secondary Deformation Zone (SDZ) and the Tertiary Deformation Zone (TDZ). Following section contains a description of these three zones.

2.5.1 Primary Deformation Zone (PDZ)

The primary deformation zone is formed as the material directly in front of the tool tip undergoes shearing and heavy plastic deformation (Fig.2.6). According to early

assumptions [1,3], the workpiece shearing takes place along a fixed plane called the primary shear plane which passes through the Primary Deformation Zone.

2.5.2 Secondary Deformation Zone (SDZ)

This zone is formed as the chip produced at the tool-tip undergoes further sliding against the rake face of the tool, thus undergoing further deformation due to friction between the two surfaces (Fig.2.6).

2.5.3 Tertiary Deformation Zone (TDZ)

Tertiary Deformation Zone is formed as the newly machined surface undergoes sliding against the flank of the tool, which imparts further deformation to it (Fig.2.6).

2.6 Theories and Mechanical Models for Chip Formation

Various theories have been proposed to explain the formation of chips during orthogonal cutting. The first type, the shear zone models, proposes the existence of a planar or slightly curved zone where shearing takes place ahead of the tool-tip. Merchant [1], Piispanen [3], and others have developed models based on this assumption in an attempt to explain the mechanism of orthogonal machining. On the basis of this kind of model, it was propounded that the shear angle formed during a given orthogonal cutting process will assume such a value that the work expended for the process will be least [1,2,64]. Wright [66] used this principle of minimum work to predict the values of shear

angles in the material ahead of the tool tip and in the chip area. A dislocation mechanics theory for explaining machining was forwarded by Turkovich [35] and was substantiated by microstructural studies of the deformation structure formed during the process by Turley [5,60,65] , which showed dense dislocation substructures in the area close to the machined surface. Another theory for explaining the process proposes that the deformation in front of the tool is not confined to a single plane and is actually spread out in the form of a zone with complex boundaries. Okushima and Hitomi, etc. have proposed models for explaining orthogonal cutting based on this second theory. The following section takes a look various such models proposed over the years:

2.6.1 Card Model by Piispanen and Merchant

The shear plane model or the card model for orthogonal cutting is one of the first attempts at explaining orthogonal cutting. It was first proposed by Merchant [1], Piispanen [3] and Ernst [10]. This model was based on the assumption that during orthogonal cutting, chip is formed by shear along a single plane, called the shear plane (Fig 2.7), inclined at an angle ϕ to the cutting direction, an assumption which is consistent with observation from samples from may interrupted cutting tests [8]. According to it, the displacement of the material due to shear during chip formation is analogous to successive displacement of cards placed in a stack, as shown in Fig.2.7. Each successive card is displaced forward by a small amount along the shear direction,

with respect to its neighbour, as the cutting tool progresses. The figure also shows the crystal structure of the metal as circles drawn on the sides of the stack of cards (Fig.2.8), elongated by in the direction of the major axis of the ellipses produced [1], which is considerably different from the direction of shear, making an angle ψ with it, which was seen to be in conformance with actual experimental results.

Angles ψ, ϕ and α, shown in Fig.2.8, are related as[1]:

$$\cot\psi = \cot\phi + \tan(\phi - \alpha) \quad (2.1)$$

where ϕ the shear is angle and α is the true rake angle of the cutting tool.

The card like elements, each having a finite thickness of ΔX, are displaced by the cutting tool through a distance of ΔS with respect to its neighbour during the formation of the chip. The shearing strain can thus be found as follows:

$$\varepsilon = \Delta S/\Delta X = \cot\phi + \tan(\phi - \alpha) \quad (2.2)$$

$$\varepsilon = \cot\psi \quad (2.3)$$

2.6.1.1 Force Relationships in Orthogonal Cutting Model by Merchant

A force diagram (Fig.2.9 was suggested by Ernst and Merchant[1,10] on the basis of the following assumptions [6]:

1) Chip is continuous with no built up edge.
2) A perfectly sharp tool tip which leads to absolutely no contact between the machined surface and the flank of the tool.

3) A perfectly planar shear plane along which shearing occurs as the tool tip pushes into the material. This shear plane extends from the tool tip to the chip root.

4) The depth of cut is assumed to be very large with respect to the feed of cut, thus reducing the problem to one of plane strain.

5) Shear stress, strain and strain rates are all assumed to be uniform.

The relationship between the various forces on the basis of this force diagrams is as follows:

$$F_s = F_c \cos\phi - F_t \sin\phi \tag{2.4}$$

$$N_s = F_c \sin\phi + F_t \cos\phi \tag{2.5}$$

$$F_f = F_c \sin\alpha + F_t \cos\alpha \tag{2.6}$$

$$N_f = F_c \cos\alpha - F_t \sin\alpha \tag{2.7}$$

where F_c is cutting force, F_t is thrust force, F_s is the shear force on the shear plane, N_s is the normal force on the shear plane, F_f is shear force on rake face and N_f is the normal force on the rake face.

The components of the forces on the rake face can be used to find the coefficient of friction on the tool face (μ):

$$\mu = \frac{F_f}{N_f} = \frac{F_c \sin\alpha + F_t \cos\alpha}{F_c \cos\alpha - F_t \sin\alpha} \tag{2.8}$$

The force of friction between the rake face and chip can be used for estimating the work expended in overcoming frictional resistance to chip motion against tool face and

hence is an important consideration in analysis of work done during orthogonal turning of samples.

2.6.1.2 Shear Plane Angle in Orthogonal Cutting Model by Merchant

Determination of shear angle (ϕ) (Fig.2.3) is critical to estimation of stresses and strains in an orthogonally cut sample. Shear angel can be determined directly from a section of the chip by microscopic observations or by using the cutting ratio (r), which is the ratio of the feed f (distance moved by the tool-bit along the workpiece revolution axis per revolution of workpiece) to the chip thickness t_c (wall thickness of the tube being machined) (refer to Fig. 2.3b and Fig.2.4) as is shown below [6]:

$$r = \frac{f}{t_c} = \frac{AB\sin\phi}{AB\cos(\phi - \alpha)} \tag{2.9}$$

or

$$\phi = \tan^{-1}\left(\frac{r.\cos\alpha}{1 - r.\sin\alpha}\right) \tag{2.10}$$

where AB equals the length of the shear plane and α is the rake angle of the tool (Fig.2.3).

A principle of minimum energy was used to estimate the Shear angle ϕ by Ernst and Merchant [10]. According to this principle, in any given machining process, the shear angle would assume such a value that the magnitude of cutting power, which is equal to the product of cutting speed or cutting velocity and cutting force ($V.F_c$) [8]. An identical

value for the shear angle is predicted if it is assumed that it leads to the maximization of shear stress on the shear plane [8].

$$\phi = \frac{\pi}{4} - \frac{\beta}{2} + \frac{\alpha}{2} \tag{2.11}$$

where β is an angle associated with the resultant of the shear and normal forces on the rake face (F_f and N_f) and can be expressed as:

$$\beta = \tan^{-1}\left(\frac{F_f}{N_f}\right) = \tan^{-1}(\mu_e) \tag{2.12}$$

However, this equation does not yield accurate shear angle predictions owing to the oversimplified assumptions that the shearing occurs along a single plane extending from the tool tip to the chip root, even though it does sufficiently provide an insight into the relation between some of the variables which can be manipulated to maximize the shear angle and as a result lead to minimization of the power consumption during the process. The shear angle can be increased by decreasing the value of β, which can be achieved by decreasing the coefficient of friction, and by increasing the value of α which can be done by changing the tool design.

Ernst and Merchant also realized that the uniform distribution of the shear stress on the shear plane may represent an oversimplifying concept and the actual scenario may be far from being this simple [6]. Experimental work by Ramalingam has shown that a curved shear surface is formed during cutting [11], leading him to conclude that

orthogonal cutting cannot be treated like a problem of plane strain, and that it consists of shear as well as compressive strain.

2.6.1.3. Stresses on the shear plane and rake face

During orthogonal cutting with continuous chip formation, a high strain rate deformation process, plastic flow on the shear plane is characterized by large strain rates and high temperatures produced with normal stresses on the shear plane, as has been pointed out by Shaw [6]. These give rise to high values of homogeneous strains in the absence of gross fracturing and progressive deformation with only small volume of material getting deformed at a time. Also, rake face's close proximity to the shear zone gives rise to a flow constraint for the material getting deformed. Comparison of stress-strain data from orthogonal cutting tests with that obtained from conventional torsional tests showed considerable disparity [6], showing that the flow conditions present during cutting are very different from any other conventional tests.

The shear plane model for explaining orthogonal cutting presents a simplified method for predicting the forces on the shear plane and rake face of an orthogonally cut sample. It assumes that the distribution of shear and normal forces on the shear plane and on the rake face (Fig.2.19) is uniform [1] [12]. From this assumption, the shear stress on the shear plane (τ_s) can be calculated as follows:

$$\tau_s = \frac{\text{Shear force on shear plane}}{\text{Area of shear plane}}$$

or

$$\tau_s = \frac{F_s}{\left[\frac{w.f}{\sin\phi}\right]} \tag{2.13}$$

Since $F_s = F_c \cos\phi - F_t \sin\phi$

$$\tau_s = \frac{F_c \cos\phi - F_t \sin\phi}{\left[\frac{w.f}{\sin\phi}\right]} \tag{2.14}$$

Normal stress on the shear plane (σ_s) can similarly be computed as follows:

$$\sigma_s = \frac{\text{Normal force on shear plane}}{\text{Area of shear plane}}$$

or

$$\sigma_s = \frac{N_s}{\left[\frac{w.f}{\sin\phi}\right]} \tag{2.15}$$

Since $N_s = F_c \sin\phi + F_t \cos\phi$

$$\sigma_s = \frac{F_c \sin\phi + F_t \cos\phi}{\left[\frac{w.f}{\sin\phi}\right]} \tag{2.16}$$

where *f* is the uncut chip thickness (Fig.2.19) that equals to the feed rate and *w* is the width of the chip that equals the depth of cut in turning process.

The shear stress on the chip in contact with the rake face (τ_f) is equal to:

$$\tau_f = \frac{\text{Shear force on rake face}}{\text{Area of rake face}}$$

or

$$\tau_f = \frac{F_f}{w.l} \tag{2.17}$$

$$\tau_f = \frac{F_c.\sin\alpha + N_s.\cos\alpha}{w.l} \tag{2.18}$$

Similarly, the normal stress on the rake face, σ_f , can be written as:

$$\sigma_f = \frac{\text{Shear force on rake face}}{\text{Area of rake face}} = \frac{F_f}{w.l}$$

or

$$\sigma_f = \frac{F_f}{w.l} \tag{2.19}$$

$$\sigma_f = \frac{F_c.\cos_\alpha - N_s.\sin\alpha}{w.l} \tag{2.20}$$

where '*l*' is the length of the sliding contact.

2.6.2 Shear Zone Model by Hitomi and Okushima

Hitomi and Okushima [13,13] outlined the following conflicts in Merchant's model for cutting, based on the simple shear along a single shear plane:

a) A moving metal particle must attain an infinite acceleration when it passes across the shear plane, changing its position from the work region to the chip region.

b) An infinite stress gradient exists on the shear plane.

c) The rate of strain is extremely large compared with that in static material tests.

d) Extremely large strain is produced abruptly on the shear plane, and the relationship between stress and strains in cutting does not agree with that in static material test.

The evidence for presence of a definite curvature at the tool tip, along with the above points of conflict lead to further investigations into cutting in order to better explain chip formation based on the idea of a fan shaped zone or a thick layer. The need to include the effects of work-hardening, a finite strain rate, chip curvature and essentially marginal stability of the flow zone were some of the other factors which contributed to the cause.

Okushima and Hitomi started with the assumption that the work material is a plastic rigid solid [6], and that the boundary surfaces of the flow or shear zone are planes emanating from the cutting edge, as seen in Fig. 2.10 (a and b). The stress in the flow zone is in the yield state. Another assumption made is that the shear stresses on the planes or surfaces OA, OB and OC are equal to each other, and to the yield stress of the material, that is:

$$\tau_{OA} = \tau_{OB} = \tau_{OC} \tag{2.21}$$

The shear stress τ_{OC} can be computed by the formula:

$$\tau_{OC} = \mathrm{R} \sin\beta / ab_1 \tag{2.22}$$

where β is the friction angle of the tool face, a = the contact length between the chip and the tool, b_1 = the width of the tool and R= the resultant force on the tool.

The assumption made in this model about the nature of the shear stresses in zone OAB necessitates that the curvature of the flow zone segment be convex and not concave which is not in compliance with experimental evidence, thus jeopardizing the applicability and effectiveness of this model.

2.6.3 Slip-line Field Theory by Lee and Shaffer

In the slip-line field theory proposed by Lee and Shaffer [14], the deformation is assumed to occur on a plane having an inclination of ϕ with the cutting direction, and is confined to a triangular region as is shown in Fig.2.11. They assume that the material is an ideal plastic, which does not strain-harden and that the shear plane represents the direction of maximum shear stress. The triangular region ABC (Fig. 2.11) is plastically rigid and gets subjected to a uniform state of stress, which equals the yield strength of the workpiece material. Both sets of slip lines are straight in the stress field, being parallel with AB and DC respectively. Also, one set of slip planes is aligned along the direction of the shear plane, which is the direction of the maximum shear stress. The model dictates that the chip does not experience any force after it passes past the plane AC, making it a free surface. Since the direction of maximum shear stress always meets a free surface at

$\pi/4$, the angle CAB is equal to $\pi/4$ [15] and it makes an angle $\pi/4$ to the direction of principle stress, making angle BCD equal to $\pi/4-\beta$ (Fig.2.11).

Assuming uniform stresses on the chip-tool interface are uniform, the principal stresses acting on the boundary BC will intersect it at angle β and $\beta+\pi/2$. The shear angle ϕ is therefore equal to:

$$\phi = \frac{\pi}{4} - \beta + \alpha \tag{2.23}$$

However, the assumptions that the workpiece is perfectly plastic, and that the stresses acting on the chip-tool interface are uniform are not realistic and do not comply well with the experimental observations.

2.6.4 Model by Oxley and Welsh

Oxley and Welsh [16] proposed a different model based on the assumption that the primary shear zone is composed of parallel flat planes, as shown in Fig.2.12, thus predicting the variations in shear angle and cutting forces with variations in cutting speed and feed rate, the results of which agree well with the experimental data. The constant shear angle leads to constancy of shear speed across the chip thickness, as the materials shear on a straight plane and a constant distance under the constant cutting speed thus dictating a straight chip with no curvature, which does not agree with the experimental results, thus limiting the applicability of this model to actual orthogonal cutting.

2.6.5 Model by Dewhurst

Dewhurst proposed a model (Fig.2.13) based on the assumption that the shear plane is made up of several curled surfaces or planes mutually parallel to each other [17]. The curved shear planes lead to curved chip as they dictate non-uniform shear on the shear plane, which lead to curved chips during orthogonal cutting.

These models lead to a physical insight into the process of metal cutting during orthogonal cutting. Various studies have found that the experimental data agrees reasonably well with those predicted by these models, while many have found that there are significant differences in the results. As such, these models are important for use as a framework to better understand the process and to interpret the data obtained by experimental studies rather than for being used for estimation of different parameters associated with the process.

2.7 Machining of Aluminum-Silicon Alloys

Aluminum alloys are extensively used for manufacturing components for automotive and aerospace industry. High strength to weight ratio and good surface finish provided by these alloys are the primary reason for their popularity. Depending on the alloying elements present and the heat treatment given to these alloys, they exhibit a vast range of mechanical properties [8][56]. Research on machinability performance of different aluminum alloys [12,53,82,83] have shown that these alloys possess wide range

of machinability. Table AII-I (Appendix II) shows the relative performance of different cast aluminum alloys during lubricated machining [12,53], where ratings A, B, C, D and E are relative ratings in increasing order of chip length an decreasing order of quality of finish (A: free cutting, very small broken chips and excellent finish; B, curled or easily broken chips and good-to-excellent finish; C: continuous chips and good finish; D: continuous chips and satisfactory finish; E: optimum tool design and machine setting required to obtain satisfactory control of chip and finish) [12]. Following section takes a look at the different aspects of and important research work done in the field of machining of different aluminum alloys.

2.7.1 Classification of Aluminum Alloys on the Basis of Machinability

Aluminum alloys can be classified into different classes for the purpose of studying their machinability [12,56]. A classification on the basis of silicon content is discussed briefly below:

2.7.1.1 Low-Silicon Content and Free-Machining Alloys

These alloys generally contain less than 12% silicon and are easy to machine as the silicon present in them is in the eutectic phase and primary silicon is absent, however, machining may be accompanied by occurrence of BUE in some cases. They are generally soft and have low melting temperatures and are machined using carbide or PCD tools. Typical examples of these alloys are 319 (6% Si), A240 (<=0.50% Si) etc. [12,56].

2.7.1.2 High-Silicon Content Alloys

Known as hypereutectic aluminum alloys, these have a silicon content of more than 12%. Besides eutectic aluminum, they have large primary silicon particles which lead to abrasive wear of the tool used for machining, with the degree of abrasion rising with a rise in the silicon content in the alloy [56]. Besides the cutting forces being high for them, their machinability is hindered by the fact that they cannot be machined using carbide tools, which are more economical than diamond based PCD tools, as the larger silicon particles lead to the tool wearing out very fast. Examples of this class of alloys are A390 (composition (in wt.%): 18.5% Si, 4% Cu, 0.23% Fe, 0.57% Mg,0.07% Mn, 0.02% Ni, 0.05% Ti, 0.1% Zn and the balance Al), etc.

2.7.2. General Machining Conditions for Aluminum Alloys

2.7.2.1 Cutting Force / Cutting Power

In general, the power required to machine aluminum alloys is less than what is expected when its mechanical properties are compared with other metals [7], which proves to be an advantage when selecting aluminum alloys for manufacturing components which need to be machined. Machining of aluminum alloys under lubricated conditions normally generates cutting forces below 1200N [12, 56]. Magnitudes of forces generated during the process have also been found to vary with use of different cutting

speeds and feed per revolution conditions and different tools [6, 7, 56]. Aluminum alloys have been found to show a drastic decrease in forces if PCD tools are used [12,56,82].

2.7.2.2 Chip Geometry and Breakability

The geometry and the ease of breaking off of the chips from the main body of the workpiece are a very direct and strong indicator of the machining performance of a given machining operation. Machining of many aluminum alloys, including 6061 Al, 1100 Al, lead to generation of very long, ribbon-like stringy chips [12,56] which pose serious hazard during the process as they have a tendency to wrap around the cutting tool and the machinery. As these do not break off easily on their own as the process is underway, they also lead to unwanted increment in power expended during the process.

Geometry and breakability of chips is very strongly dependent on the aluminum alloy under consideration. Alloys such as 2011 Al produce chips which break off easily and thus possess excellent chip control, whereas 2024 and 2017-T4 produce long and continuous chips and hence necessitate the use of chip breakers. However, certain aluminum alloys, such as 6061-T6 and 5056-H38 produce chips which are extremely long, sharp and stringy and very difficult to break, even while using a tool with a chip breaker [56]. Softer aluminum alloys, on the other hand, produce soft, gummy chips which require very careful selection of tool-geometry. These also lead to formation of BUE during machining, which leads to a deterioration in surface finish of the component.

2.7.2.3 Surface Roughness

Surface quality of machined component is another performance measure which needs to be taken into account for analyzing the machinability performance of a material (refer to Section 2.2). Study of the quality of surface obtained by machining a material at different conditions is used as a way to find out the relative degree of performance of different machining conditions [6,12,56]. Depending on the composition, aluminum alloys show a wide variation in surface roughness obtained during turning. Softer aluminum alloys such as 2024 have been reported to generate surfaces with roughness values (Ra) as high as 0.18 microns [56]. On the other hand, hypereutectic alloys, such as A390 generate surfaces with comparatively higher roughness values (with Ra values as high as 3microns). High thermal conductivity of aluminum alloys and their low melting temperatures are important concerns during machining of these alloys as they may lead to deformations in the material being machined due to the heat generated during the process [56]. They may also lead to high residual stresses being introduced in the component due to unequal heating of different parts of the component being machined.

Surface quality is also influenced by cutting speed (roughness decreases with an increase in feed), feed per revolution (roughness increases with an increase in feed rate) and cutting tool being used and have been reported to improve if a PCD tool were used instead of a carbide cutter [6,8,12,56,82].

2.7.3 Dry Machining of Aluminum Alloys

Besides carrying away the unwanted chips and material, thus providing a cleaner work surface during machining, lubrication also dissipates the heat produced during machining of materials. However, with time, the machining industry is seeing an increasing trend towards dry machining of materials [6,56,72]. The primary reason for the shift are increasing concerns over the contamination of environment due to the use and disposal of the coolants and lubricants, due to the huge expenses that the use of these cutting fluids mandates and due the health hazard their use poses to the operators.

The increasing thrust towards dry machining has seen aluminum alloys frequently being subjected to the practice, however, their high thermal conductivity leads to unwanted deformation of surface produced and increased adhesion of workmaterial to the tool [56]. This makes the surface characteristics obtained without use of lubrication a continued subject of concern for industry. Formation of BUE and adherence of the machined alloy to the tool surface have lead to further aggravation of the problem. Use of minimum quantity lubrication (MQL) which is machining with minimal use of coolants and lubricants [72], and use of diamond based tools like PCD cutter (used for this study) have been suggested as probable solutions to the above problems [56,72]. However, dry machining of aluminum alloy still remains an attractive alternative to wet machining and hence efforts towards realization of this purpose have been met with continued interest.

2.7.4 Research into Machining of Aluminum Alloys

Substantial research has been done towards exploring the machinability and deformation of aluminum alloys during orthogonal cutting [5,18-20,56]. Zhang and Alpas [21] have investigated the deformation microstructures and variation of shear angles in hot extruded 6061 Al alloy. They also proposed a method for determining the equivalent plastic strains in the sample lying ahead of the tool tip. Ni et al [5] also carried out an extensive analysis of microstructural evolution taking place in the alloys during their orthogonal machining. Microstructural investigations and equivalent plastic strain and flow stress estimation methods used by Zhang and Alpas [21], Elmadagli and Alpas [4,5] and Song [20] has been discussed in details in Sections 2.7.4.1 to 2.7.4.4 below:

2.7.4.1 Microstructural Evolution

Ni et al [5] studied the microstructure generated during orthogonal cutting of Al 1100. Samples were examined under TEM and a mechanism was proposed for evolution of microstructure during the process, as is shown in Fig.2.14. The small elongated subgrains resulted from the initial grain structure fragmenting into smaller units at relatively lowers strains as are present at the lower boundary of the primary deformation zone, with the boundaries between these units accommodating the lattice misorientation accompanying the process. Elongated subgrains with almost dislocation free interiors and smaller equiaxed grains are formed as strains increased further. Sections from the primary deformation zone showed presence of grains elongated along the direction of the induced

strain, forming lamellar structure when examined under TEM (Fig 2.15). The microstructure present in the zone was found to be considerably smaller than the bulk microstructure with newly formed grains showing almost identical orientation in the primary deformation zone. Evidence for recrystallization in the zone was also found in the form of presence of very small grains (Fig.2.16). The chip microstructure was also investigated to reveal elongated grains and high volume fraction of small equiaxed grains with aspect ratio same as those formed in the primary deformation zone which showed that there was no further refinement in grain size after passing through primary deformation zone, even as the plastic strains increased in magnitude from around 0.8 in primary deformation zone to 2.3 in the chip. Based on the microstructural evidence, It was concluded that dynamic recrystallization started as strains rose to about 1.0 and was completed in the secondary deformation zone where evidence of extensive grain growth was found.

2.7.4.2 Estimation of Shear angle

As discussed in Section 2.6.1.2, shear angles can be estimated using the ratio between the feed and chip thickness, directly measureable from a micrograph of a machined section. Principal of minimization of energy (Eqn.2.11) also has been proposed as a method to estimate the magnitude of shear angle.

Zhang and Alpas [21], on the other hand, used the change in orientation of extrusion lines present on the microstructure to estimate the values of shear angles at different locations (Fig.2.17) in the material ahead of the tool tip (Fig.2.22):

$$\phi = \tan^{-1}\left(\frac{\Delta y}{\Delta x}\right) \tag{2.24}$$

Elmadagli and Alpas [4,5] have used the orientation change of the deformed grain boundaries on the cross-sectional plane, which behave like flowlines, to estimate the values of shear angle ϕ at different locations in front of the tool tip during orthogonal machining of Copper (Fig.2.19).

2.7.4.3 Strain Estimation

Effective plastic strain or equivalent plastic strain ($\bar{\varepsilon}$) is the most commonly used invariant function to describe plastic deformation [63]:

$$d\bar{\varepsilon} = \frac{\sqrt{2}}{3}\left[(d\varepsilon_1 - d\varepsilon_2)^2 + (d\varepsilon_2 - d\varepsilon_3)^2 + (d\varepsilon_3 - d\varepsilon_1)^2\right]^{1/2} \tag{2.25}$$

which can be reduced to

$$d\bar{\varepsilon} = \left[\frac{2}{3}(d\varepsilon_1^2 + d\varepsilon_2^2 + d\varepsilon_3^2)\right]^{1/2} \tag{2.26}$$

or

$$\bar{\varepsilon} = \left[\frac{2}{3}(\varepsilon_1^2 + \varepsilon_2^2 + \varepsilon_3^2)^2\right]^{1/2} \tag{2.27}$$

where ε_1 , ε_2 and ε_3 are the three principal strains.

For a worn surface subjected to sliding wear, it has been shown that the equivalent strain generated due to subsurface deformation can be estimated from local shear angle θ measured using deformation of microstructural features like dendrites, flowlines or grain boundaries which show bending in the direction of applied shear stresses [87,89,90]. The shear angle θ is equal to the angle between tangent drawn to the deformed marker at a point of interest and its original orientation at the point (before deformation). The relation between equivalent plastic strain $\bar{\varepsilon}$ and shear angle θ is:

$$\bar{\varepsilon} = \frac{\sqrt{3}}{3}\tan\theta \tag{2.28}$$

It is assumed that since the displacement of the feature, which acts like microstructural markers, are the result of shear deformation parallel to surface, any contribution of compression or rotation of the features is ignored. This theory has been widely used for estimation of equivalent strain in wear experiments [21,88-89] and as has been confirmed by Zaat et al [90], is useful for estimation of equivalent strain in other processes where substantial deformation occurs.

This method of equivalent strain estimation has been found to be applicable and been used for investigating the plastic strain generated due to high deformation and resulting flow of material occurring during machining [4][21,22]. Zhang and Alpas [21] have used this method to estimate the equivalent strains from the orientation change of the extrusion lines or flow lines (Fig.2.21) during orthogonal cutting of 6061 Al. The

same method has been used successfully by Elmadagli et al [4,5] to estimate the strains during dry machinability of commercial purity copper and Al 1100 (Fig 2.22 and Fig.2.23).

According to the definition of shear strain given in Eqn.2.26, its value should remain constant for a given value of shear angle. However, Zhang and Alpas [21] and Elmadagli et al [4] have used the flow line method to show that the strains are non-linearly distributed in the primary deformation zone and the adjoining areas (Fig.2.21, Fig.2.22 Fig.2.23), which prove that the single shear strain values predicted by Shaw for fixed rake angle and cutting velocity (Eqn.2.27) is an over simplification of the problem at hand.

Song [20] has investigated the dry machining of aluminum alloy A380 which produces discontinuous chips during orthogonal machining. It was found that the chip morphology changed from discontinuous chips for as cast sample to serrated type chip when the material was subjected to solution treatment [20]. No secondary deformation zone was found (Fig.2.24), unlike the case of continuous chips produced during studies of Al 1100 and 6061 Al [5,21].

An important observation made during the study by Song [20] was that the second phase particles present in the area in front of the tool tip in the workpiece had fractured and had aligned themselves along the direction of deformation and flow of material being sheared away during the process (Fig.2.24 a and b). Adiabatic shear band formation was

thought to accompany the formation of discontinuity as a result of strain localization in the chips (Fig.2.24a).

Song [20] estimated the plastic strain distribution in the material ahead of the tool tip using the alignment of the fractured particles as an indication of the direction of material flow. Lines were drawn along these patterns traced out by fractured particle flow (Fig.2.24b), and deformation angles along these flowlines were measured by drawing tangents to these. Eqn.2.28 was used for plastic strain estimation (Fig.2.25) in a manner similar to strain estimations using flow lines in Al 1100, 6061-T6 and commercial grade copper done by Alpas et al [4,5,21]. Plastic strain distribution results obtained by Song [20] (Fig.2.24) showed that the strains were mainly concentrated in the region adjoining the shear bands, with the area between the shear bands experiencing relatively smaller strains. She also predicted shear strains (γ) of magnitude up to 12 in the shear bands using the relation between shear displacement between the shear bands formed (d_s) and thickness of shear bands (t_s) proposed by Turley and Doyle [58]:

$$\gamma = \frac{d_s}{t_s} \tag{2.29}$$

Based on the experimental analysis, Song predicted plastic strain of 1.5 (in the vicinity of the shear bands), shear strain equal to 12 (in the shear zone) and flow stress equal to 285 MPa as the initial failure conditions for aluminum alloy A380 [20].

2.7.4.4 Hardness Measurements and Flow Stress Measurements

Flow stress in a material is defined as the instantaneous value of stress required to continue deforming the material plastically or the stress required to sustain plastic deformation at a particular strain. Flow stress of a material is a function of strain and strain rate. The relationship between flow stress and strain rate ($\dot{\varepsilon}$) (at constant strain (ε) and temperature (T)) can be expressed as [63]:

$$\sigma = C(\dot{\varepsilon})^m \Big|_{\varepsilon,T} \tag{2.30}$$

where m is the strain rate sensitivity of the material. Besides strain, flow stress depends on material properties of the workpiece which include chemical composition, crystal structure, phase constitution, exit microstructure, grain size etc.

Indentation hardness measurements done on a material can be used to find the flow stress of the material in front of the tool tip [4,5]. Since indentation hardness test measures the resistance offered by the material to plastic indentation, the quantity measured is equivalent to the flow stress at a relatively small strain ($\bar{\varepsilon} < 0.1$), low strain rate ($\sim 10^{-3} s^{-1}$). An elastically deformed zone is present around the plastic zone of a hardness indentation which offers resistance to plastic flow, whereas in a compression test, the entire specimen deforms plastically, and side-flow of material happens without any resistance from the surrounding air. Thus, the mean flow stress required to cause plastic flow in the hardness test is greater than that for a compression test, both being related as [6]:

$$H = C\sigma \tag{2.31}$$

where H is the hardness value from Vickers Hardness test (in MPa), σ is the equivalent flow stress from compression test, and C is the constant factor for the hardness test. Experimentally determined value of C equals three for Brinell, Vickers and Knoop hardness tests, with its origins still remaining a subject of study [6].

Elmadagli and Alpas [4] have used microhardness measurements taken along regular intervals lying along the points of intersection of a grid in the material ahead of the tool tip to characterize the deformation taking place in Al 1100 and copper during orthogonal cutting. Flow stress values were calculated using Eqn. 2.31 to get an estimate of the stresses present in the matrix at these locations, which in turn were used to find the iso-stress contours (Fig.2.26).

Similar method was used by Song [20] to estimate the flow stress of orthogonally cut A380 (Fig.2.27). It was found that in A380, stress magnitudes increased from a lower value of 220MPa to a highest of 285MPa, while lower stresses were present in the shear zone (246MPa), a phenomena which was attributed to thermal softening in the bands during shearing [20].

2.8 Discontinuous Chip Formation

Discontinuous chips or serrated chips were one the last kinds of chips to be identified as distinct type of chip produced during orthogonal cutting processes [47].

These are characterized by saw-tooth like features on the chips which may or may not be present as isolated segments (Fig.2.28 (a and b)). These were identified during the machining of titanium and its alloys. Research into the generation of sawtooth type chip has been mainly concentrated on machining of titanium alloys [48,49,50,51,58] and machining of steel [52,53]. The steps in the formation of discontinuous or serrated chip formation can be summed up as shown in Fig 2.29.

According to Cook et al. [23], the chip formation process starts at a high shear angle, which is followed by sliding up the rake face which in turn leads to an increase in the friction force, deterring the motion of the newly formed chip and causing it to bulge, with a simultaneous decrease in the shear angle. The strain along the shear plane increases constantly while the bulging occurs, until it reaches the point of ductile shear fracture. This fracture leads to the formation of a segment similar to saw-teeth. This process continues cyclically leading to discontinuous or serrated chip formation. Davis and Burns [54,55] compared the repeated adiabatic shear band formation in machining of certain metals at large cutting speeds with the formation of a single shear band taking place during dynamic torsion test at sufficiently large strain rates to come up with an explanation for the cyclic formation of adiabatic shear bands during machining, which leads to the generation of the saw-tooth segments. They concluded that there were many differences in the physics of machining and dynamic torsion processes with the shear stress in machining existing over the contact area between the tool and the work-piece

material being completely inhomogeneous. They also came up with the explanation that in high-speed machining, flow of workpiece material in front of the tool tip can become convection-dominated, which may lead to the tool moving faster than the flow of the thermal front generated due to the heat produced during the process, which in turn may lead to cyclic oscillations in the plastic flow of the workpiece material, hence leading to formation of the repeated adiabatic shear bands and saw-tooth morphology.

Several theories have been proposed to explain the mechanism of discontinuous chip formation. Cowie et al. [46] presented a review of several flow localization processes taking place during similar processes. Adiabatic shear theory of discontinuous chip formation suggests that sawtooth chip is formed primarily because of a catastrophic thermoplastic instability in the material being cut [53], which is characterized by a decrease in flow stress due to thermal softening associated with an increase in strain which more than offsets the effects of the associated strain hardening [6]. This mechanism is also called the adiabatic shear deformation (refer to Section 2.8.1).

According to Drucker [24], discontinuity in chips increases with lowering of cutting speed and with an increase in feed. For completely homogeneous material, the transition from continuous to discontinuous chips would be abrupt. However, it would be rather gradual for a non-homogeneous material. At lower speeds, fractures produced in the chips are almost complete and deep, leading to segmental chip formation. With an increase in cutting speed, time available for fracture decreases, which results in incomplete fracturing

and plastic deformation without fracture on all planes sheared for any rake angle replacing the complete fracturing taking place at lower temperatures, thus making the chip continuous. It has also been suggested that the discontinuous chip formation is favored by lowering of cutting speeds during cutting of steel because of low temperatures at the tool-chip interface, which lead to a rise the strength of the workpiece as well as frictional stresses near the cutting edge [8]. Low rake angles, rigidity of tool, high feed rates and presence of inhomogeneities in the workpiece material, like second phase particles also lead to formation of discontinuous chips in metals.

Titanium and nickel based superalloys, hardened AISI 4340 steel etc have been seen to produce discontinuous chips during orthogonal cutting.[25].

2.8.1 Adiabatic Shear Bands

Adiabatic shearing is an important part of high-strain rate deformation, such as happens during machining of metals, impact, penetration, fragmentation, etc. In metals, normally, around 90% of the work of deformation at slow strain rates is converted to heat and is dissipated. However, as shown by Semiatin et al [62], high strain rates and low thermal conductivity in workpiece material may lead to heat not getting dissipated from localized bands occurring as zones of intense shear deformation, which in some cases occurs together with microstructural modification of the original material, separated by regions of relatively lower and more homogeneous deformation. These bands are also

very conducive to crack propagation which leads to catastrophic failure in the workpiece [26][44]. Thus, shear bands are formed due to thermo-mechanical instability that arises when strength loss due to thermal softening becomes greater than the increase in strength due to strain or strain rate hardening [27]. Even though some heat is always lost, making the process not an ideal adiabatic one, the term is used here to show that the amount of heat lost is very low and that the heat produced is mostly trapped in the bands [26][27][28].

2.8.1.1 Types of Adiabatic Shear Bands

Shear bands can be classified as deformed or transformed depending upon whether or not they are accompanied with a phase change in the material and the extent of adiabatic strain localization [29].

a) Deformed bands: These are very narrow bands occurring at very high shear strains (up to 100) (Fig.2.30). This kind of process is not accompanied with any phase change in the material, even though the grains present in the band show extremely high amount of distortion [26]. Band thicknesses vary inversely with the hardness of the work material and microhardness measurements show an incremental trend in hardness values towards the band-centre. [30]

b) Transformed bands: These bands are extremely thin bands and possess extremely high hardness (Fig. 2.31). Formation of transformed bands is accompanied with phase change in the material lying in the region where the band is formed.

Both of these bands may occur concurrently in a workpiece undergoing deformation, depending upon the material properties and the type of deformation process it is subjected to.

Discontinuous or serrated chips formed during orthogonal cutting also exhibit shear bands. Orthogonal cutting experiments carried out on steel [52,53] have shown evidence that adiabatic instability in the shear zone resulting from the reversion of martensitic to austenite contribute to discontinuity in the chips [31] . Similar results were found during orthogonal cutting experiments on titanium alloys [6] [48- 51]. These results have lead to the conclusion that catastrophic shear occurs at a plastically deforming region within a material when the slope of the true stress-strain curve or that of the load deformation curve for the material in this zone equals zero [26,32]. A criterion for this failure in the primary shear zone, based on the thermo-mechanical properties of the material was thus formulated by Recht [32] (Eqn.2.31):

$$0 \le \frac{\dfrac{\partial \tau}{\partial \gamma}}{-\left(\dfrac{\partial \tau}{\partial T}\right).\left(\dfrac{dT}{d\gamma}\right)} \le 1.0 \qquad (2.32)$$

where τ is the shear stress, γ is the shear strain and T denotes the temperature respectively. The local rate of change of temperature has a negative effect on the strength of material at the point (making $\frac{dT}{d\gamma}$ carry a negative sign). This reduction in strength more than compensates for the effect of strain hardening when the ratio lies between 0 and 1, thus resulting in catastrophic failure. No catastrophic failure will occur when it is greater than 1, in which case, the effect of strain hardening is more than that of thermal softening.

2.9 Measurement of Cutting Forces

Analysis of forces involved in cutting is an important part of analyzing a machining operation. These forces determine the power needed for the process and the bearing loads, they cause deflections in the tool holder as well as in the entire machine and may also lead to vibrations in the machine and tool chatter. They also give a fair idea about machinability of work-material. Several theoretical methods have been suggested for estimating the machining forces from various cutting parameters, for example, Brown et al. suggest a way to estimate the forces from the contact area between the tool and the chip formed [45]. Measurement of cutting forces during the actual process and using it to estimate other factors like friction and shear stress [1] is a very common way of analyzing a given orthogonal machining process.

During orthogonal cutting, the force on the chip, applied by the tool, lies in a plane normal to the cutting edge of the tool (Fig.2.32). This force can be broken into two components, the cutting force (F_c) which lies in the direction of the tool's movement into the material and the thrust force (F_t) which is perpendicular to the cutting edge, and goes into the material (Fig. 2.32). These two forces may be used to calculating many other important parameters for the cutting operation as given by equation 2.4-2.7.

Measurement of cutting forces is usually done using specially designed dynamometers which are generally mounted between the tool or workpiece and a non-rotating part of the machine being used for cutting [12]. In most of the dynamometers used for measuring cutting forces, the tool forces is determined by measuring the deflections or strains in the elements supporting the cutting tool. High rigidity of the instruments along with good strain responses are required for ensuring dimensional accuracy, minimum tool chatter and accuracy in measurement of forces during the cutting operation [33]. The frequency response of the dynamometer is an important concern during force measurements at high cutting speeds. Piezoelectric platform dynameters, one of the most popular devices being used for the purpose presently, have bandwidths between 800 and 1000 Hz [8].

2.10 Energy Considerations in Orthogonal Cutting of Metals

Specific cutting power, unit cutting power, or specific cutting energy is the power required to machine a unit volume of the sample and can be measured from the measured cutting forces. Magnitude of cutting power provides a means to compare the machinability of different materials and also gives an idea about the efficiency of the process [8][59].

In turning, the power consumption is calculated by finding the product of the cutting speed (V_c) and tangential cutting force (F_c). The volume of material removed per unit time during a turning operation on a tubular sample with wall thickness '*d*' and feed per revolution equal to *f* is equal to:

$$Q = d.f.V_c \tag{2.33}$$

The specific cutting power, u_s, is given by:

$$u_s = \frac{F_c + F_v}{d.f} \tag{2.34}$$

where '*d'* is equal to the wall thickness of the sample and '*f*' is equal to feed rate.

The area under the stress-strain diagram resulting from the material deformation in a machined sample also can be used for finding the energy expended during the process. This method has been used by Elmadagli and Alpas [4] to predict the energy consumption during orthogonal cutting of commercial grade copper, using the strain gradients on the sectioned sample. Fig.2.33 (a) shows the cumulative stress strain

relationship for the workpiece materials (commercial copper and Al 1100) and Fig.2.33 (b) shows the resulting distribution of plastic work in Al 1100 ahead of the tool-tip. For each increment of equivalent strain $\bar{\varepsilon}$ in the workpiece, the work of plastic deformation per unit volume of material removed (W) is given by:

$$W = \int_{\bar{\varepsilon}_n}^{\bar{\varepsilon}_{n+1}} d\bar{\varepsilon} \tag{2.35}$$

They found that the equivalent stress-strain relationship in the material ahead of the tool tip followed Voce's equation [61] for both commercial copper and Al 1100 subjected to orthogonal machining [4] and hence the energy expended in plastically deforming the materials during the process was estimated using Eqn.2.35 and the Voce's equation (Eqn.2.36):

$$\bar{\sigma} = \bar{\sigma}_s - (\bar{\sigma}_s - \bar{\sigma}_o)\exp\left(-\frac{\bar{\varepsilon}}{\bar{\varepsilon}_c}\right) \tag{2.36}$$

$$W = \int_{\bar{\varepsilon}_n}^{\bar{\varepsilon}_{n+1}} \left(\bar{\sigma}_s - (\bar{\sigma}_s - \bar{\sigma}_0)\exp\left(-\frac{\bar{\varepsilon}}{\bar{\varepsilon}_c}\right)\right) d\bar{\varepsilon} \tag{2.37}$$

where $\bar{\sigma}$ is the equivalent stress, $\bar{\sigma}_s$ is the saturation stress, $\bar{\sigma}_0$ is the flow stress of the material and $\bar{\varepsilon}_c$ is a constant.

Steep rise in the work of deformation was estimated in the vicinity of the tool tip and in the secondary deformation zone which showed a concentration of plastic work in these areas.

2.11 Temperature Distribution in Orthogonal Cutting

Cutting temperatures influence the mechanical properties of the work material in the zones where a temperature rise takes place, mainly the primary deformation zone, and hence affect the cutting forces. They also affect the productivity and life of the cutting tool [8] as excessive rise in temperature may lead to wearing out of the tool faster, or may lead to dimensional changes in it, thus affecting the quality and surface finish of the turned sample.

During cutting of metals, energy is consumed mainly in deforming the workpiece to produce the chip and in overcoming friction between the tool and the workpiece, almost all of which gets converted to heat [6,8,34]. This heat generation leads to a rise in temperatures mainly in the primary shear zone where an enormous amount of plastic deformation occurs due to shearing, in the secondary shear zone where the chip undergoes friction against the rake face of the tool and between the machined surface and the flank surface of the tool.

Various methods have been suggested for estimation of temperature distribution in an orthogonal cutting process, including use of a thermocouple, measurement of infrared radiations emitted from the cutting zone and coating specimens with thermosensitive paints [8].

A method to predict the rise in temperature (ΔT) in the primary deformation zone has been proposed by Turkovich [35] and Nakkalil [36] :

$$\Delta T = \frac{\zeta}{\rho C_p} \int_{\bar{\varepsilon}_n}^{\bar{\varepsilon}^{n+1}} (\sigma) d\bar{\varepsilon} \tag{2.38}$$

where is the flow stress, ζ is the fraction of deformation energy converted to heat, ρ is the density of material and C_p is the specific hear capacity of the material. Elmadagli and Alpas [5] used this method to estimate the temperature distribution in the primary deformation zone during orthogonal cutting of Al 1100 to find a considerable rise in temperature near the tool tip. They also noticed that the temperature steadily rises as one moves from the chip root to the tool tip, along the shear plane (Fig.2.34).

Shaw and Loewen [6] present a method to estimate the temperature in the shear zone:

$$T_{sz} = \frac{\tau.\gamma}{\rho C_p} \left(\frac{1}{1 + 1.328\sqrt{\frac{k.\gamma}{v_c.d}}} \right) + T_{amb} \tag{2.39}$$

where τ is the shear stress, γ is the shear strain, ρ is the density, C_p is the specific heat and k is the thermal diffusivity of the material, T_{amb} is the ambient temperature, v_c is the cutting speed and d is the depth of cut for the sample. Song [20] applied the above method to estimate the temperatures in the shear zone for orthogonally turned aluminum alloy A380 to find that the heat produced during segmented or discontinuous chip formation is concentrated in the shear zones, with negligible rise in temperatures in the zones separating the shear zones.

2.12 Friction in Orthogonal Cutting

As the newly formed chip undergoes sliding against the rake face of the tool, it experiences a force of friction due to the relative motion between the two surfaces. This friction in orthogonal cutting influences the primary deformation, built-up edge formation, cutting temperatures, tool wear, etc and hence it is important to analyze it in order to better understand the process. The conditions present on the interface between the tool and the chip are very crucial in determining the tool temperatures and the stresses which are very important parameters in tool design with the objective of minimizing power consumption and developing better surface finish [67,68]. However, even after extensive amount of studies directed towards understanding the friction in turning, the inaccessibility of the interface due to the geometry and configuration of the process makes generation of any accurate model to explain this phenomena an elusive task [67].

Various models have been suggested, which include Zorev's [69] model which is based on the assumption of existence of a sticking zone and a sliding zone in the region of contact between the tool and the chip. Studies into the contact between the two surfaces by Trent [28,70,71] also showed evidence of high friction leading to development of a seizure zone. Analyzing the forces and stresses on the rake face of the workpiece or the chip, when in contact with the tool on the basis of Coulomb sliding friction [63], the friction coefficient, μ_e, in terms of the component of the force applied by the tool on the

workpiece parallel to the rake face F_p and the component perpendicular to it N_p can be estimated as follows [6,43]:

$$\mu_e = \frac{F_p}{N_p} \tag{2.40}$$

From (Fig.2.35)

$$F_p = F_c \sin\alpha + F_t \cos\alpha \tag{2.41}$$

and

$$N_p = F_c \cos\alpha - F_t \sin\alpha \tag{2.42}$$

Thus,

$$\mu_e = \frac{F_p}{N_p} = \frac{F_c \sin\alpha + F_t \cos\alpha}{F_c \cos\alpha - F_t \sin\alpha} \tag{2.43}$$

It has been observed that values for friction coefficient measured for cutting tests are higher than those for conventional sliding tests, with values above 1.0 being very common [8,56]. Fig.2.36) shows values of coefficient of friction (COF) (μ_e) measured for cutting steel as reported by Bailey et al [84]. Higher magnitudes of COF in these processes can be attributed to the fact that the chip surface undergoing sliding against the rake face is newly formed and hence more prone to forming atomic bonds with the rake face, thus opposing the relative motion of the two surfaces [8].

It can thus be inferred from the literature reviewed above that machining is an extremely complex process and in spite of extensive research having been directed into understanding of the process, there still remains a great need for conducting further

investigations into the filed, which should include actual machining experiments to study the process and analysis of samples after they have been machined. Investigations also need to be directed towards comparing dry machinability performance of different alloys and ultimately with wet machinability performance of the same alloys in order to minimize the use of lubricants and coolants during the process. Efforts towards understanding the mechanisms that lead to a certain type of chip geometry over another type are also required. Apart from the prototype testing, research is also required to gather data and use it for construction of numerical models which would be able to predict the outcome of a given machining process accurately, thus leading to freedom from the vagaries of procuring the sample and subjecting it to the actual cutting process.

2.13 Fracture of Second Phase Particles

Study of damage to the second phase particles present in an alloy constitutes an important part of investigations into a given deformation process. Machining is a high deformation process and the material being cut is subjected to extensive distortion and deformation in the region ahead of the tool tip. Any second phase particle present in the material is thus subjected to high stresses and strains during cutting. As such, a complete analysis of machinability of a material should include an investigation into the particle fracture accompanying the same.

Research has shown particle cracking to be a function of particle size [40-43,85], general microstructure [43] and stress applied [43]. Cracking of silicon particles present in alloys with different microstructures subjected to plastic deformation processes were studied by Caceres et al [42]. It was found that the number of cracked particles increased with an increase in applied strain. Research [40-43] has also shown that larger and longer particles, with higher aspect ratio are more prone to cracking and fracturing during plastic deformation. Stresses in the particles during cracking were found to follow a Weibull model [42]. Caceres [42] concluded that if fracture is assumed to occur at a critical damage level to the particles, the alloy ductility can be expressed as a function of microstructure (dendritic cell size and average particle size and aspect ratio) [42].

Riahi et al [85] studied the fracture of silicon-rich intermetallic particles in an eutectic Al–Si alloy subjected to sliding contact (using a pyramid indenter) and concluded that stress at the particle root/matrix surface interface was a function of hardness of the particle under consideration. High tensile stress (2.5 GPa) were estimated in the particles when the alloy was subjected to sliding wear. Riahi et al also show that below a critical thickness, particles fractured easily and decohesion of the particles from the matrix was observed. Study of particle fracture in an Al-Si alloy subjected to scratch test revealed that particles fracture in two different ways, first with fracture initiating from the root of the particles, and second with fracture initiating from the edges of the particles [86].

Zhang [73] showed that during machining of 6061-10vol%Al2O3 composite, the secondary reinforcement particles show rotation and decohesion from matrix. Also, the decohesion was found to occur in certain fixed directions which were attributed to the high amount of deformation in these directions. Severe particle fracture was also observed by Song [20] during machining of A380 alloy and the fractured particles were found to align themselves in the direction of plastic deformation of the matrix.

2.14 Focus of This Work

As can be concluded from the literature survey above, machining is one of the most important and an extremely complex shaping process. It is influenced by a number of parameters, which include properties of workpiece and the tool, the machining conditions being used, use of lubricants and coolants, etc. A large proportion of the metal cutting carried out in the industry today is wet machining, one which uses coolants and lubricants for providing lubrication between and cooling down the workpiece and tool during the actual process, for removing chips or swarf generated and in some cases for preventing edge build-up on the workpiece [8]. However, use of lubrication during cutting is accompanied by several concerns which include high cost of cutting fluids, concerns regarding their safe disposal and health hazards to workers resulting from occupational exposure to cutting fluids [56,8]. This has resulted in a growing interest in reducing the use of cutting fluids and in dry machining of materials.

This brings into focus this work, which investigates the dry machining of cast aluminum 6% Si alloy 319 Al, a material used extensively in the automotive industry. As has been discussed above (Section 2.3), parameters like cutting speed, feed per revolution are one of the main factors influencing the outcome of a given machining operation. Thus, this work examines the effect of change in cutting speed and speed on dry machining of the alloy by subjecting it to turning under an array of different cutting conditions. Since 'machinability' of a material is judged on the basis of forces generated and the corresponding power requirements for the process, the surface finish of the component subjected to the operation and the geometry and breakability of the chips generated, this work investigates each of these parameters to assess the dry machinability performance of 319 Al.

As the literature survey highlights, the study of deformation structures produced during the process is important for understanding the micromechanisms of the chip formation process. As such, this work also studies the plastic deformation in the workpiece subjected to dry orthogonal machining with the area of interest being the region ahead of the tool tip, where the chip formation starts, and the region beneath the machined surface, which is the actual surface generated when a component is subjected to machining.

This work also investigates the mechanism that leads to the discontinuous chip formation that takes place when 319 Al is machined under dry conditions, and studies the

applicability of the several models proposed to explain chip formation, as discussed in the literature survey, to the microstructural observations made during the work. This study also investigates the fracture of silicon particles present in the alloy during machining.

Thus, this work aims at carrying out in-depth analysis of the various aspects of machining 319 Al under dry conditions to assess its dry machinability performance and understand the deformation of the material during the process.

FIGURES – CHAPTER 2

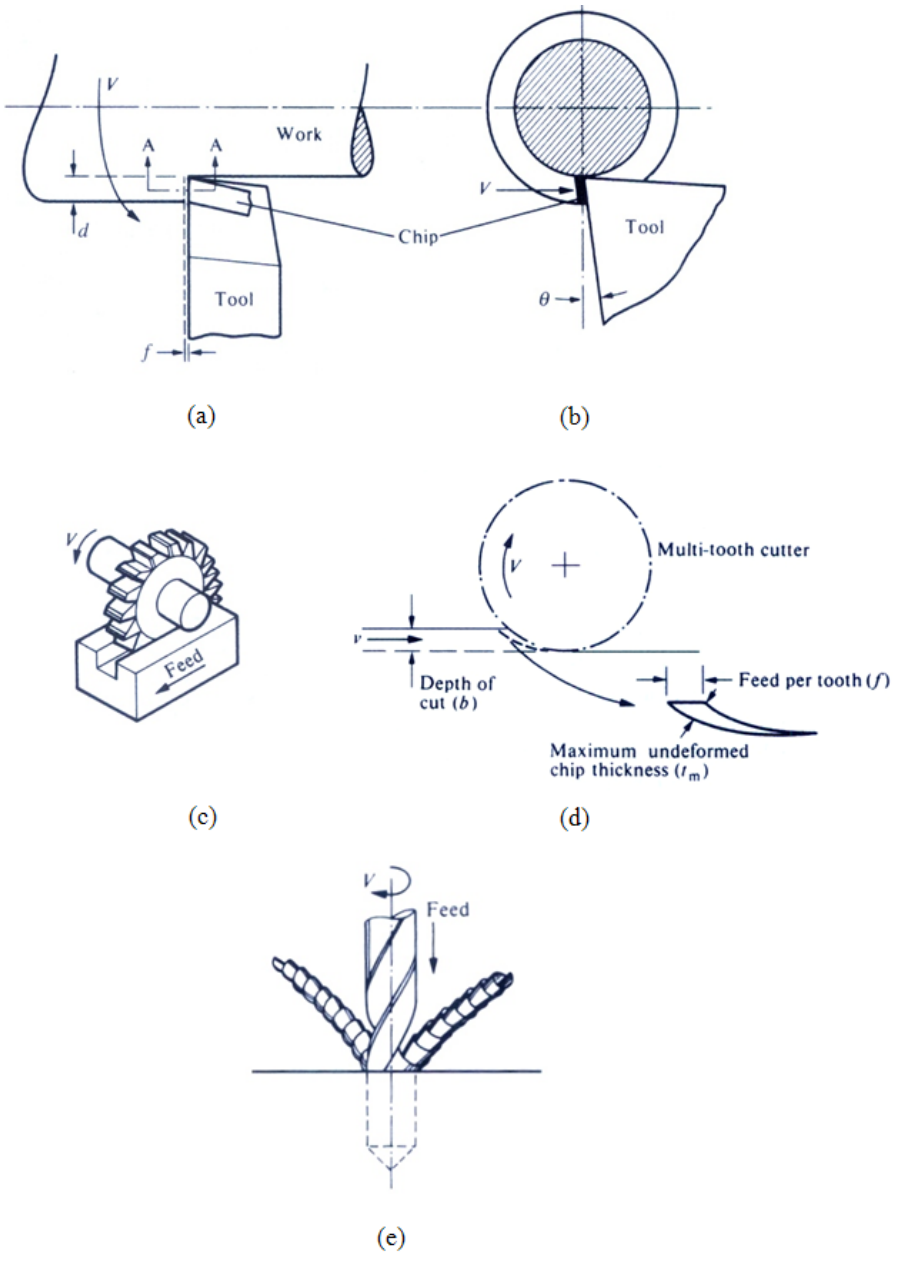

Fig.2.1. Types of machining processes: (a) Single point turning operation plan view, (b) Single point turning operation side view, (c) face milling process, (d) chip production during face milling process, (e) Twist drilling process showing chip production during turning [6]

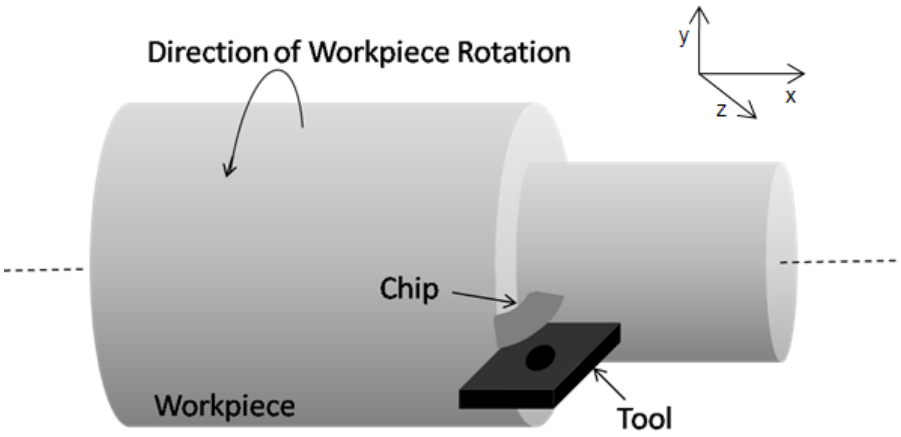

(a)

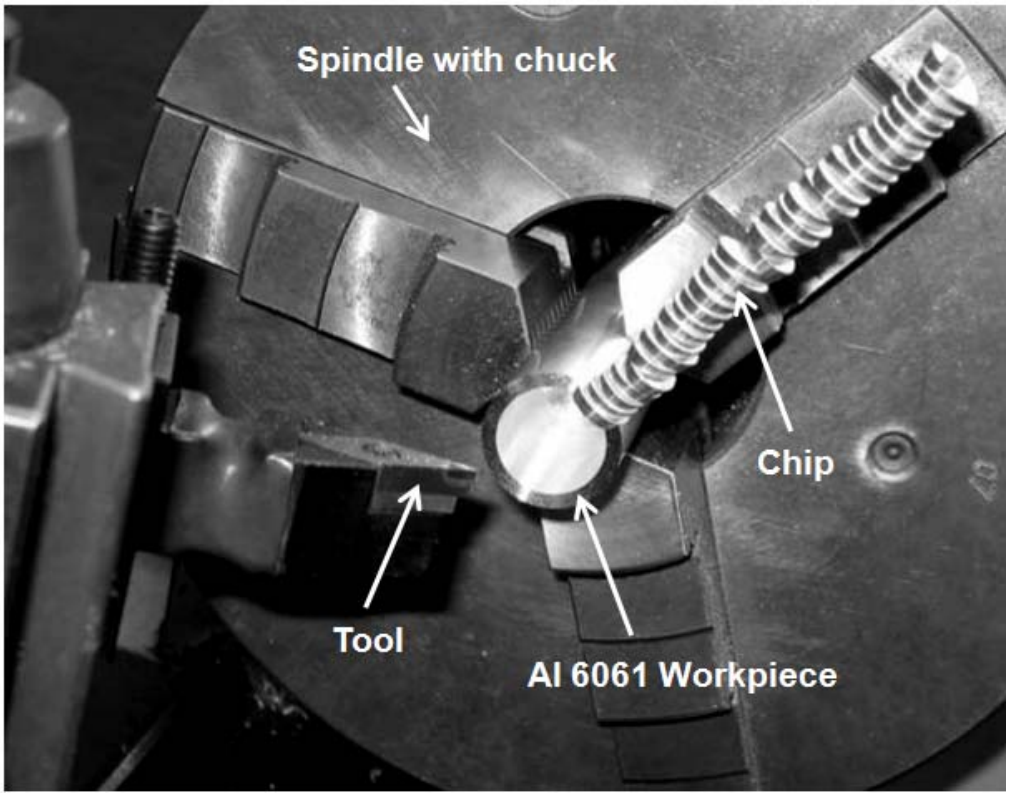

(b)

Fig.2.2. (a) Schematic diagram showing orthogonal cutting process, and (b) chip generation during orthogonal cutting process.

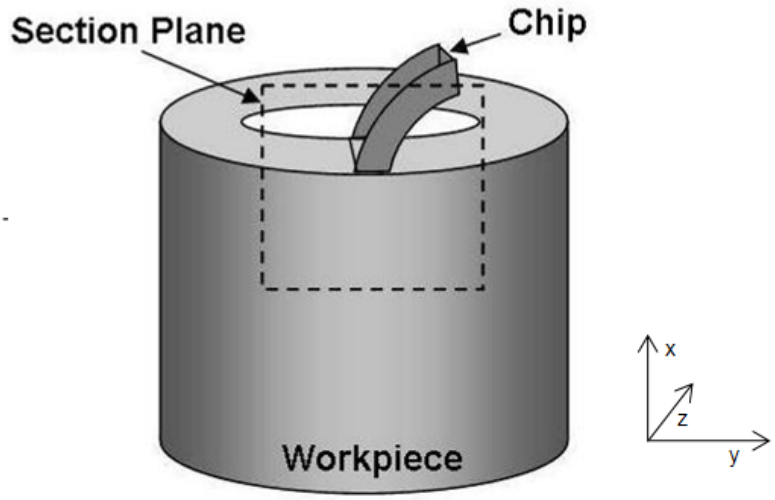

(a)

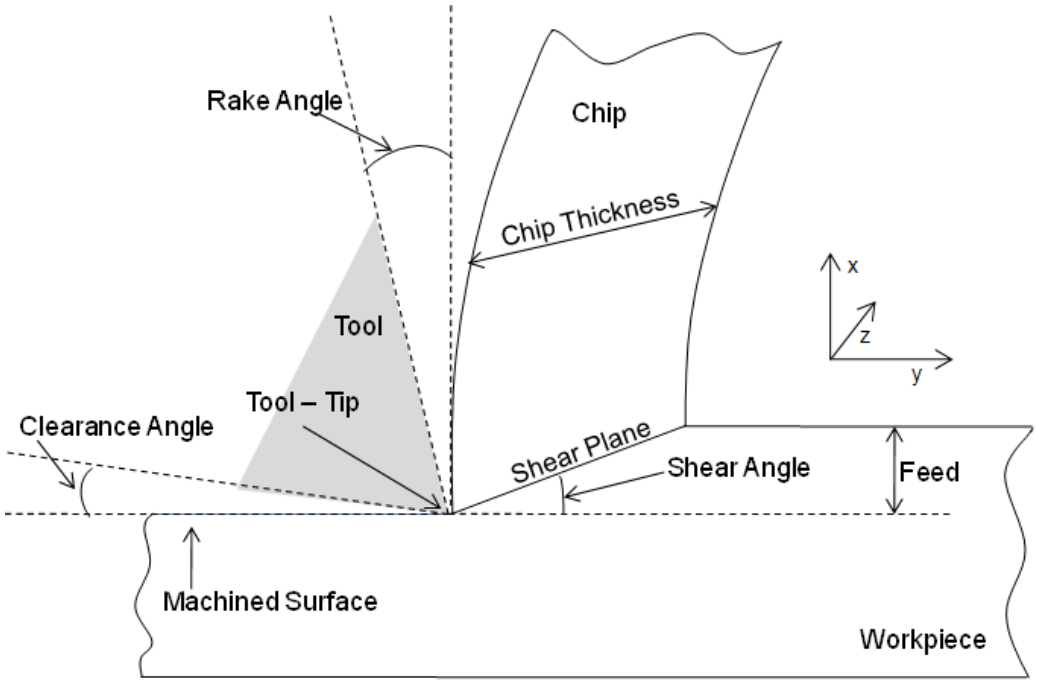

(b)

Fig.2.3 Schematic diagram showing (a) plane of sectioning of machined samples for analysis, (b) important machining parameters on a metallographic section obtained by sectioning the orthogonally cut sample.

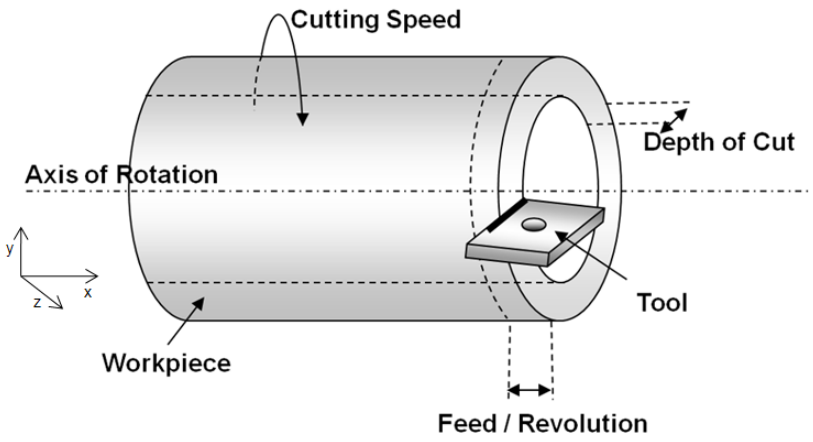

Fig.2.4. Schematic showing parameters like cutting speed, feed and depth of cut in an orthogonal cutting set-up.

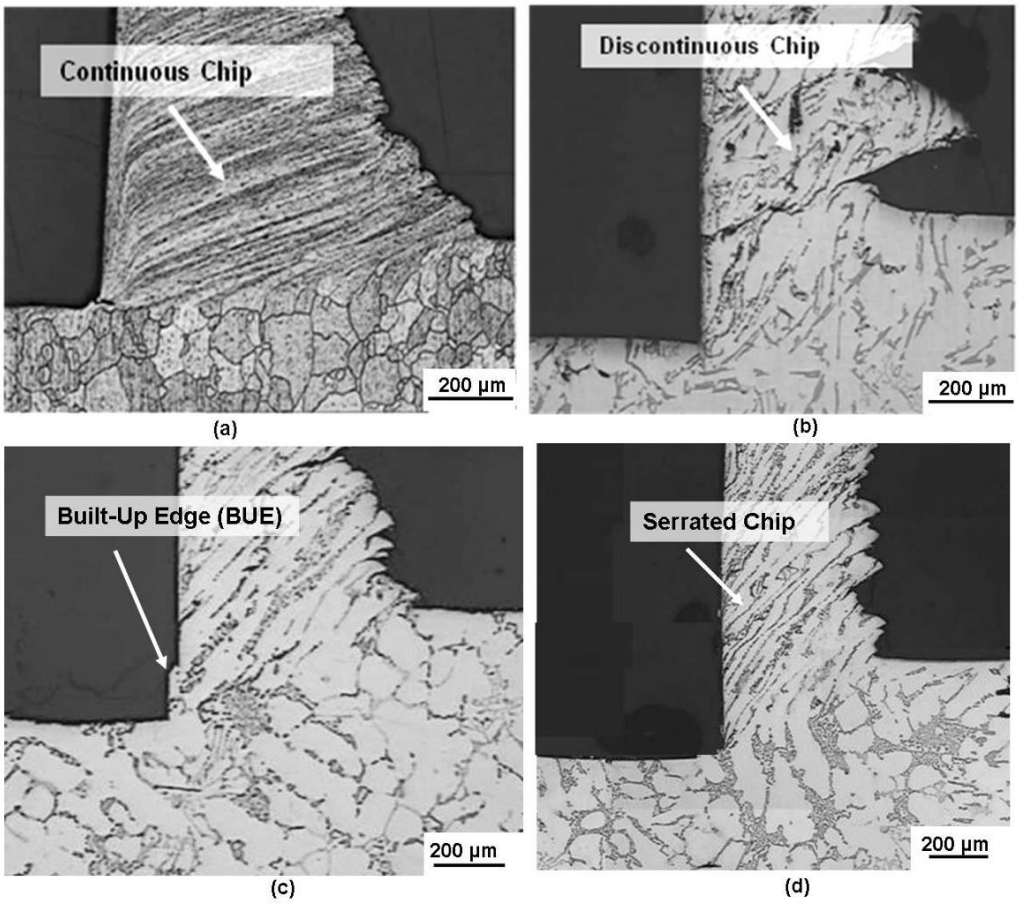

Fig.2.5. Various types of chips produced during orthogonal machining: (a) Continuous Chip, (b) Discontinuous or sawtooth chip, (c) Chip with BUE, (d) Serrated Chip.

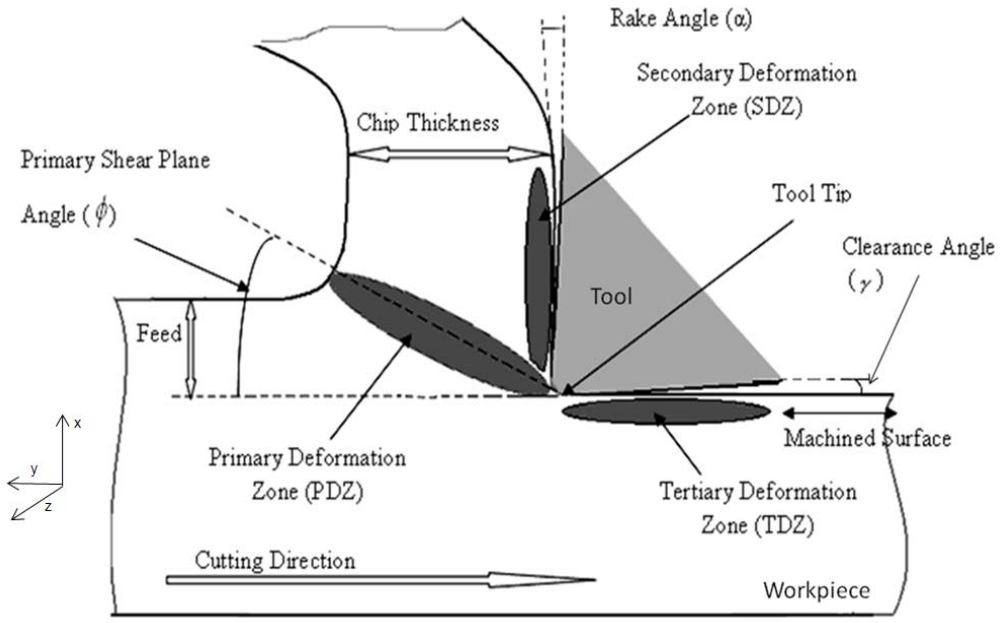

Fig.2.6.Schematic diagram of sectioned orthogonally cut sample showing important deformation zones and cutting parameters.

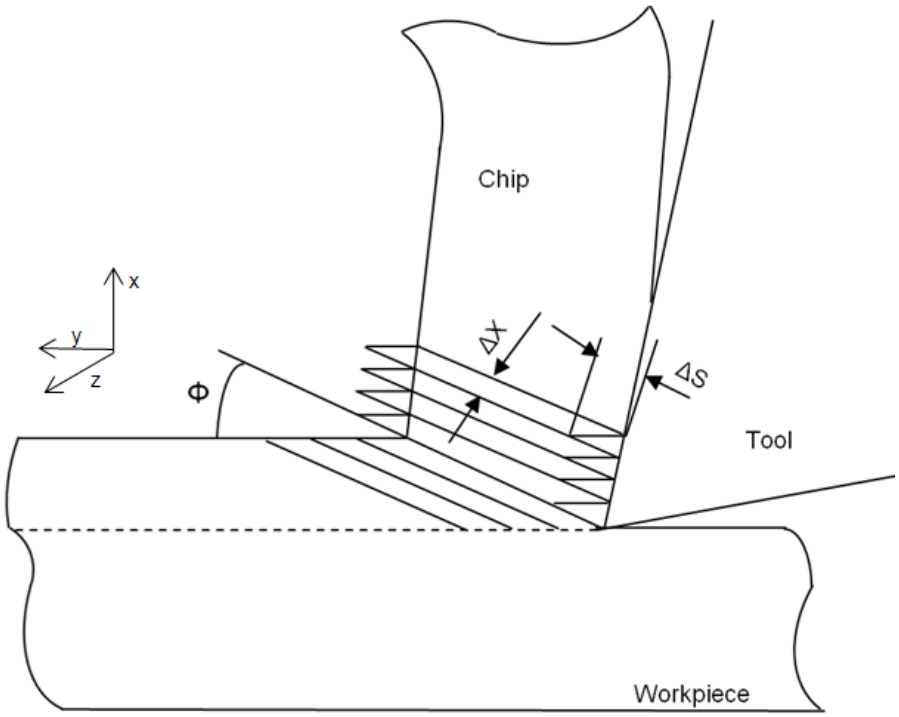

Fig.2.7. Merchant and Piispanen 'Stack of Cards' Model, illustrating mechanism of formation of continuous chip and the resulting deformation of crystal structure [1].

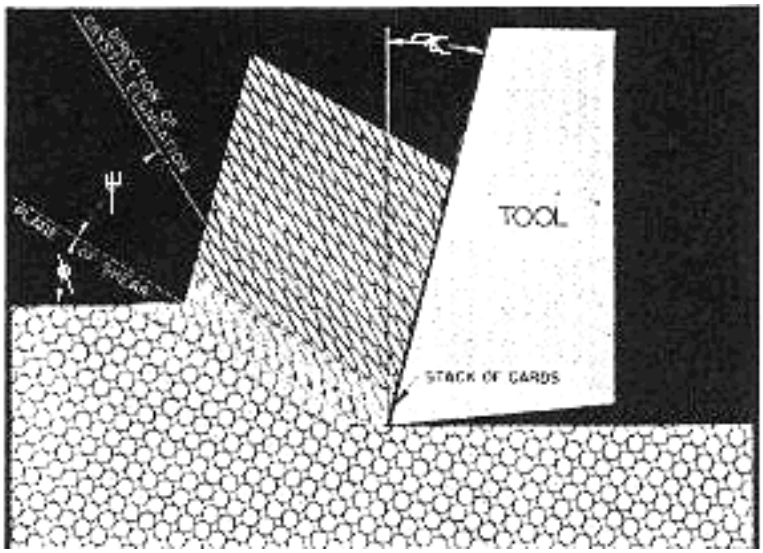

Fig.2.8. Idealized model for the Orthogonal Cutting [1].

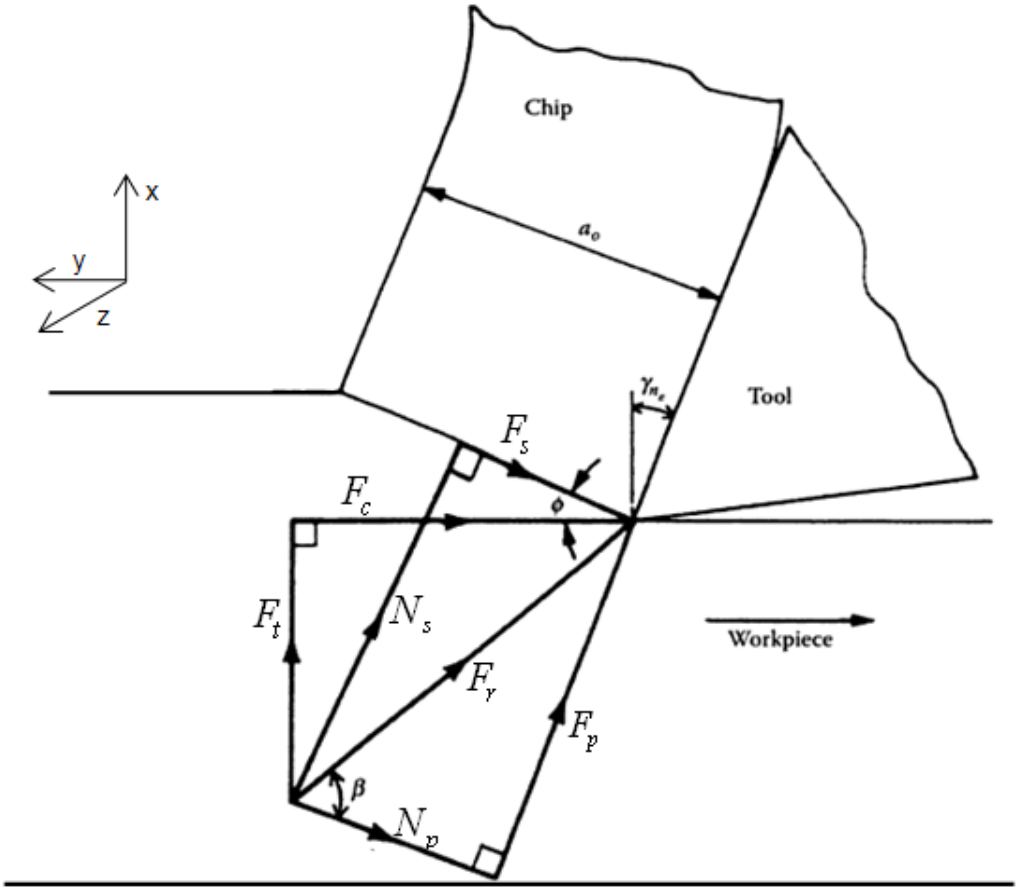

Fig.2.9. Force diagram for orthogonal cutting where F_c is cutting force, F_t is thrust force, F_s is the shear force on the shear plane, N_s is the normal force on the shear plane, F_p is shear force on rake face and N_p is the normal force on the rake face [1].

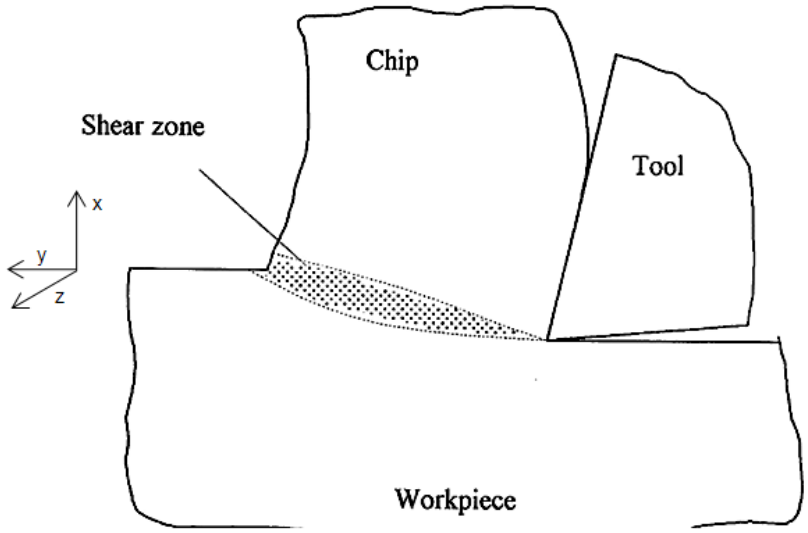

(a)

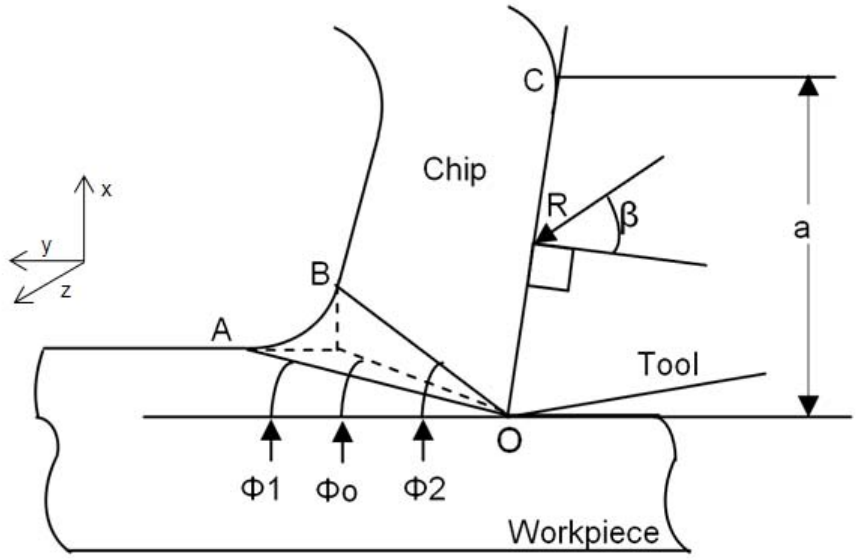

(b)

Fig.2.10. Schematic showing suggested shape of shear zone, (b) Chip formation in orthogonal cutting model proposed by Okushima and Hitomi [37,38]

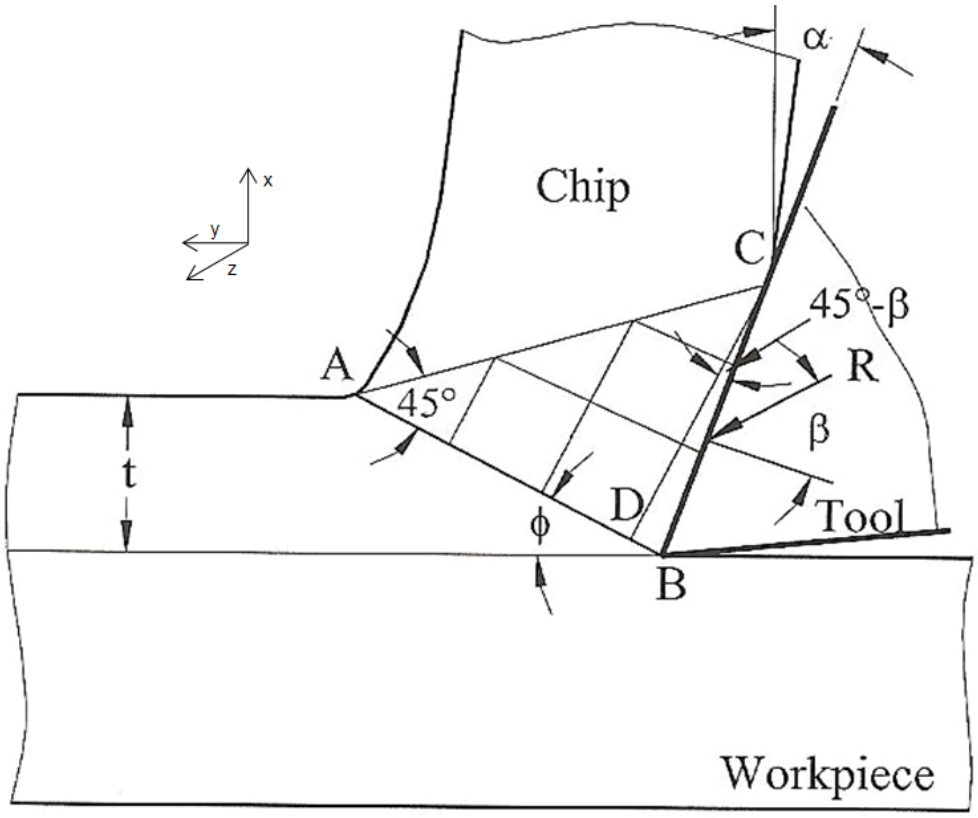

Fig.2.11. Schematic depicting slip line field model for orthogonal cutting, proposed by Lee and Schaffer [15].

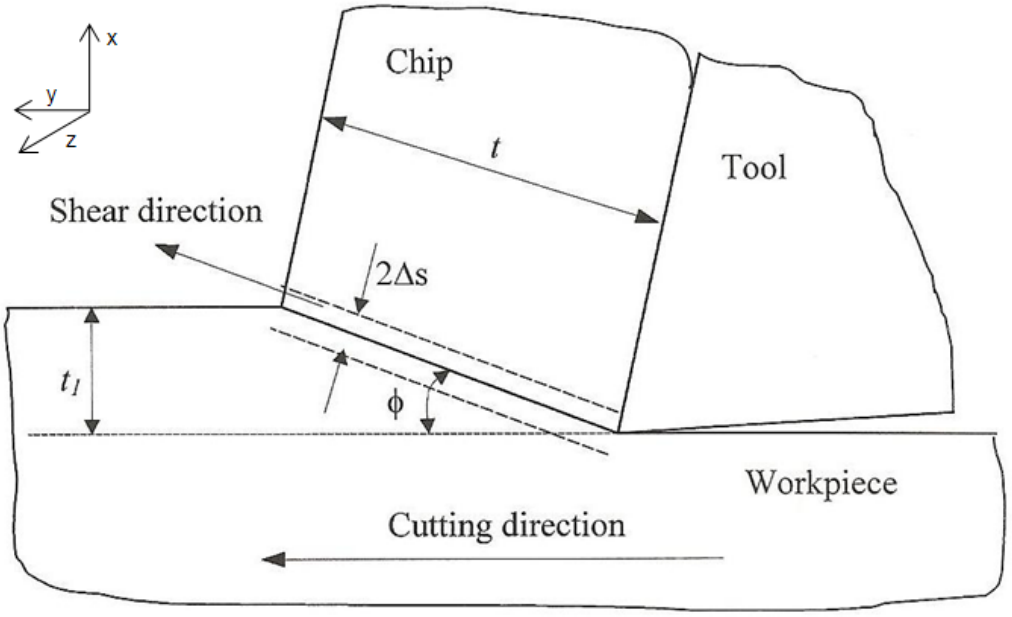

Fig.2.12. Schematic showing orthogonal cutting model consisting of multiple and mutually parallel shear planes, as suggested by Oxley and Welsh [16]

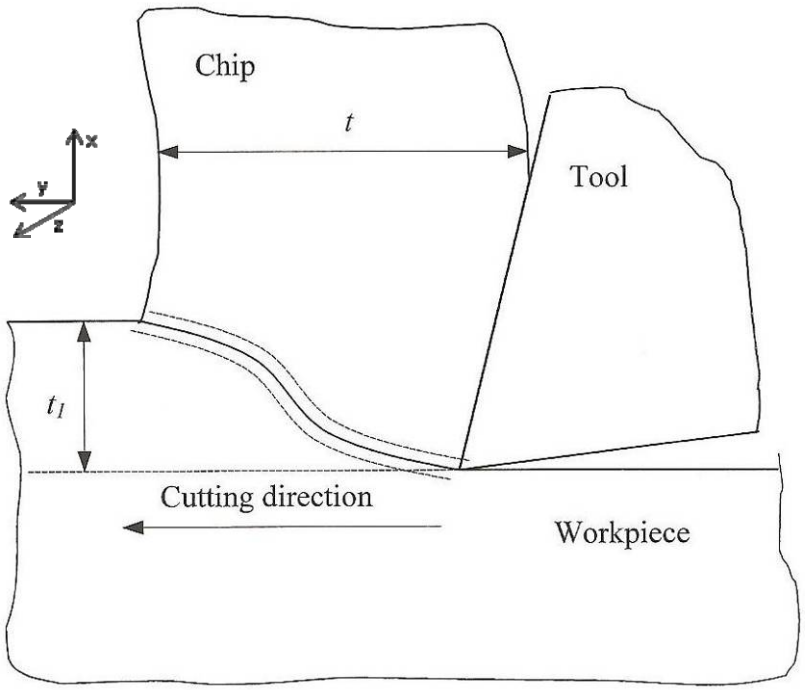

Fig.2.13. Schematic outlining curled chip model for orthogonal cutting, proposed by Dewhurst [17]

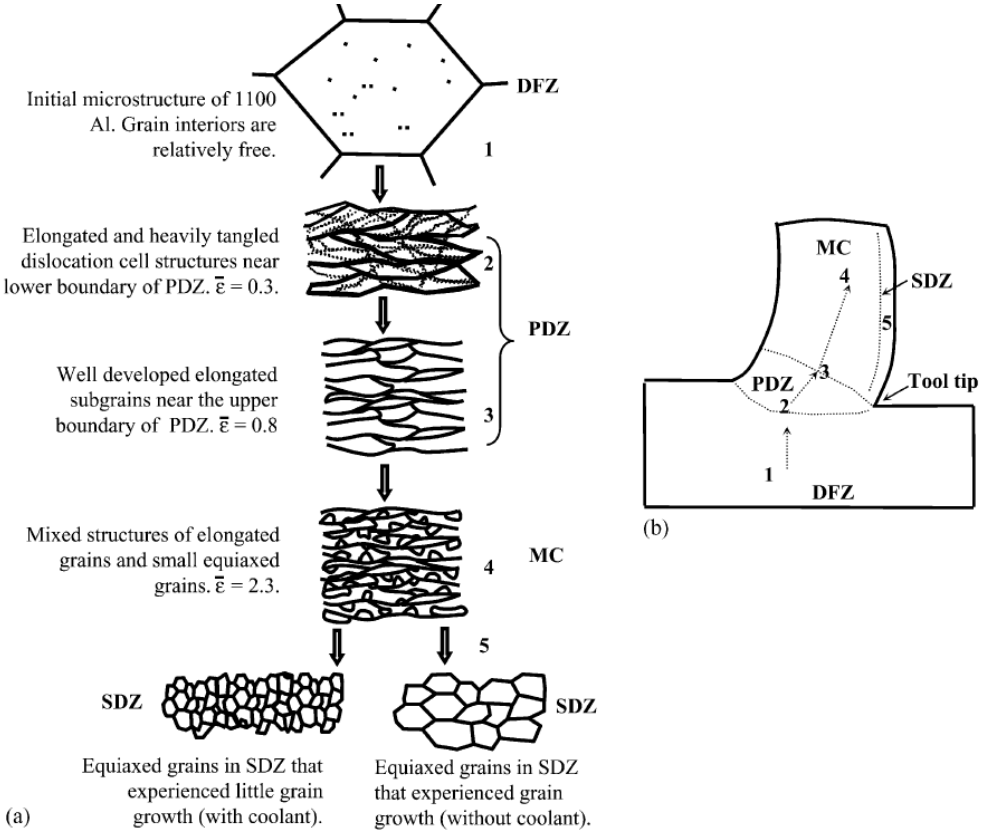

Fig.2.14. (a) Schematic diagram showing the evolution of microstructure in Al 1100 during its orthogonal machining; (b) Sequence of grain refinement events taking place in the material ahead of the tool tip [5]

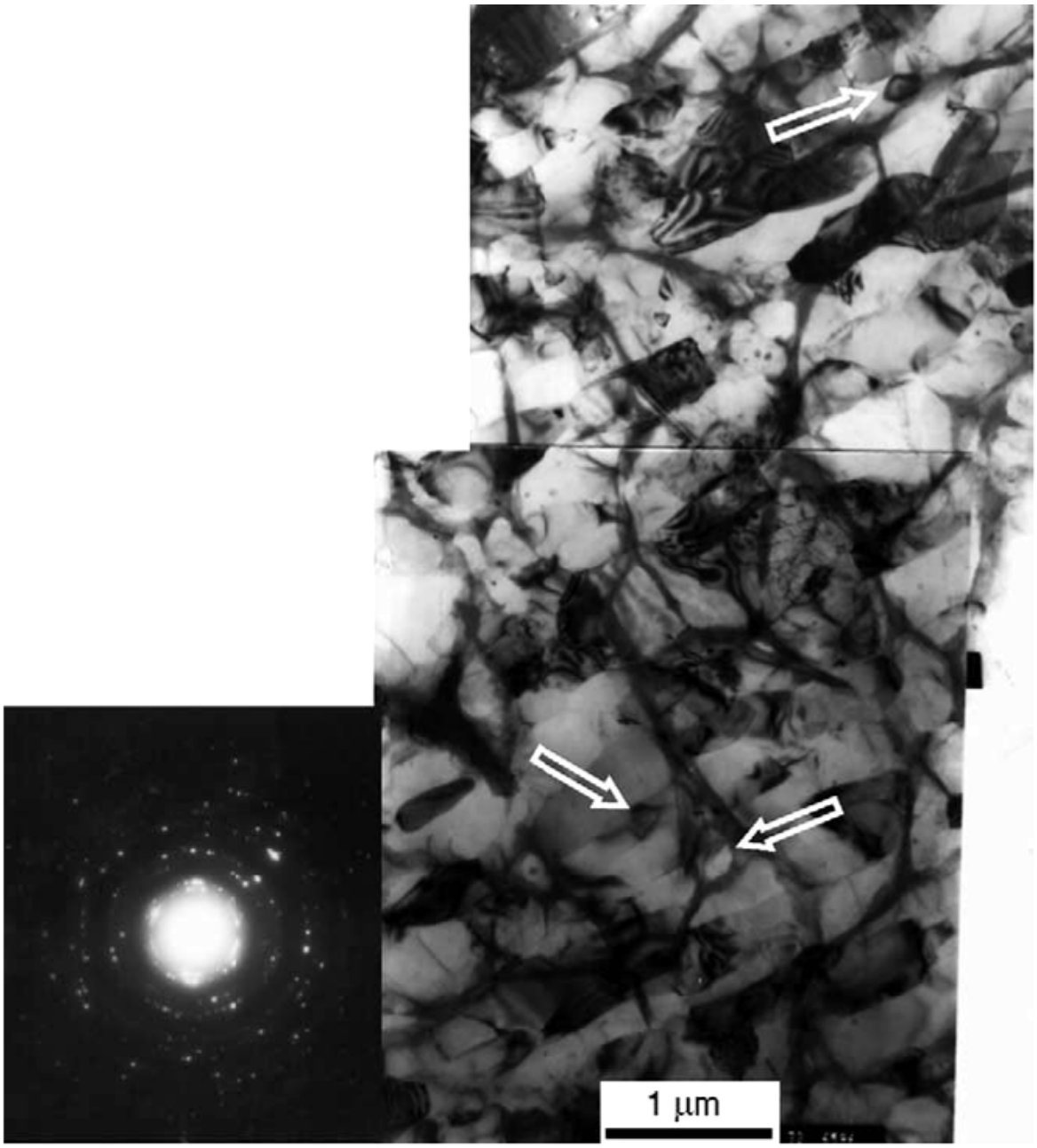

Fig.2.15. TEM micrographs of primary deformation zone showing elongated subgrains and smaller equiaxed grains (indicated by arrows) formed during orthogonal machining of Al; and the corresponding Selected Area Diffraction Pattern 1100. [5]

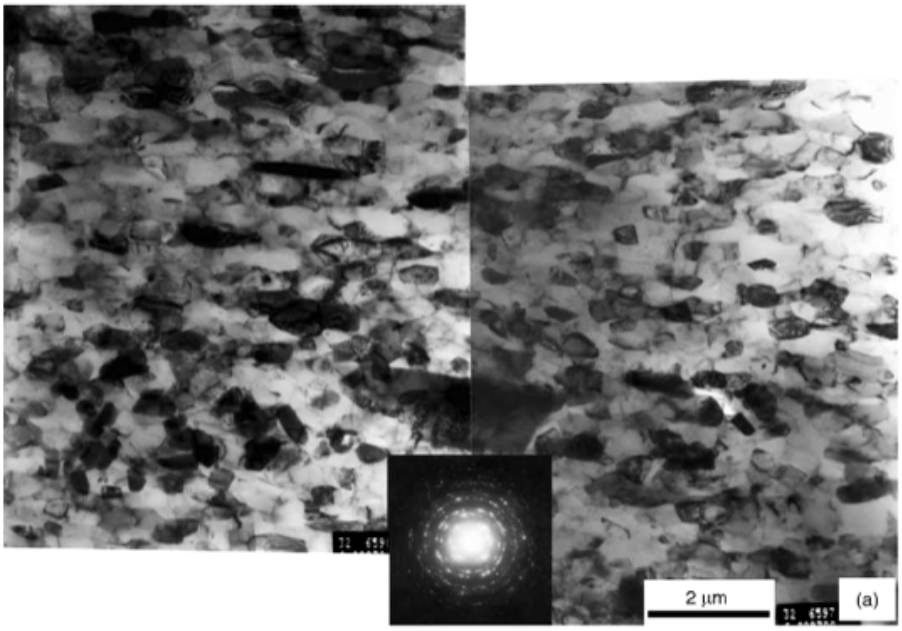

(a)

(b)

Fig.2.16 (a) TEM micrographs of machined chips showing elongated subgrains and small equiaxed grains formed during machining of Al 1100; (b) Higher magnification TEM micrograph showing nano-scale equiaxed grains [5].

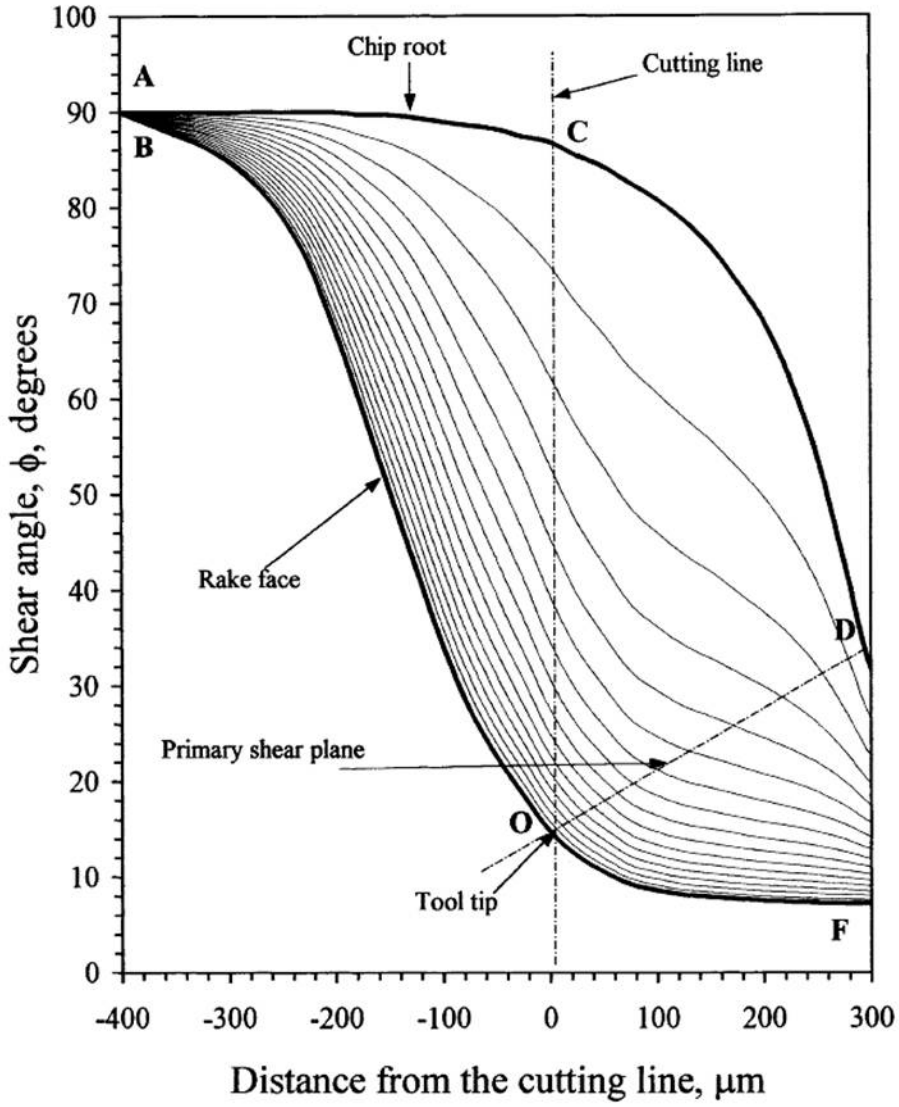

Fig.2.17.Shear angle distribution diagram for an orthogonally cut 6061 Al sample, showing the magnitude of shear angle at different locations in the material in front of tool tip [21]

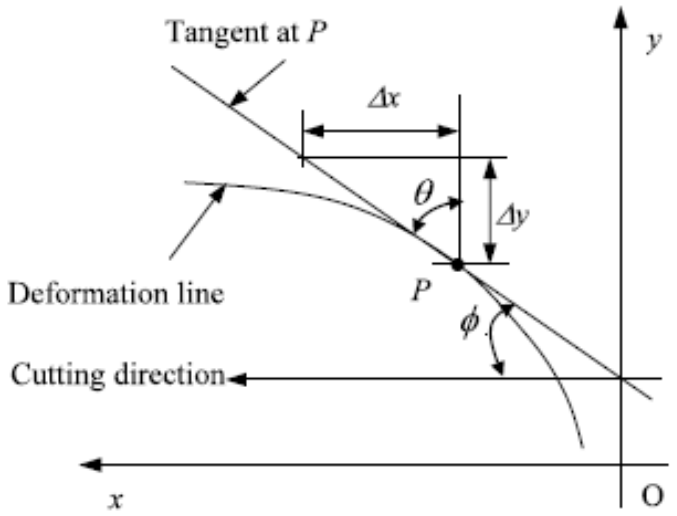

Fig.2.18. Schematic diagram showing the method to measure the shear angles from the slope of the deformation lines [21].

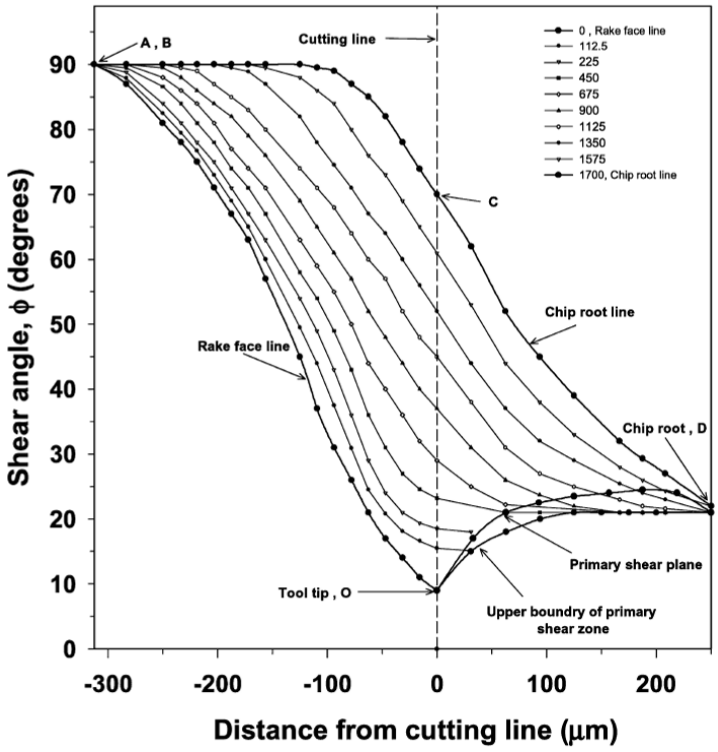

Fig.2.19 Shear angle distribution diagram showing the variation of shear angle in material ahead of tool tip for orthogonally cut commercial copper sample [4].

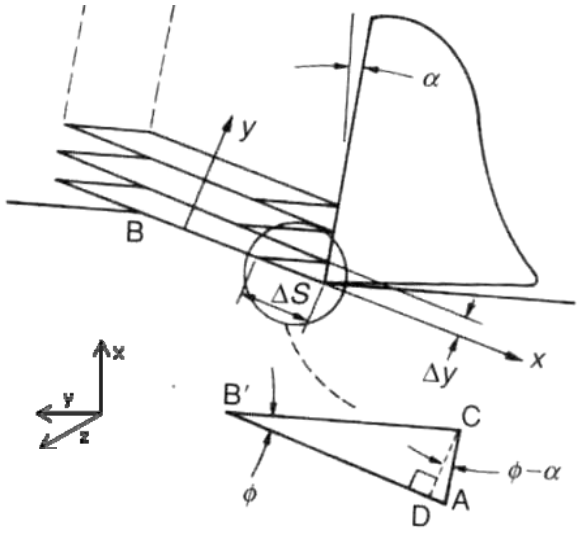

Fig.2.20 Determination of shear strain in orthogonal cutting [6,8].

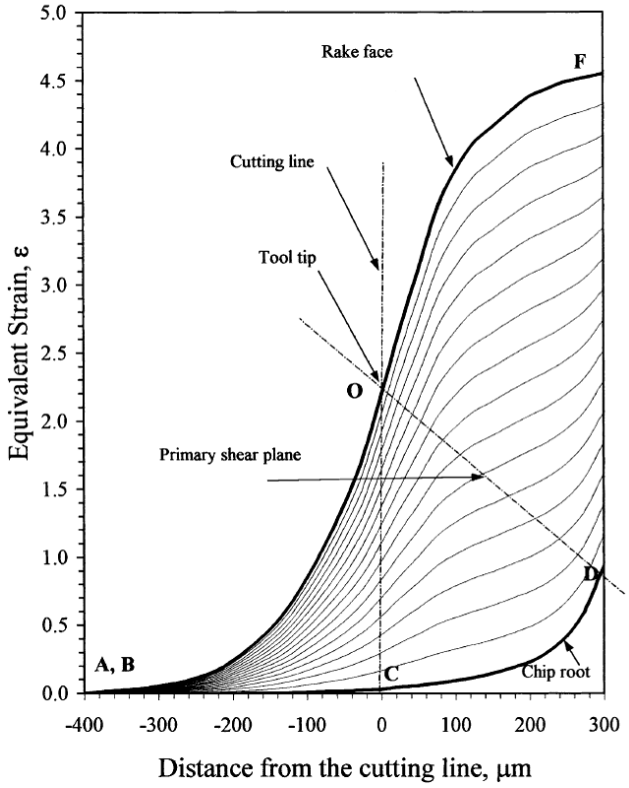

Fig.2.21. Strain distribution diagram showing distribution of equivalent strain in orthogonally cut 6061 Al [21]

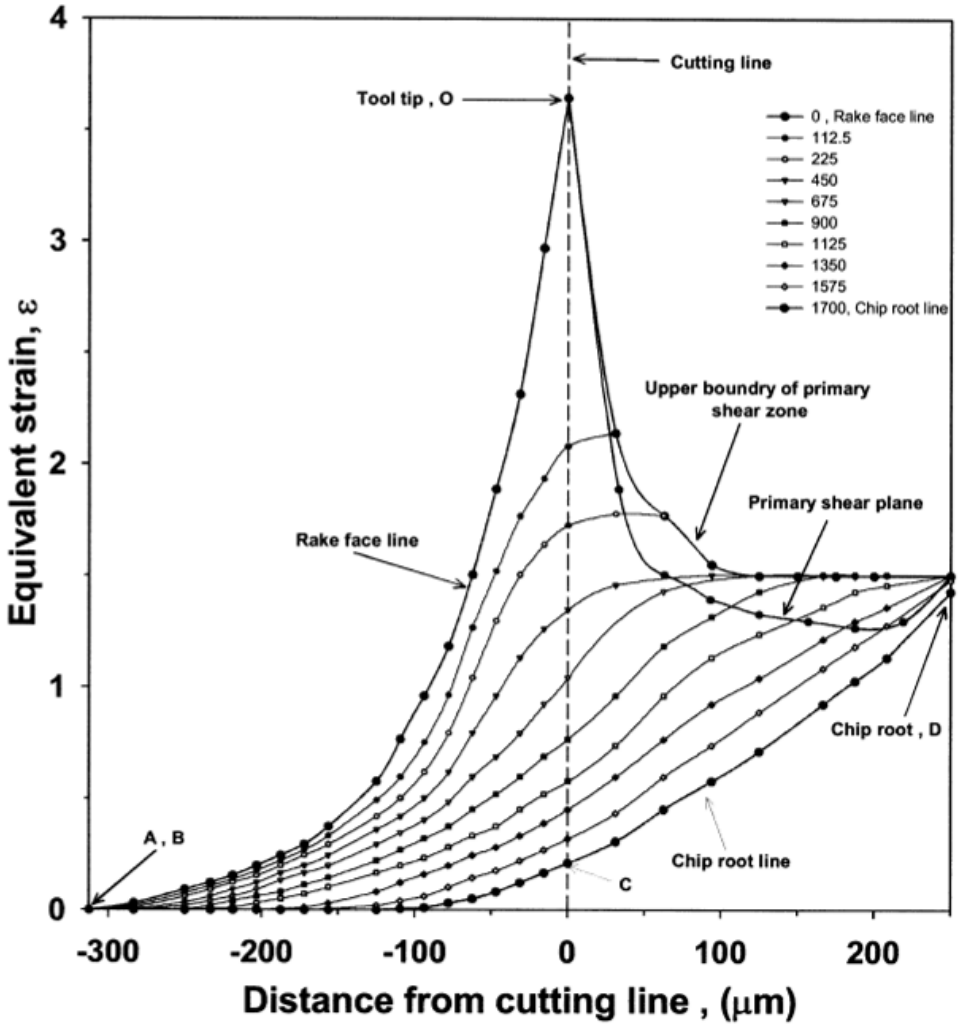

Fig.2.22 Strain distribution diagram showing the values of equivalent shear strain in material ahead of tool tip and along primary shear plane in orthogonally cut copper [4].

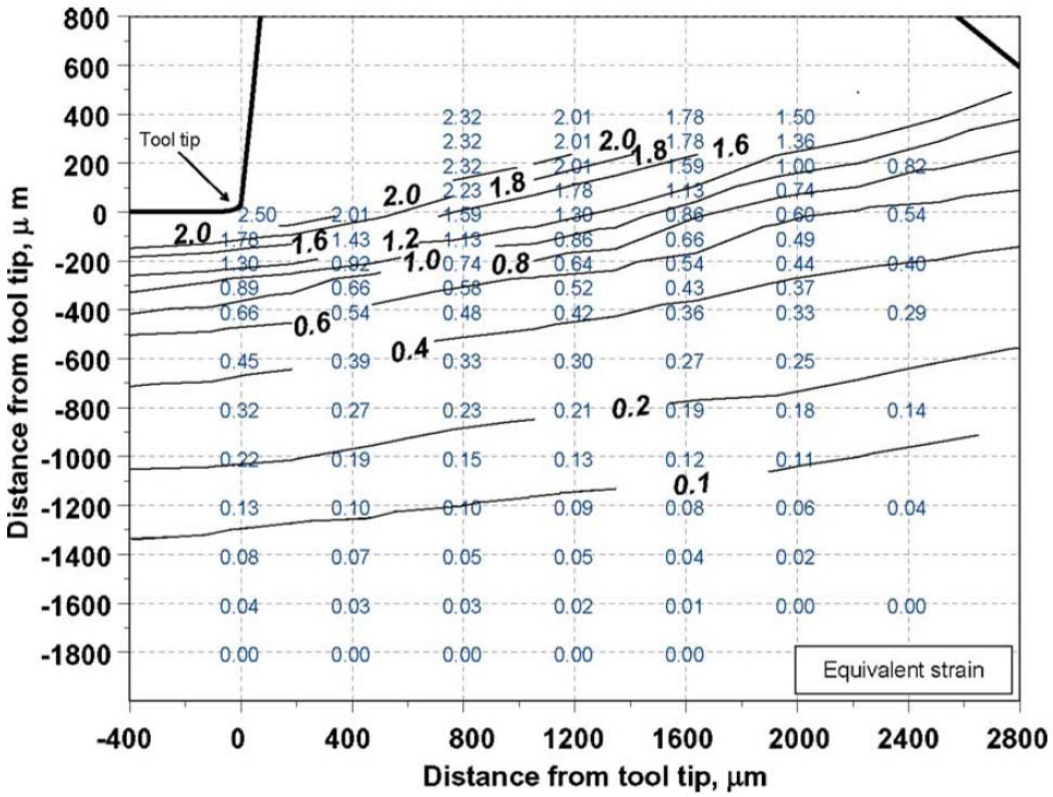

Fig.2.23 Strain distribution diagram showing values of equivalent shear strains and iso-strain contours in Al 1100 in the region ahead of the tool tip [5].

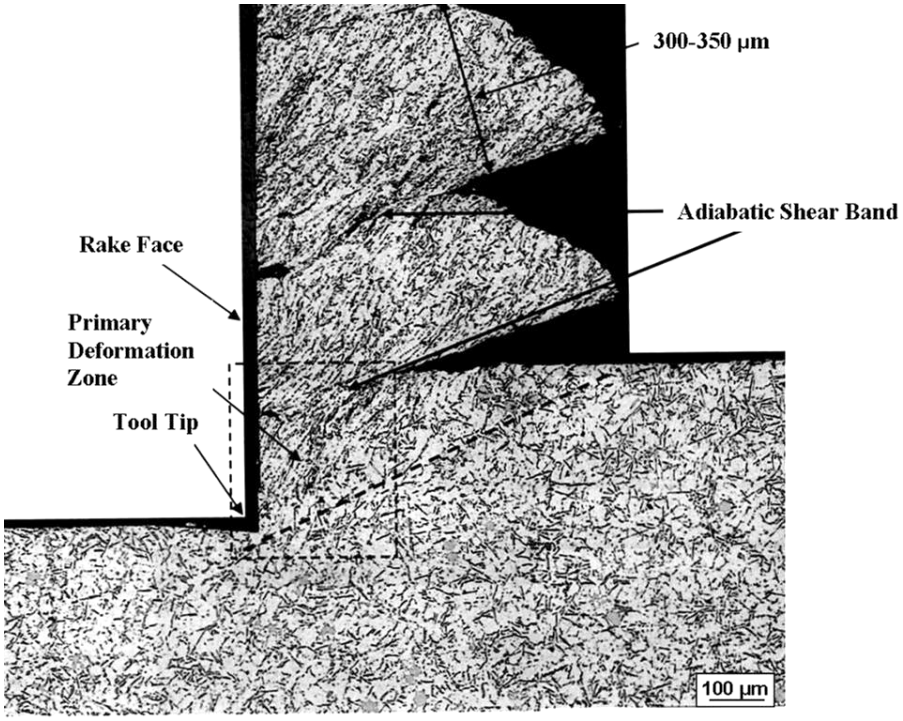

(a)

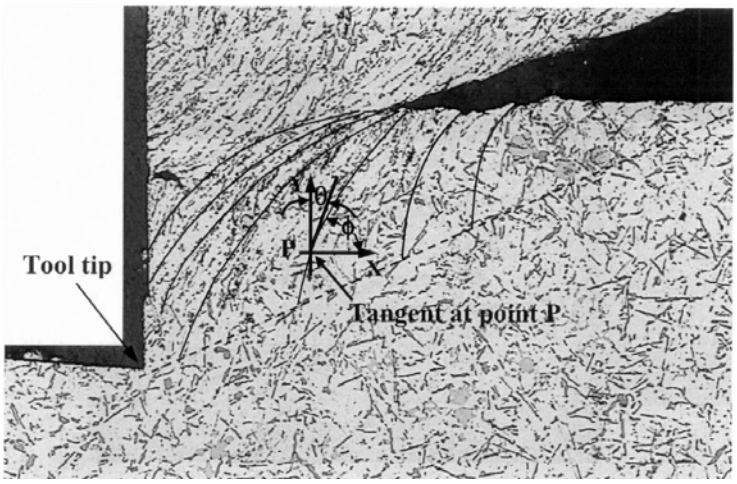

(b)

Fig.2.24.(a) Optical micrograph of orthogonally cut A380 (solution treated at 480 degrees for 12 hours followed by water quenching) showing area ahead of the tool tip;(b) schematic drawing of equivalent plastic strain measurement in the same sample [20].

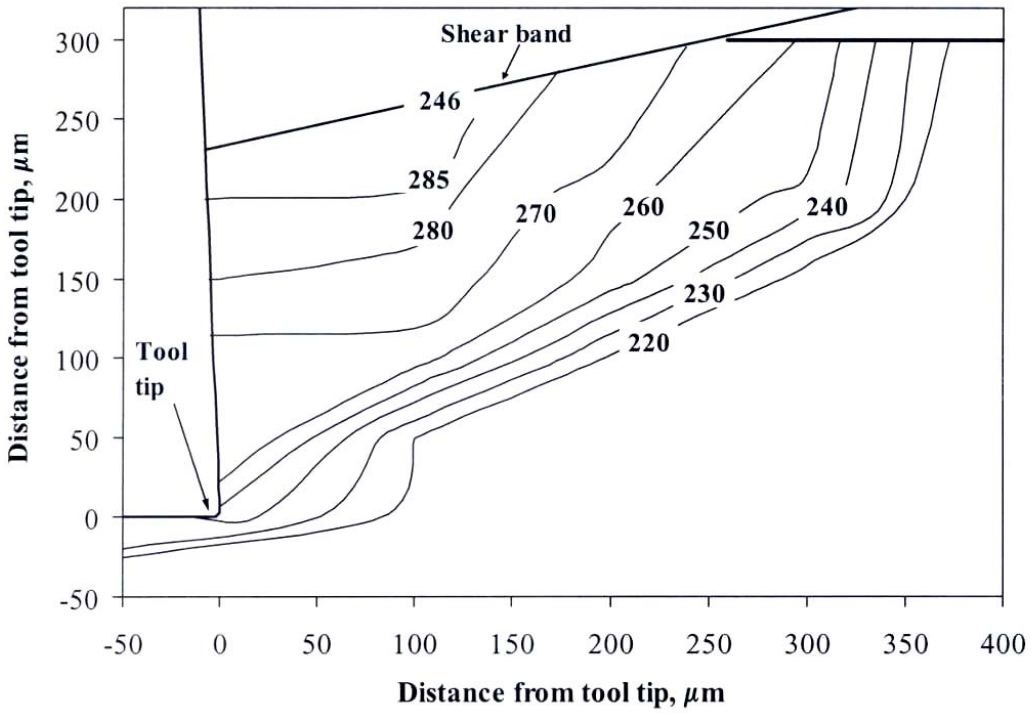

Fig.2.25. Distribution of flow-stress (in units of MPa) in an orthogonally cut A380 (solution-treated) sample [20].

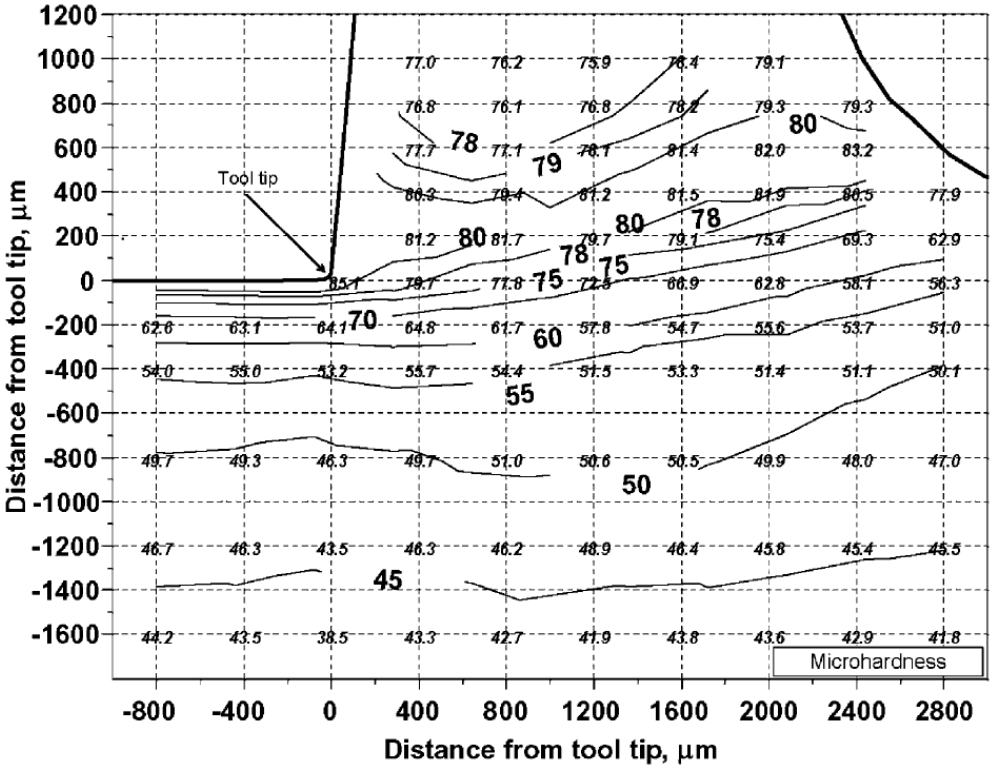

Fig.2.26 Variation of microhardness of Aluminum 1100 and iso-hardness contours ahead of the tool tip, as reported by Ni, Elmadagli and Alpas [5].

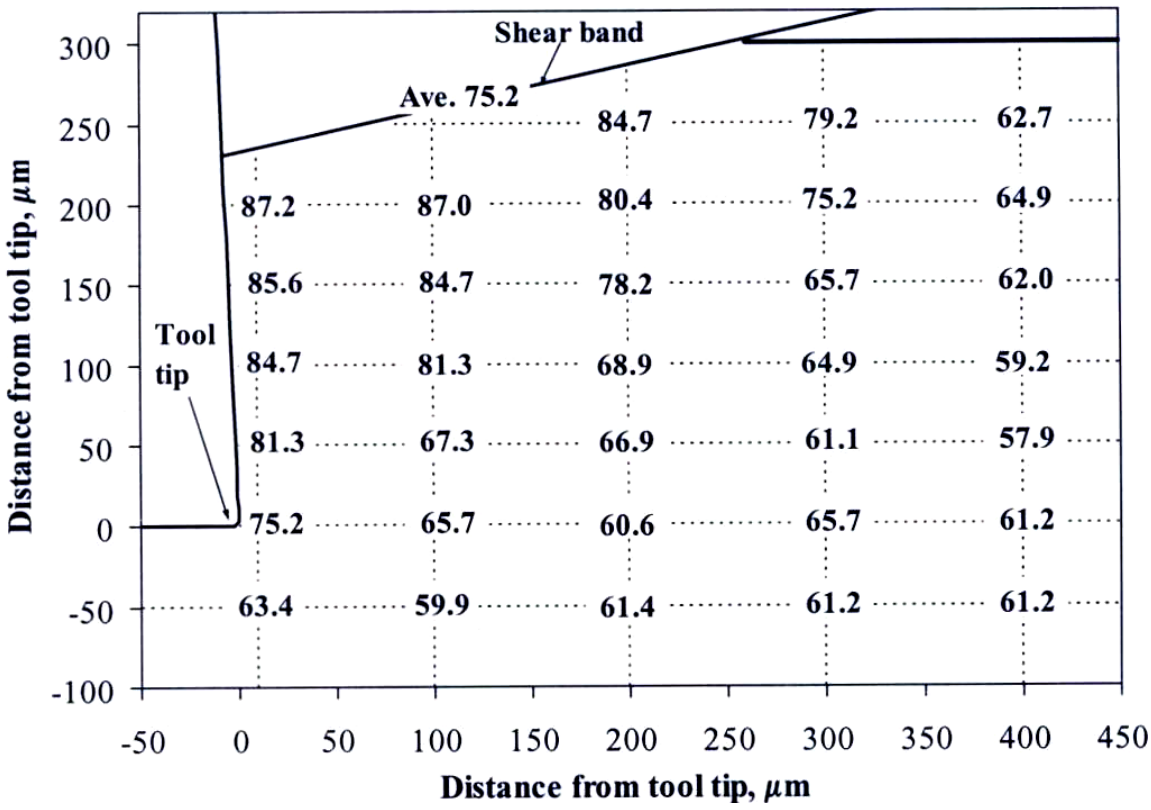

Fig.2.27 Variation of microhardness in material ahead of tool tip in an orthogonally cut A380 (solution treated) sample [20]

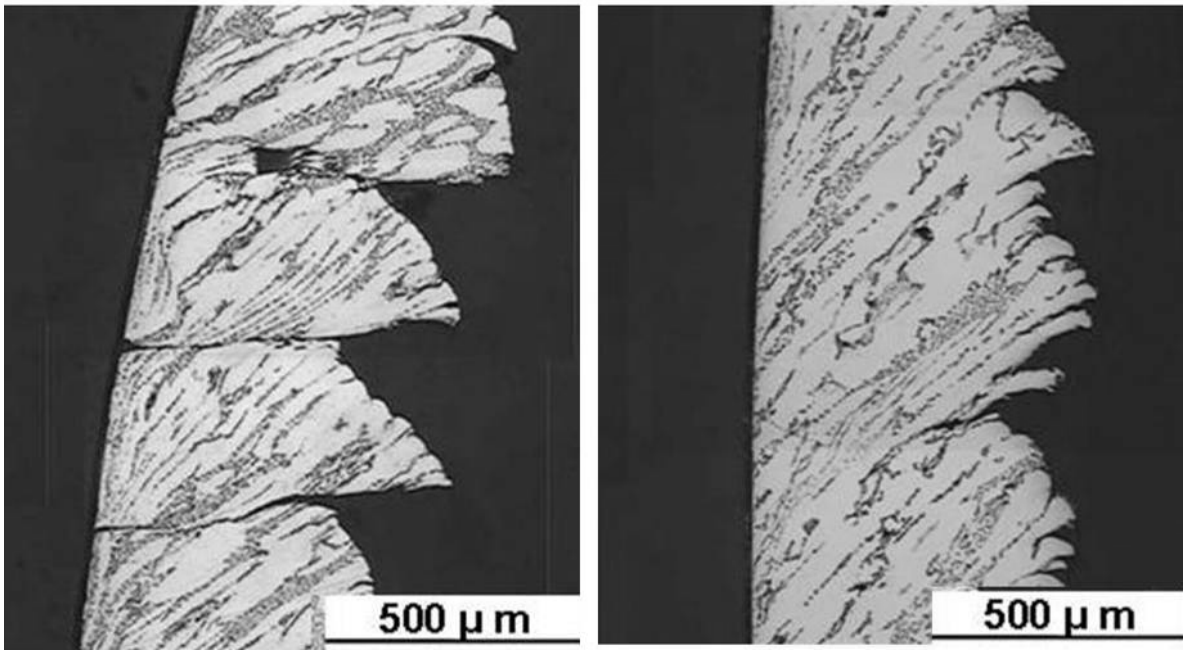

(a) (b)

Fig.2.28. (a) Discontinuous and (b) serrated types chips produced during orthogonal cutting of Aluminum alloy Al 319, machined under cutting conditions of cutting speed of 75m/min, feed per revolution of 0.25mm and cutting speed of 50m/min and feed per revolution of 0.10mm, respectively [Ref: Experimental Studies on the Deformation State of Aluminum (319 Al) Subjected to Orthogonal Cutting at Different Speed and Feed Rates].

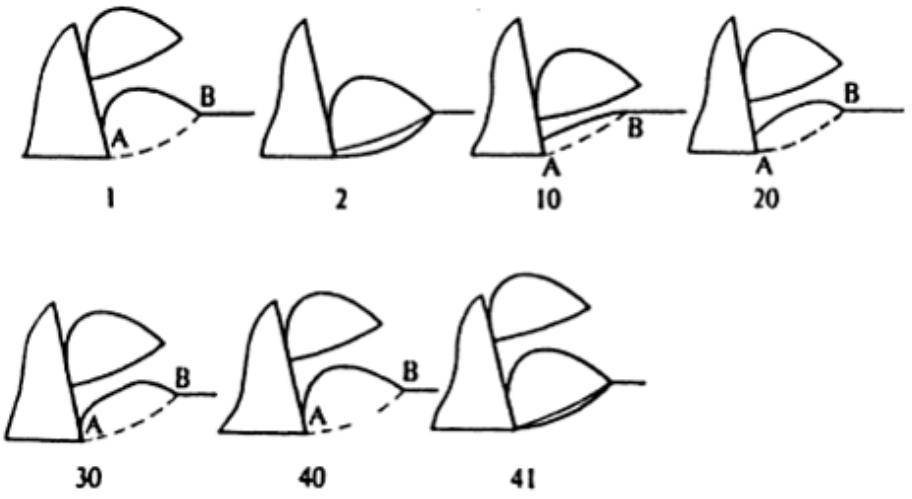

Fig.2.29. Formation of discontinuous chips when cutting brittle material. The numbers beneath successive stages are frame numbers from high speed films [23]

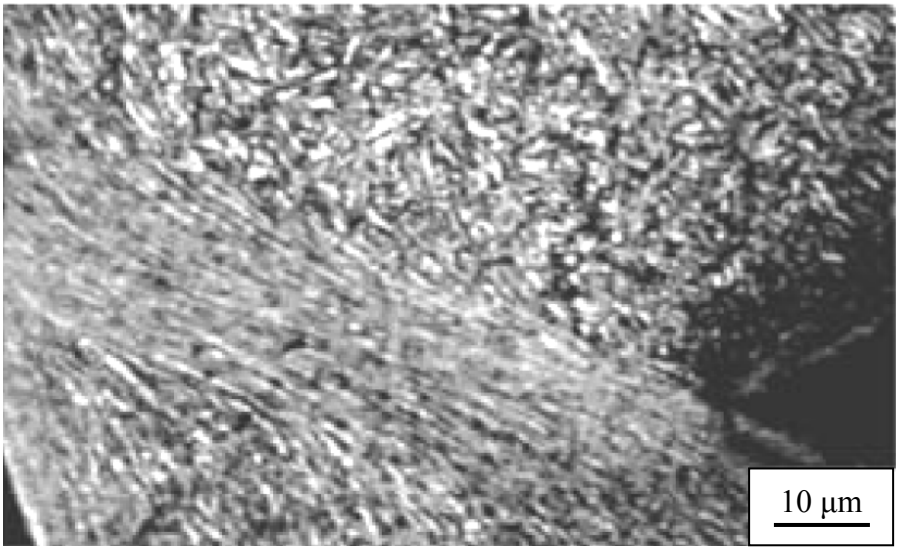

Fig.2.30. Deformed band in H13 steel generated during orthogonal cutting [39]

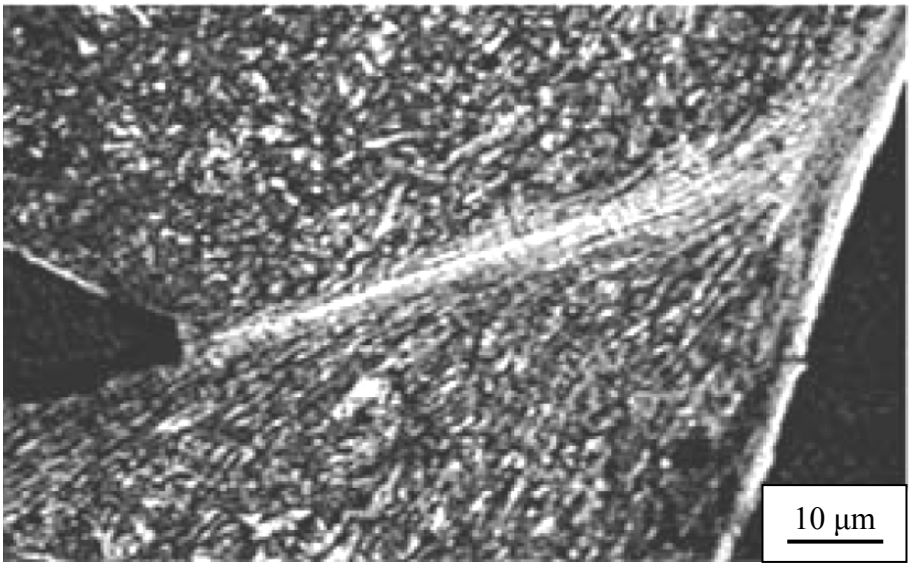

Fig.2.31. Transformed band in H13 steel generated during orthogonal cutting [39]

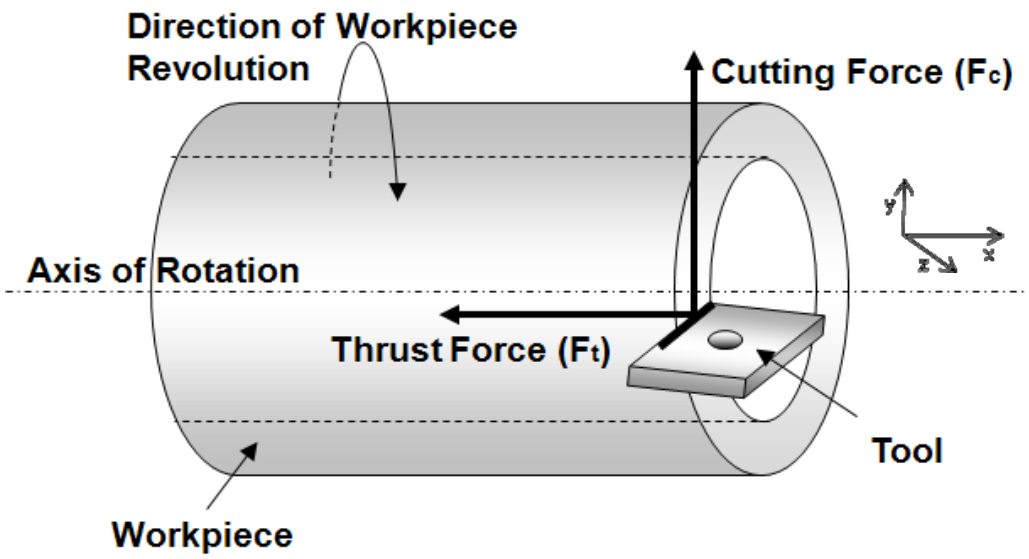

(a)

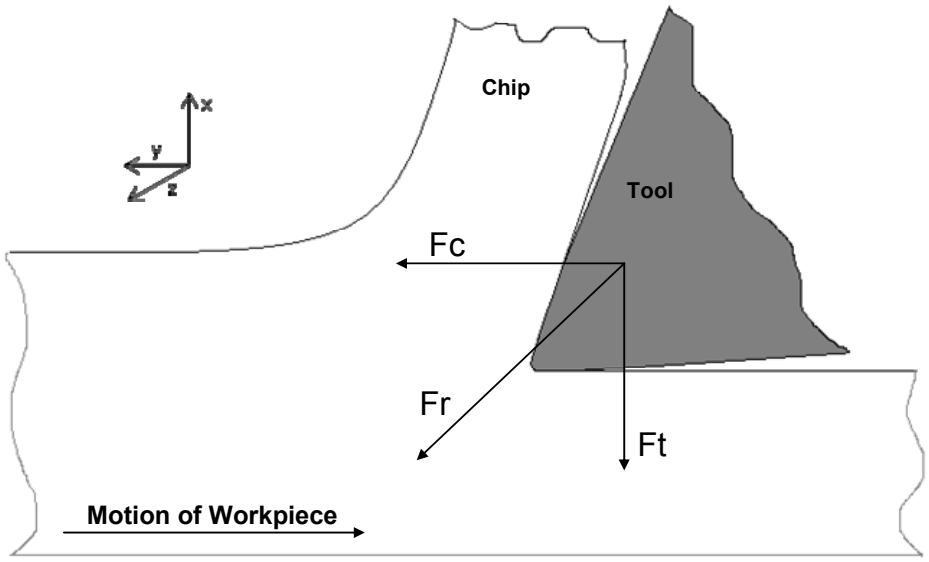

(b)

Fig.2.32. Schematics diagrams showing cutting force (Fc), thrust force (Ft) (a) on the tube shaped sample, (b) as components of resultant tool force (Fr) on the cross-section of the machined sample [33].

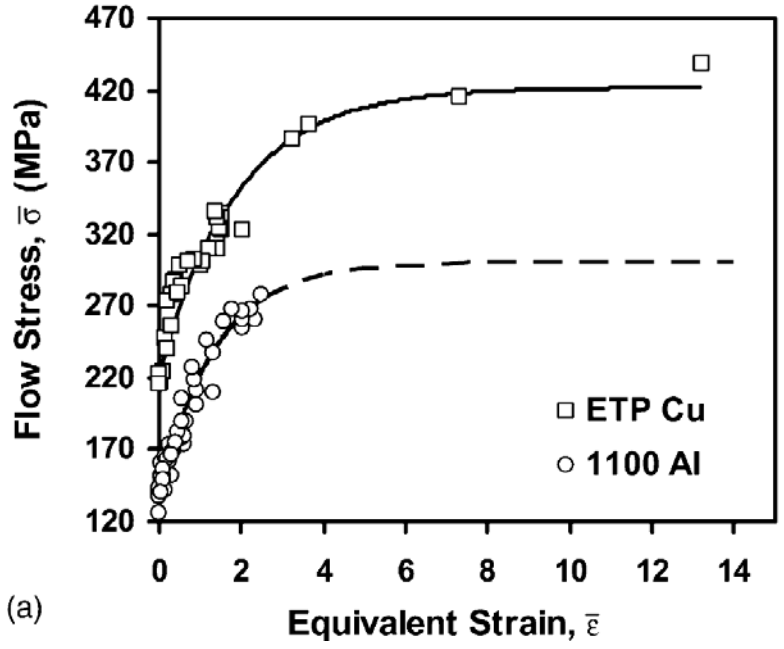

(a)

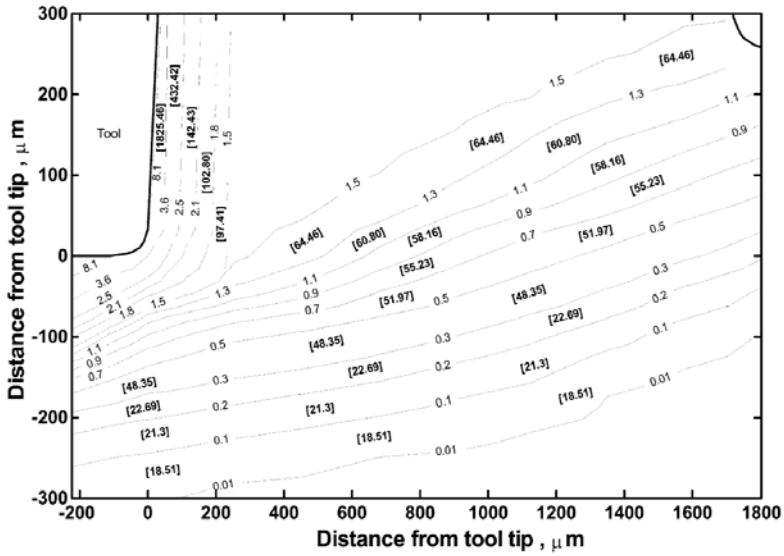

(b)

Fig.2.33.(a)Cumulative stress strain relationship for material in front of tool-tip in commercial copper sample and Al 1100 subjected to orthogonal cutting [4], (b)Distribution of work expended in plastic deformation during orthogonal cutting of Aluminum 1100 (in units by MJ m^{-3}), measured between each increment of equivalent strain and indicated between square brackets for each strip of material between two iso-strain lines [5].

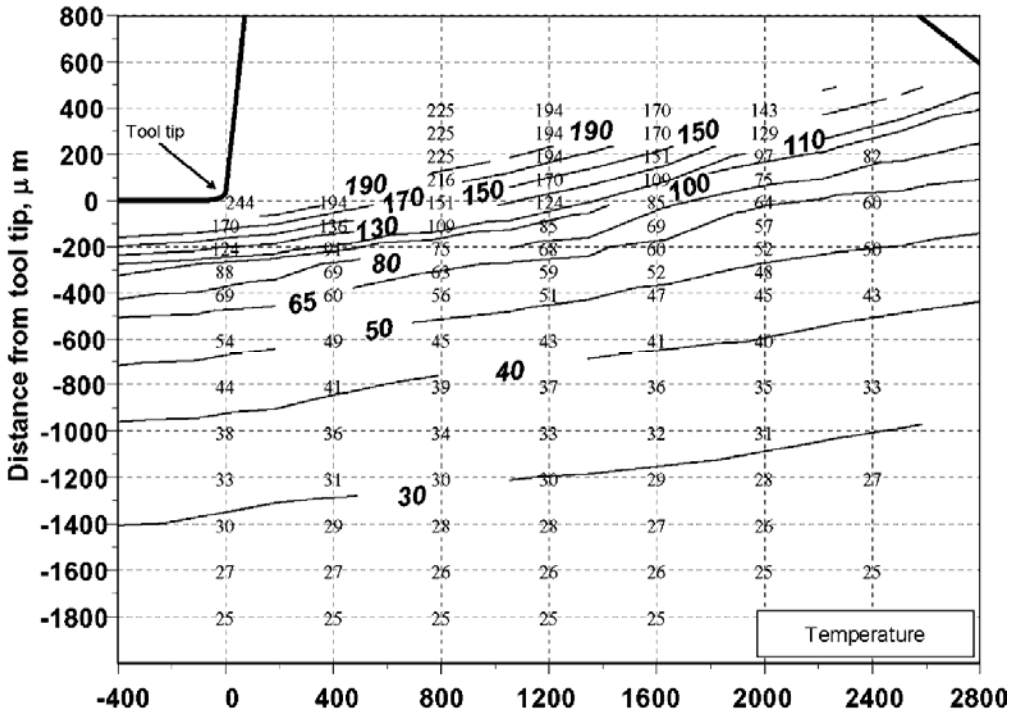

Fig.2.34 Temperate distribution map showing local increment in temperature (in units of degree C), in the region ahead of the tool tip for an orthogonally cut Al 1100 sample [5]

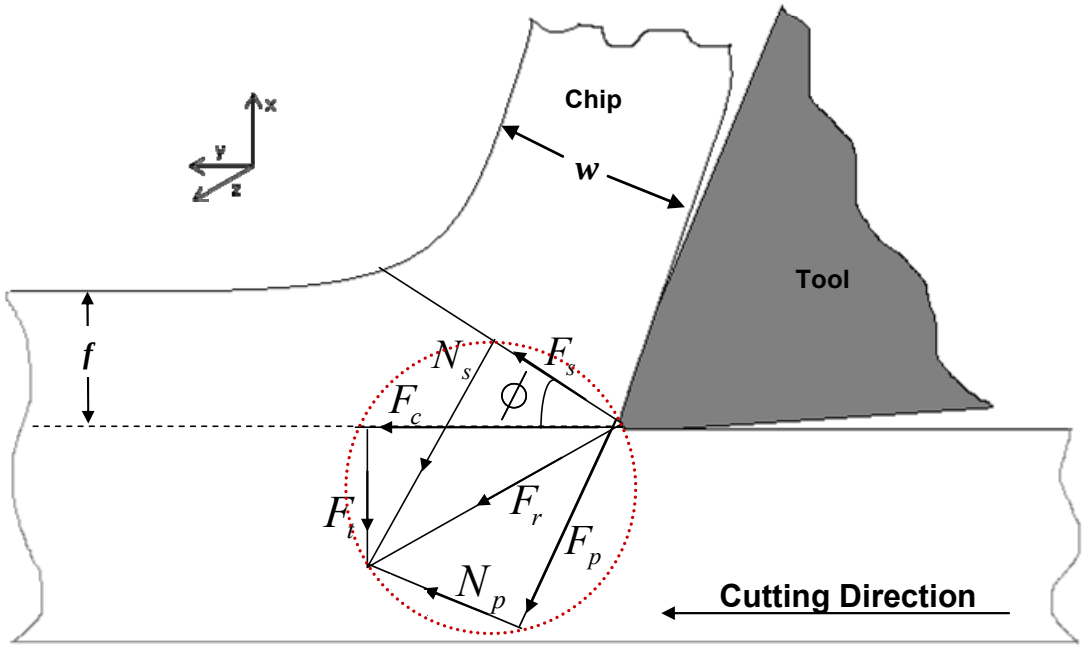

Fig.2.35. Schematic diagram of Shear plane model of orthogonal cutting showing different forces in the Primary Deformation Zone (PDZ). F_c is cutting force, F_t is thrust force, F_s is the shear force on the shear plane, N_s is the normal force on the shear plane, F_p is the force parallel to rake face of tool, N_p is force perpendicular to rake face and F_r is the force exerted by the tool on the workpiece [1,6].

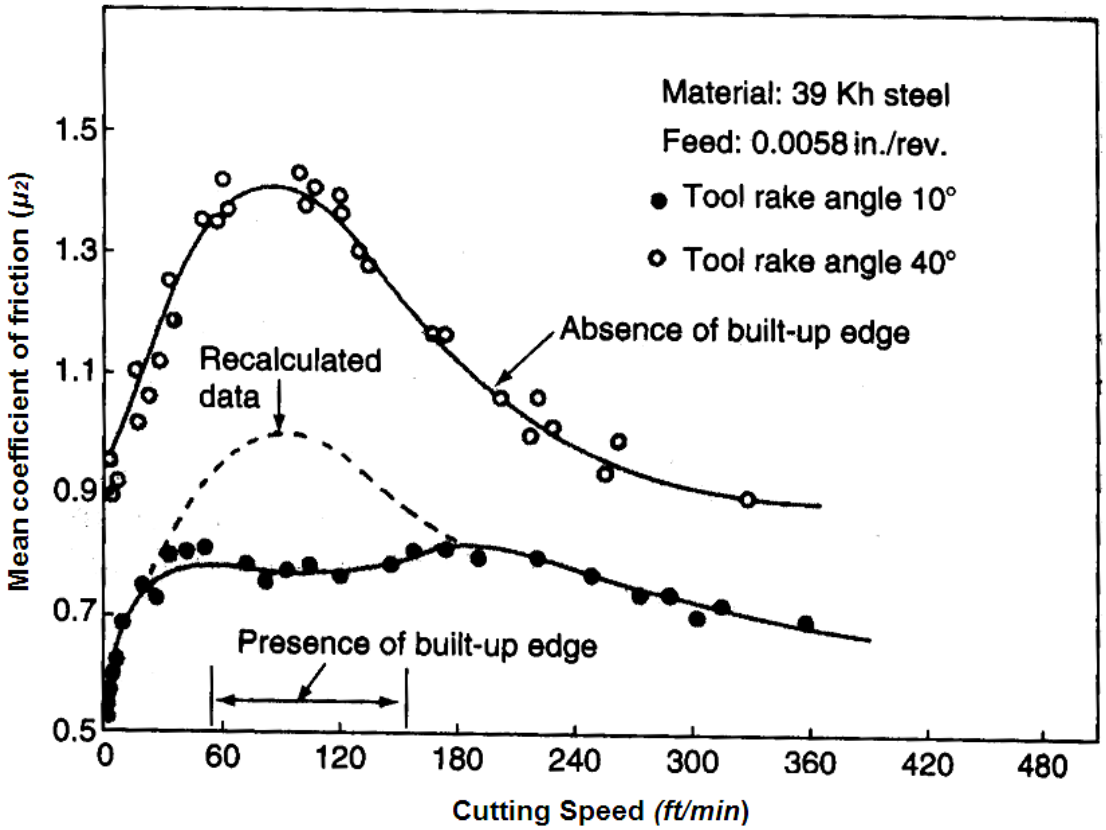

Fig.2.36 Plot showing variation of coefficient of friction with cutting speed while cutting steel. [84]

CHAPTER 3

MOTIVATION FOR INVESTIGATING DRY MACHINING OF 319 AL

3.1 Motivation

The prime motivation behind the work was the study of dry machining performance of 319 Al by measuring and analyzing the forces generated, chip geometry and surface finish produced and by estimating the power requirements of the process. Another driver for the work was carrying out a comparison of the above parameters with other aluminum alloys to find out if it is reasonable to machine the alloy under dry conditions. Understanding the deformation state of an alloy producing discontinuous chops was another reason for undertaking this work. The study also aimed at generating data which can be used for constructing a numerical model for simulating the orthogonal cutting process of material with properties similar to 319 Al.

For achieving the above, this study analyzed the machinability of hypoeutectic aluminum alloy 319 Al under a wide range of machining conditions. Five different cutting speeds and four different feed per revolution or feeds were selected from the range of cutting speeds and feeds normally used for machining of aluminum alloys (Section 4.3) to investigate dry machining of 319 Al. A two axis force sensor with wireless data acquisition system was also designed and constructed as a part of this study for measuring

the cutting and thrust forces generated during the turning experiments. Forces were measured for 319 Al, which is a cast alloy and has a microstructure containing 6% silicon, and compared with forces measured for 6061-T6, which is a wrought alloy of aluminum. These two alloys were chosen as 319 Al generates discontinuous chips and 6061-T6 generates continuous chips.

Surface finish of the machined samples (319 Al) was studied using white light optical profilometer. The deformation microstructure formed during orthogonal machining was characterized using optical microscope and scanning electron microscopy studies. The stress strain distribution in the material ahead of the tool tip was estimated in order to better understand the process of shearing of material taking place during orthogonal cutting and the accompanying chip formation. Fracture of Silicon particles under the machined surface and in the primary deformation zone was studied extensively using an optical microscope to understand the behaviour of silicon particles during orthogonal cutting.

CHAPTER 4

MATERIAL SPECIFICATIONS AND EXPERIMENTAL DETAILS

4.1 Experimental Details

The following sections describe the experimental set-up for the turning operation including the cutting conditions employed, a description of the machinery used for the cutting operations and the tool used. A detailed account of the two axis force sensor designed and constructed for measuring the cutting and thrust forces during the turning operations has also been presented. Also, the surface preparation techniques used for characterizing of the microstructures have been described in details. The microscopes used for studying the surface morphologies of the machined sections, white light surface profilometer (WYKO) used for characterizing the surface finish of the machined surface, and the hardness measuring instruments used for the study have also been discussed in the following sections. Besides the above, the chapter also discusses the steps followed for estimating the plastic strains from the orientation of the particle flow observed in the machined section. The methodology followed for estimation of flow stresses using Vickers's Hardness indentations at different locations in the machined sections has also been described. The chapter also describes the preparation of the marker specimen that was used for estimation of plastic strains below the machined surface.

The chapter also enlists the properties of the work-piece material and gives description of the methods used for sample preparation for metallographic studies. The methods employed for hardness and stress estimation have been described in details. Also, the methodology followed for estimation of plastic strains in the machined sample using the orientation of the fractured second phase particles has been discussed.

4.2 Composition and Workpiece Geometry

4.2.1 Alloy 319 Al

Aluminum alloy 319 or 319 Al is widely used in the automotive industry for casting engine blocks and cylinder heads. Besides good machinability (under lubricated conditions) [12], it possesses good castability, high resistance to corrosion and good mechanical properties, making it a good choice for a number of applications.

319 Al is a hypo-eutectic cast alloy of Aluminum with low Silicon content (6%), Copper (3.5%) and Mg (0.1%). The phases identified in the microstructure using SEM and EDS were Si particles, $Al_{15}(Mn,Fe)_3Si_2$ which occurred as brown Chinese script, needle shaped Al_5FeSi and Cu_2Al . Fig.4.1 (a and b) shows typical microstructures of the alloy and Fig.4.1 (c) shows the size distribution of silicon particles a typical microstructure of 319 Al. Fig.4.2 (a, b, c and d) shows the EDS peaks for different phases present in the alloy, identified during the studies.

The workpiece material was supplied in the form of rectangular blocks in as cast condition. Tube shaped samples used for orthogonal cutting were shaped out of these blocks. Sample dimensions were fixed at an outer diameter of 3cm and wall thickness of 0.3cm.

Table 3.1 Chemical Composition of 319 Al

Si	*Cu*	*Fe*	*Mg*	*Mn*	*Ni*	*Al*
6	3.5	0.5	0.1	<0.01	<0.01	Rest

4.2.2 Alloy 6061 Al

6061 Al (T6) is a hypoeutectic alloy of aluminum with silicon content (0.4-0.8%) much lesser than that in 319 Al (6.0%) (T6 refers to heat treatment of the alloy: solution heat-treated and then artificially aged). Research on orthogonal machining of this alloy has well established the fact that it generates continuous chips upon orthogonal machining [21,73-76]. As a part of this study, 6061 Al was machined under cutting speeds of 25m/min, 35m/min, 50m/min, 75m/min and 115m/min and feeds of 0.10mm, 0.25mm and 0.35mm, that is, under the same cutting conditions as employed for machining of 319 Al, with the exception of the highest feed of 0.45mm being excluded for 6061 Al for the sake of comparing the force responses of the two alloys. Geometry of

6061 Al samples subjected to orthogonal cutting was maintained exactly identical as 319 samples, as has been specified in Section 4.2.2.

4.3 Selection of Cutting Conditions

The schematic shown in Fig.2.4 illustrates cutting speed and feed per revolution during orthogonal machining of a tubular sample. This study compared the machining performance of 319 Al by cutting samples under twenty different machining conditions. Four different feed per revolution or feeds, 0.10 mm, 0.25mm, 0.35mm, and 0.45 mm were selected and five different cutting speeds (260, 370, 540, 800 and 1200 rpm) were selected for carrying out a comparative analysis of machinability of the alloy.

4.3.1 Selection of Cutting Speed

Generally, the selection of speed for turning aluminum alloys is done on the basis of the limitations set by the machine tools and the workpiece. The influence of the aluminum alloy properties on the selection of cutting speed is limited [12] and the tool material and types are more important considerations in the selection. Normally, speeds used for machining of aluminum alloys are less than 1250 rpm with the nominal speed being approximately 800 rpm [37]. As such, five speeds were chosen for this study (260 rpm, 370 rpm, 540 rpm, 800 rpm and 1200 rpm or 25m/min, 35m/min, 50m/min, 75m/min and 115m/min), values well within the range commonly used for these alloys.

The use of five different values ensured enough data points for analyzing the variation of various machining parameters in terms of cutting speed.

4.3.2 Selection of Feed per Revolution

Surface finish desired in the machined product, along with the type of work-material and rigidity of the machine used for the process are the main determinants of feed per revolution used in a given machining process. Final finishing cuts are done at lighter feeds, generally in the range of 0.05 mm to 0.15 mm, and rough turning feed ranges from 0.15 mm to 0.65 mm for Aluminum alloys [37]. Among the feeds chosen for this work, 0.10 mm lies in the range of feeds used for finish turning of aluminum alloys, while the rest three, i.e. 0.25 mm, 0.35 mm and 0.45 mm lie in the range of feeds used for rough turning.

3.4 Machinery Used for Turning Experiments

4.4.1 Lath for Turning Experiments

All orthogonal cutting tests were executed on a Harrison M300 lathe which is a compact, simple-to-operate and reliable centre lathe (Fig.4.3). It has a long, foot-operated and very powerful spindle-brake with electrical disengagement for interrupted cutting and is powered by a fan-cooled 2.2 kW (3 HP.) 3-phase, 1500 rpm motor. The spindle rotation speed can be chosen from twelve different speeds ranging from 40 to 2500 rpm. The range of power sliding feeds varies from 0.03 mm to 1 mm per revolution of the

spindle in metric mode. Feeds are selected using a traditional push-pull plunger which can be engaged and disengaged using a very light-action, flick-up-and-down lever.

4.4.2 Cutting Tool

The cutting tool used for the cutting experiments was a polycrystalline diamond (PCD) insert (VCMW 332FP) with a rake angle of zero degrees (Fig.4.4). A polycrystalline diamond insert was chosen for the experiments as it is hardest of all the tool materials in use and possesses excellent resistance to wear and high dimensional stability. It also shows comparatively lesser friction during turning, has high thermal conductivity and very high fracture strength [8]. These properties make PCD an excellent choice for machining of soft metals like aluminum, magnesium, copper etc [6,8,37,56].

Fig.4.5 shows the relative positions of the workpiece (mounted on the lath) and the cutting insert (mounted on the tool holder) during orthogonal cutting process.

4.5 Force Measurement System

Cutting force and thrust force are two important forces exerted by tool on the workpiece during the process of orthogonal cutting. Fig.2.32(a) is a schematic showing the direction of these forces on the tube shaped sample that has been used for this study and Fig.4.7 shows their direction on a micrograph of the machined sample. A two-axis force sensor system for measuring cutting and thrust forces was designed and constructed as a part of this study.

4.5.1 Set-up and Design

Generally, the measurement of turning forces using force measuring systems requires shutting down the machinery for extended periods of time in order to facilitate installation of the system. It may also pose problems in terms of requiring a significant change in the configuration of the machinery or workpiece in order to accommodate the components of the force measuring device. This problem was tackled by specially modifying the tool-holder and mounting strain gauges on it. The modified tool holder along with the tool-holder-mounting with the strain sensor with the wireless transmitter attached to it (Fig.4.8) together formed a detachable unit which could easily be installed on the machine without requiring any change in the normal configuration of the lath or the work-piece.

The tool holder, a rectangular block of steel on which the cutting insert is mounted, was modified by cutting slots on it (Fig.4.9). The narrowed down section was a rectangular block of dimension 1cm by 1cm. The purpose of this modification was to increase the strain sensitivity of the holder as it gets subjected to the cutting and thrust forces during cutting of a sample. Strain gauges were mounted on the modified-narrow cross section and were connected to a strain sensor attached to the tool-holder mounting.

4.5.2. Components of the Force Measurement System

The data acquisition system comprised of a strain sensor, a wireless transmitter system (V-Link 2.4 GHz Wireless Voltage Node), an analog base station (MicroStrain

Micro TxRx wireless base station w/ analog outputs) and a computer loaded with data acquisition software 'Agile Link' (Fig.4.10). The strain sensor attached to the narrow groove in the modified tool holder picked up the strains produced in the tool holder as it bent under the loads exerted on it during the turning operation. It transmitted the signals via electrical wires (Fig.4.10) to the strain sensor which then wirelessly transmitted them to the base station. The bases station transmitted the data to the PC via a USB cable and 'Agile Link' was used to convert the streamed data to a readable format, which was also displayed in form of curves for the two measured forces (Fig.4.11a).

4.5.3. Calibrating the Force Measurement System

Dynamic force measurements are required for a number of industrial and research operations like material testing and crash testing [39][38]. The force measuring system designed and constructed as a part of this study, for the purpose of measuring cutting and thrust forces, was calibrated by step loading and unloading of predetermined weight on the system under near static conditions, which was followed interpretation of the output data and finding an equation which defines the relationship between the applied load and the output. The maximum cutting force and thrust force the system was calibrated for measuring were 1400N each. Also, the sampling rate that was used during calibrations and during all turning experiments was 2000Hz.

4.5.3.1 Experimental Setup for Calibration

The experimental set-up for calibrating the force measuring system has been described here:

The system was calibrated using 'step-wise increment of static loading' technique [38,39] used for calibrating similar systems. The system was first mounted on a vice in such a way that the force of gravity, acting vertically downwards, acted in the direction cutting force would act in during cutting tests. This was followed by a weight-hanger pan (weighing 713gms) being suspended from the location of the tool's cutting edge. This ensured that any weight subsequently placed on the pan would act in the direction of cutting force. Care was taken to choose a pan sturdy enough to be able to bear the load of approximately 150Kg on it without slipping off the force measurement system or without the system toppling over due to the high magnitudes of suspended weight. Thereafter, weights in steps of 10lb (4.54Kg), 12.4lb (5.62Kg) and 20lb (9.07Kg), adding up to a total of 285lb (130Kg) were gently placed on the pan one after the other. Sufficient time was allowed to elapse in order for the system to overcome any fluctuations in output and to regain stable state before the next weight was placed on it. Two sets of readings were taken, one for loading the system and second for unloading the system, maintain all the precautionary measures as has been mentioned above.

In order to calibrate the system for measuring thrust forces, it was remounted on the vice in such a way that the force of gravity would now act in the direction of thrust

force. The rest of the steps followed were same as described above for calibrating the system for cutting forces.

4.5.3.2 Interpretation of Output Data

The output data from the software, Agile Link, was correlated with the force applied by the corresponding weights placed on the force measurement system. The force was calculated using Eqn.4.1

$$F_{sys} = M.g + m.g \tag{4.1}$$

where F_{sys} is the force on the force measurement system, M is the total weight on the weight-hanger pan, m is the weight of the weight hanger pan (713grams) and g is the acceleration due to gravity (taken to be equal to $9.8\, ms^{-2}$).

Fig.4.12a shows the loading and unloading curves obtained for the relationship between the force applied and readings on the lower curve (refer to Fig.4.11a), which shows the cutting force for the relative configuration of the force measurement system, cutting tool and the lath. Fig.4.12b shows the loading and unloading curves showing the same relationship for upper curve (Fig.4.11a) which shows the measurements for the thrust force. It was found that the readings for loading and unloading (for both forces) showed very good matching with each other (R^2 =1), showing the system to be very consistent.

The average values for loading and unloading were calculated for both cutting and thrust forces from the results shown in Fig.4.12 (a) and Fig.4.12 (b). The results have

been presented in Fig.4.13(a) for cutting forces and in Fig.4.13(b) for thrust forces. The relationships between the cutting force and thrust force applied and the corresponding output readings on Agile Link were found to be linear and equations for defining them were found from Fig.4.13 (a and b), and have been shown in Eqn.4.2 and Eqn.4.3 below:

Cutting Force Equation:

$$F_c = -0.657.a + 1340 \quad \text{(in units of Newton)} \tag{4.2}$$

Thrust Force Equation:

$$F_t = 0.739.b - 1507 \quad \text{(in units of Newton)} \tag{4.3}$$

where F_c is the cutting force, 'a' is the reading shown on the lower curve of Agile Link (refer to Fig.4.11a) , F_t is the thrust force and 'b' is the reading on the upper curve of Agile Link (refer to Fig.4.11a).

4.6 Measurement and Specification of Surface Finish

The finish of a machined surface is one of the most important aspects of a given machining operation as it represents part of the end goal of the process. Earliest method to quantitatively analyze the smoothness or roughness of a machined surface was with the help of a diamond stylus instrument. The stylus traversed the surface to be analyzed, and using transducers, converted the motions of the stylus into vertical and horizontal traces. The centre line average (CLA) or arithmetic average (AA) roughness (R_a) usually used to express the roughness of a surface uses a line designated as the centre-line, which is

drawn in such a way that there is an equal area between the line and the surface trace, both above and below the line. The resultant roughness R_a is calculated using the mean deviation of the peaks from the centre-line for a trace. The roughness values generally expected in a finish-turning operation fall in the range of 0.75 μm to 1.5 μm [6].

The surface finish of a machined sample varies as a function of its cutting speed and feed. Shaw [6] reported that the surface finish improves with an increase in the cutting speed and a decrease in feed pre revolution (Fig.2.27). Other factors influencing surface finish are presence of BUE, magnitude of cutting temperatures, etc.

Surface roughness of the samples machined under the different conditions described above was measured after the turning experiments to quantitatively analyze the finish of the surface produced. The Wyko NT9100 Optical Profiling System was used to analyze the finish of the machined surfaces for the samples turned under the different cutting conditions. Wyko uses non-contact three-dimensional surface metrology to produce high quality three-dimensional surface maps of the surface being studied. Coherence scanning interferometry, or white-light interferometry or vertical scanning interferometry is used for obtaining the image. The surface roughness value is expressed in terms of Centre Line Average or Ra.

4.7 Steps in Sample Preparation for Metallographic Analysis

The procedure used for preparing the machined samples for metallographic observations started with cleaning the samples in acetone using an ultrasonic cleaner for 10 minutes, following which they were washed in acetone and dried completely. This process removed any metal dust or unwanted chip fragments that might have been sticking to the samples.

The samples were ground using silicon carbide paper and water, starting with. grade 180 followed by 240, 400, 1200 using light pressure applied to the centre of the mounted sample. After the final grinding operation on 1200 paper, the samples were cleaned by washing with water followed by rinsing in alcohol and drying. Next, they were polished using diamond suspension, starting from 6 micron and going down to 1 micron. Care was taken to wash the sample thoroughly with soapy water before moving on to the 1 micron stage so as to avoid contamination of the disc. Polishing was followed by etching of the samples with 0.2% HF solution (by volume) for bringing out the surface relief clearly when seen under light microscope and SEM.

4.8 Metallographic Analysis using Light Microscope and SEM

The samples prepared as described above are examined under a light microscope (Leitz-Laborlux 12 ME). The main areas examined included the primary and secondary deformation zones, the chip region, the machined surface and the work-piece bulk

material region. The samples were further analyzed using a scanning electron microscope (Jeol 5400-LV) to get further insight into the deformation structures produced during the process of machining. Machined surface and the fractured phases present on it were studied in details using the SEM. Energy dispersive spectroscopy or EDS was done on different sites of the sample to analyze the chemical composition of the phases. Surface roughness of the machined surfaces generated under each cutting condition was quantified using Wyko analysis.

4.9 Strain Estimation

4.9.1 Using orientation of fractured silicon particles

Plastic strains induced in the workpiece during cutting were estimated by following the orientation of fractured particle flow in the material ahead of the tool tip. The second phase particles present in the matrix undergo cracking and fracture when subjected to deformation during the orthogonal cutting, and get aligned along distinct patterns, as can be seen in Fig. 4.14 (a and b). Lines were drawn along the orientation of fractured particle flow on the cross-sectional optical-micrograph of the sample and assuming that the particles get aligned along the direction of strain experienced, these lines following their orientations were used for estimation of local plastic strains in the material. Plastic strains were estimated at the points of intersection of an imaginary grid (50μm by 50μm) using Eqn.2.28. The strains were then plotted on an outline of the micro-

graph and points having same magnitude of strains were connected together to yield iso-strain lines. The procedure for estimating the strains has been described in greater details in the Section 6.2.

4.9.2 Using 6061 Al markers inserted inside 319 Al samples

Plastic strains in the material below the machined surface (for 319 Al samples) are important for studying the conditions leading to fracture of second phase particles, particularly silicon particles in the region. The plastic strains below machined surface were estimated in the tube shaped 319 Al samples by inserting markers made up of aluminum alloy 6061 Al and studying the deformation of the interface (between 319 Al workpiece and 6061-T6 markers) with respect to its original orientation. It is to be noted that although attempts were made to run this kind of test with a modified 319 Al specimen with markers made up of 319 Al into holes drilled into it, subsequent analysis showed that marker inserts made up of 319 Al was broken into fragments due to fracture of second phase particles near the machined surface. As a result, inserts made up of 6061-T6 were used as markers.

The tubular 319 Al samples used for orthogonal cutting tests under this study was modified by drilling twelve equally spaced longitudinal holes, each with diameter equal to 1.5mm, as has been shown if Fig.4.15a. Twelve rods of 6061 Al, having diameter equal to 1.5mm, were gently hammered into these holes. Care was taken to maintain a tight fit

between the markers and the workpiece material. The samples thus modified were subjected to orthogonal machining under interrupted cutting conditions. After the turning experiments were over, the portion of the workpiece which underwent machining and had the chip still attached to it was cut off from the workpiece body using a saw, as has been shown in Fig.4.15b. This portion was mounted and polished; following the procedures described in Section 4.7 and was examined under light microscope (Section 4.8) with particular attention to the interface between the marker and the workpiece body (Fig.4.15c) and the displacement of the marker with respect to its original orientation. The amount of displacement undergone by the marker was used for finding the plastic strains in the material lying below the machined surface using Eqn.2.28.

4.10 Hardness Measurements and Flow Stress Estimation

Vickers Hardness (HV) was measured using a Buehler Micromet II microhardness tester. The load used for all the indentations was 10 grams. Indentations were taken on the aluminum matrix and care was taken to place all indentations at least 30 microns away from the nearest second phase particle. Indentations were place at the points of intersection of an imaginary grid of 100μmX75μm. Care was taken to place the indentations in the aluminum matrix and at least 20μm away from any second phase particles. Additional measurements were taken in and around the grid points to

substantiate the hardness data further. The procedures followed and the results have been described in greater details in Section 5.10.

Flow stresses in the workpiece at the locations of the indentations were estimated using Eqn.2.31. The points on an outline of the micro-graph for the area ahead of the tool tip location, which exhibited same magnitude of stresses have also been connected together to obtain iso-stress contours (Section 5.10).

FIGURES - CHAPTER 4

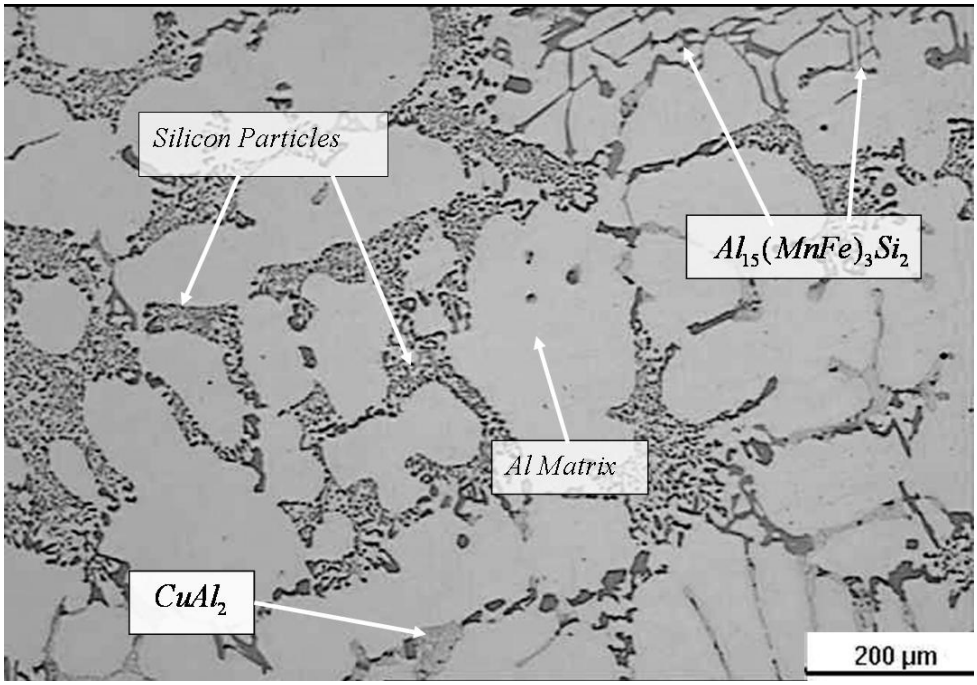

(a)

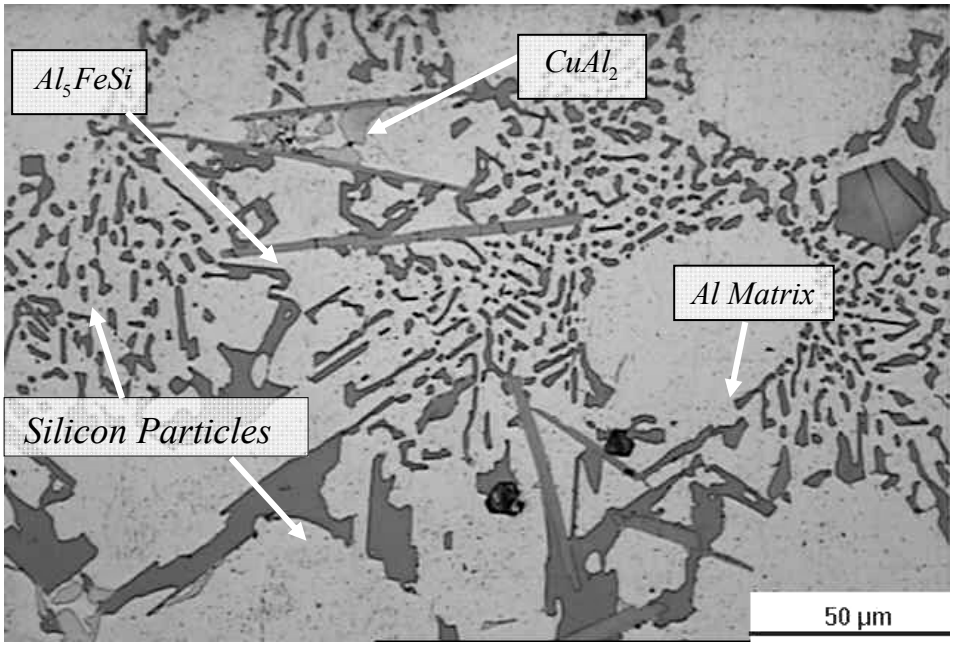

(b)

Fig.4.1 contd.

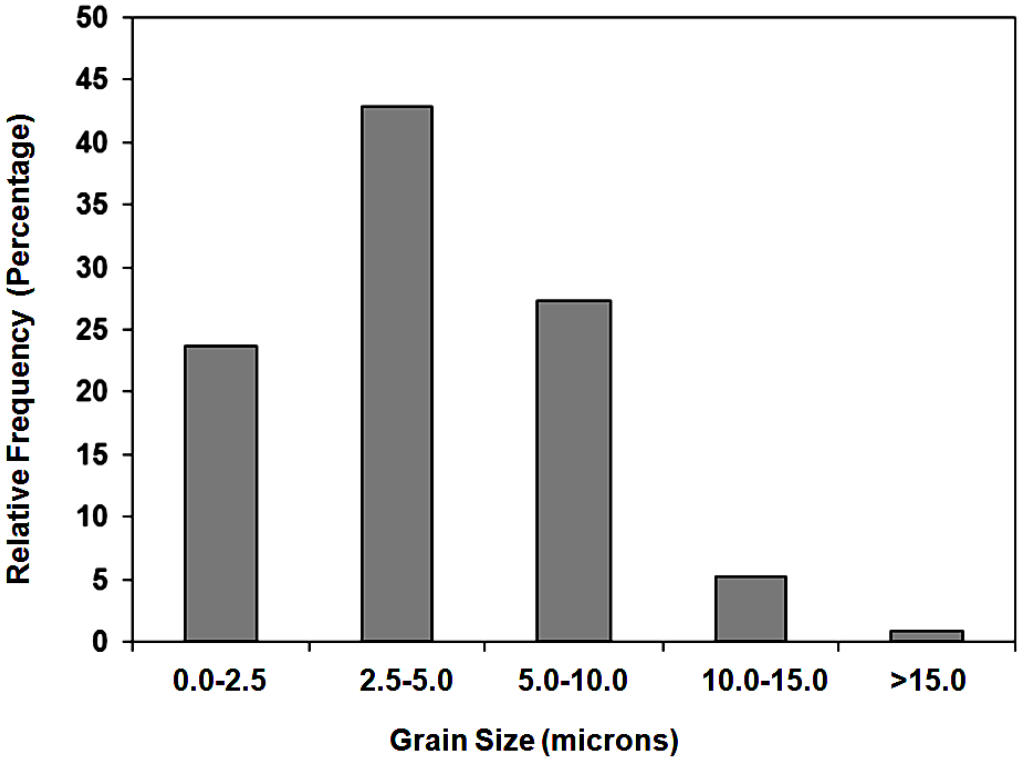

Fig. 4.1 (a) and (b) Optical microstructures of Aluminum alloy Al 319 showing aluminum matrix Si particles, $Al_{15}(Mn,Fe)_3Si_2$ which occurs as brown Chinese script, needle shaped Al_5FeSi and Cu_2Al ; and (c) Histogram showing size distribution of silicon particles in Al 319.

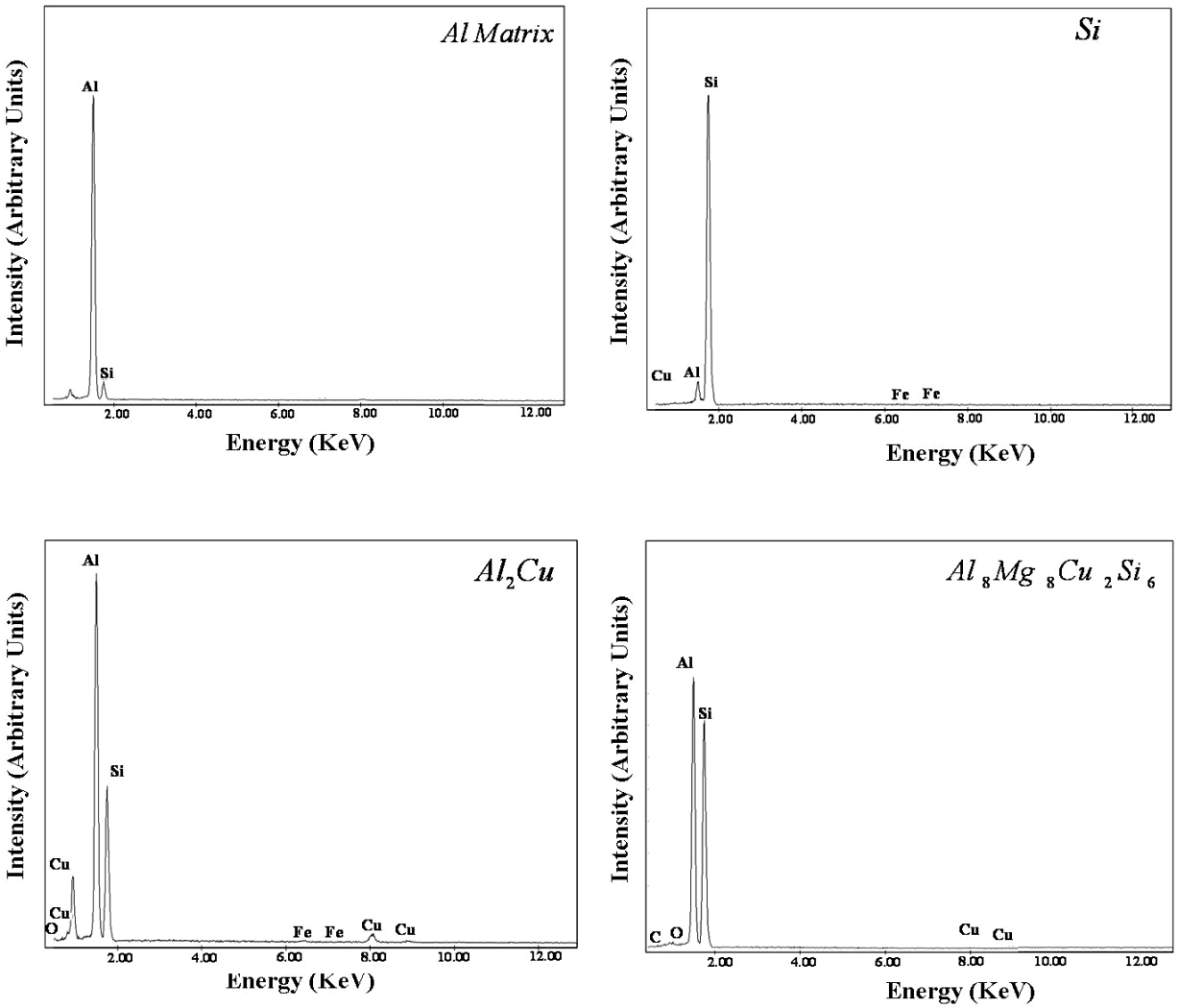

Fig.4.2 EDS spectrum of different phases present in A 319. EDS spectrum of (a) Al matrix; (b)Silicon Phase; (c) Al_2Cu phase; and (d). $Al_8Mg_8Cu_2Si_6$

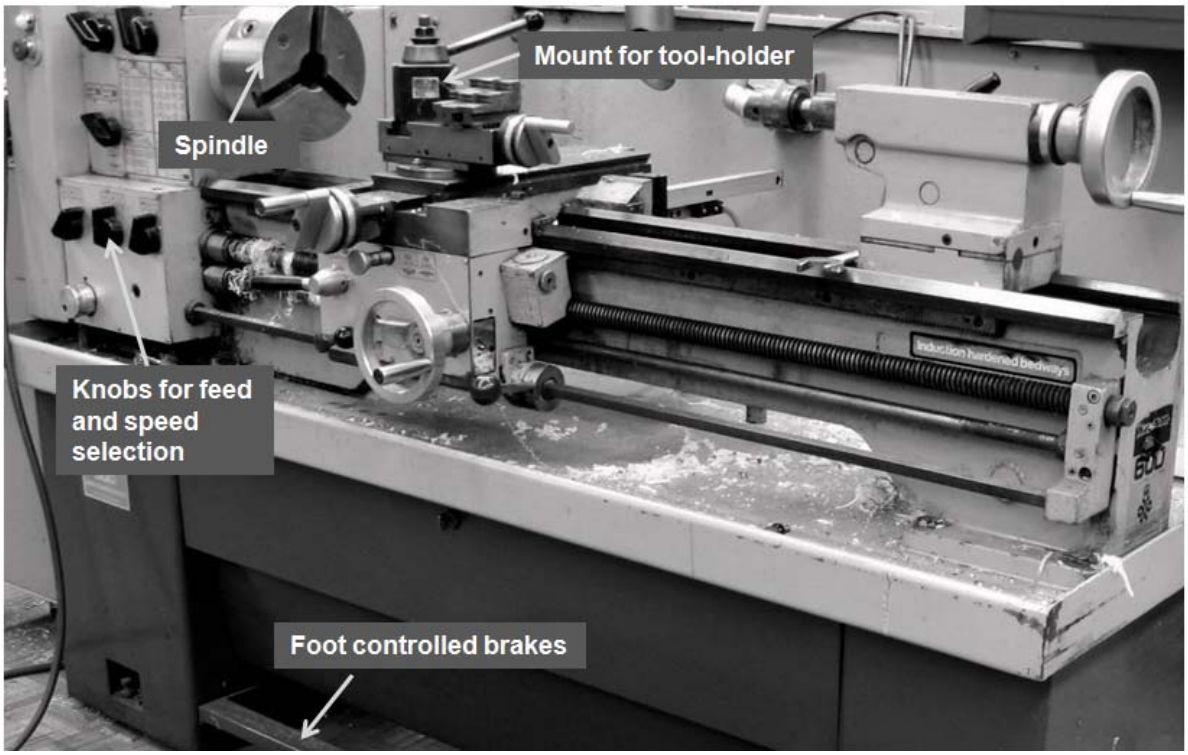

Fig.4.3. Harrison M300 lath used for the orthogonal cutting experiments.

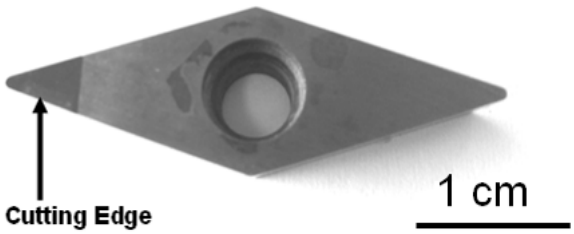

Fig.4.4. Polycrystalline diamond (PCD) insert (VCMW 332FP) with a rake angle of zero degree, used for orthogonal turning of Al 319.

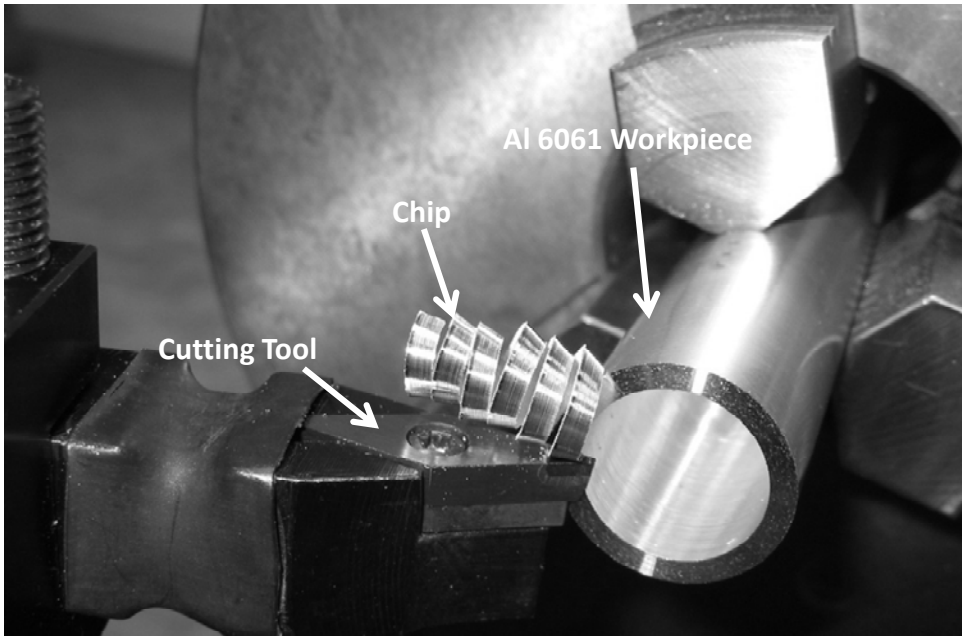

Fig.4.5. Chip produced during orthogonal turning experiment

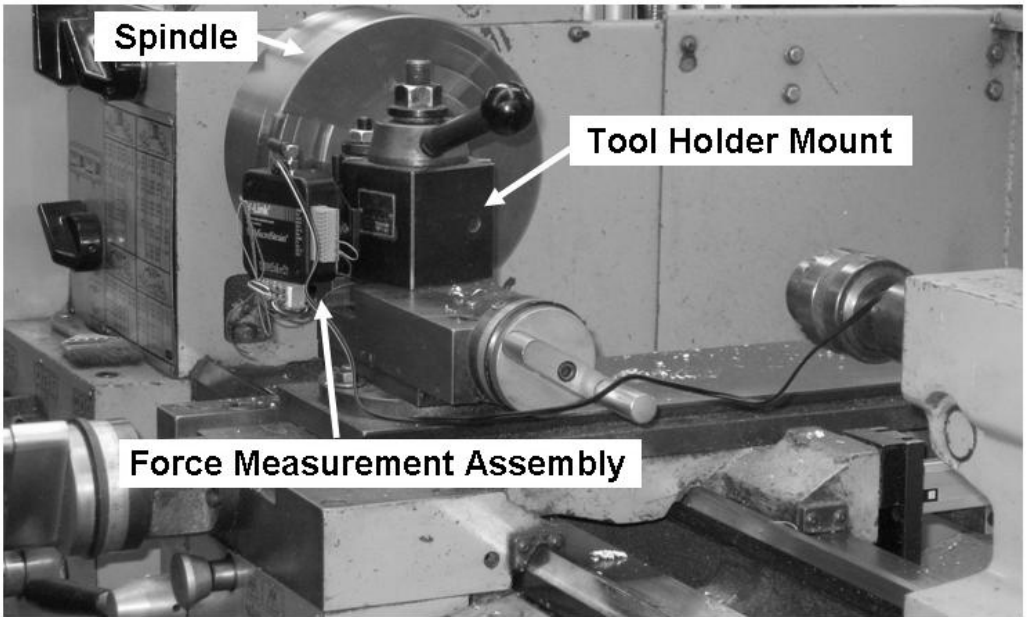

Fig.4.6. Set up showing the force measurement system mounted on a lath during the process.

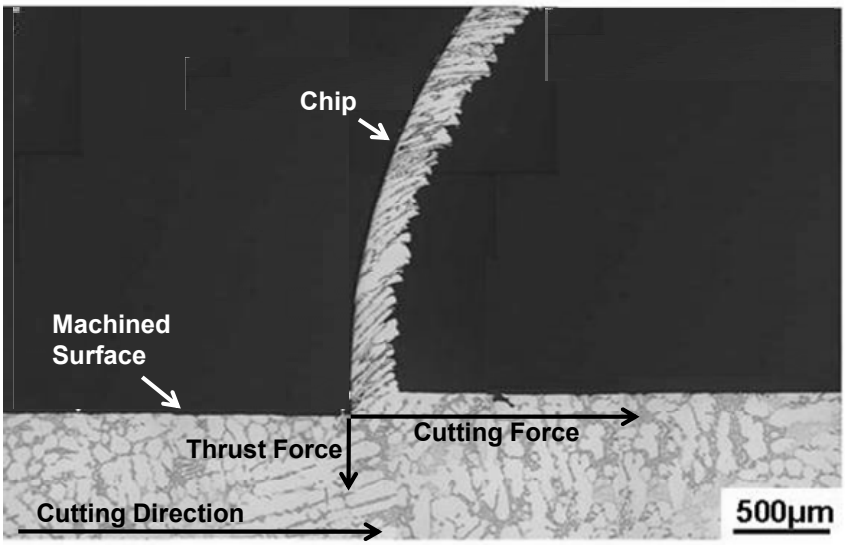

Fig.4.7. Optical micrograph showing the direction of cutting force and thrust force on a section of an orthogonally cut sample. Cutting conditions: cutting speed 35m/min and feed per revolution 0.10mm.

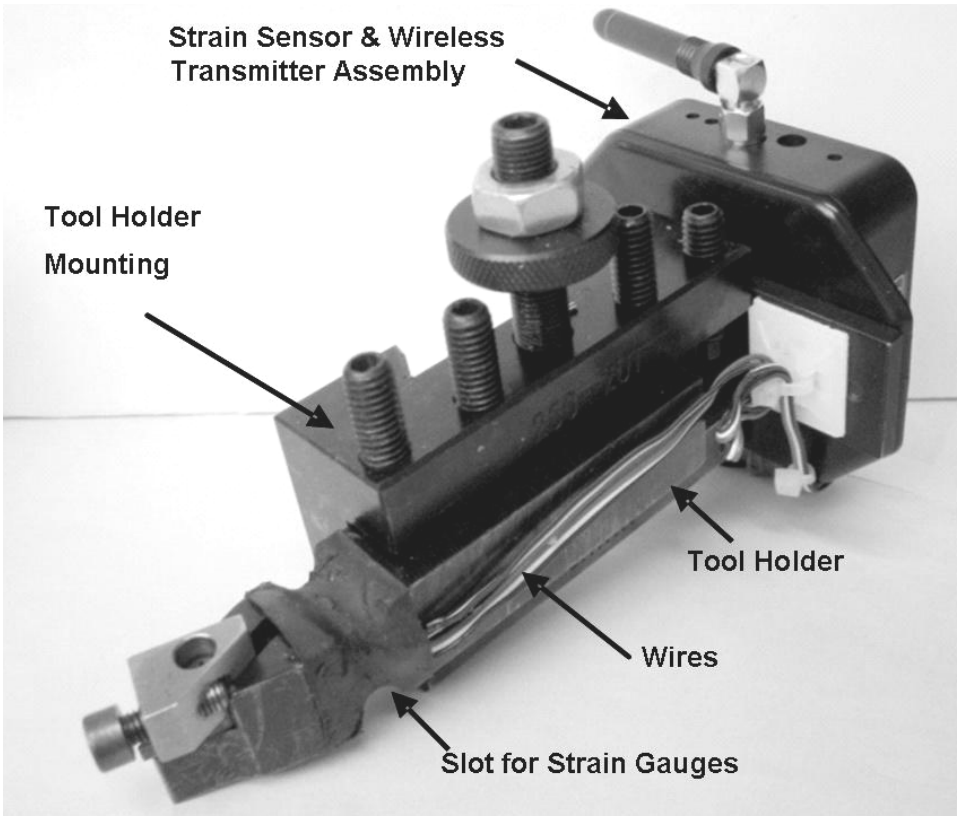

(a)

(b)

Fig.4.8. Part of the portable force measurement system which was mounted on the lath during machining experiments: (a) modified tool-holder with tool-holder mounting and strain sensor, (b) strain sensor (V-Link 2.4 GHZ voltage node) with wireless data transmitter.

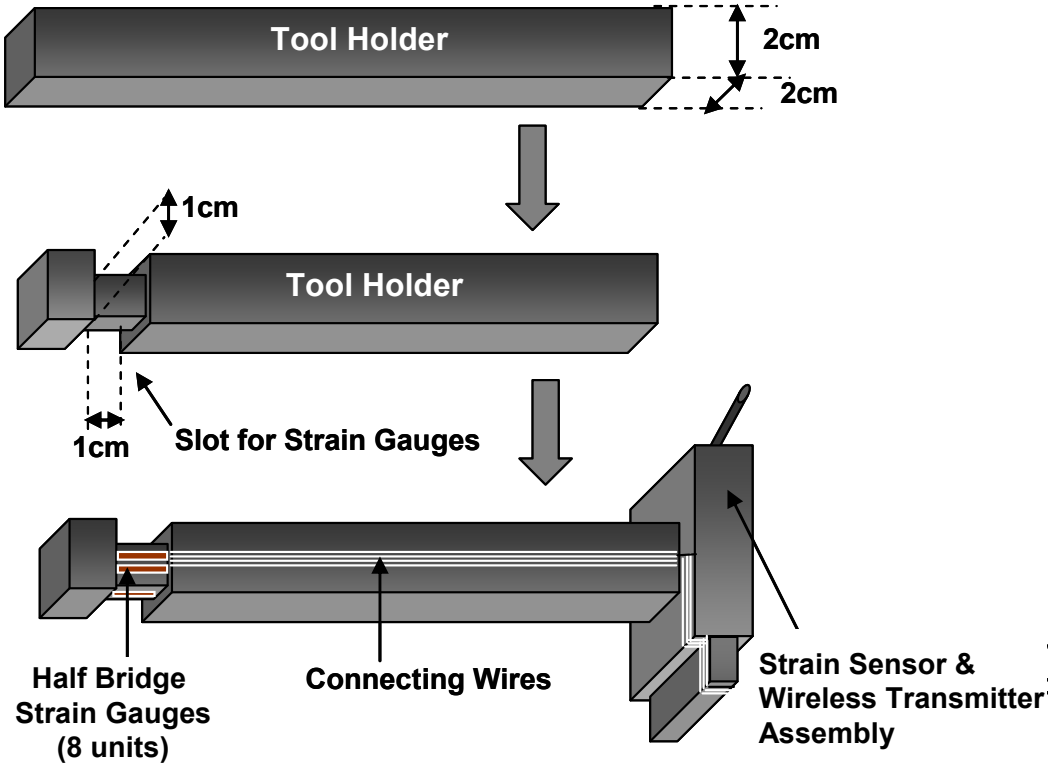

Fig. 4.9. Schematic showing step-wise modification of the tool-holder for construction of the two-axis force sensor for measurement of forces during orthogonal turning experiments.

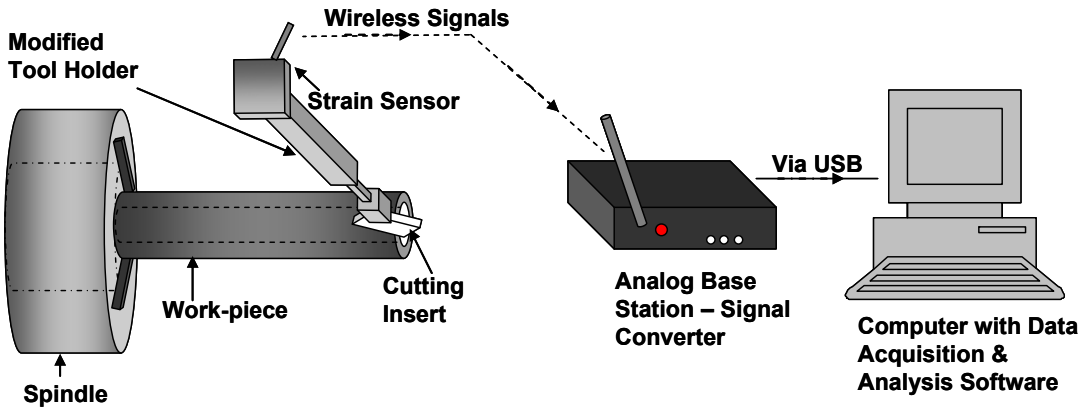

(a)

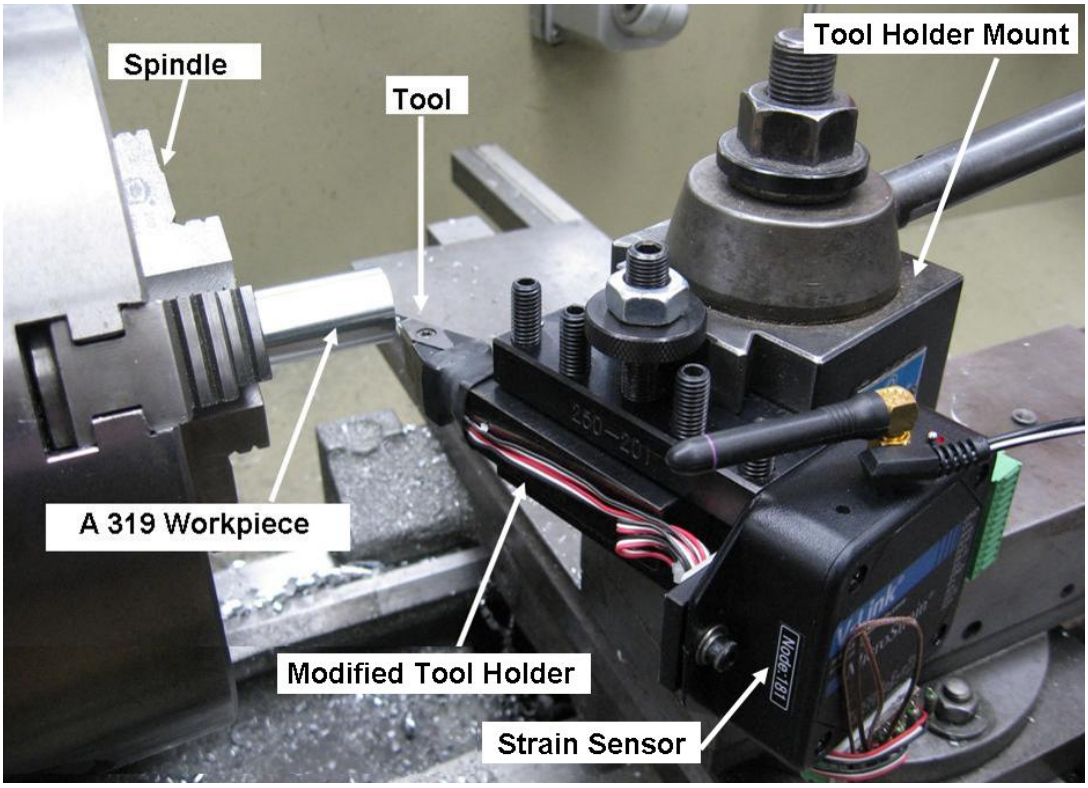

(b)

Fig.4.10 (a) Schematic diagram showing the different components of the force sensor and data acquisition system; (b) Actual arrangement showing the set-up for measurement of forces with force measurement system mounted on the lath, cutting tool mounted on the tool holder and workpiece mounted on the lath spindle.

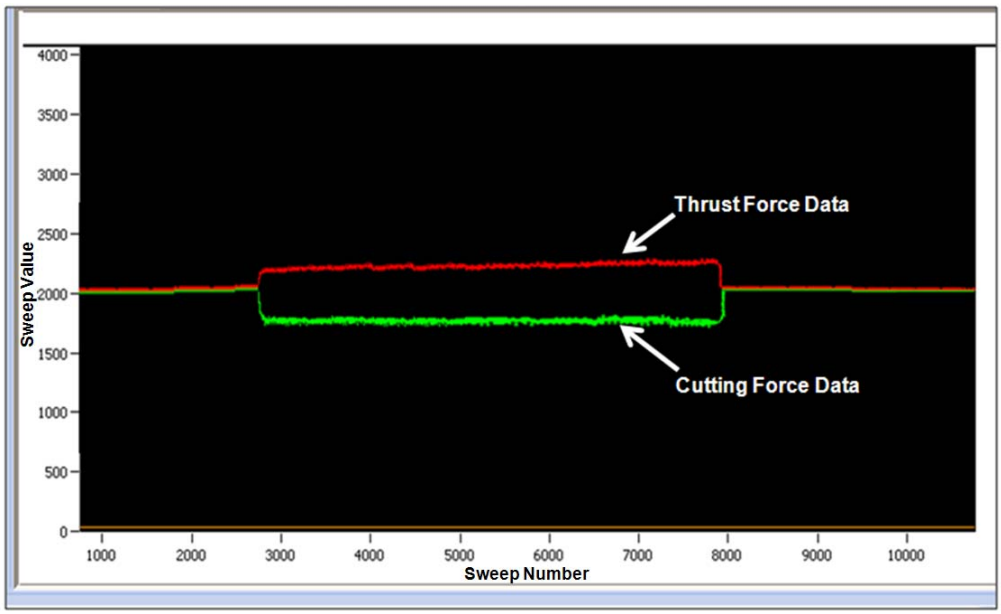

(a)

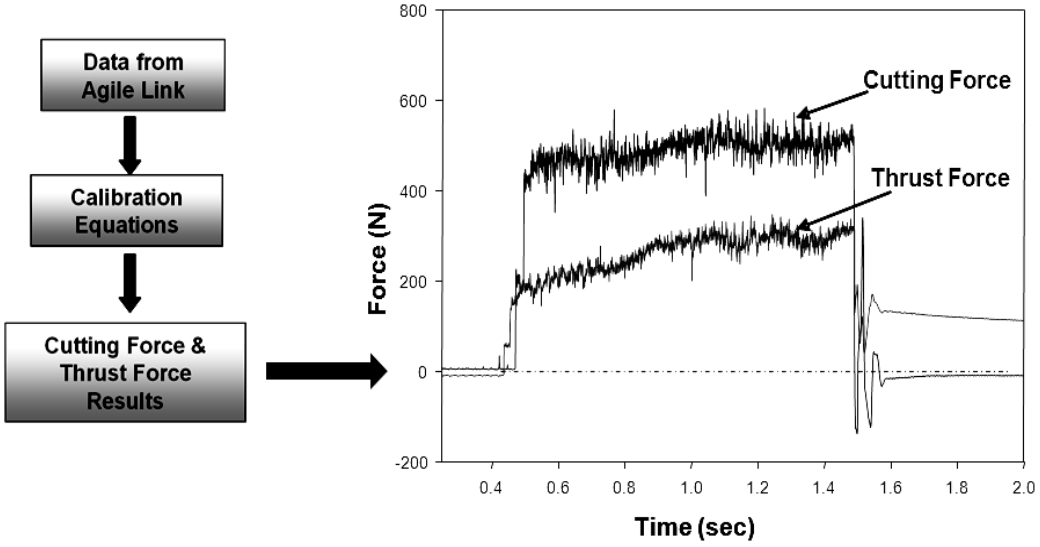

(b) (c)

Fig.4.11. (a) A snapshot from Agile Link software showing data collected for a sample orthogonal machining run as output. The lower curve shows the measurements for cutting force while the upper curve shows the output for thrust force, (b) Flow chart showing the steps in processing of data obtained from Agile Link software using calibration equations, (c) Typical output plot showing cutting and thrust forces results.

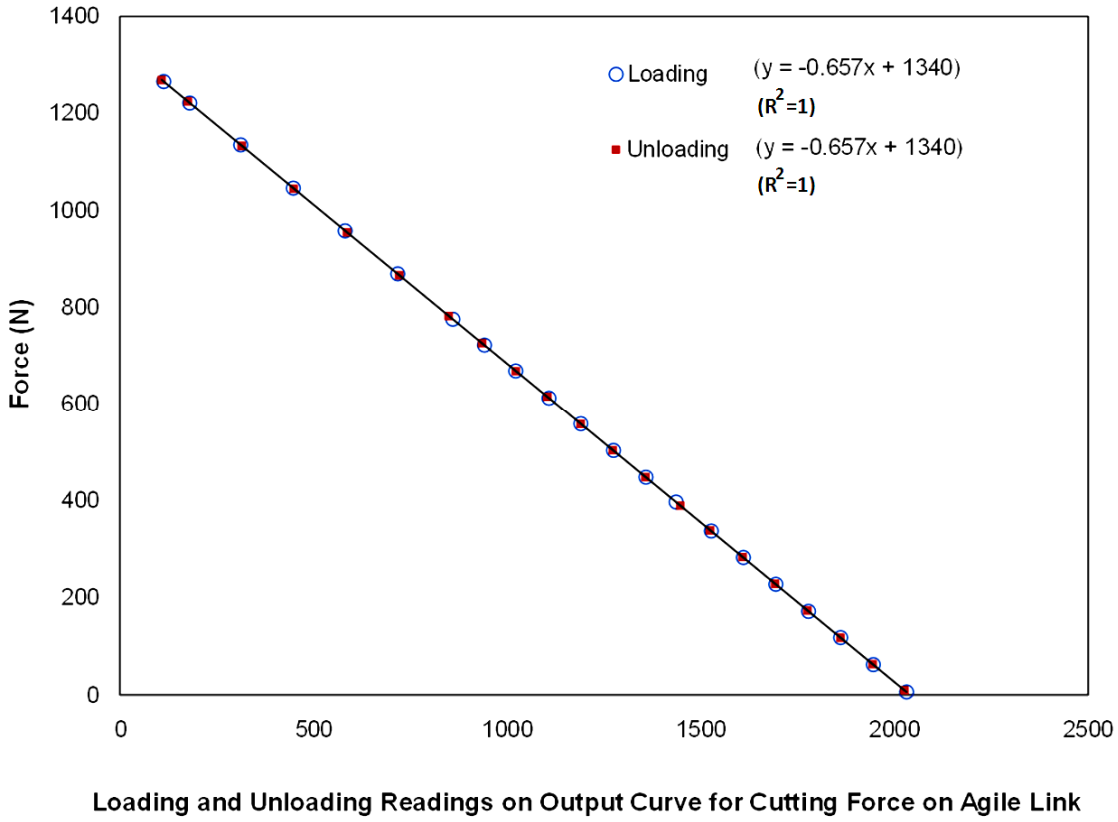

(a)

Fig.4.12 contd.

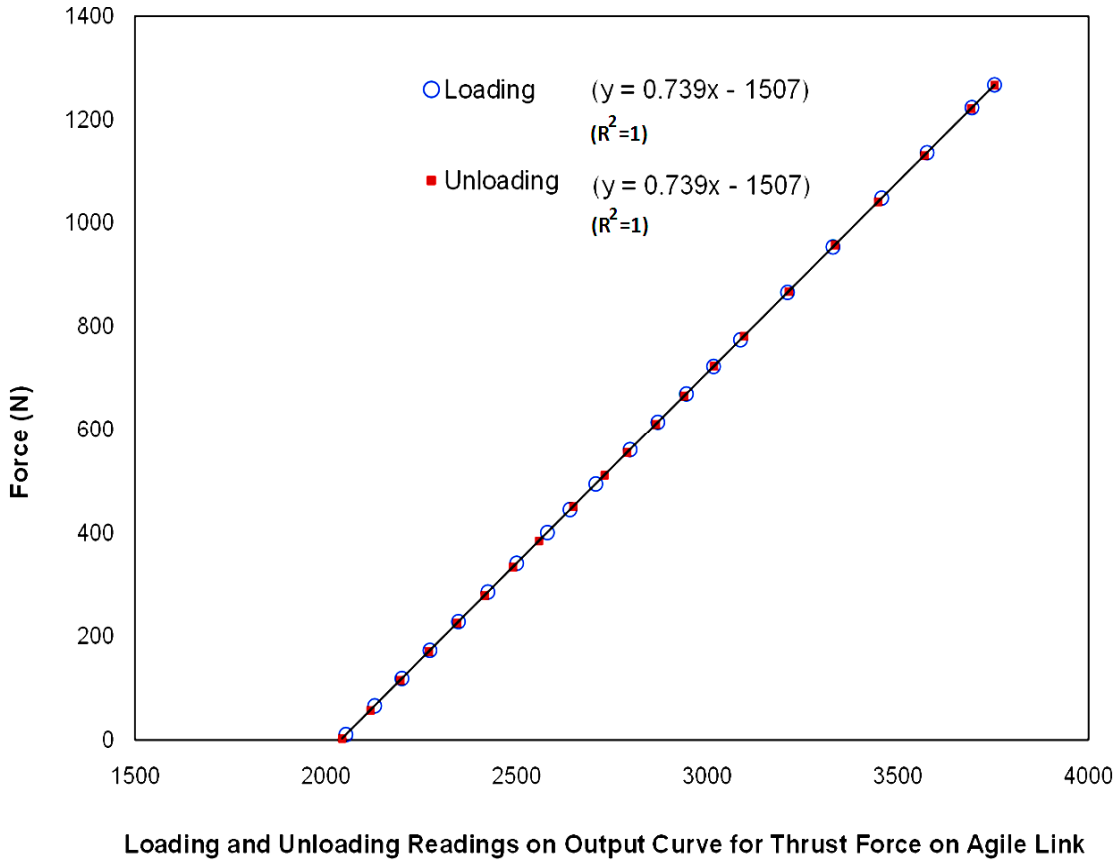

(b)

Fig.4.12. Curves for relation between readings on Agile Link output and force applied on force measuring system during loading and unloading for (a) cutting forces (shown in the lower curve in output plot of Agile Link in output curve); (b) thrust forces (shown in the upper curve in output plot of Agile Link in output curve); The corresponding equations for loading and unloading are also shown on the plots.

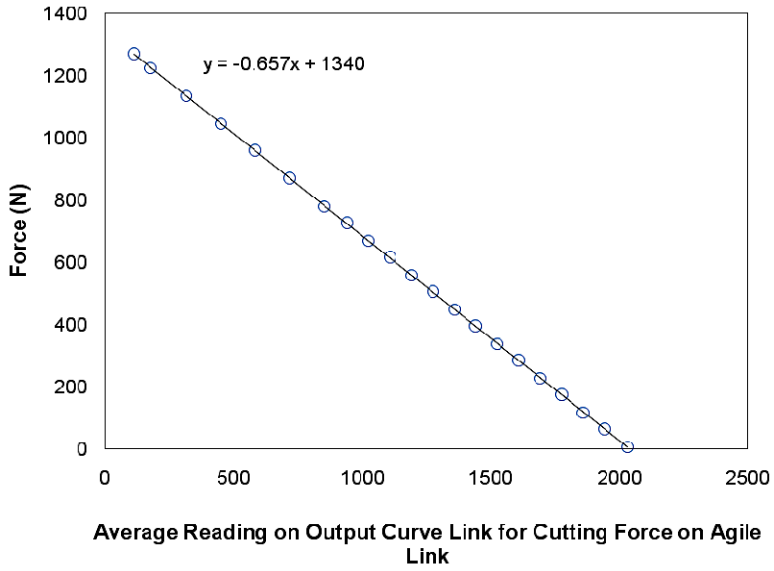

(a)

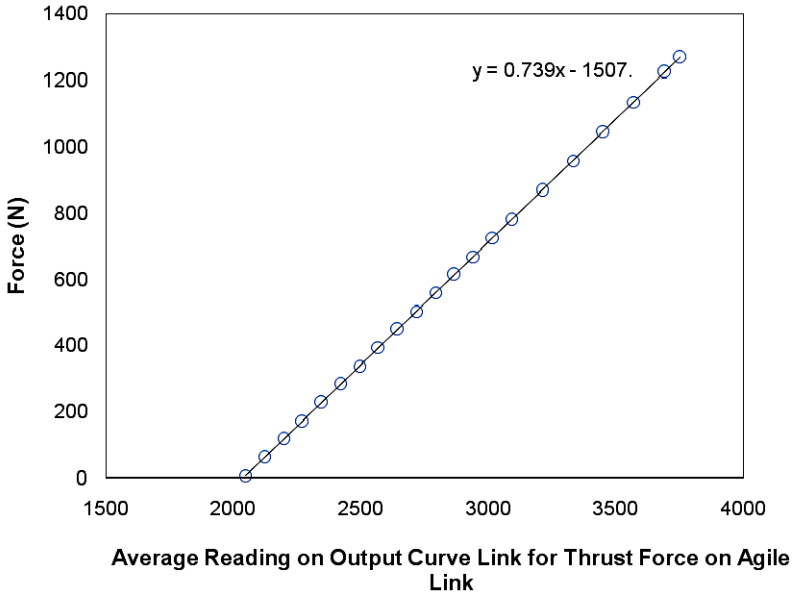

(b)

Fig.4.13. Calibration curve for relation between average value of readings collected during loading and unloading for forces applied on the force measuring system for (a) cutting forces (shown in the lower curve in output plot of Agile Link in output curve); (b) thrust forces (shown in the upper curve in output plot of Agile Link in output curve); The corresponding equations defining the relation between readings on Agile Link and force applied are also shown on the plots. These two equations were used for conversion of all Agile Link data collected as part of this study.

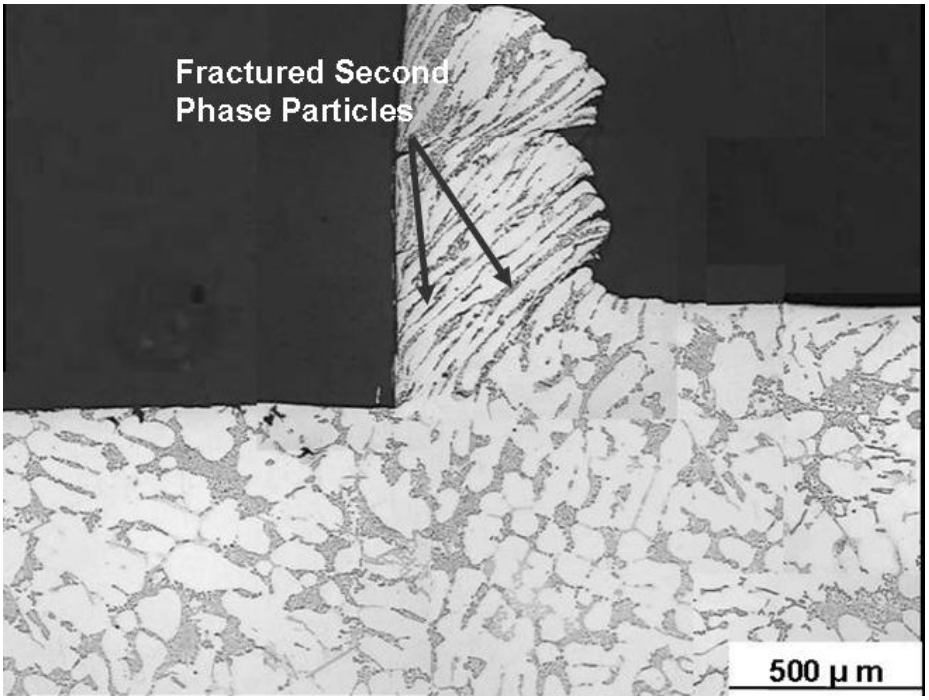

(a)

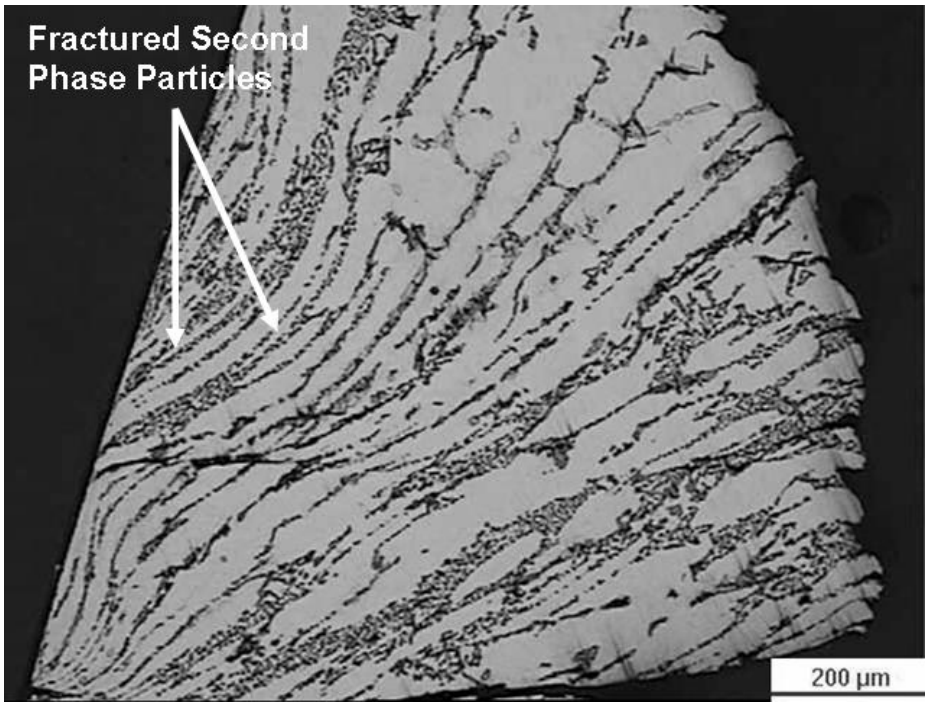

(b)

Fig.3.14 contd.

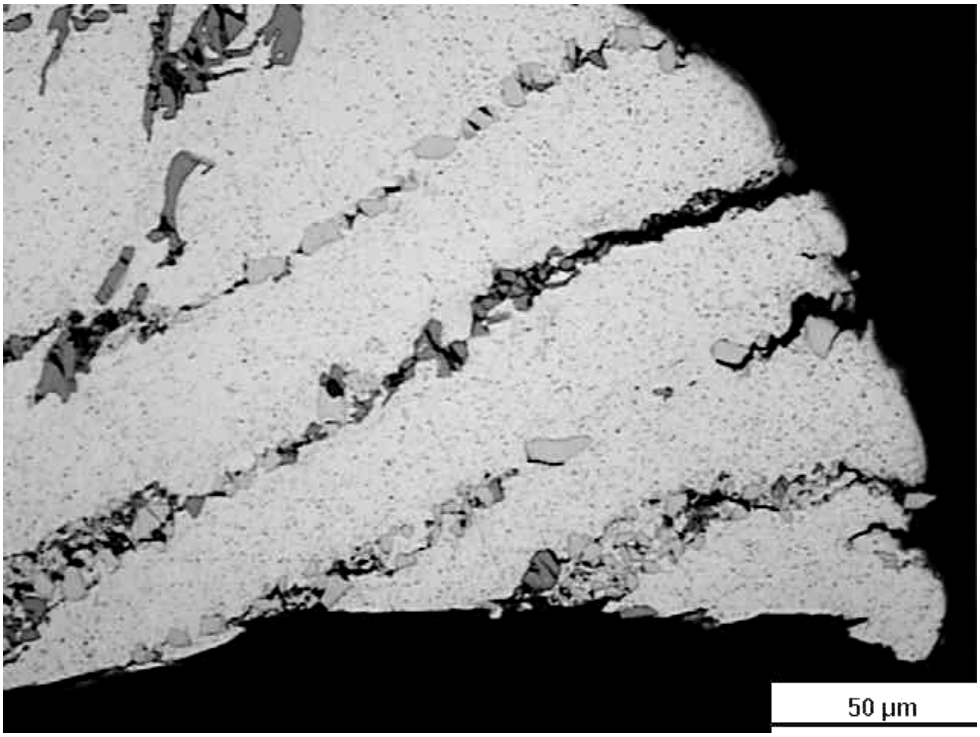

(c)

Fig.4.14 Optical micrograph of orthogonally cut 319 Al (cutting speed 25m/min, feed 0.25mm) showing orientation of fractured particles in (a) area ahead of tool tip, (b) in the chip (c) on the outer edge of the chip.

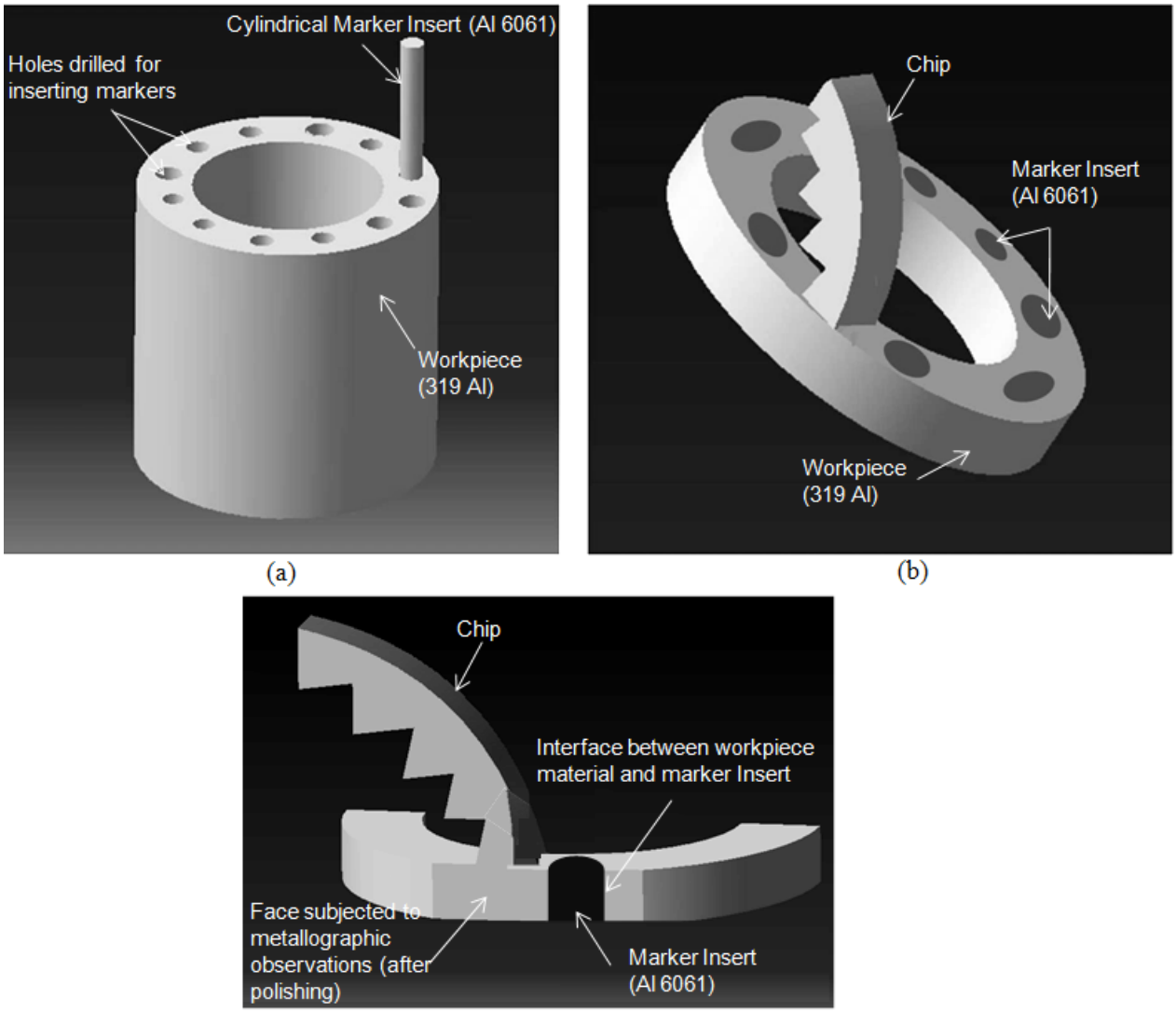

Fig.4.15(a) Schematic diagram showing 319 Al sample modified by drilling holes into it and cylindrical marker made up of 6061 Al being fitted into it,(b)chip attached to Al 319 sample fitted with marker inserts of 6061 Al after being orthogonally turned and sawed off the main body of the tubular workpiece, (c) schematic diagram of a section of the turned sample as it looked after polishing (mounting not shown here) showing the base material (319 Al) and marker insert (6061 Al) on the face subjected to metallographic observations.

CHAPTER 5

EXPERIMENTAL RESULTS

5.1 Introduction

This chapter describes the results of the experiments done in order to assess the machinability performance of Aluminum alloy 319 Al by subjecting the alloy to orthogonal cutting under different cutting conditions. The effect of different cutting speeds and feed rates on turning of the material was studied by conducting turning experiments on the material at twenty different conditions followed by a detailed analysis which included measurement of cutting and thrust forces generated during the operations using the 2-axis force measuring system, estimation of the corresponding frictional force between tool and chip and the resulting power consumptions. Optical and scanning microscopy studies were conducted in order to examine and characterize the deformation microstructure produced during machining of the samples. The surface produced after machining were analyzed using surface profile study and roughness measurements using SEM and WYKO. Hardness of chips and material below machined surface was measured and analyzed. Also, deformation of material in front of the tool tip was studied by estimating flow stress and plastic strain distribution in the region. These results were used subsequently to find the theoretical work of deformation in the material. Fracture of Silicon particles under the machined surface and in the primary deformation zone was

also studied to understand the effect of second phase particles on orthogonal cutting. The results of the above experiments and analyses have been presented in the following sections:

5.2 Chip morphology produced during dry orthogonal cutting of 319 Al

Aluminum alloy 319 Al produced discontinuous chips with saw-tooth morphology when subjected to turning on a lath under the turning conditions studied. Fig.5.1 shows a typical cross-sectional micrograph of the alloy when machined under cutting conditions of cutting speed 50m/min and feed per revolution of 0.35mm. Fig.5.2 (a and b) show SEM images of details of the saw-tooth geometry or the serrations in the chips. Micrographs of chips produced under the twenty different cutting conditions studied have been shown in Appendix I. Important results related to form and geometry of chips generated during this study are discussed in details in Section 5.8.

5.3 Analysis of forces generated during dry orthogonal cutting

The results and analysis of the forces measured for 319 Al and 6061-T6 and a comparative study of the forces generated during cutting of the two alloys are described below:

5.3.1 Stages and Trends in a Typical Turning Force Curve

Cutting and thrust forces were measured for different cutting conditions. Fig.5.3 shows a typical output curve from the force measurement system, post preliminary analysis for conversion of the result data into forces using the calibration equations.

A careful examination of the curves leads to identification of different stages in the force plots (Fig.5.3). After the tool came into contact with the workpiece, force measurements showed a rapid rise in magnitude of forces till it stabilized (in most cases) at the cutting value when both the cutting and thrust forces form a plateau like zone where they oscillate roughly (Fig.5.3). The cutting insert is in constant contact with the workpiece in this stage resulting in continuous generation of machined surface and formation of chips.

As the quick stop foot controlled brakes are applied almost instantaneously, the forces rapidly fall and reach zero. In some cases however, some oscillations are seen in the force curves before they finally reach and stabilize at zero, which can be attributed to vibrations induced in the lath during the sudden hitting of the foot-controlled brakes.

5.3.2 Cutting Force Measurement for 319 Al

Fig.5.4 (a-e) shows cutting forces measured for 319 Al under different conditions of cutting speed and feed per revolution. An examination of the curves revealed that there was no significant change in measured force values in the cutting zone for fixed cutting

conditions. It was noted that the amplitude of oscillations were higher for lower speed of cuttings (at a constant feed per revolution conditions (Refer to Fig.5.4)). Also, the amplitudes of oscillations were seen to increase markedly with an increase in feed for same values of cutting speed.

Average cutting force for each cutting condition studied was estimated from the force data collected for six rotations of workpiece in the cutting zone, immediately before brakes were applied. The initial part of the cutting zone was avoided as force measurements done under some cases, as in the case of cutting speed 75m/min and feed per revolution of 0.35mm and 0.45mm (Fig.5.4 d) showed a rise in cutting forces during the initial part of cutting, which later stabilized. Fig.5.5 presents the average cutting forces for different feeds as a function of cutting speed. The standard deviations shown in the plot were estimated from the deviation in data collected for the aforementioned six rotations in the cutting part of force measurements. Thus, the standard deviation was equal to the amplitude of oscillation for these six rotations.

The general trend outlined was that of cutting forces increasing in magnitude with an increase in feed and with a decrease in cutting speed. The lowest cutting forces measured were approximately 200N for a feed of 0.10mm (for all five different cutting speeds). The highest cutting forces were seen to be approximately 1000N, which occurred for the combination of lowest cutting speed (25m/min) and highest feed (0.45mm). Also, it was found that with an increase in cutting speed from 25m/min to 115m/min, cutting

forces dropped by 183N, 241N, 279N for feed rates equal to 0.25mm, 0.35mm and 0.45mm respectively. However, cutting forces did not show any marked change for the lowest feeding rate used for the study, i.e. 0.10mm, showing a variation of maximum 10N for the different cutting speeds studied.

Fig.5.6 presents the average cutting forces measured for different cutting speeds as a function of feed used. The plot re-emphasizes the fact that at the a feed of 0.10mm, which is the lowest feed studied, the magnitudes of cutting forces for all five cutting speeds are in close vicinity of each other. It also shows that with an increase in feed, the cutting forces increase for all cutting speeds. The magnitude of increase, however, is higher for a lower feed rate.

5.3.3 Thrust Force Measurement for 319 Al

Fig.5.7 (a-e) shows thrust forces measured for 319 Al under the different conditions studied. Some of the thrust force curves showed variation in values of measured thrust for fixed cutting speed and feed conditions (Fig.5.7 (b-d)).

The thrust force values at the lowest feed rate of 0.10mm showed almost no significant variation in magnitude for different cutting speeds. However, with a rise in feed, the thrust force values showed an increase, stabilizing later as cutting proceeded further. This trend was evidenced for all cutting speeds except for the lowest cutting

speed condition of 25m/min. Also, the difference in magnitude became more pronounced with an increase in feed.

Average thrust force for each cutting condition studied was estimated from the force data collected for six rotations of workpiece, in a manner similar to estimation of average cutting force (Section 5.3.2). The standard deviations shown in the plot were estimated from the deviation in data collected for the aforementioned six rotations in the cutting zone of force measurements and are equal to the amplitude of oscillations in data collected for the six rotations.

Fig.5.8 shows the variation of thrust forces with change in cutting speed, for different feed conditions. The trends outlined by thrust forces were similar to those outlined by cutting forces, that is, thrust forces increased with an increase in feed and with a decrease in cutting speed. The lowest thrust forces measured were approximately 100N for a feed of 0.10mm and the highest magnitudes were found to be approximately 600N for the combination of lowest cutting speed (25m/min) and highest feed (0.45mm), i.e. same condition which also exhibits highest cutting forces. It was observed that the thrust forces dropped in magnitude by 156N, 119N and 96N for feeds of 0.25mm, 0.35mm and 0.45mm respectively, for an increase in speed from 25m/min to 115m/min. However, for feed 0.10mm, thrust forces showed a slight rise in magnitude (by 25N) as cutting speed was increased from 25m/min to 115m/min.

Magnitude of thrust forces were found to be lower than those of cutting force for all cutting conditions. This can be attributed to the direction in which the two forces act (refer to Fig.4.6 and Fig.4.7). Cutting force acts in the direction of cutting and is primarily responsible for shearing of the material leading to chip formation and for deforming the material in front of tool tip. Thrust force, on the other hand, acts downwards, into the bulk of workpiece and is mainly responsible for deforming the bulk of the workpiece below the cutting line.

Fig.5.9 showing the average thrust forces measured for different cutting speeds as a function of feed used emphasizes the similarity in trends in cutting and thrust forces. The magnitudes of thrust forces for the lowest feed studied, 0.10mm, for all five cutting speeds are found to be close to each other. At higher feeds, however, thrust forces show higher magnitudes for lower cutting speeds. Also, the standard deviation in thrust force measurements, which represent the amplitude of oscillations found from measurements during cutting also rises with a rise in feed.

Thus, both cutting force and thrust force's magnitude increased with an increase in feed and decreased with an increase in speed of cutting. The smallest magnitudes for both cutting forces (184N, 192N, 199N, 195N and 188N for cutting speed of 25m/min, 35m/min, 50m/min, 75m/min and 115m/min respectively) and thrust forces (90N, 101N, 119N, 114N and 115N for cutting speed of 25m/min, 35m/min, 50m/min, 75m/min and 115m/min respectively) were measured for the lowest feed per revolution (0.10mm)

conditions. Cutting forces dropped when speed was increased from the lowest cutting speed of 25m/min to highest speed of 115m/min (cutting forces dropped by 183N, 241N, 279N for feeding rates equal to 0.25mm, 0.35mm and 0.45mm respectively, as the cutting speed increased from 25m/min to 115m/min and thrust forces dropped by 156N, 119N and 96N for feeds of 0.25mm, 0.35mm and 0.45mm respectively, with an increase in speed from 25m/min to 115m/min), except for feed per revolution of 0.10, which showed a very slight deviation from it.

In summary, a lower feed per revolution and a higher cutting speed (within the range studied under this work) were the conditions that lead to lowering of cutting and thrust forces, and hence are desirable conditions for machining, as they lead to a lowering of power consumption during the process.

5.3.4 Cutting Force Measurement for 6061-T6

Fig.5.10 (a-e) shows cutting forces measured for 6061-T6 under different conditions of cutting speed and feed per revolution. An examination of the curves revealed that there was no significant change in measured force values in the cutting zone for fixed cutting conditions. Cutting forces were measured for feed per revolution conditions of 0.10mm, 0.25mm and 0.35mm and average cutting force for each cutting condition studied was estimated from the force data collected for six rotations of workpiece in the cutting zone, immediately before brakes were applied, in a manner

similar to that described in Section 5.3.2. Fig.5.11 shows the average cutting forces for different feeds as a function of cutting speed. The standard deviations shown in the plot were estimated from the deviation in data collected for the aforementioned six rotations in the cutting part of force measurements. Cutting forces were found to increase with an increase in feed per revolution and with a decrease in cutting speed. The lowest cutting force measured for this alloy was approximately 220N for a feed of 0.10mm and cutting speed of 115m/min. The highest cutting force was found to be approximately 760N, which occurred for the combination of lowest cutting speed (25m/min) and highest feed (0.35mm).

It was found that the cutting forces for 6061-T6 dropped by 55N, 172N, 113N for feeding rates equal to 0.10mm, 0.25mm and 0.35mm respectively, as the cutting speed increased from 25m/min to 115m/min.

Fig.5.12 shows the average cutting forces measured for different cutting speeds as a function of feed used during dry turning of 6061-T6. An almost liner increase in thrust force was found to occur with an increase in cutting speed.

Thus, average cutting forces measured for dry turning of 6061-T6 were found to increase with an increase in feed and decrease with an increase in cutting speed.

5.3.5 Thrust Force Measurement for 6061-T6

Fig.5.13 (a-e) shows thrust forces measured for 6061-T6 under different conditions of cutting speed and feed per revolution. An examination of the curves revealed that there was no significant change in measured force values in the cutting zone for fixed cutting conditions. Thrust forces were measured for feed per revolution conditions of 0.10mm, 0.25mm and 0.35mm and average thrust force for each cutting condition studied was estimated from the force data collected for six rotations of workpiece in the cutting zone, immediately before brakes were applied, in a manner similar to that described in Section 5.3.2.

Fig.5.14 shows the average thrust forces for different feeds as a function of cutting speed. The standard deviations shown in the plot were estimated from the deviation in data collected for the aforementioned six rotations in the cutting part of force measurements. Thrust forces were found to increase with an increase in feed per revolution and with a decrease in cutting speed. The lowest thrust force measured for this alloy was approximately 87N for a feed of 0.10mm and cutting speed of 115m/min and the highest thrust force measured was approximately 252N, which occurred for the combination of lowest cutting speed (25m/min) and highest feed (0.35mm). It was observed that the thrust forces for 6061-T6 dropped by 56N, 46N, and 40N for feeding rates equal to 0.10mm, 0.25mm and 0.35mm respectively, as the cutting speed increased from 25m/min to 115m/min.

Fig.5.15 shows the average thrust forces measured for different cutting speeds as a function of feed used during dry turning of 6061-T6. This curve emphasizes the trends outlined in Fig.5.14, that the thrust forces increase with a rise in feed rate. Also, the thrust forces rise with a decrease in cutting speed.

As is evident from Fig.5.14 and Fig.5.15, average cutting forces measured for dry turning of 6061-T6 were found to increase with an increase in feed and decrease with an increase in cutting speed.

5.3.6 Comparison of Force Responses of 319 Al and 6061 Al

The force responses recorded and discussed for the two aluminum alloys, 319 Al and 6061-T6, in the above sections, were compared to assess the relative ease of their machinability, in terms of forces generated during dry turning of the alloys. The following section describes the note-worthy trends observed during the study:

5.3.6.1 Magnitudes of Cutting Forces and Thrust Forces

Fig.5.16 shows the average cutting force and Fig.5.17 thrust force measured for dry orthogonal turning of 319 Al and 6061 under identical conditions of cutting speed and feed per revolution conditions. As is evident from Fig.5.16, for lowest feed conditions used of 0.10mm, the cutting forces generated during machining of 319 Al (184N, 192N, 199N, 195N, and 188N for cutting speeds of 25m/min, 35m/min, 50m/min, 75m/min and 115m/min respectively) were lower than those for 6061-T6 (275N, 263N, N241, 226N, and 219N for cutting speeds of 25m/min, 35m/min, 50m/min, 75m/min and 115m/min

respectively) . For feed per revolution of 0.25mm the same trend was observed. For feed per revolution of 0.35mm, it was seen that at lower cutting speeds of 25m/min and 35m/min, the cutting forces were higher for 319 Al (being 988N and 902N respectively as compared to 759N and 739N respectively for 6061-T6). However, with an increase in cutting speed to and above 50m/min (for feed per revolution of 0.35mm), 6061-T6 led to higher cutting force magnitudes again (Fig.5.16)).

Fig.5.17 shows a comparison between the average thrust forces generated during the machining of the two alloys. It is evident from the plot that thrust forces generated for 319 Al are generally higher than those generated during machining of 6061-T6. It was also observed that the difference between the measured magnitudes of thrust forces between the two alloys increased with an increase in feed rate used. For feed per revolution of 0.10mm, the thrust forces measured for 319 Al at cutting speeds of 25m/min, 35m/min, 50m/min, 75m/min and 115m/min were 90N, 101N, 119N, 114N, 115N respectively and for 6061-T6, they were 144N,123N,96N,95N,87N respectively. With increase in feed per revolution to 0.35mm, the difference between this force's magnitude rose with average thrust force measured for 319 Al for cutting speeds of 25/min, 35m/min, 50m/min, 75m/min and 115m/min going up to 525N, 510N, 494N, 453N, and 406N respectively while the corresponding values for 6061-T6 were measured to be 252N, 238N, 235N and 212N respectively.

5.3.6.2 Fluctuations in Cutting and Thrust Force Measurements

Another noteworthy feature present on both the cutting force and thrust force curves (for both 319 Al and 6061-T6) were the oscillations or fluctuations present in the force curves recorded during cutting (refer to Fig.5.3). It was observed that the amplitude of these fluctuations increased with an increase in feed (Fig.5.18 and Fig.5.20).

The frequency of these fluctuations were counted for 319 Al (Fig.5.19 (a and b)) and 6061-T6 (Fig.5.21 (a and b)) and it was observed that even though the amplitudes of these fluctuations increased with feed, the frequency did not show any significant variation. On comparing these fluctuations for 319 Al (Fig.5.18) and 6061 Al (Fig.5.20), it was found that the amplitudes of the fluctuations were much higher for 319 Al as compared to the fluctuations for 6061 Al. Morphologies of the respective chips, namely serrated in 319 Al and continuous in 6061-T6, could be a possible reasons for this difference in force responses of the two alloys [6,8]. As 319 Al generates smaller chips with higher frequency of chips breaking off as compared to 6061-T6, which generates long and ribbon-like chips, which do not break off easily, this indeed might be one of the reasons for the higher frequency of fluctuations in the force measured for 319 Al.

5.4 Estimation of Coefficient of Friction

The newly formed chip undergoes sliding against the rake face of the tool as it moves away from the body of the workpiece after being sheared away from it. This

friction force may be the reason for change in the surface profile of the chip as compared to that of the machined surface. Fig.5.22 (b-d) shows the SEM images of the surface of the chip which undergoes sliding against the rake face and Fig.5.23 (b-d) shows the images of the machined surface; the machined surface does not undergo any considerable amount of friction with the tool after being formed. The images showed a marked difference in the surface profiles, the chip face being much smoother than the machined surface, which showed regular groove like marks in the aluminum surface. The coefficient of friction was estimated using Eqn.2.43 and has been presented as a function of cutting speed in Fig.5.24.

$$\mu_e = \frac{F_p}{N_p} \tag{2.40}$$

Thus

$$\mu_e = \frac{F_p}{N_p} = \frac{F_c \sin\alpha + F_t \cos\alpha}{F_c \cos\alpha - F_t \sin\alpha} \tag{2.43}$$

Since $\alpha = 0$ for the PCD tool used in the study, Eqn.2.43 was reduced to:

$$\mu_e = \frac{F_t}{F_c}$$

which was used for estimating the coefficient of friction for the conditions studied. With an increase in cutting speed, the magnitude of coefficient of friction did not show any significant change for feeds of 0.35mm and 0.45mm per revolution. For feed 0.25mm, a

reduction in magnitude of coefficient of friction from approximately 0.75 to 0.60 is seen. Overall, the highest coefficient of friction was found for cutting conditions with a feed of 0.45 (all speeds) (refer to Fig.5.24). It must be noted here the average cutting force and average thrust force used in estimation of coefficient of friction were measured during the turning tests (Section 5.3.2-5.3.5) and were associated with a standard deviation in data (Refer to Fig.5.5 and Fig.5.8).

5.5 Analysis of Surface Finish of Machined Surface

Surface finish obtained at the end of a given machining operation is one of the most important factors in determining the machinability of an alloy and usability of a component for a given application and hence in selection of the machining parameters. Surface roughness of the samples subjected to different cutting conditions were studied in order to investigate the effect of cutting conditions like cutting speed and feed per revolution on surface roughness of the material. Fig.5.25 shows a relatively low magnification SEM image of the machined surface for a sample machined under cutting conditions of cutting speed 50 m/min and feed per revolution of 0.35mm and a corresponding EDS profile for the area marked by a square in the EDS profile. The surface showed ploughing like marks on the aluminum matrix and fractured second phase particles (Fig.5.26). Fig.5.27 shows SEM images of the fractured second phase particles

on the surface in details. EDS profiles of the damaged second phase particles are shown in Fig.5.28 (a-d).

Surface roughness of the samples machined under the conditions studied was examined using white light optical surface profilometer and analyzed for estimating the comparative performance of the cutting parameters (Fig.5.29 (a-c)). It was found that the roughness (Ra) of the regions showing ploughing-like marks (refer to Fig.5.26) were much smaller (Fig.5.29b) than the roughness of regions showing fractured particles (Fig.5.29c). Plots shown in Fig.5.30 (a-d) show the variation of surface roughness values for the aluminum matrix on the machined surface plotted against cutting speed for different feeds. The error lines on the plots show the difference in the surface roughness values (Ra) between the zones showing fractured second phase particles and the aluminum matrix. It is remarkable that the difference in the roughness values between the two zones increase drastically with an increase in feed rate.

Fig.5.31 compares the values of average surface roughness (Ra) values for different feeds plotted against variation in cutting speeds. The surface roughness values show a rising trend with an increase in cutting speed and with an increase in feed. The lowest roughness values of approximately 0.6 microns were obtained for machining at lowest feed rate (0.10mm/rev) and the highest roughness values of approximately 0.9

microns were obtained for the combination of highest cutting speed and feed rate (115m/min and 0.45mm).

5.6 Subsurface Damage below Machined Surface

5.6.1 Depth of Fractured Particle Zone

Examination of sub-surface microstructure under the machined surface reveals extensive damage to the second phase particles (Fig.5.32a). Si particles, $Al_{15}(Mn,Fe)_3Si_2$ which occur as Chinese script morphology, needle shaped Al_5FeSi and Cu_2Al, all show fracture to varying extend in the region in the immediate vicinity of the machined surface. Extensive microstructural examination using optical microscopy and SEM revealed that the damage depth below surface depends on the machining parameters of cutting speed and feed rate. Fig.5.29b shows the depth of damage zone, which can be defined as the zone where most of the second phase particle damage is confined to for sample machined under cutting speed of 50m/min and feed per revolution 0.45mm.

Optical microscopy studies were used to estimate the depth of damage zone for different cutting conditions. At least 25 different locations below the machined surface, in the region behind the chip (on the side opposite to tool location) were examined carefully to find the depth of this zone. Also, only extensive particle fracture, as shown in Fig.5.29a was taken into consideration, and minor cracking or hairline fractures were not into account. 319 Al also contains voids that form during casting of the alloy. The regions in

the vicinity of such voids were excluded while doing this analysis. Fig.5.33 shows the variation of depths of the damage zones for different cutting conditions. The plot reveals that for lower feed rates of 0.10mm and 0.25mm, the depth of the zone shows only a slight increase with an increase in cutting speed. For feed of 0.35mm, this depth is comparable with those for lower feeds of 0.10mm and 0.25mm at lower feeds. However, with an increase in speed to and above 50m/min, the depth shows a sudden increase. The same trend is observed for the highest feed of 0.45mm which shows very high depths of deformation zone at higher speeds (approximately 150 microns below machined surface).

5.6.2 Estimation of Strain below Machined Surface using 6061 Al Marker

Strains below the machined surface were estimated using 6061 Al markers inserted inside the tubular 319 Al samples, following the procedure described in Section 4.9.2. The cutting conditions used for this test were cutting speed 50m/min, feed per revolution 0.35mm. Fig.5.34 is micrograph showing the interface between the workpiece material 319 Al and the marker insert (6061 Al) in the machined section on a polished and etched sample. It was found that the marker underwent bending in the direction of cutting. Plastic strains were estimated along different depths from the machined surface using the displacement of the 6061 Al marker with respect to its original straight line

orientation, as has been described in Section 4.9.2. Fig.5.35 shows the resulting plastic strain as a function of depth below the machined surface.

The depth of fracture zone (Section 5.6.1) for the sample was found to be 68.4μm (Fig.5.33). The plastic stain found using marker insert method (Section 5.6.2) at this depth was 0.06. Thus, it can be inferred that equivalent plastic strain equal to 0.06 is required for initiation of fracture of silicon particles in the material lying under the machined surface for a sample machined under cutting speed of 50m/min and feed per revolution of 0.35mm.

5.7 Cumulative Stress Strain Relationship in 319 Al

For the purpose of finding the cumulative relationship of stresses and strains in 319 Al subjected to dry turning, estimation of plastic strains and flow stresses present below the machined surface was done using the modified 319 Al sample with marker inserts made up of 6061-T6 (discussed in Section 4.9.2). Plastic strain estimation in the material (319 Al) below the machined surface (Fig.5.35) was used for this purpose. Vickers hardness measurements (load used 10 grams) were done (in 319 Al) at different depths along the interface between the work-material (319 Al) and the maker (6061-T6) and Fig.5.36 shows the variation of hardness measured with depth below machined surface. Flow stresses were estimated from the measured hardness values using Eqn.2.31.

Subsequently, values of plastic strains at different locations and corresponding flow stresses estimated using Vickers hardness test as tabulated in Table 4.1 (load used 10grams) were plotted together to establish the cumulative stress-strain relationship for the material orthogonally machined (machining conditions used for this sample were cutting speed of 50m/min and feed per revolution of 0.35mm). The resulting plot has been shown in Fig.5.37. A regression analysis was conducted which showed that the relationship between the above stresses and strains was closely defined by Voce's Equation (Eqn.2.36) [61] (Fig.5.37), as is shown below:

$$\bar{\sigma} = \bar{\sigma}_s - (\bar{\sigma}_s - \bar{\sigma}_o)\exp\left(-\frac{\bar{\varepsilon}}{\bar{\varepsilon}_c}\right) \tag{2.36}$$

where $\bar{\sigma}$ is the equivalent stress, $\bar{\sigma}_s$ is the saturation stress for the material (equal to 287 MPa), $\bar{\sigma}_0$ is the flow stress of the material (equal to 186 MPa) and $\bar{\varepsilon}_c$ is a constant equal to 0.12. These values compare well with the tensile yield strength (YS) (150 MPa) and ultimate tensile strength (UTS) (210MPa) 319 Al.

5.8 Geometry and Hardness of Chips Produced

Chips produced during orthogonal cutting under the conditions studied were examined to observe the change in geometry of the chips with change in cutting parameters. Fig.5.38 (a and b) shows SEM images of chips produced during machining at a constant cutting speed of 75mm/sec with feeds of 0.25mm and 0.45mm respectively.

The size and definition of the saw-tooth segments in the chips was found to be drastically larger for sample cut under higher feed conditions.

Table 4.1 Equivalent Strain and corresponding flow stress below machined surface

Depth below machined Surface (microns)	Equivalent Strain	Flow Stress (MPa)	Depth below machined Surface (microns)	Equivalent Strain	Flow Stress (MPa)
5.20	1.74	287.36	46.8	0.08	262.27
7.80	1.23	285.80	49.4	0.11	257.91
10.40	0.84	284.19	52	0.08	252.49
13.00	0.51	280.70	54.6	0.09	243.00
15.60	0.47	282.51	57.2	0.08	237.45
18.20	0.45	280.76	59.8	0.08	231.84
20.80	0.40	278.96	62.4	0.06	222.43
23.40	0.37	276.50	65	0.06	226.17
26.00	0.34	279.50	67.6	0.05	216.64
28.60	0.32	277.09	70.2	0.05	210.78
31.20	0.29	275.16	72.8	0.04	208.86
33.80	0.22	273.17	75.4	0.03	200.88
36.40	0.19	271.11	78	0.02	194.83
39.00	0.14	268.99	80.6	0.01	190.73
41.60	0.11	266.81	83.2	0.00	186.56
44.20	0.13	264.58	-	-	-

Fig.5.39 (a and b) shows the change in geometry of chips with rise in cutting speed for a constant feed rate of 0.45mm and for rise in feed per revolution for a constant speed of 25m/min respectively. Careful examination of the chips revealed that the chips became thicker with clearer saw-tooth morphology as the feed rate is increased. The influence of cutting speed at a constant feed, however, is not very clear from optical

observations of the chips. Chip thickness values were therefore measured from optical micrographs of sections of orthogonally cut samples in order to better understand the influence of cutting parameters on the chip geometry. The results presented in Fig.5.40 showed that the chip thickness values increased with a rise in feed per revolution. However, only a small rise in chip thickness values was seen for a rise in cutting speed. Chip thickness values showed an increase from 0.22mm to 0.76mm with a rise in feed per revolution from 0.10mm to 0.45mm for a constant speed of 25m/min.

As can be seen from the SEM micrographs shown in Fig.5.38 and microstructures shown in Appendix I, the sizes of serrations increased with an increase in feed. Optical micrographs of 319 Al chips were used to measure the length and width of the largest serration (as observed on the polished section). The results were used to plot histograms showing the variation of length of serrations (Fig.5.41a) and that of width of serrations (Fig.5.41b) with a change in cutting speed (for different feed rates). The observation stated earlier, that a rise in feed rate leads to an increase in thickness and definition of serrations is evident in Fig.5.41.

Vickers hardness tester was used to measure the hardness of the chips in order to get an idea about their relative hardness. The load used for the indentations was 10 grams. Care was taken to place the indentations in the aluminum matrix portion of the microstructure. At least ten indentations were done for each sample in order to find the

averaged hardness of the chip region. Fig.5.28a shows the resultant variation in magnitudes of hardness values (in units of HV) plotted against cutting speed for the tests. The general trend outlined in the plot is seen to be that of a decrease in hardness values with an increase in cutting speed from 25m/min to 50m/min, after which the values do not show any major fall in magnitude. Also, for each cutting speed studied, hardness values were found to be higher for higher feed rates used. This can be attributed to the higher residual stresses introduced in the sample while cutting with higher feed rates, as has been reported by Trent et al [77].

Fig.5.28b shows the chip hardness measured plotted against the corresponding chip thickness values. It was found that with an increase in chip thickness, chip hardness also increased. It is evident from the plot that for a constant speed, if feed was increased, both thickness and hardness of chips increased. Also, at a constant feed rate, if speed was increased, chip hardness decreased, while chip thickness did not show significant change.

5.9 Strain Estimation in PDZ and Chip

A close and careful examination of the cross-sectional area of the machined section revealed that the fractured particles in the primary deformation zone and the chip region trace out well defined patterns which are very similar to flow lines present in the machined cross-section of softer materials like copper and Aluminum 1100 [4,5,20].

Fig.5.44(a-d) shows these orientations in samples cut under different machining conditions. These patterns traced out by the fractured particles were used to estimate the displacements in the PDZ and in the chip region for the machined samples.

5.9.1 Methodology for Estimating Strains in Machined Workpiece

Aluminum 319 sample subjected to orthogonal cutting under a cutting speed of 50m/min and feed of 0.35mm per revolution was selected for estimating the strains induced in the workpiece during cutting. Fig.5.45a shows a detailed optical microstructure of the sample and distinct flowline-like patterns can be seen in the image. Fig.5.45b shows some of the lines traced out along these patters in order to facilitate the estimation of strains in the workpiece.

Fig.5.46 (a and b) outlines the basic steps followed for estimating the plastic strains in the sample. The first step in the process constituted of drawing of flowlines on the cross-sectional optical-micrograph of the sample following orientation of fractured particle flow. This was followed by placing a 50μm by 50μm grid over the micrograph and estimating the strains using Eqn.2.28 at each of the intersection points of the grid. The strains were then plotted on an outline of the micrograph and points having same magnitude of strains were connected together to yield iso-strain lines. Fig.5.47a shows the strains estimated on the intersection points of a 200μm by 100μm grid and Fig.5.47b

shows the estimated value of plastic strains and the lines drawn for the purpose (following fractured particle flow).

It can be seen from the iso-stress contours that the strains increase as the distance from the rake face increases. The lowest strains encountered in the chip are equal to 0.01 found near the rake face and the highest are equal to 0.65 near the free surface of the chip. The lower strains found in the vicinity of rake face also points to an absence of secondary deformation zone, as was also reported was Song [20] for dry orthogonal machining of A380. This, however, contradicts the results showing presence of higher strains in the secondary deformation zone (formed in region adjacent to rake face) in 1100 Al and commercial grade copper subjected to dry turning, as reported by Elmadagli et al [4,5]. Also, the highest strains in the micrograph are close to 1.8 and are seen to occur in the shear zones (Fig.5.47b). The strain results are in conformance with the fact that the material flow is restricted in the region in close proximity to the rake face due to presence of the solid and unyielding rake face (refer to Section 6.1). However, with an increasing distance from the rake, the material flow takes place more freely, thus leading to higher degree of plastic flow traced out by fractured particles and as a result higher magnitudes of strains. Also, presence of highest strains in the shear zone is supported by evidence of very high amount of shear present in the shear zones which are the precursors to crack formation in chips producing saw-tooth morphology in chips [6,8,20,32,35].

5.10 Hardness and Flow Stress Distribution in Machined Workpiece

Vickers hardness measurements were used to find the variation in hardness in the PDZ and chip region for an orthogonally cut sample machined under cutting speed of 50m/min and feed rate of 0.35mm per revolution. Using a load of 10gms, indentations were taken at or around the points of intersection of an imaginary grid of 100μm by 75μm, carefully avoiding any second phase particles. Additional measurements were taken around the grid points to substantiate the hardness data further. Estimation of hardness around the area of shear zone was done by placing the indentations very close to the shear cracks that separate two segments of the chips. Fig.5.45 (a and b) shows the polished section of the chip that was used for this analysis, and as can be noted from it, the region in the shear zone had a considerable amount of fractured second phase particle free area on which indentations were placed for hardness estimation of this zone.

Fig.5.49 shows the resulting hardness distribution in the outline of the cross-section of the optical profile of the sample. The overall hardness of the PDZ zone (above the shear plane) is higher than the bulk material and increase in hardness is seen to commence along the region in the vicinity of the line connecting the tool-tip to chip-root or the imaginary shear plane. An interesting observations was that the hardness values measured very close to the shear cracks (in the shear zone) were very close to each other

in magnitude (hence they are shown as ‘average hardness’ in Fig.5.49. Also, the hardness values were found to be highest in the vicinity of the shear zones, being equal to 106.4HV and 112.7HV for the lower and upper shear zones shown in the Fig.5.49. The hardness values were also found to be high near the rake face side of the chip measuring up to approximately 103 HV. The magnitudes of matrix hardness was found to decrease down to values close to 85HVas one approached the middle part of the chip-segment, away from the shear zones and the rake-facing side of the chip. Lower stresses, close to 78HV, were encountered near the free surfaces of the chip.

Eqn.2.31 was used to estimate the local flow stress values from the Vickers hardness measurements. The resulting profile showing the distribution of stresses (in units of MPa) has been shown in Fig.5.50. The points on the micro-graph outline having the same value for stresses have also been connected together to obtain iso-stress contours (Fig.5.50). The contours outline an increase in the stress as the shear zone is approached, an area where highest stresses of magnitude 348MPa and 369MPa are encountered.

5.11 Hardness near Tool-Tip Location and Below Machined Surface

Vickers hardness measurements were done for the samples in the vicinity of the tool tip area and under the machined surface in a polished sample (refer to Fig.2.3 for

location of tool-tip and machined surface). The results of hardness measurements at the location of the tool tip are shown in Fig.5.51. Flow stresses were calculated from the hardness measurements using Eqn.2.31 and plotted against cutting speed for all conditions (Fig.5.52). A total of 5 indentations were taken in the vicinity of the tool tip region to arrive at the average hardness of the tool-tip region in the samples.

For estimating average hardness of the machined surface, a total of 10 indentations per sample were taken within the depth of 60 microns below surface (Fig.5.53). Flow stresses were found from the hardness measurements in the same way as described above (Fig.5.52). Similar trends are outlined by the plots for both the tool-tip region and the machined surface, which show a decrease in hardness with an increase in cutting speed. This trend can be attributed to the fact that higher machining speeds lead to generation of higher temperatures in the primary deformation zone and in the immediate vicinity of the machined surface [6,8]. These higher temperatures lead to a relative softening of matrix, which is reflected in the lower hardness values for higher cutting speeds. Fig.5.51 and Fig.5.53 also show an increase in hardness values with an increase in feed rate, a phenomena which can be explained on the basis of increasing levels of stresses in the workpiece area close to the tool tip with an increase in feed per revolution [6,8].

5.12 Fracture of Silicon Particles

This section describes the effect of the high deformation during machining on the silicon particles in the alloy 319 Al. Silicon particles are the main load bearing particles in the alloy, embedded in a soft ductile aluminum matrix. As such, cracking and fracturing of these are detrimental for the usability of the alloy. Sample used for this study had been machined under cutting conditions of cutting speed 50m/min and feed per revolution of 0.35mm.Particle fracture has been studied in two zones in the machined section, first of which is the zone between two consecutive shear bands, the second being the area in the vicinity of shear bands, or shear zone. Effects of silicon particle size and plastic strains present in the matrix in the zones have also been studied and are presented in the following sections.

5.12.1 Effect of Particle Size on Fracture

High magnification optical microscopy and SEM images were used to study the fracture of silicon particles in the sample. Fig.5.55 (a-c) shows SEM images of silicon particle fracture taken at different locations on the sample. As can be deduced from the micrographs, larger particles undergo fracture more than the smaller particles. Fig.5.50 shows the variation of percentage of particles fractured with particle size in the primary deformation zone (PDZ), an area which also corresponded with the zone lying between

shear zones in case of the sample studied. It can be inferred from the histogram that fraction of fractured particles rises with a rise in particle size; with most silicon particles having size above 5 microns showing cracks and fractures (Fig.5.55 (a and b)). The fact that larger particles undergo cracking and fracture to a higher degree is in agreement with trends reported in literature [40][41].

Examination shear zone region showed a higher degree of silicon particle fracture than the area between two shear zones, a trend that can be attributed to the shearing that takes place in the zone which is a precursor to fracturing and formation of sawtooth morphology in the chip. Fig.5.56 shows a comparison of fracture behaviour of silicon particle of different sizes in PDZ and in Shear zone. As can be seen from the figure, fracturing of particles with sizes smaller than 5 microns is more pronounced in the shear zone.

A close examination of the fractured particles (Fig.5.55(a and b)) also revealed that longer particles undergo fracture more often than rounded ones, which agrees with literature on particle fracture which have reported higher aspect ratio leading to brittle fracture during tensile testing of Al-Si alloys [41][42].

Thus, dry orthogonal machining of 319 Al alloy showed that it possesses good machinability when compared to wet or lubricated machining of other Al alloys (Section

2.7) in terms of cutting force (highest of 1000N and lowest of 200N), thrust force (highest of 600N and lowest of 100N), chip geometry (small to medium length chips, good chip breakability except for highest feed rate of 0.45mm), good surface roughness values (0.6μm to 1 μm). The study also shed light on the plastic strain and flow stress distribution in machined material, showing an absence of secondary deformation zone and higher strain and stress concentration in shear zones. Depth of damage zone for silicon particles, below machined surface, was found to vary with an increase in feed rate and the highest depth of this zone was found to be approximately 150 μm for feed rate 0.45mm and cutting speed of 115m/min. Fracture of silicon particles was found to increase with an increase in particle size and was observed to be higher in shear zone than in primary deformation zone. Comparison of specific work calculated using force measurements (1160MJm$^{-3)}$ with that estimated from the sum (1019MJm^{-3}) of specific energies spent in overcoming friction between chip and rake (515MJm^{-3}) and in plastically deforming the material (504MJm^{-3}) showed very good match between them.

5.13 Assessment of Power Expended during Machining

The force measurements were used to estimate the power requirements for carrying out orthogonal cutting under the different conditions studied. The power expended in a given cutting operation can be defined as the product of force and velocity. Hence, the cutting power and feed power can be defined as:

$$P_{cutting} = F_c . v_c \tag{5.1}$$

$$P_{feed} = F_f . v_c \tag{5.2}$$

where $P_{cutting}$ is the power expended by cutting force and P_{feed} is power expended by thrust force.

Fig.5.58 and Fig.5.59 shows the variation of cutting power with the cutting speed and feed power with cutting speed respectively. Both cutting and feed power increase with an increase in the cutting velocity and with an increase in feed. Also, it can be seen that the relationship between cutting power and cutting speed and that of feed power with cutting speed are almost linear for a given feed rate. Highest cutting power is found to be approximately 80 kJ/min for a combination of highest cutting speed and feed rate (115m/min and 0.45mm).

5.14 Volume of Material Removed during Turning

One of the primary objectives of turning is removal of excess material from the component being machined. This makes measurement of volume removed a crucial parameter in assessment of effectiveness of a given machining operation. Higher the rate of volume removed by a given machining operation, higher is its efficiency. The rate of volume removed in orthogonal turning can be calculated as the follows:

$$Q = V_c . f . d \tag{5.3}$$

where Q is the volume removed per minute during cutting, V_c is the cutting speed, *f* is equal to the feed per revolution and '*d*' is the depth of cut which is equal to the wall thickness (3mm) of the tubular samples used (refer to Section 4.2). Fig.5.57 shows the variation of rate of material removal or volume removed per min for the conditions studied. The highest magnitude of volume removed per second is found to be in the vicinity of 160 centimetre cube per minute, attained while cutting under the highest feed (0.45mm) and highest speed (115m/min) examined. The volume removed rises linearly with an increase in cutting speed for all feeds (Fig.5.57). However, it is only one of the factors in deciding efficiency and other factors like energy consumption, surface characteristics, etc must be taken into account before finalizing the cutting conditions.

5.15 Specific Cutting Energy

Specific energy is the energy expended per unit volume of material. Following is a description of different specific energy estimations done for orthogonal cutting process during this study.

5.15.1 Specific Cutting Energy Using Force Results

Fig.5.61 shows the specific cutting energy or the energy consumption per unit volume of the material removed during cutting, calculated for different cutting conditions, using average cutting and thrust forces for each condition, as shown below:

$$U = V_c(F_c + F_t) \tag{5.4}$$

$$R = d.f.V_c \tag{5.5}$$

$$u_s = \left(\frac{U}{R}\right) = \left(\frac{F_c + F_t}{tf}\right) \tag{5.6}$$

where U is total energy consumed per unit time or power, F_c is cutting force, F_t equals the thrust force, 'd' is the depth of cut, 'f' equals the feed rate , 'R' is the material removal rate and u_s is the specific power required for cutting.

From Fig.5.61, specific work for machining condition of cutting speed equal to 50m/min and feed of 0.35mm (with F_c = 722N and F_t=495N) was found to be equal to $1160\,MJm^{-3}$.

5.15.2. Specific Cutting Energy from Stress-Strain Plot for orthogonally cut 319 Al

Work of deformation can also be estimated using the area under the stress strain curve for the machined section. Eqn.2.35 gives the area under the stress-strain curve and has been used to estimate the work of plastic deformation in the PDZ region.

$$W = \int_{\bar{\varepsilon}_n}^{\bar{\varepsilon}_{n+1}} d\bar{\varepsilon} \tag{2.35}$$

The stress relationship obtained from cumulative stress-strain plot shown in Fig.5.37 was found to follow Voce's equation and this relationship was used for estimation of work of plastic deformation (cutting conditions for this sample were cutting speed of 50m/min and feed per revolution of 0.35mm) from Eqn.2.35 as:

$$W = \int_{\bar{\varepsilon}_n}^{\bar{\varepsilon}_{n+1}} \left(\bar{\sigma}_s - (\bar{\sigma}_s - \bar{\sigma}_o) \exp\left(-\frac{\bar{\varepsilon}}{\bar{\varepsilon}_c} \right) \right) d\bar{\varepsilon} \tag{2.37}$$

Using Eqn.2.37 with $\bar{\sigma}_s$ equal to 287 MPa, $\bar{\sigma}_0$ equal to 186 MPa and $\bar{\varepsilon}_c$ equal to 0.12 (refer to Section 5.7), the amount of plastic work between the iso-strain gradients shown in Fig.5.48 were found and have been shown in Fig.5.60.

The total plastic work in the region between the lowest and the highest strains measured in Section 5.9, that is 0.00 and 1.8 strains generated was found (using Eqn.2.37) to be 504 MJm^{-3}.

5.15.3. Specific Cutting Energy from Frictional Force between Rake and Chip

Fig.5.62 shows specific cutting energy due to force of friction between the tool and the workpiece for machining conditions, which was estimated as:

$$F_{friction} = \mu F_c \tag{5.7}$$

$$U_{friction} = V_c(F_{friction}) = V_c(\mu F_c) \tag{5.8}$$

Also

$$R = d.f.V_c \tag{5.5}$$

Therefore

$$u_{friction} = \left(\frac{U_{friction}}{R}\right) = \left(\frac{\mu F_c}{tf}\right) \tag{5.9}$$

From Fig.5.62, specific cutting energy due to force of friction between the tool and the workpiece ($u_{friction}$) for machining conditions of cutting speed equal to 50m/min and feed of 0.35mm was found to be equal to $515 MJm^{-3}$.

FIGURES – CHAPTER 5

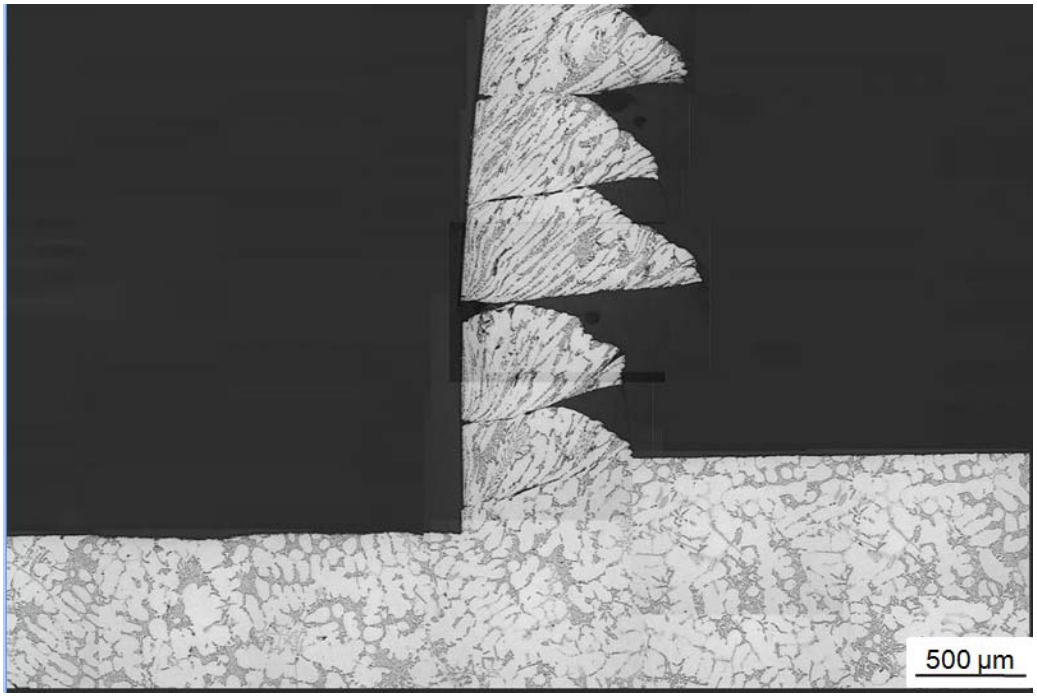

Fig.5.1. Optical micrograph of Al 319, cut at cutting speed of 50m/min and feed of 0.35mm showing discontinuous chips with sawtooth morphology.

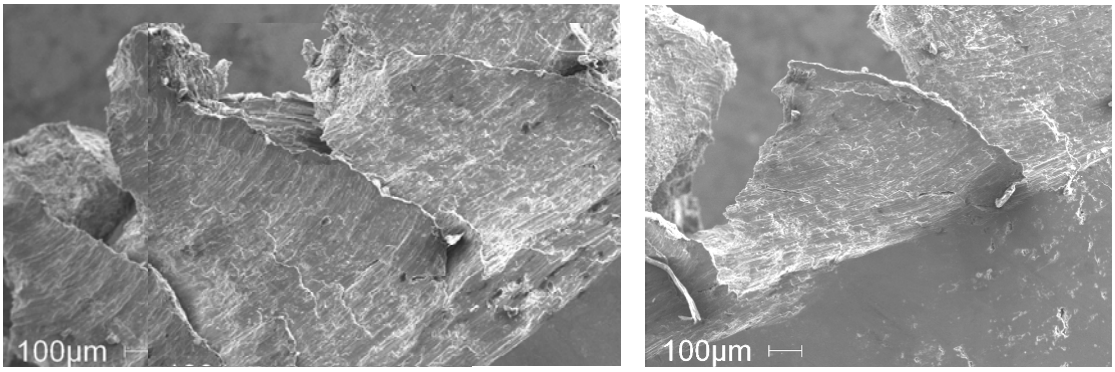

(a) (b)

Fig.5.2. SEM images showing saw-tooth like segments in chips formed during orthogonal machining of Al 319 (a) for sample machined at cutting speed of 75m/min and feed of 0.45mm (b) for sample machined at cutting speed of 50m/min and feed of 0.35mm.

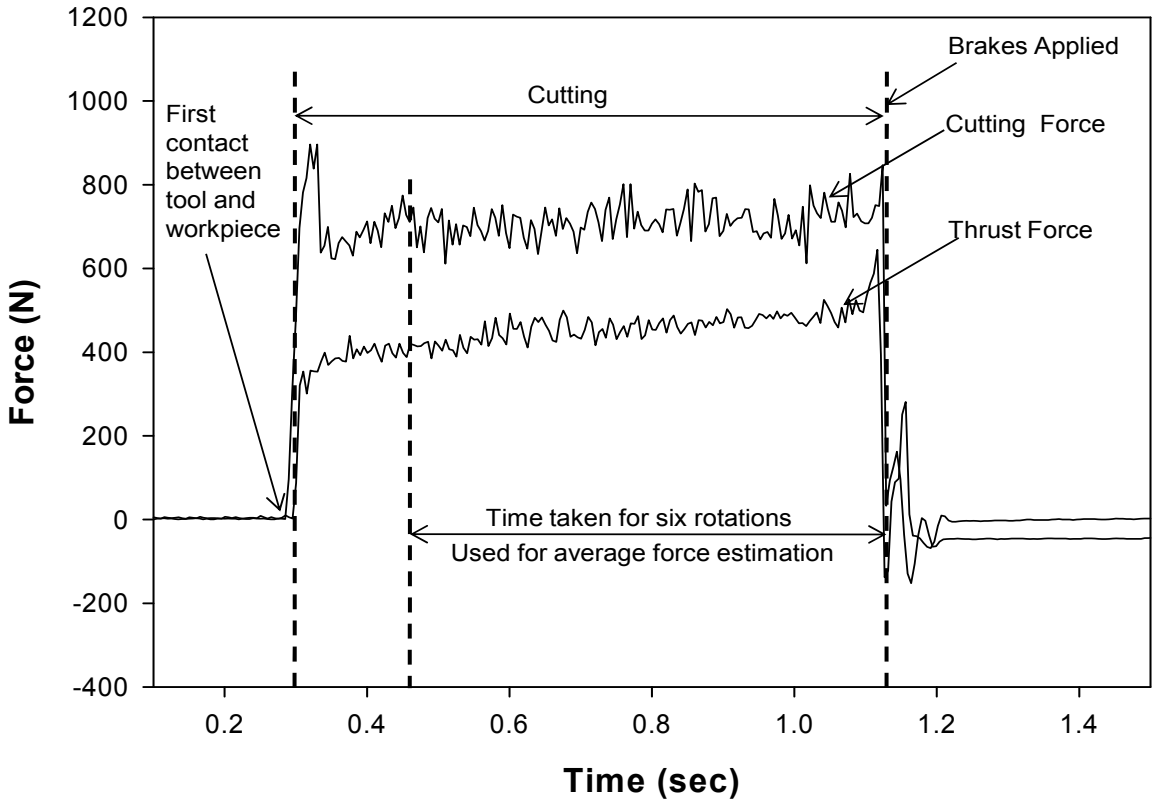

Fig.5.3. Typical force plot showing cutting and thrust forces obtained after analysis of output data from the force-measuring system and different stages in a typical force vs time plot obtained for orthogonal cutting experiments. The sampling rate was 2000Hz.

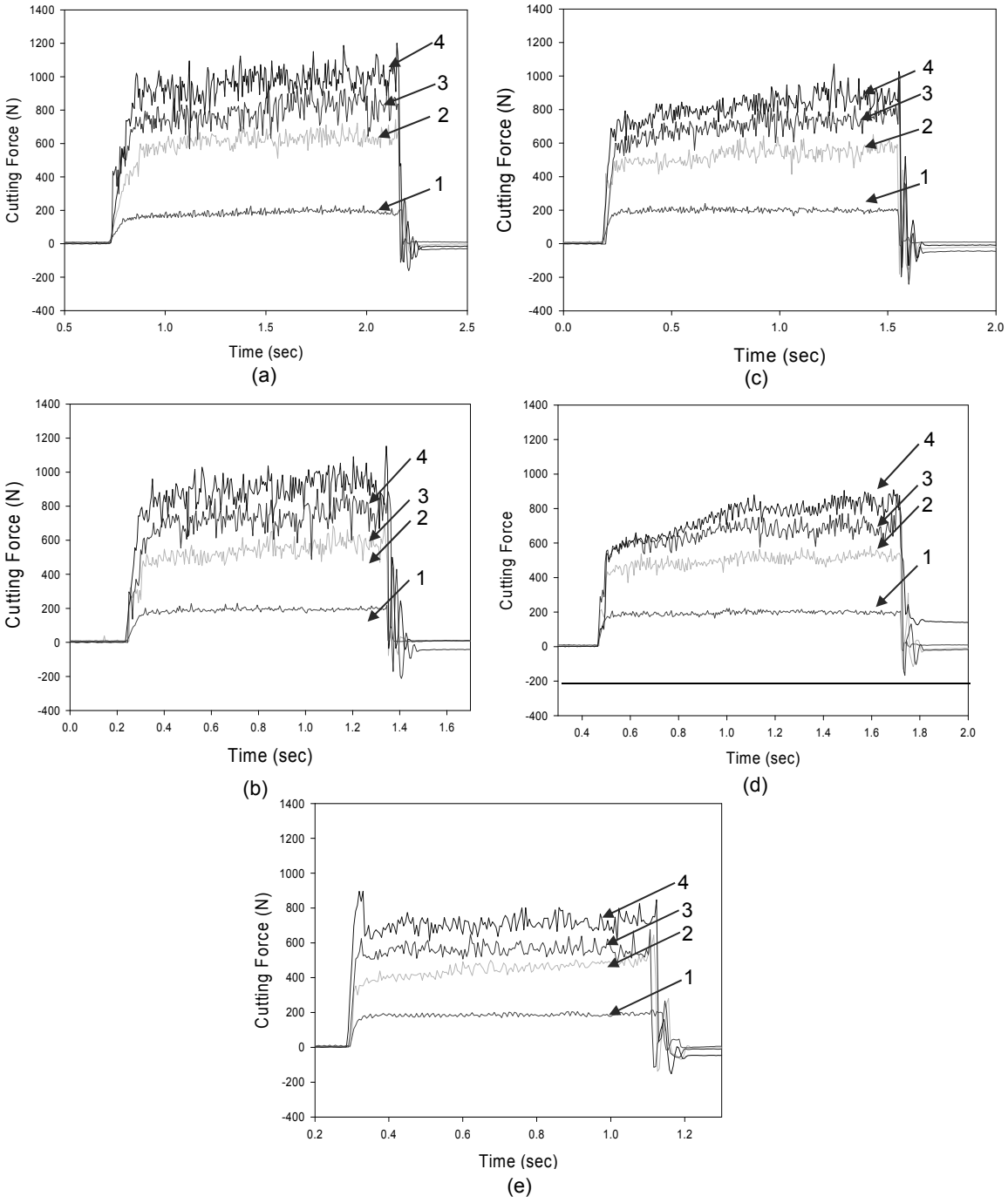

Fig.5.4. Plots showing variation of cutting forces (N) with time (second) for 319 Al when machined under different magnitudes of feed per revolution (denoted by numbers as follows: 1: 0.10mm, 2: 0.25mm, 3: 0.35mm, 4: 0.45mm) for cutting speed equal to (a) 25m/min, (b) 35m/min, (c) 50m/min, (d) 75m/min, and (e)115m/min.

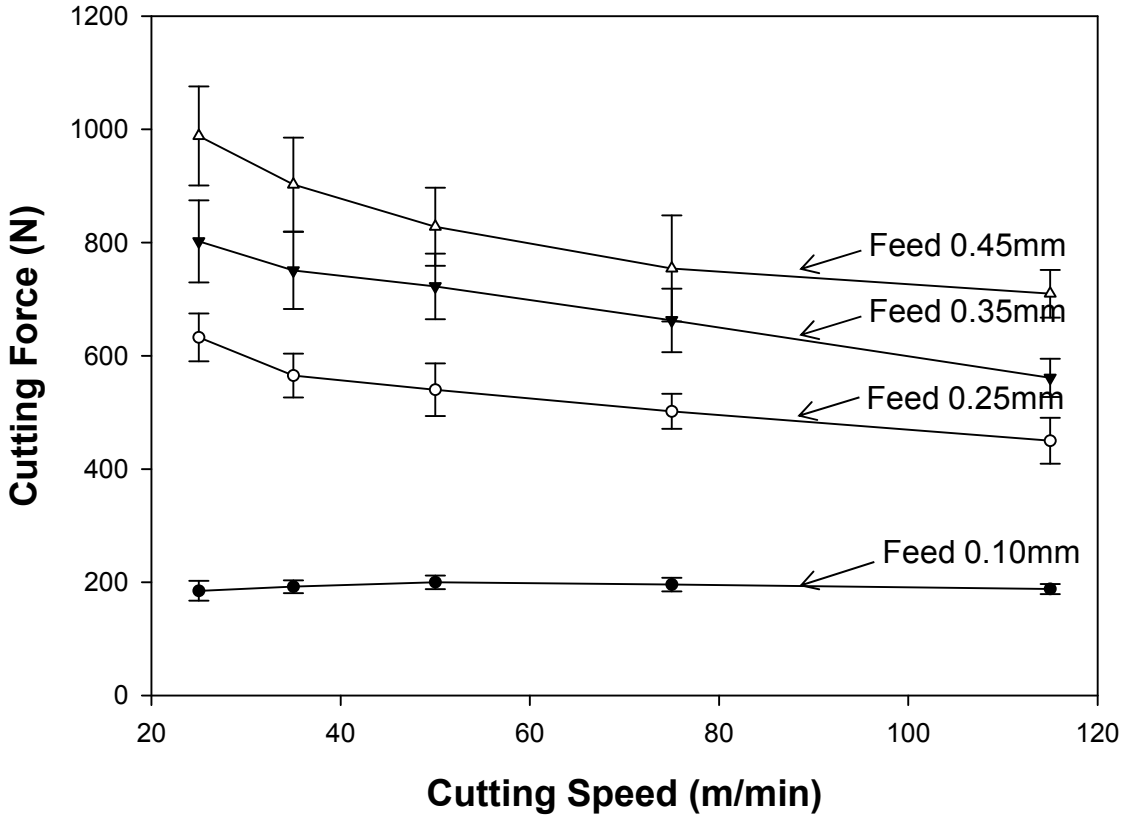

Fig.5.5. Plot showing variation of cutting forces with increase in cutting speed for feed per revolution equal to 0.10mm, 0.25mm, 0.35mm and 0.45mm. Cutting forces were found to decrease with an increase in cutting speed for all feed rates except for 0.10mm in which case it showed a slight increase in values with an increase in cutting speed. Cutting forces were also found to exhibit an increase in magnitude upon an increment in feed per revolution.

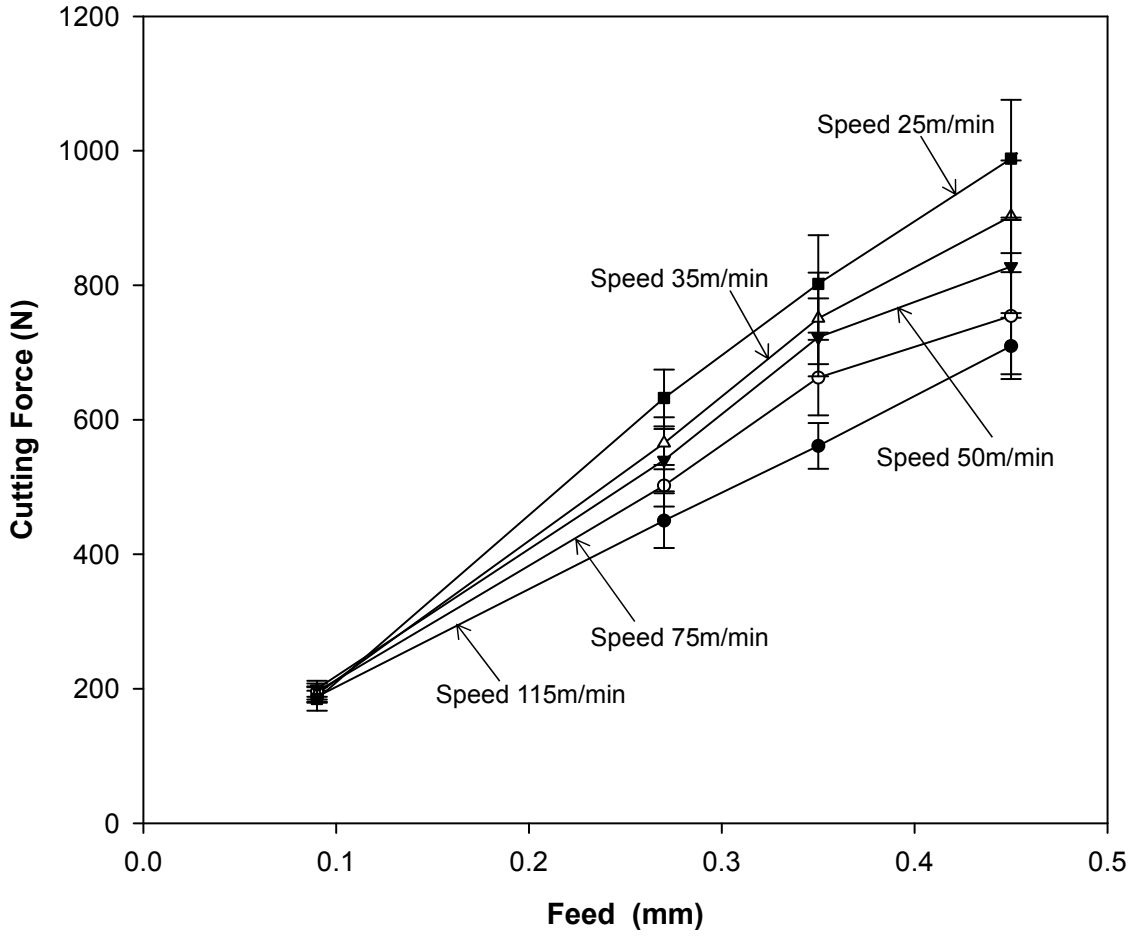

Fig.5.6. Plot showing variation of cutting forces with increase in feed for cutting speeds equal to 25m/min, 35m/min, 50m/min, 75m/min and 115m/min. Cutting force values were found to almost equal for all cutting speeds investigated when cutting with feed equal to 0.10mm. For feed per revolution equal to 0.25mm, 0.35mm and 0.45mm, higher cutting speeds resulted in lower cutting forces.

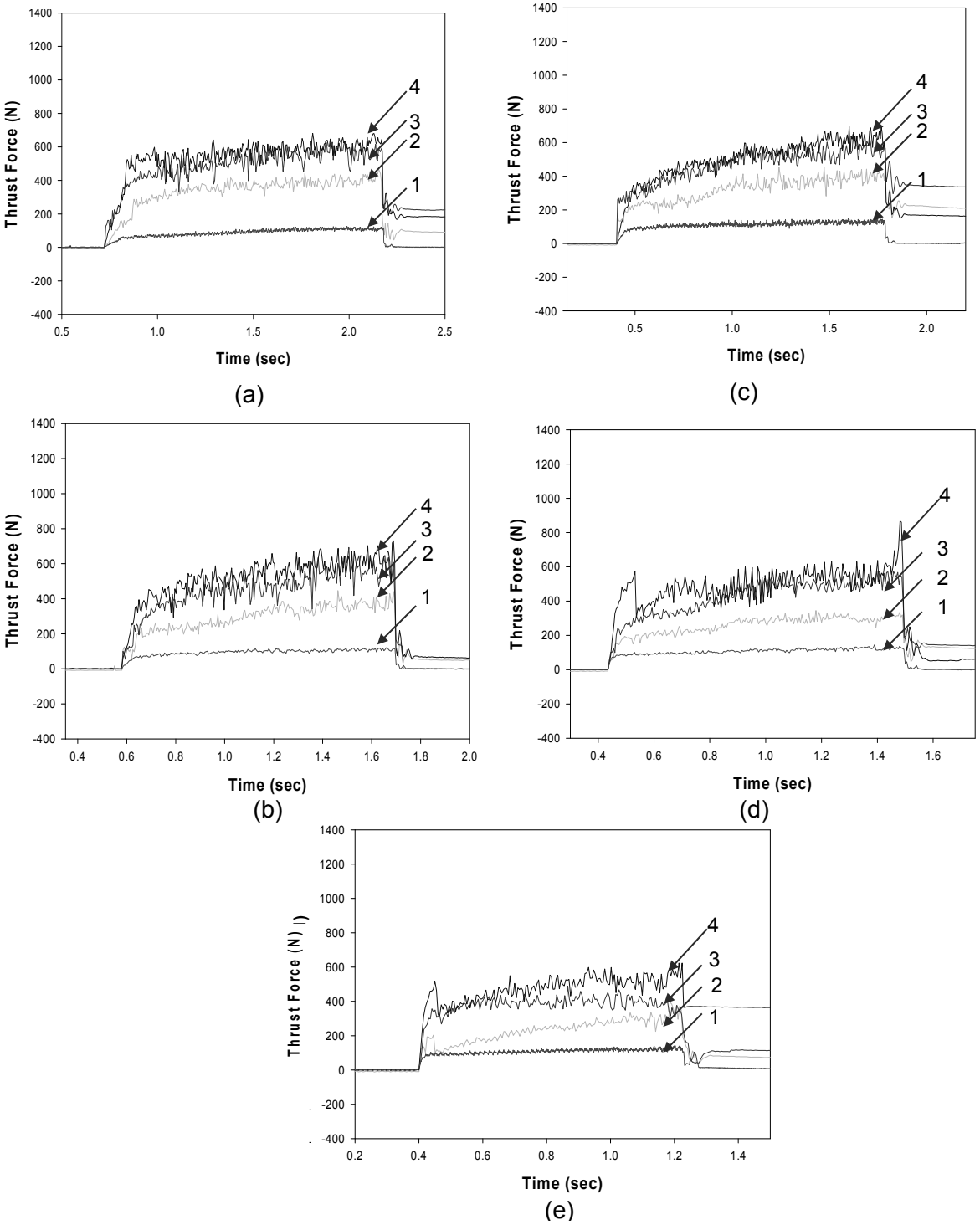

Fig.5.7. Plots showing variation of thrust forces (N) with time (second) for 319 Al when machined under different magnitudes of feed per revolution (denoted by numbers as follows: 1: 0.10mm, 2: 0.25mm, 3: 0.35mm, 4: 0.45mm) for cutting speed of (a) 25m/min, (b) 35m/min, (c) 50m/min, (d) 75m/min, and (e) 115m/min.

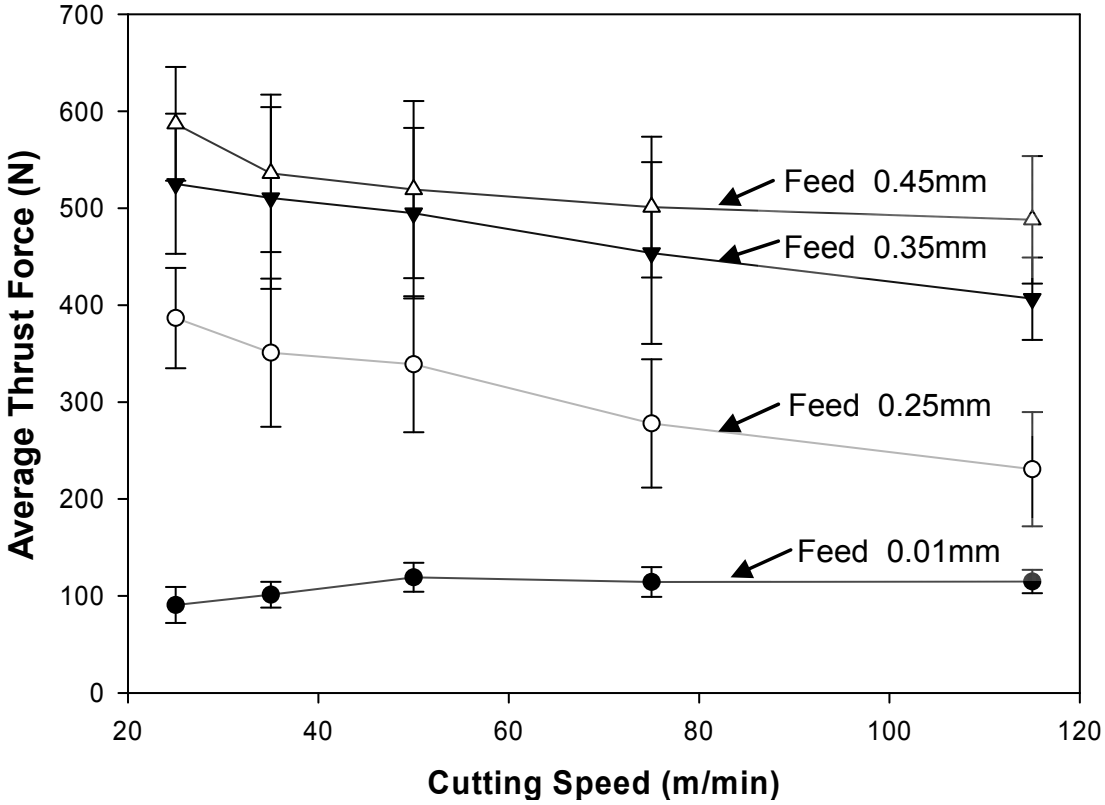

Fig.5.8. Plot showing variation of thrust forces with increase in cutting speed for feed per revolution equal to 0.10mm, 0.25mm, 0.35mm and 0.45mm. Thrust forces were found to decrease with an increase in cutting speed for all feed rates except for 0.10mm.

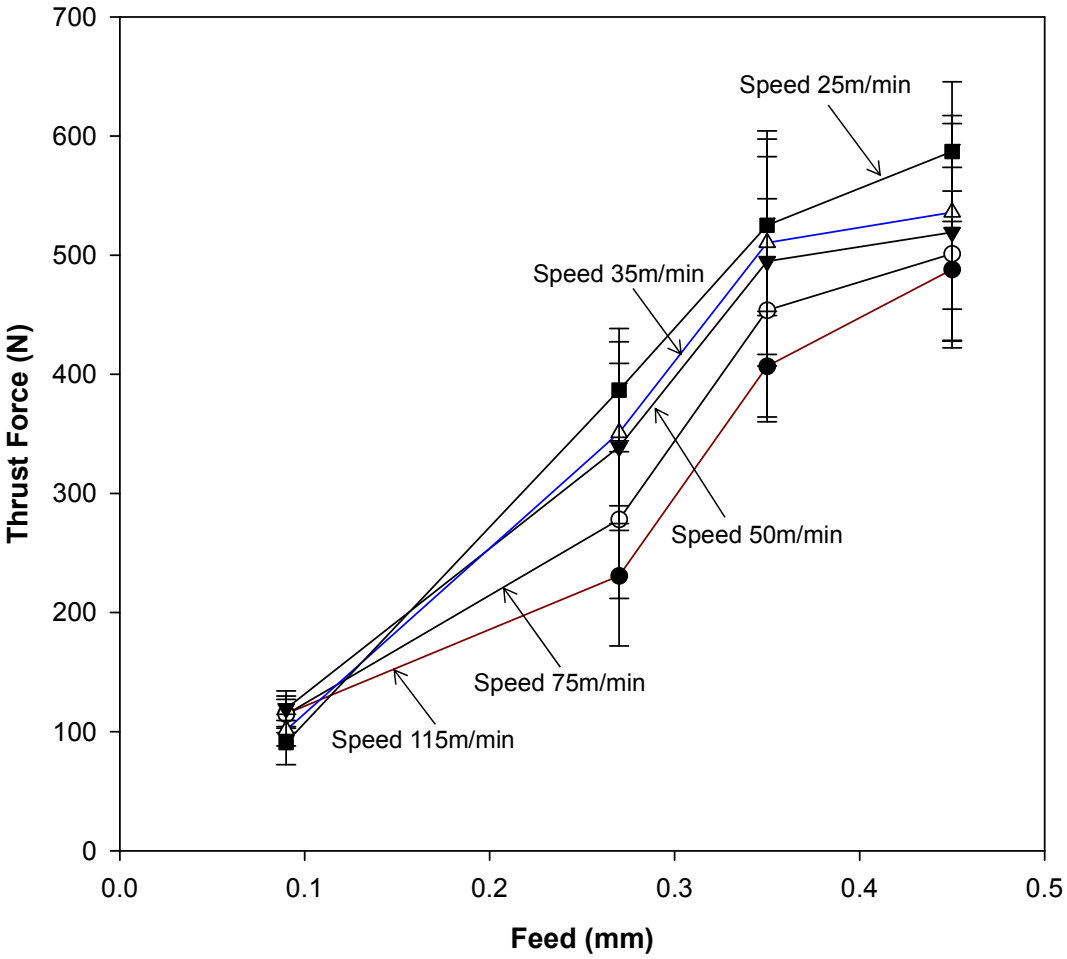

Fig.5.9. Plot showing variation of thrust forces with increase in feed for cutting speeds equal to 25m/min, 35m/min, 50m/min, 75m/min and 115m/min. Thrust forces were found to exhibit an increase in magnitude upon an increment in feed per revolution.

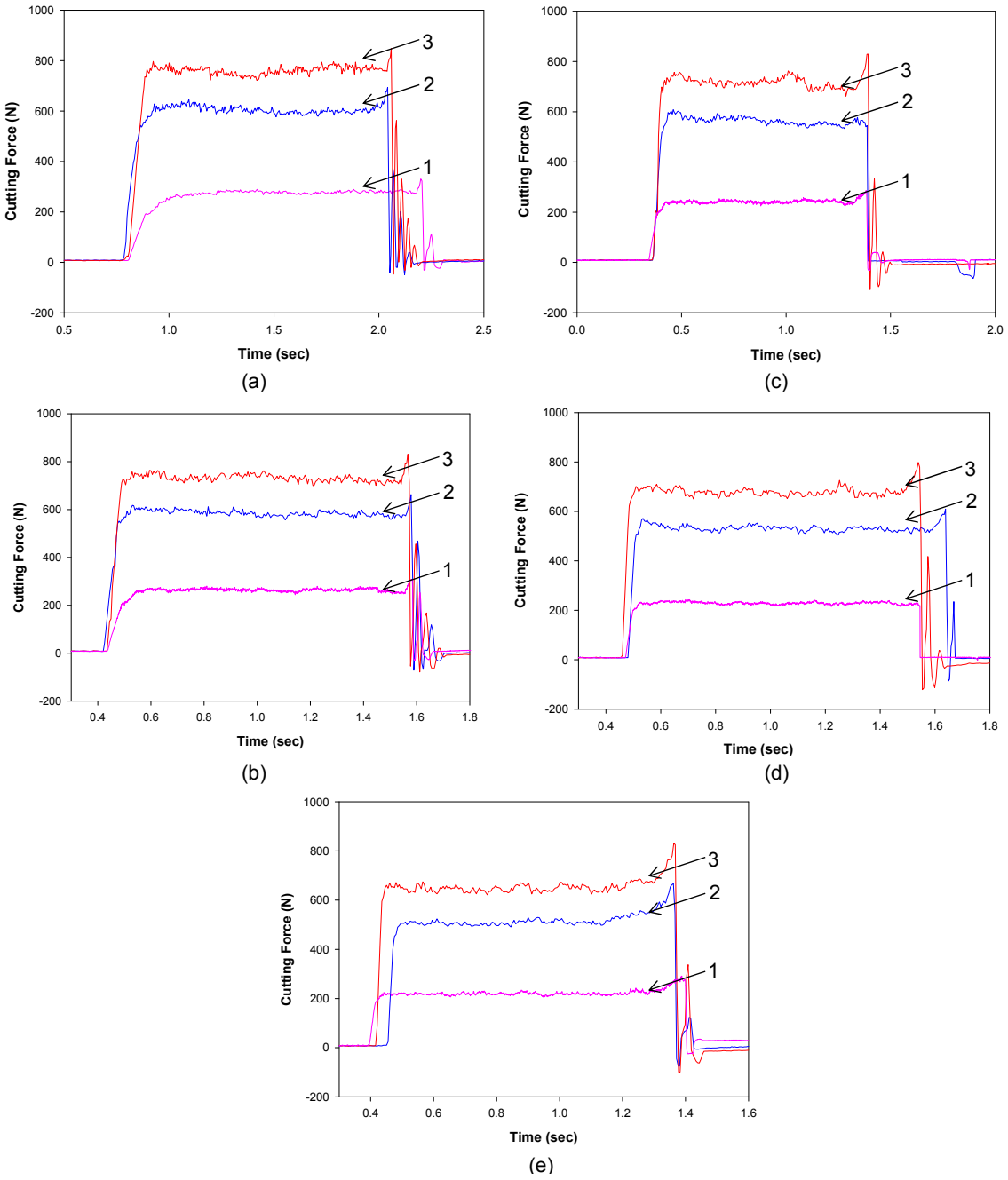

Fig.5.10. Plots showing variation of cutting forces (N) with time (second) for 6061-T6 when machined under different magnitudes of feed per revolution (denoted by numbers as follows: 1: 0.10mm, 2: 0.25mm and 3: 0.35mm) for cutting speed of (a) 25m/min, (b) 35m/min, (c) 50m/min, (d) 75m/min, and (e) 115m/min.

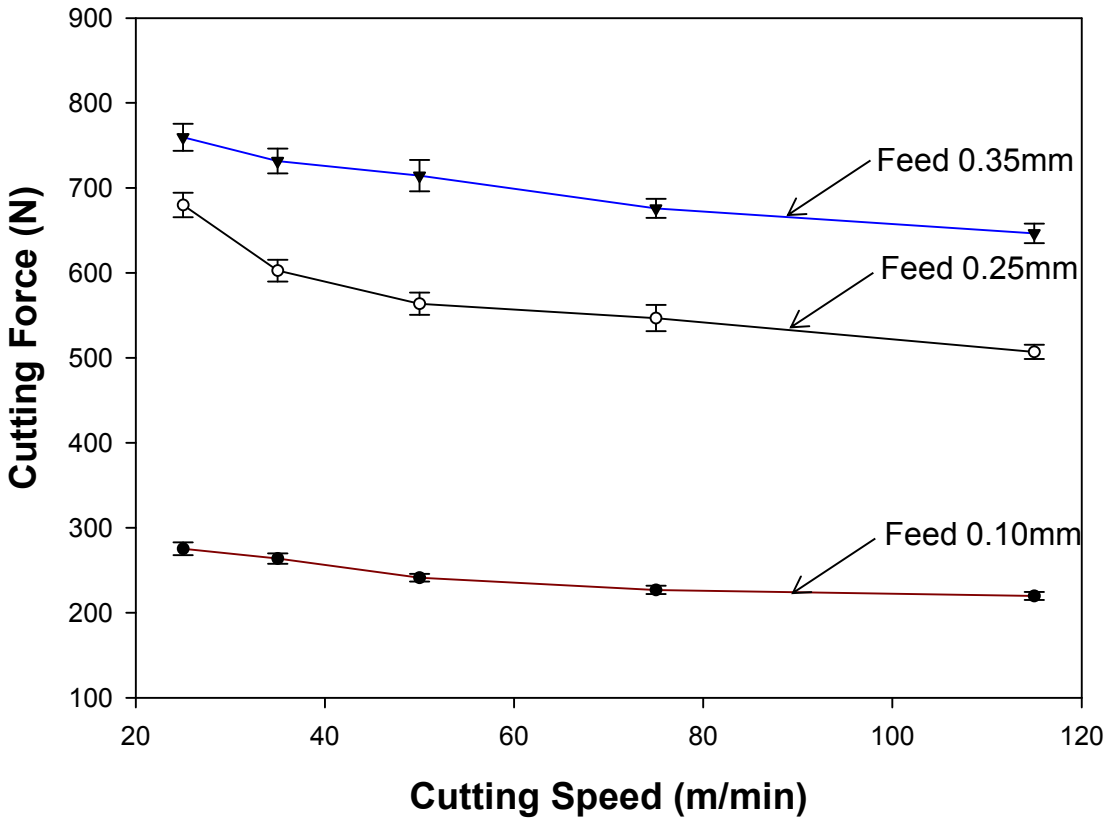

Fig.5.11. Plot showing variation of cutting forces for 6061-T6 with increase in cutting speed for feed per revolution equal to 0.10mm, 0.25mm and 0.35mm.

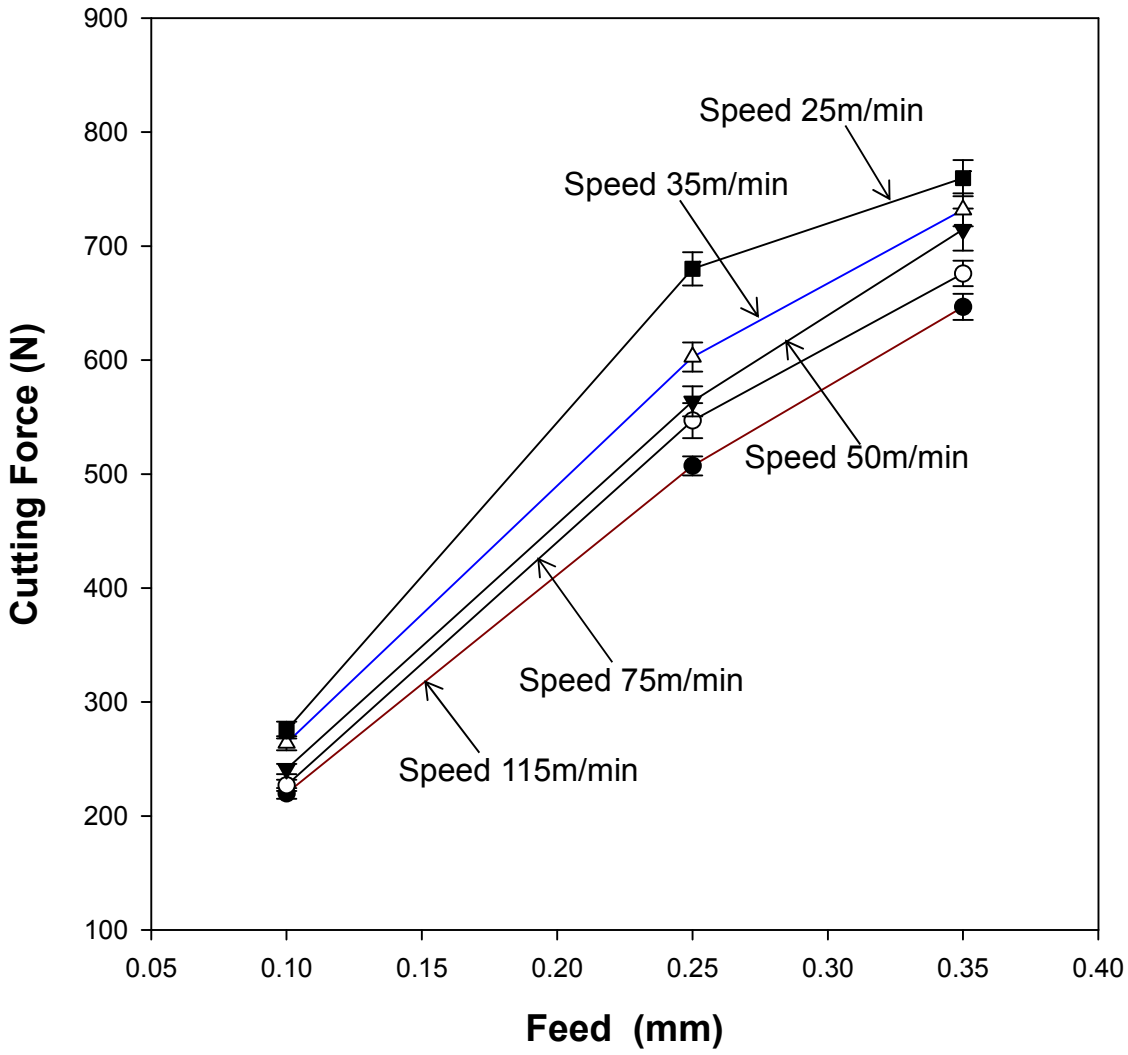

Fig.5.12. Plot showing variation of cutting forces (for 6061-T6) with increase in feed for cutting speeds equal to 25m/min, 35m/min, 50m/min, 75m/min and 115m/min.

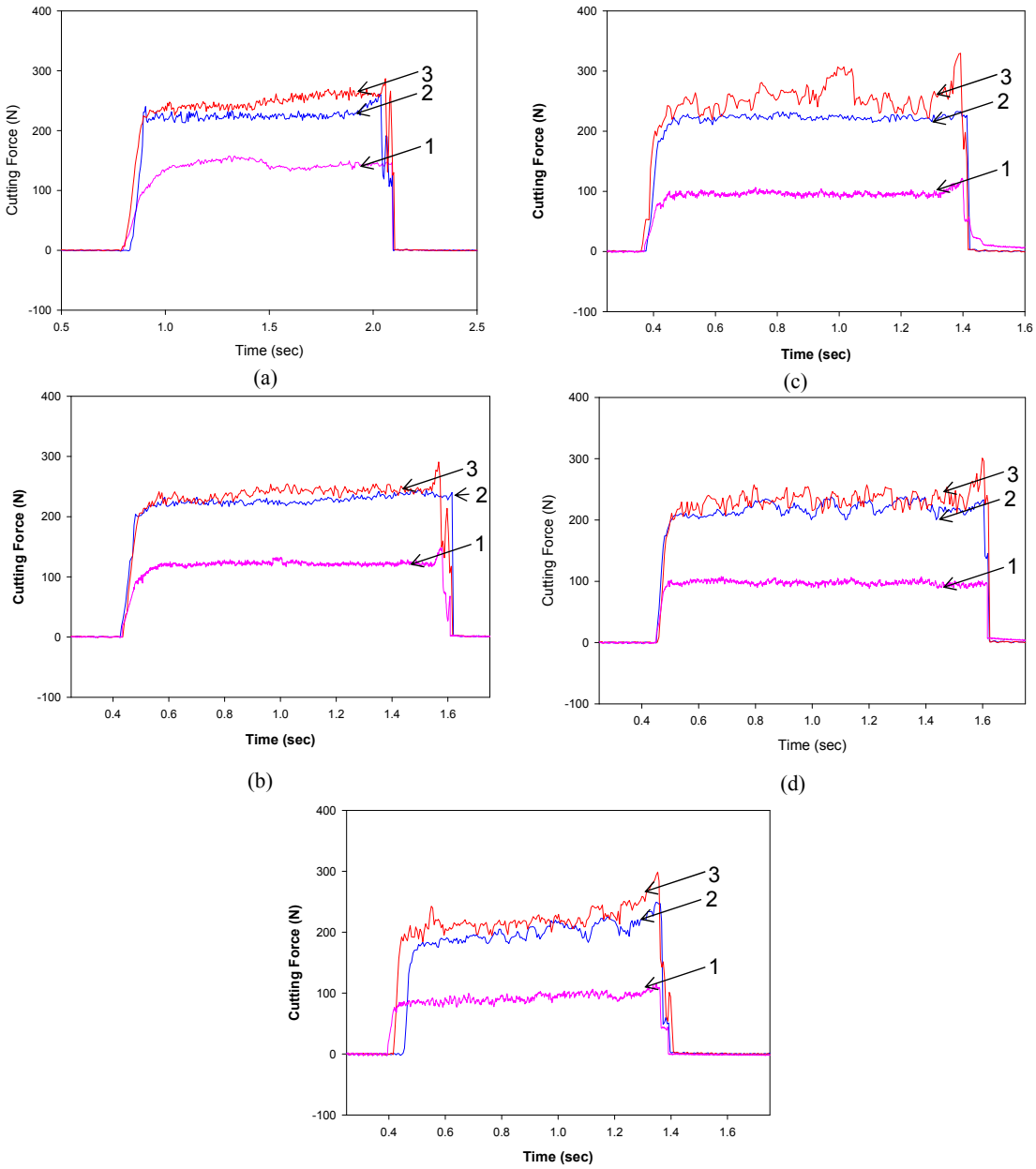

Fig.5.13. Plots showing variation of thrust forces (N) with time (second) for 6061-T6 when machined under different magnitudes of feed per revolution (denoted by numbers as follows: 1: 0.10mm, 2: 0.25mm and 3: 0.35mm) for cutting speed of (a) 25m/min, (b) 35m/min, (c) 50m/min, (d) 75m/min, and (e) 115m/min.

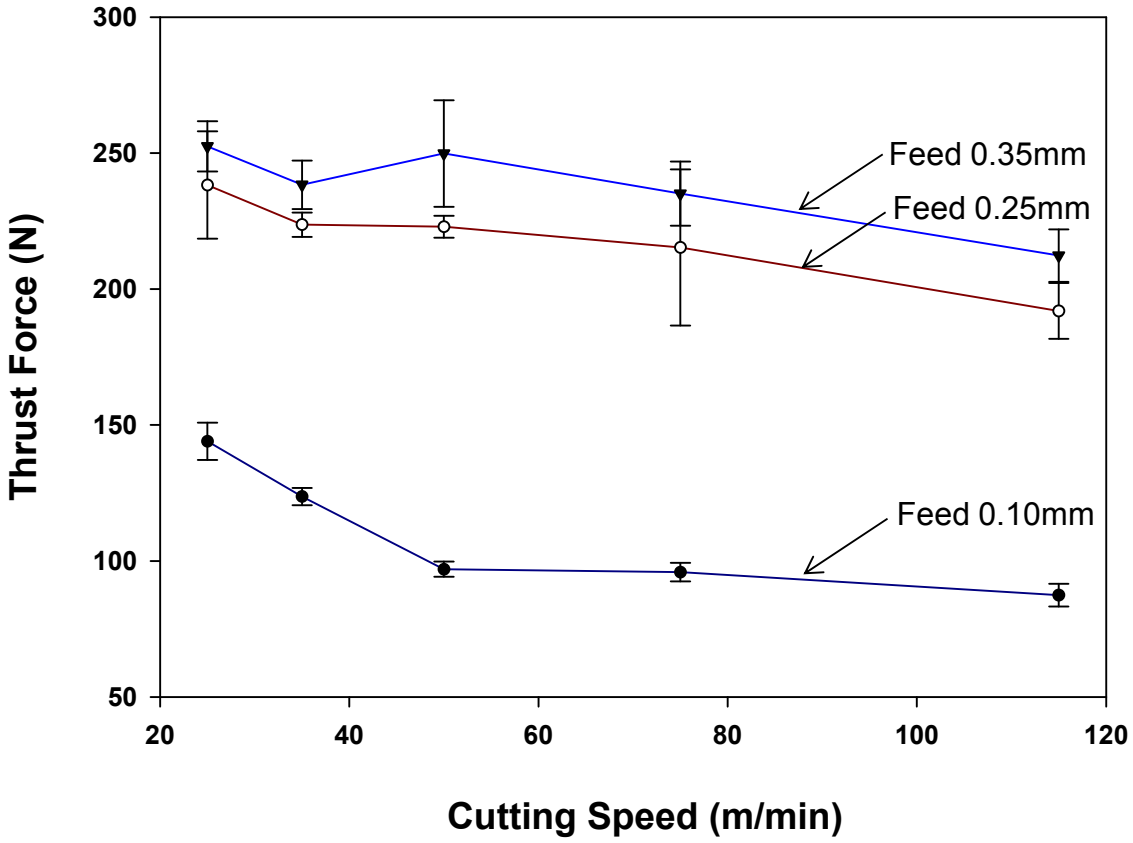

Fig.5.14. Plot showing variation of thrust forces for 6061-T6 with increase in cutting speed for feed per revolution equal to 0.10mm, 0.25mm, 0.35mm and 0.45mm.

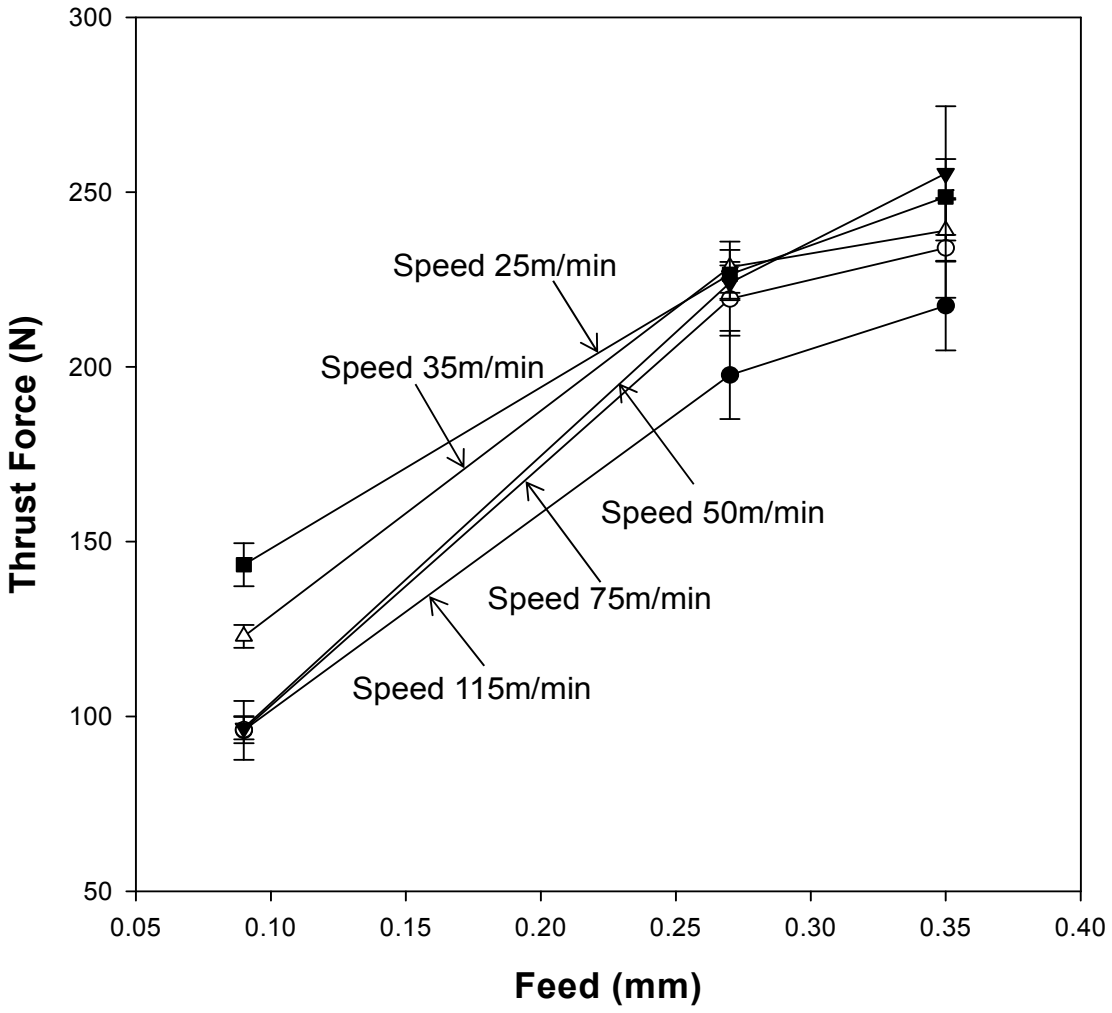

Fig.5.15. Plot showing variation of thrust forces (for 6061-T6) with increase in feed for cutting speeds equal to 25m/min, 35m/min, 50m/min, 75m/min and 115m/min.

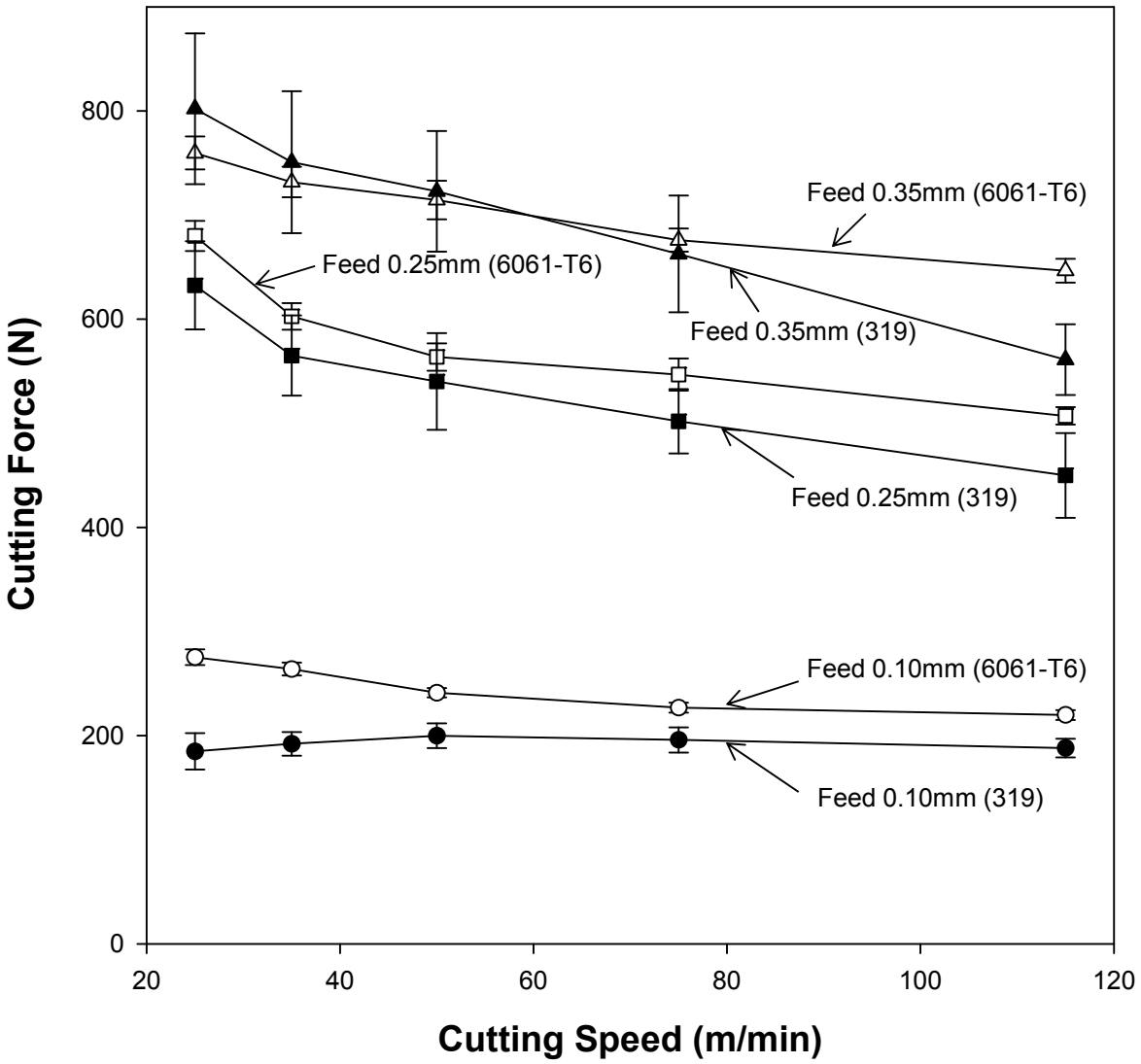

Fig.5.16. Plot showing comparison of cutting forces measured for 319 Al and for 6061-T6 as a function of cutting speed for feed rates of 0.10mm, 0.25mm and 0.35mm.

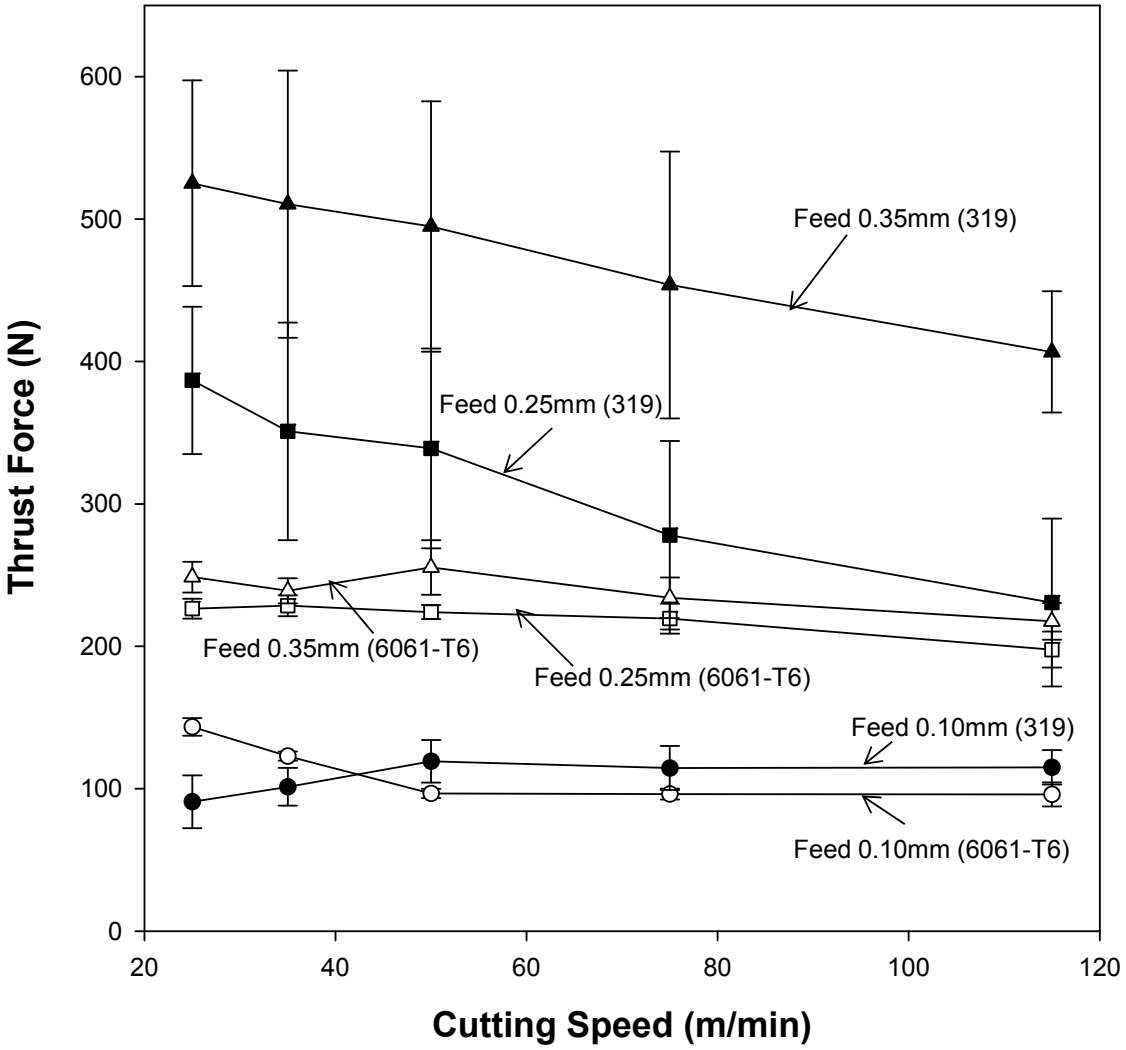

Fig.5.17. Plots showing comparison of thrust forces measured for 319 Al and 6061-T6 as a function of cutting speed for feed rates of 0.10mm, 0.25mm and 0.35mm.

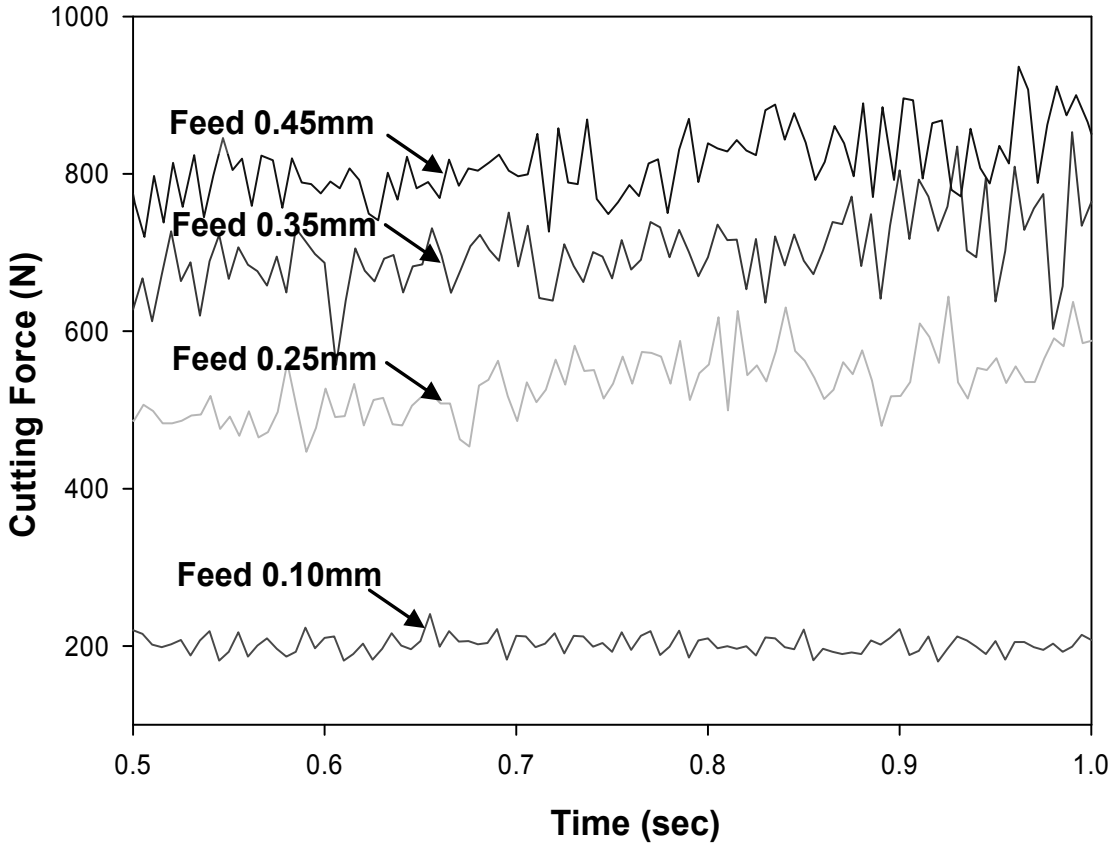

Fig.5.18. Plot showing variation in amplitudes of oscillations in measured cutting forces during cutting with change in speed for orthogonal cutting of Al 319 at cutting speed of 50m/min.

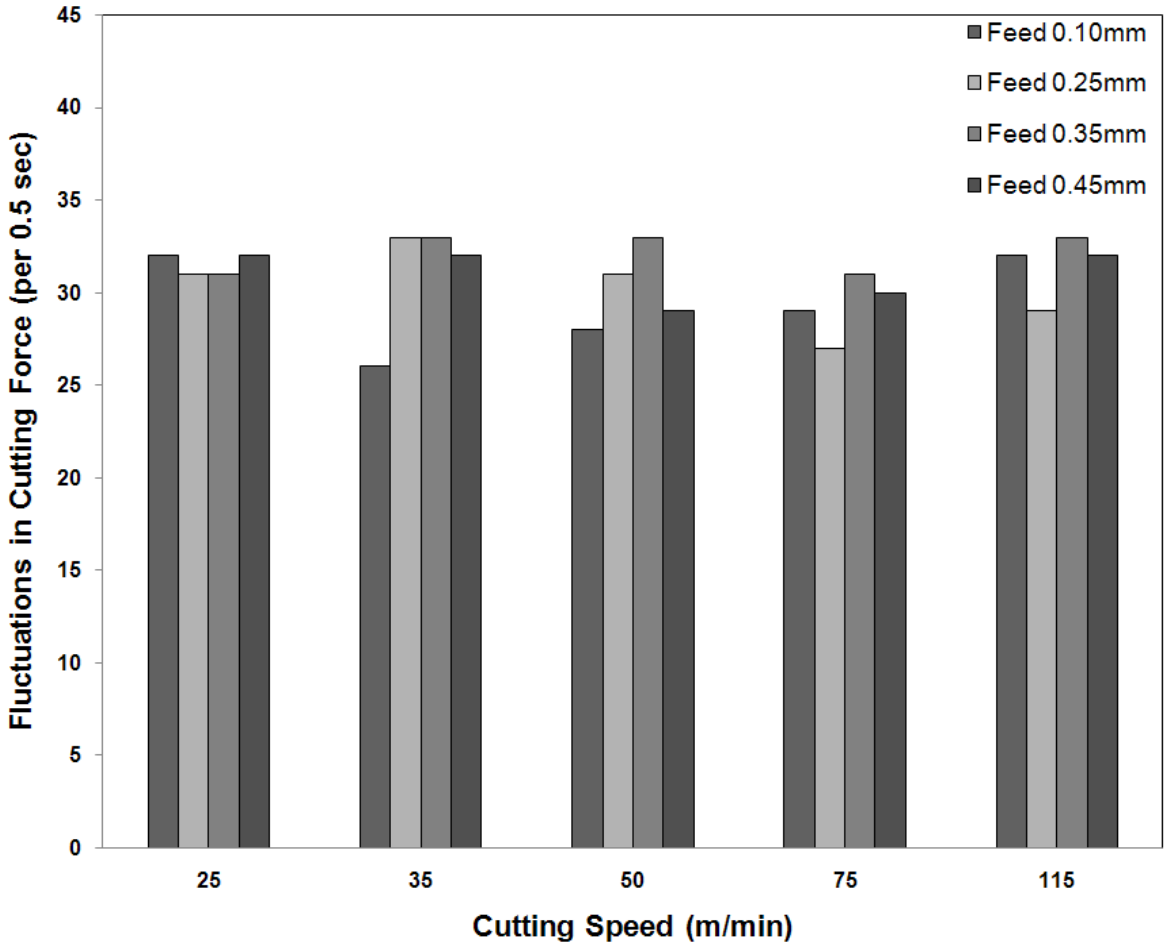

(a)

Fig.5.19 contd.

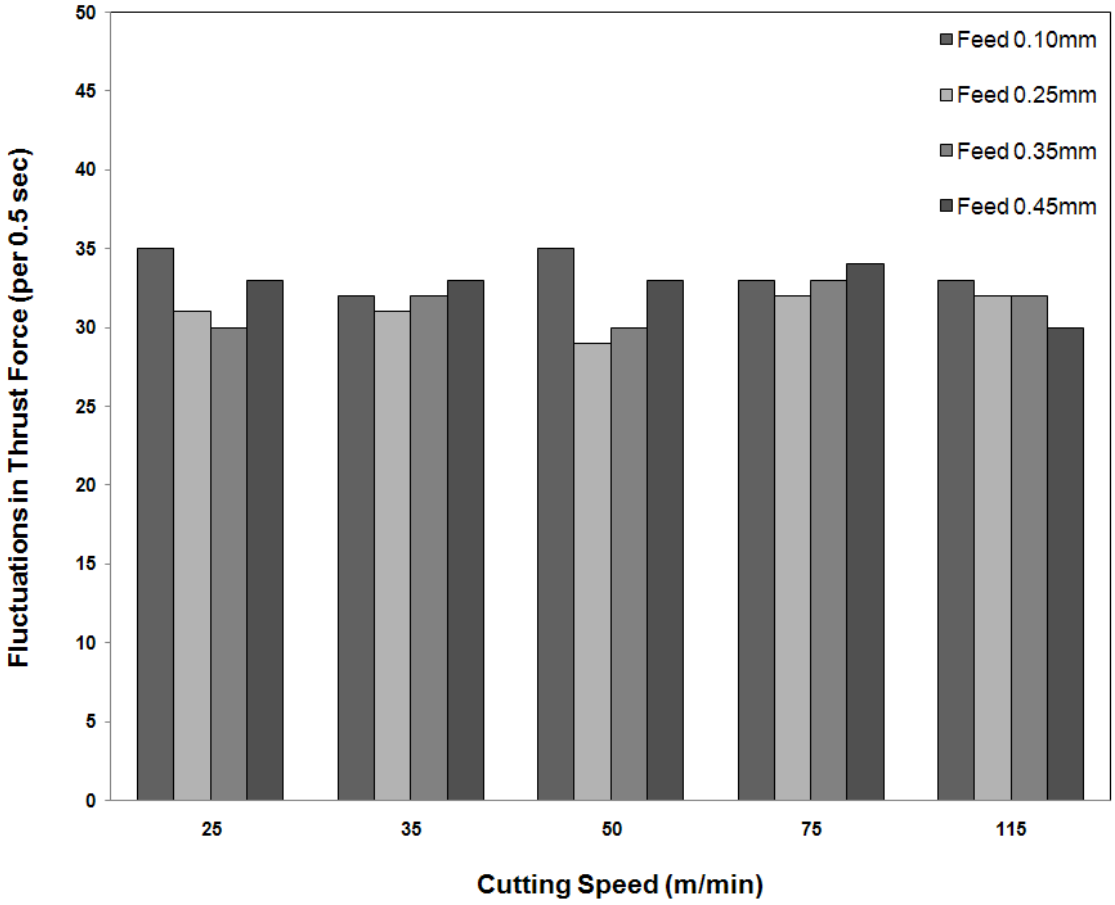

(b)

Fig.5.19. Histogram showing number of fluctuations in (a) cutting force response for 319 Al for different feed rates as a function of cutting speed, (b) thrust force response for 319 Al for different feed rates as a function of cutting speed. Sampling rate used was 2000 Hz.

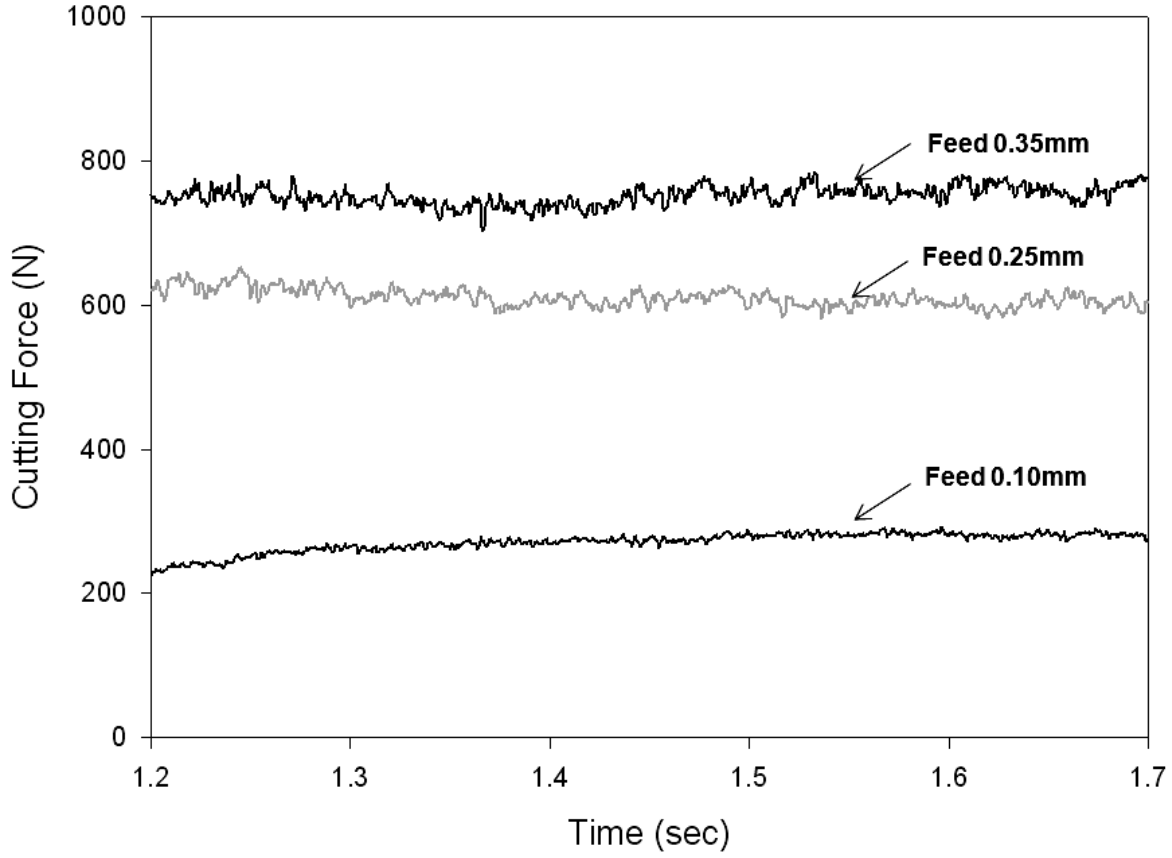

Fig.5.20. Plot showing variation in amplitudes of oscillations in measured cutting forces during cutting with change in speed for orthogonal cutting of 6061-T6 at cutting speed of 50m/min.

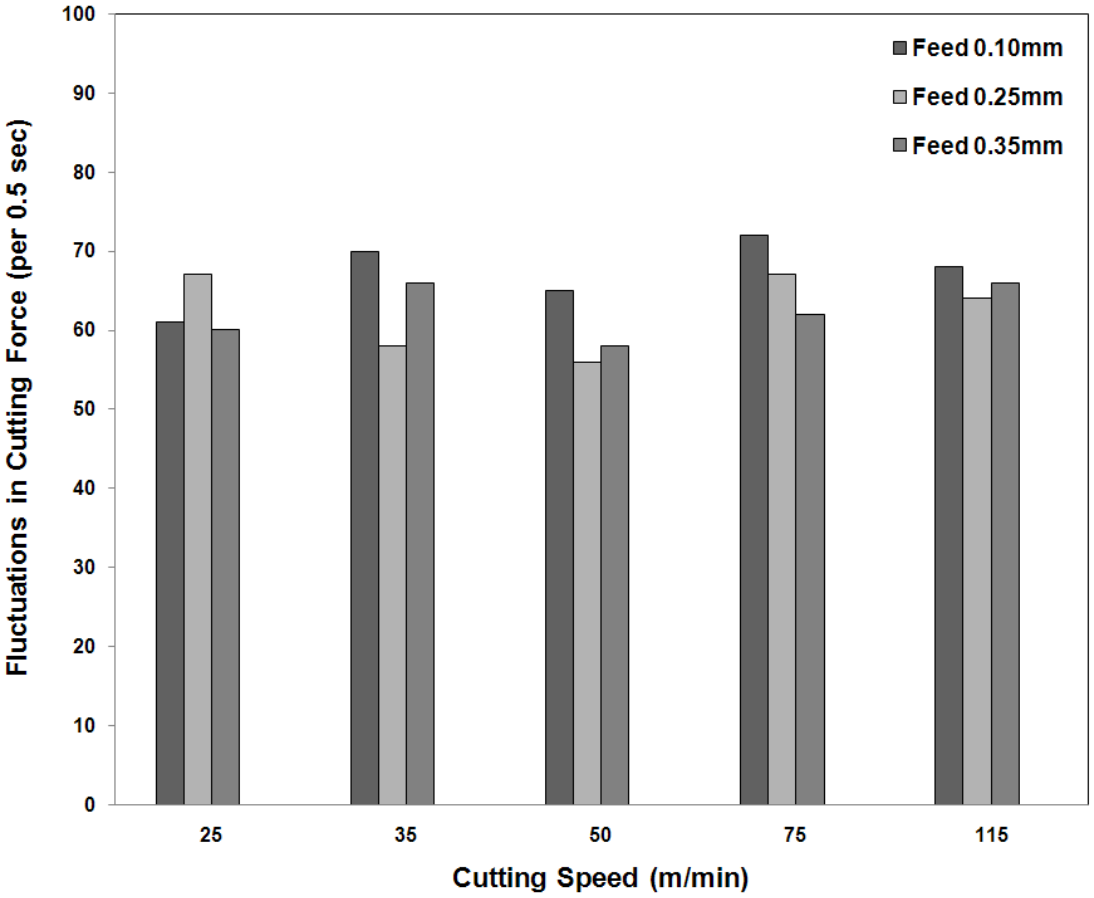

(a)

Fig.5.21 contd.

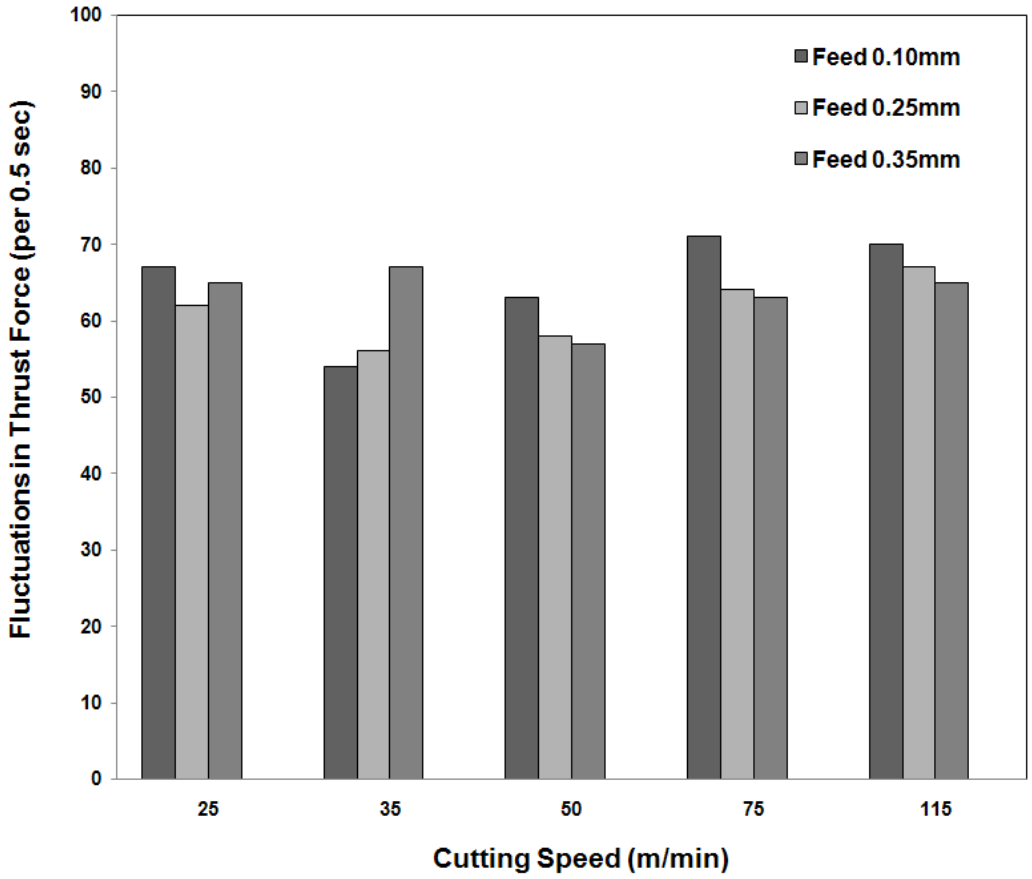

(b)

Fig.5.21. Histogram showing number of fluctuations in (a) cutting force response for 6061-T6 for different feed rates as a function of cutting speed, (b) thrust force response for 6061-T6 for different feed rates as a function of cutting speed. Sampling rate used was 2000 Hz.

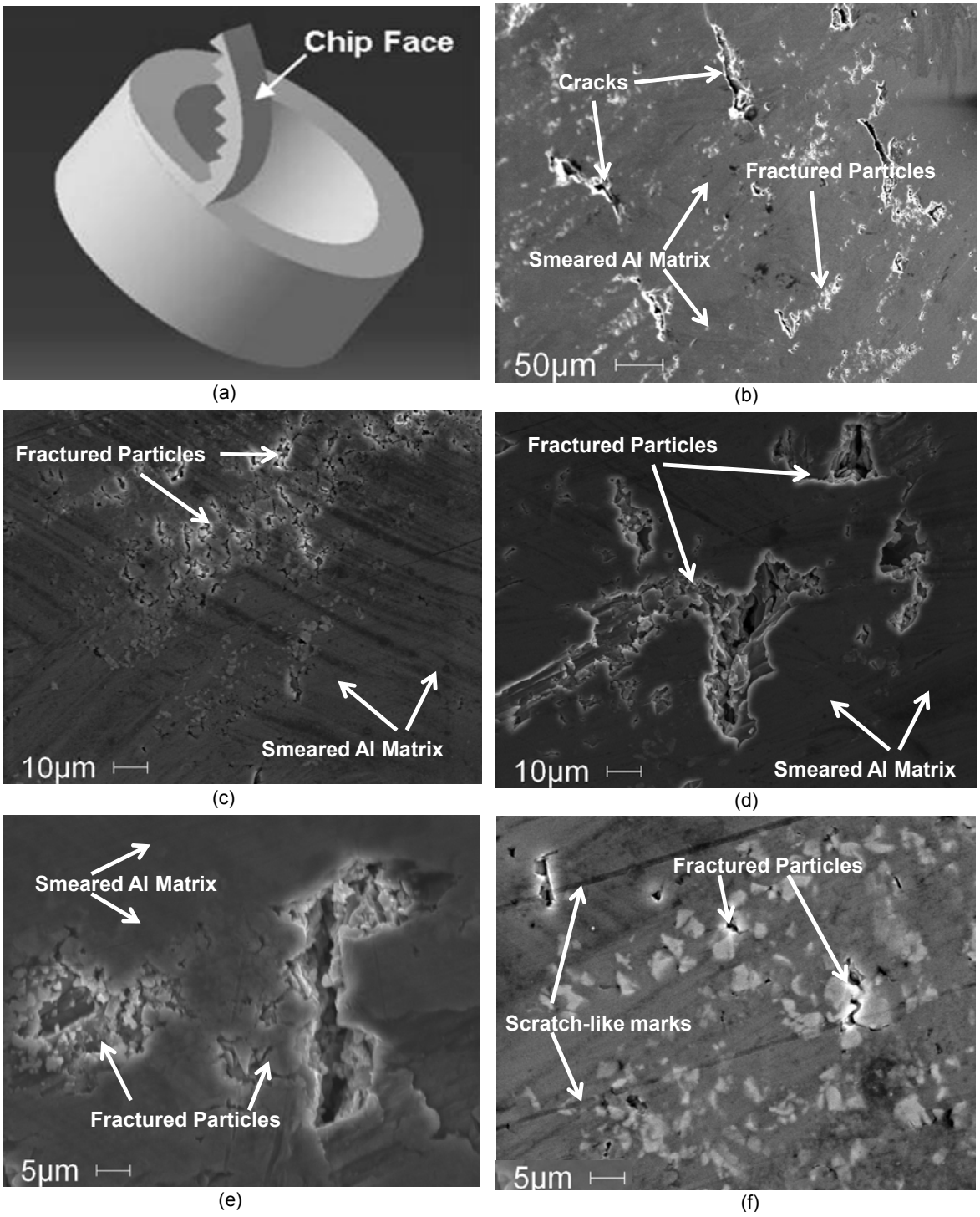

Fig.5.22.(a) Schematic diagram showing surface of chip or 'chip face' which undergoes sliding against rake face of tool , (b-f) SEM images of chip face showing surface conditions on this surface.

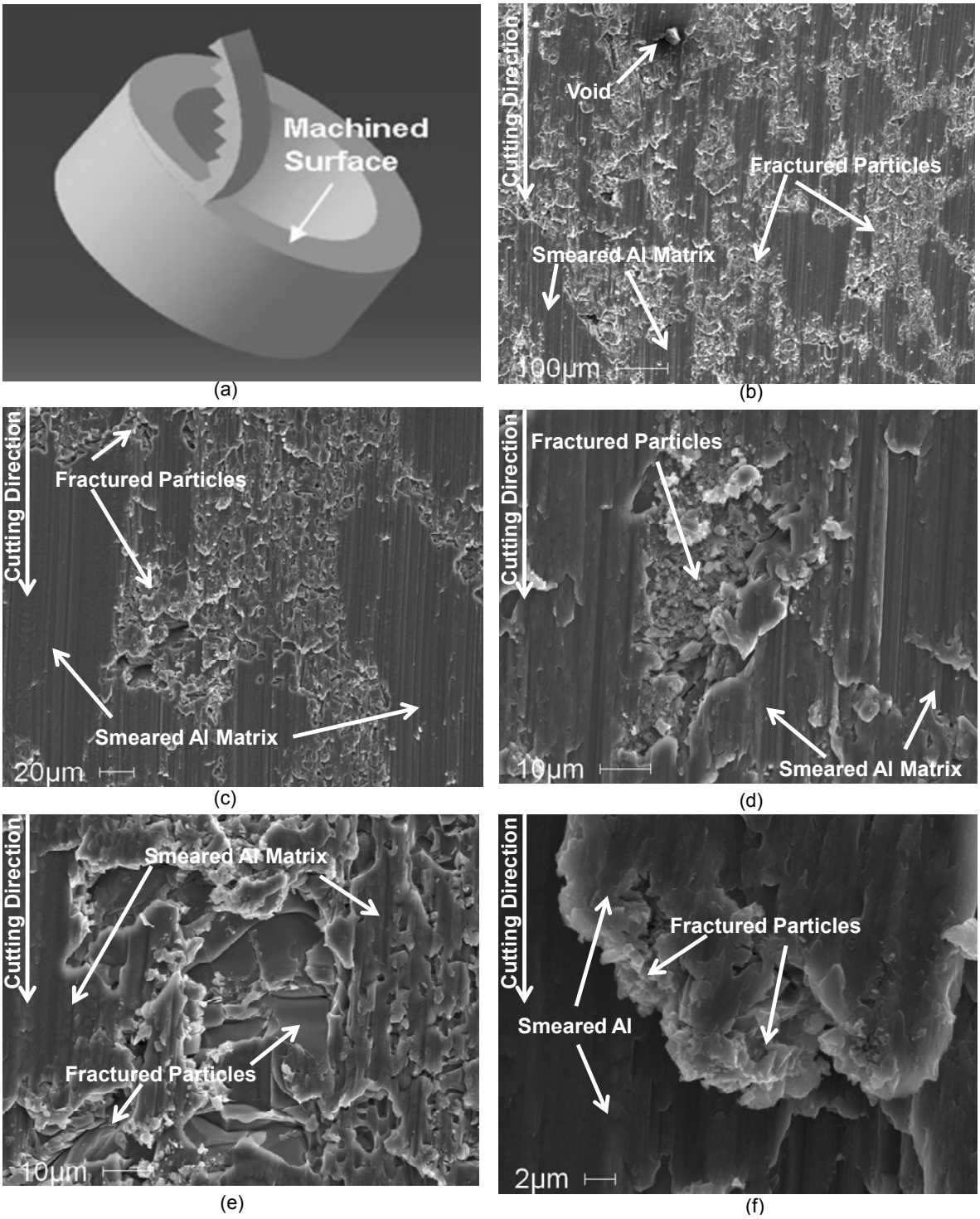

Fig.5.23.(a) Schematic diagram showing surface generated after machining or 'machined surface', (b-f) SEM images of machined surface showing surface conditions on this surface.

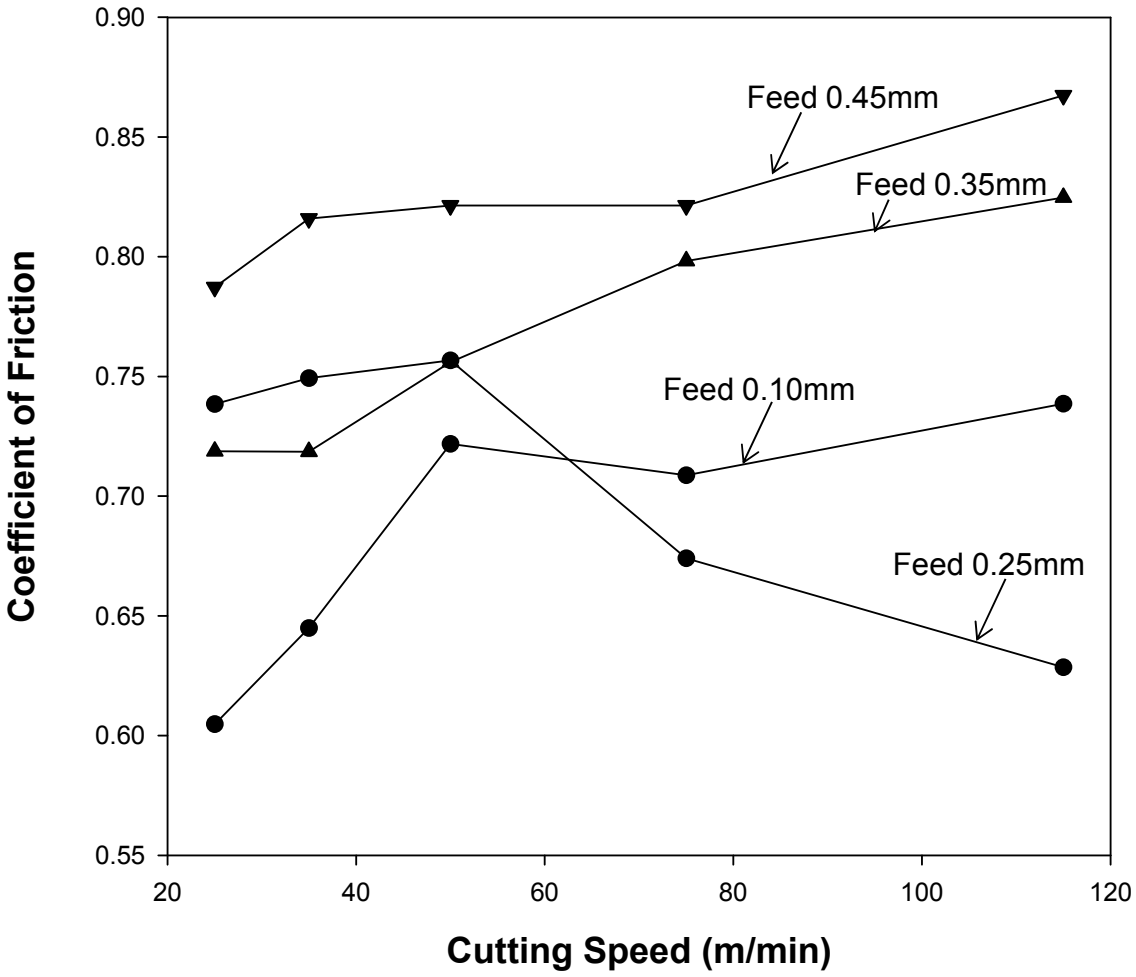

Fig.5.24 Plots showing variation of coefficient of friction with cutting speed. With an increase in cutting speed, the magnitude of coefficient of friction shows no significant change for feeds of 0.35mm and 0.45mm per revolution. For feed 0.25mm, a reduction in magnitude of coefficient of friction is seen.

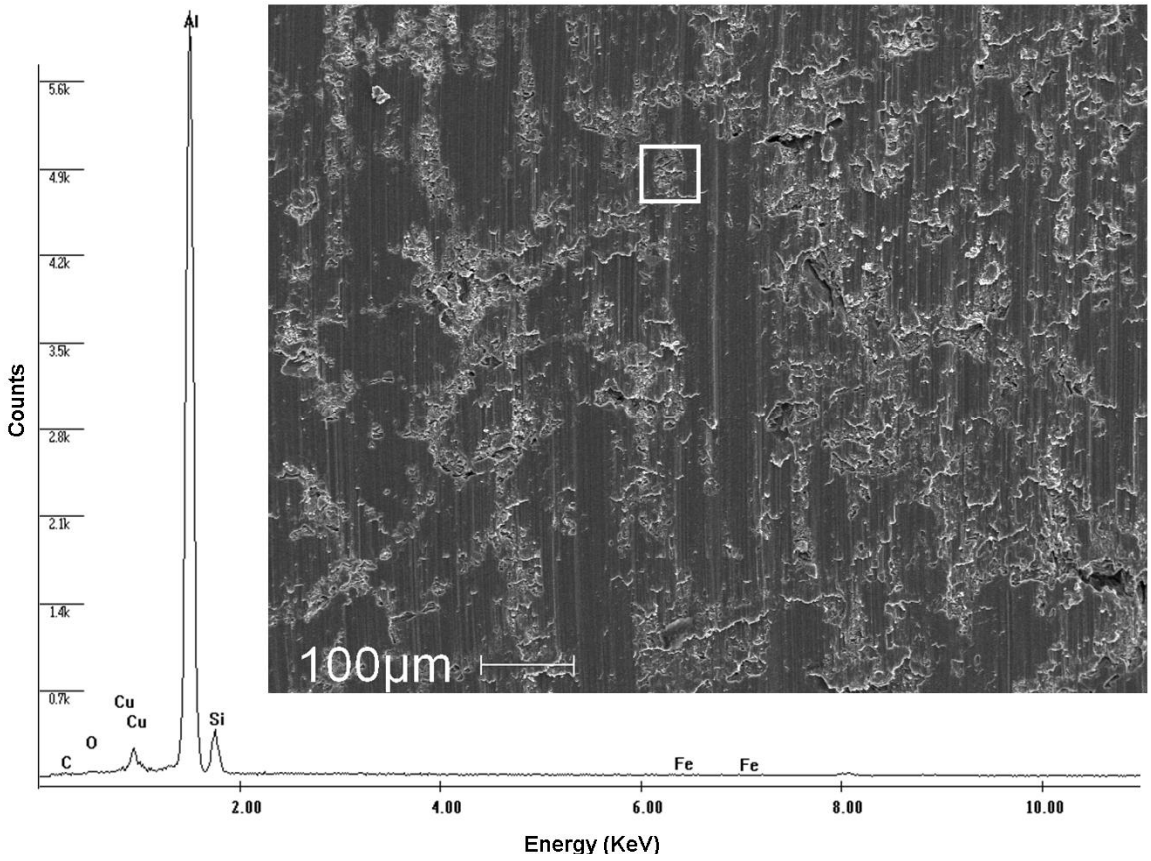

Fig.5.25 SEM image and EDS spectrum of machined surface from sample machined under cutting speed of 75m/min and feed per revolution of 0.25mm. Surface shows fractured second phase particles and relatively smoother aluminum matrix. EDS spectrum taken from the area marked by the square in the image shows a predominance of Aluminum.

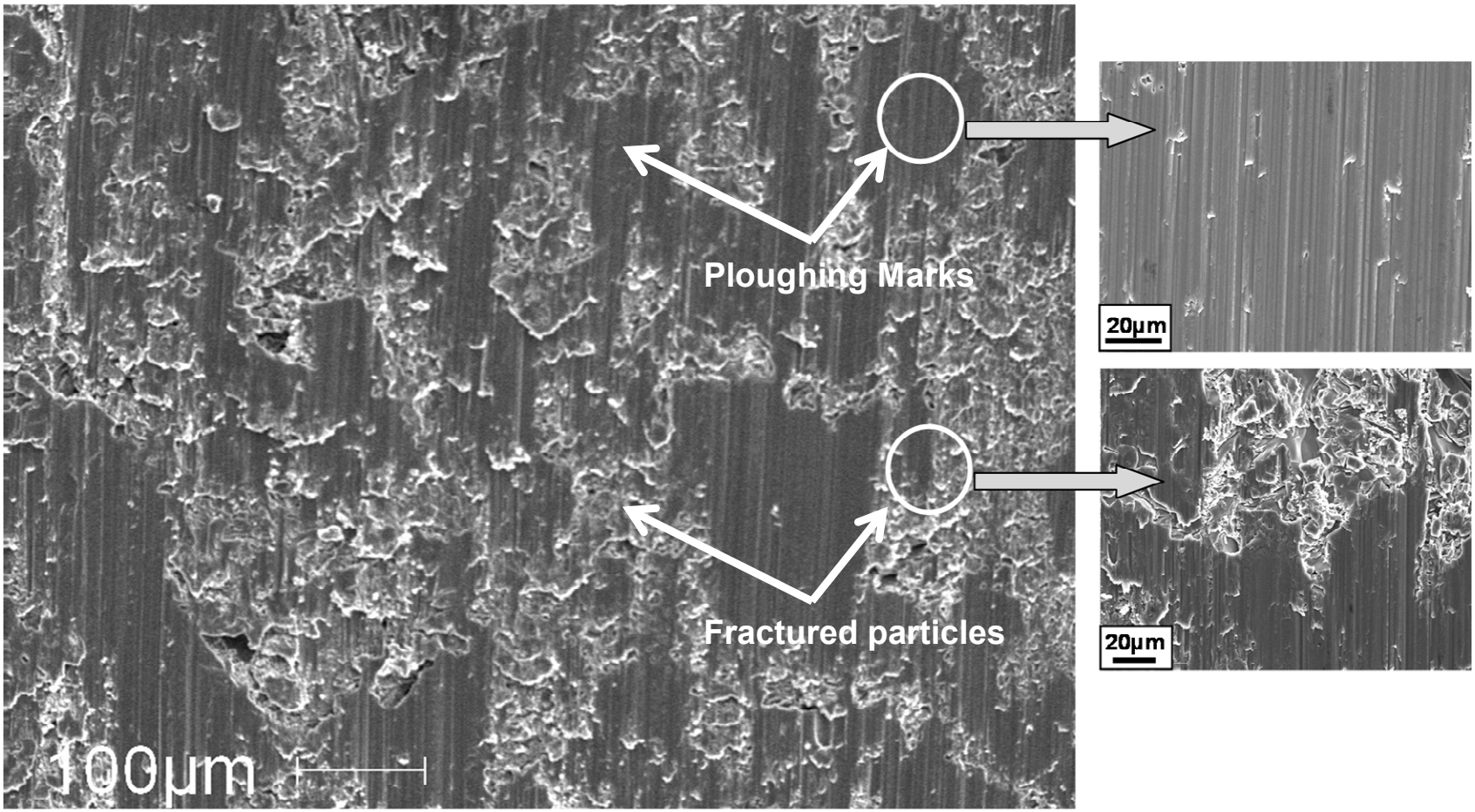

Fig.5.26. SEM image of machined surface from sample machined under cutting speed of 75m/min and feed per revolution of 0.25mm, showing smoother aluminum matrix and rougher areas with fractured second phase particles.

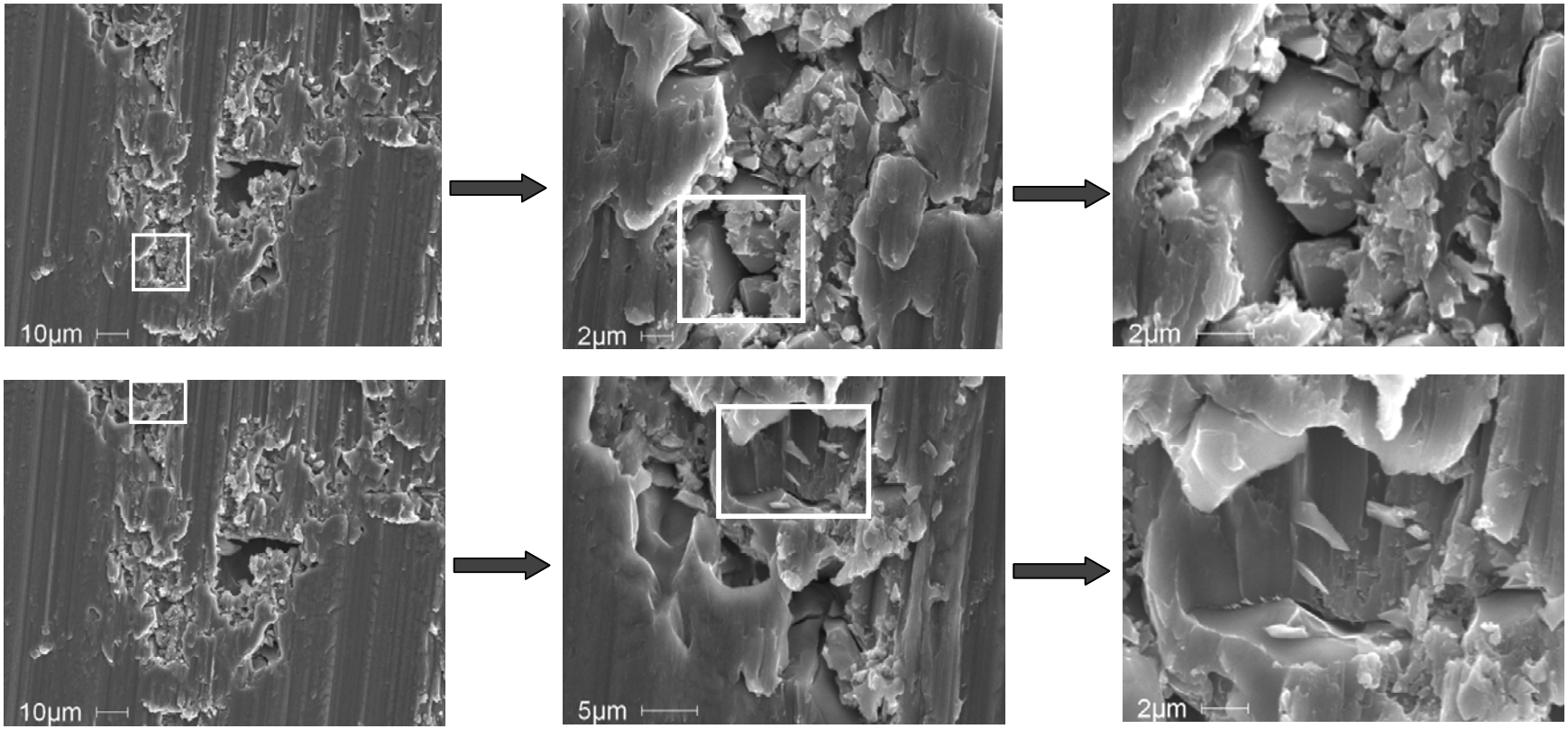

Fig.5.27. SEM images showing extensive fracture of second phase particles on the machined surface from sample machined under cutting speed of 115m/min and feed per revolution of 0.45mm.

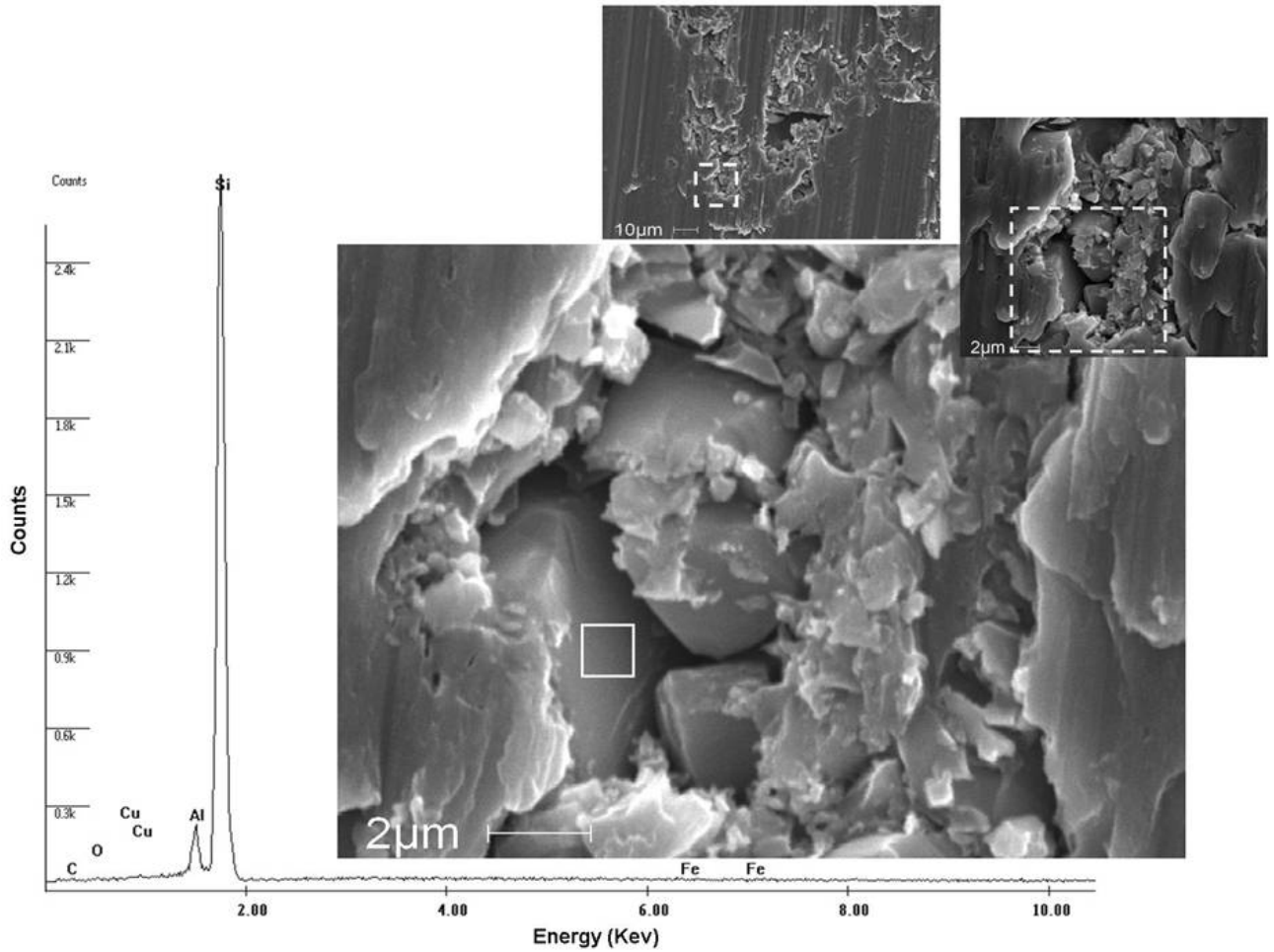

(a)

Fig.5.28 contd

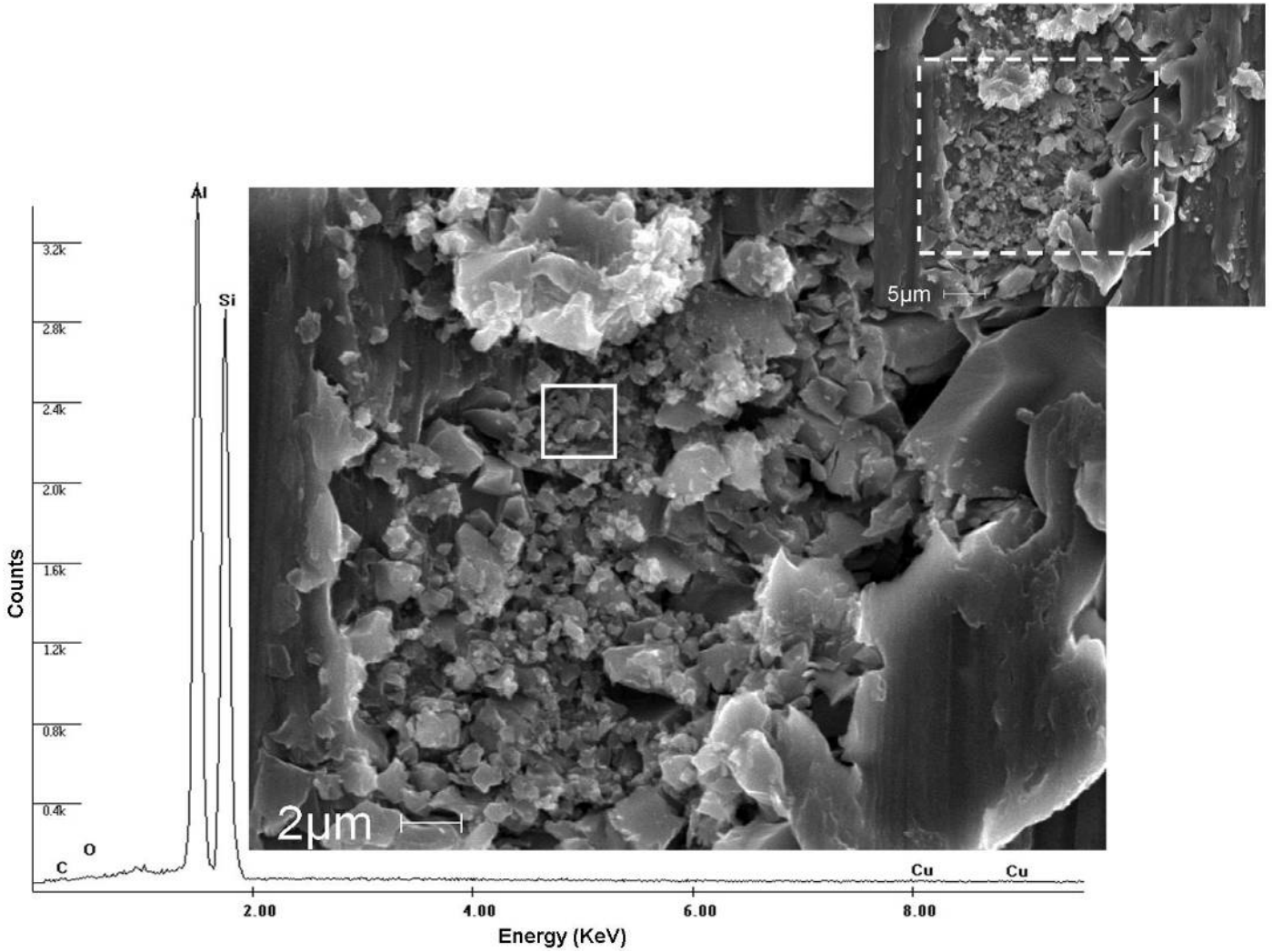

(b)

Fig.5.28 contd.

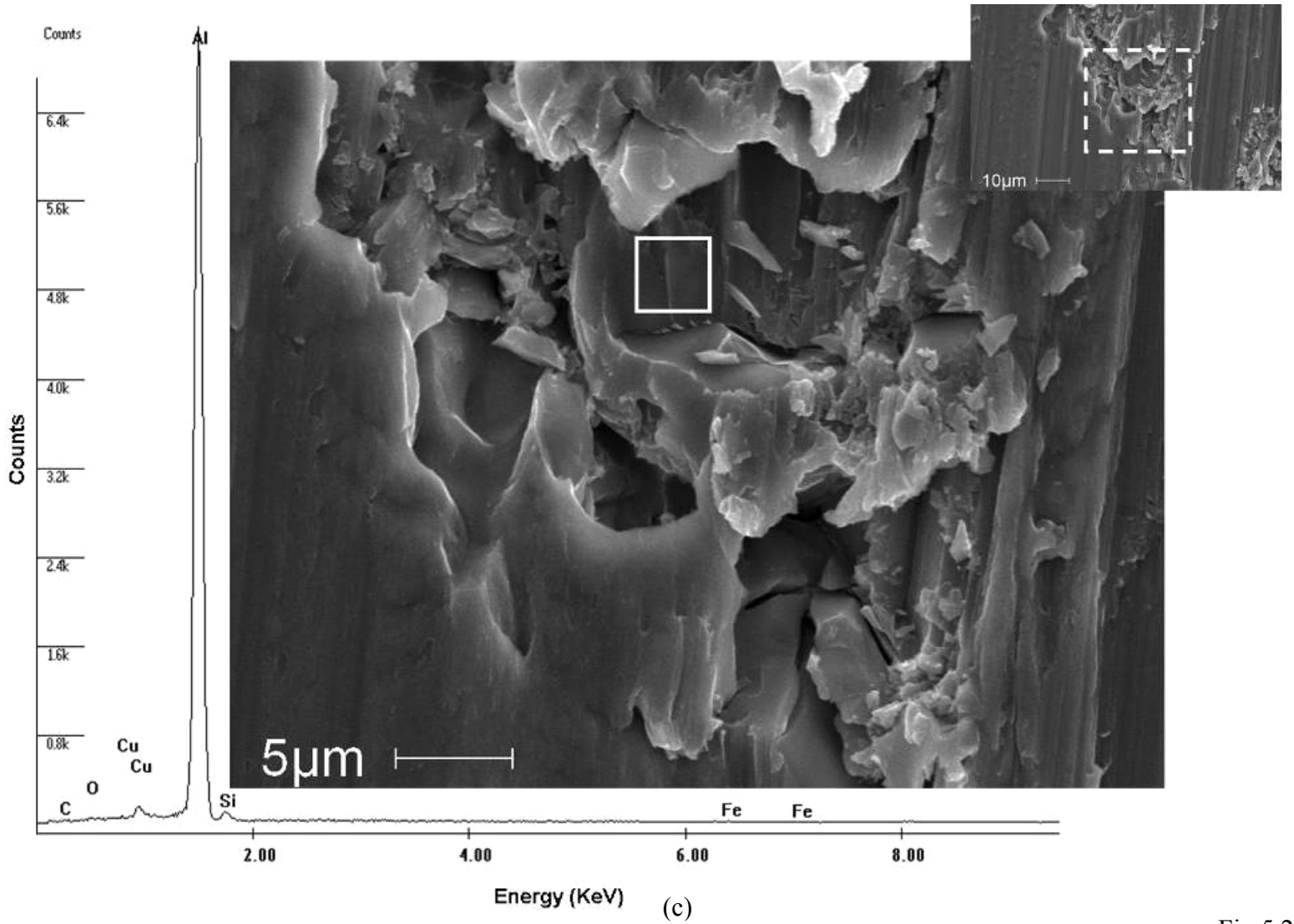

(c)

Fig.5.28 contd.

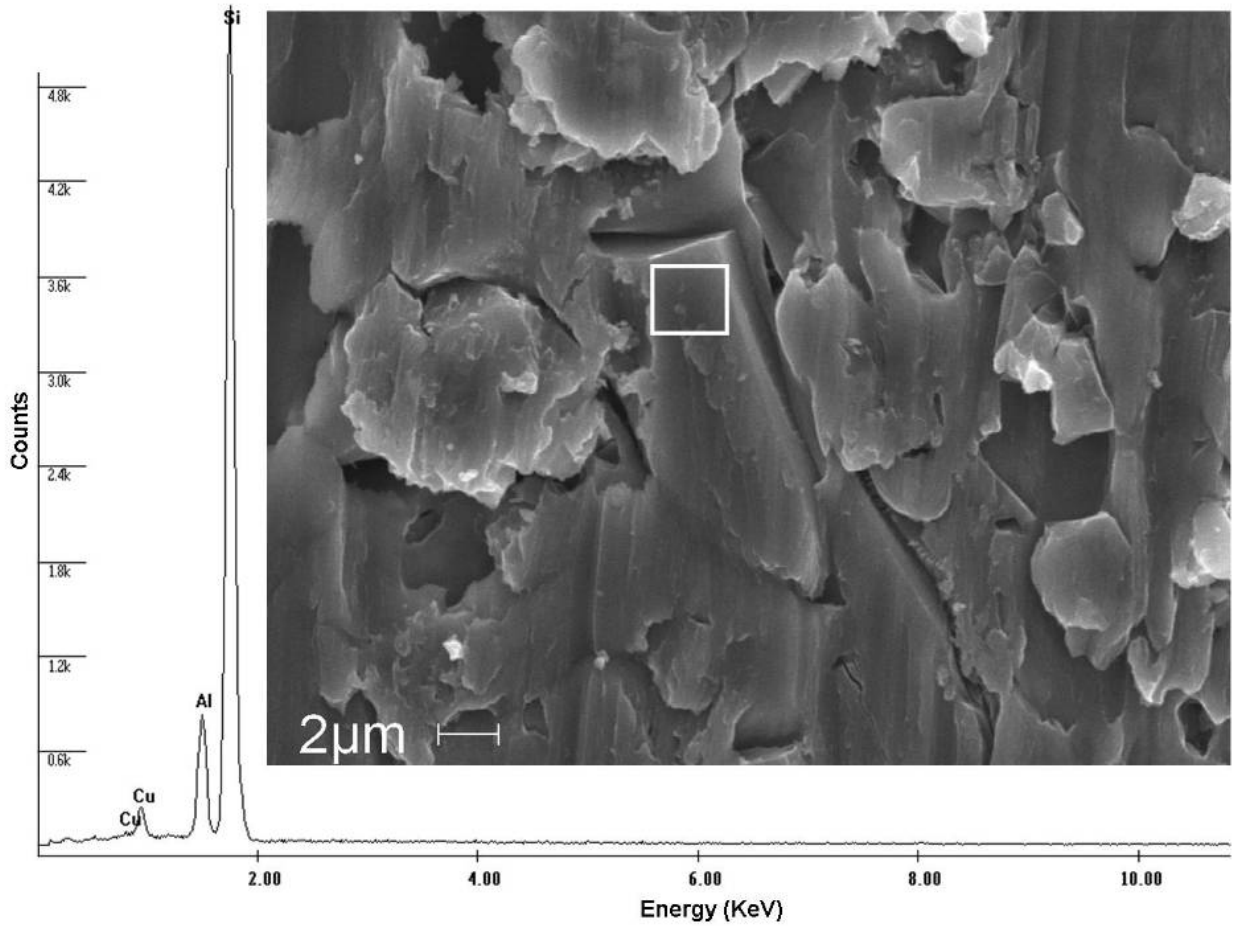

(d)

Fig.5.28 (a-d) SEM images and EDS profiles of the damaged second phase particles showing extensive damage of Silicon particles on the machined surface of sample machined under cutting speed of 115m/min and feed per revolution of 0.35mm.

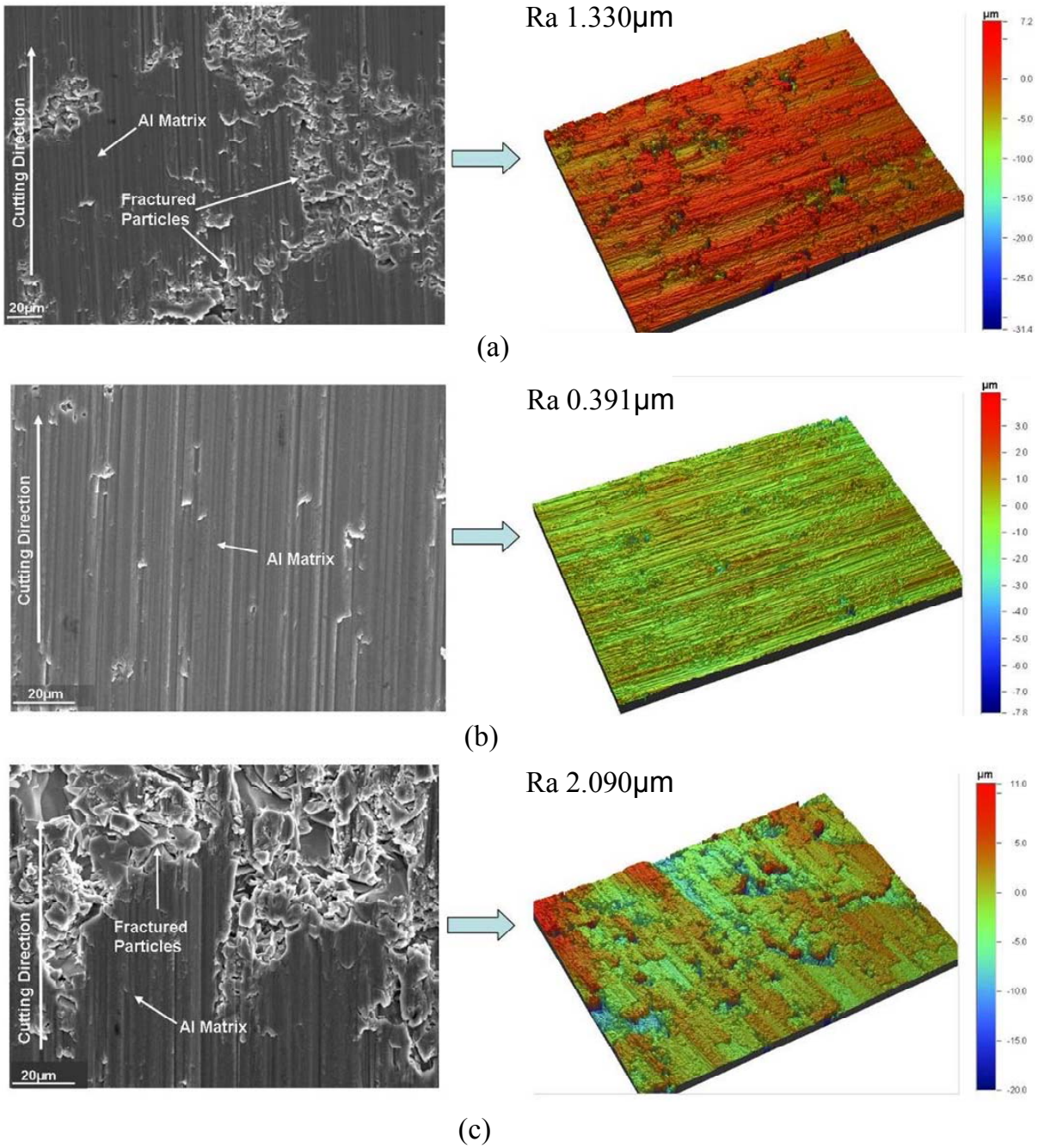

Fig.5.29. SEM images and WYKO images showing surface profiles of machined surface (a) of an area containing ploughing marks and fractured particles; (b) of an area containing ploughing like marks only; (c) of an area containing fractured particles. Machining conditions used were cutting speed of 75m/min and feed per revolution of 0.25mm.

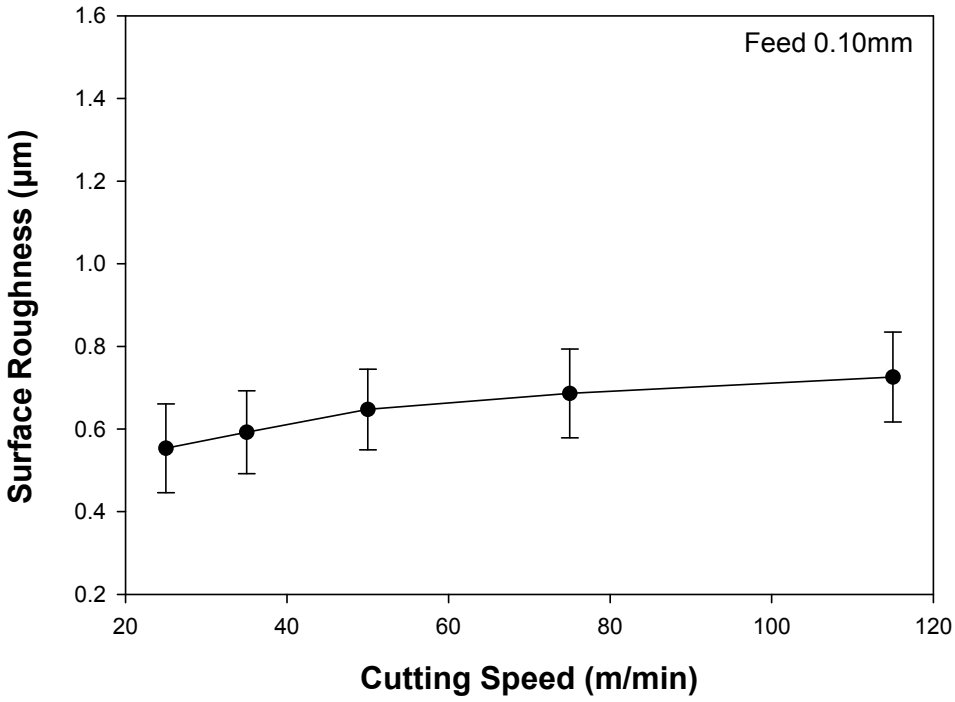

(a)

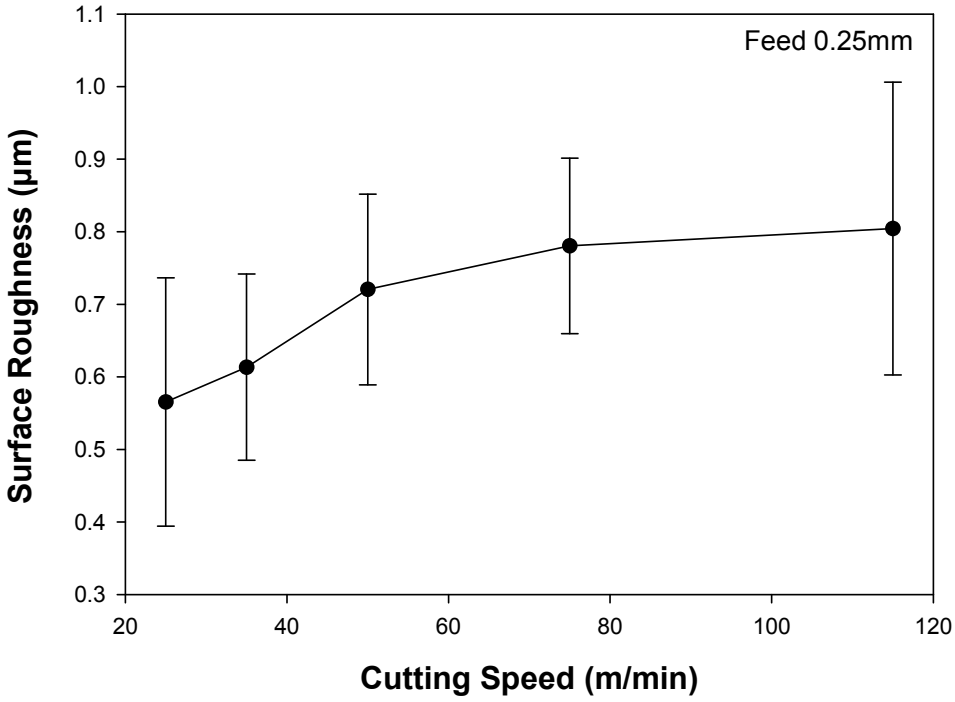

(b)

Fig.5.30 contd.

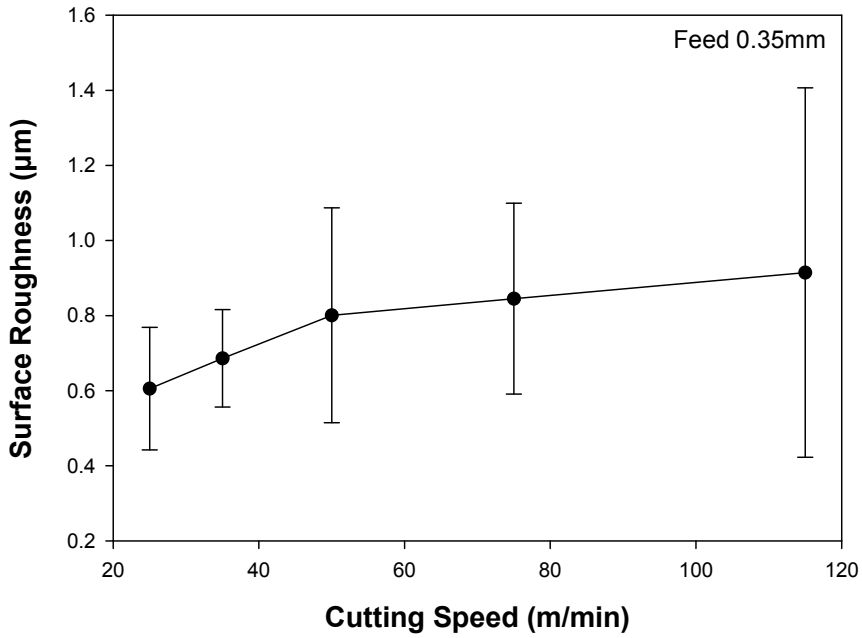

(c)

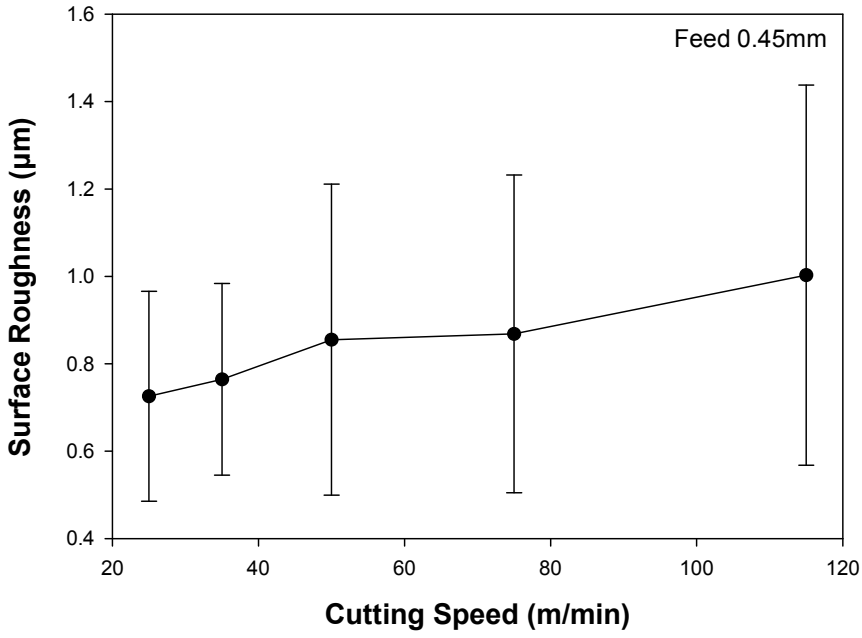

(d)

Fig.5.30. Plots showing variation of surface roughness values for the aluminum matrix on the machined surface plotted against cutting speed for different feeds. The error lines on the plots show the difference in the surface roughness values (Ra) between the zones showing fractured second phase particles and the aluminum matrix.

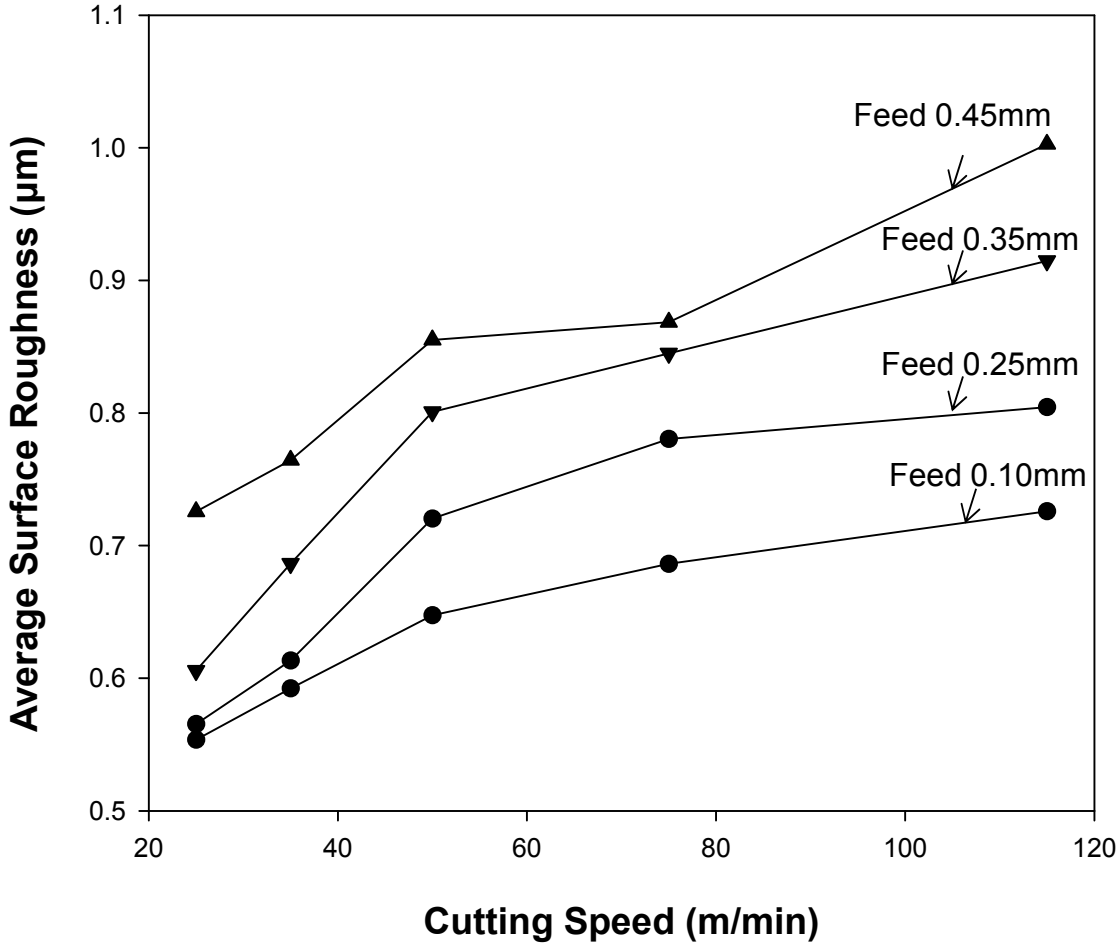

Fig.5.31. Plot showing surface roughness (Ra) values for different feeds plotted against variation in cutting speeds. The surface roughness values show a rising trend with an increase in cutting speed and with an increase in feed.

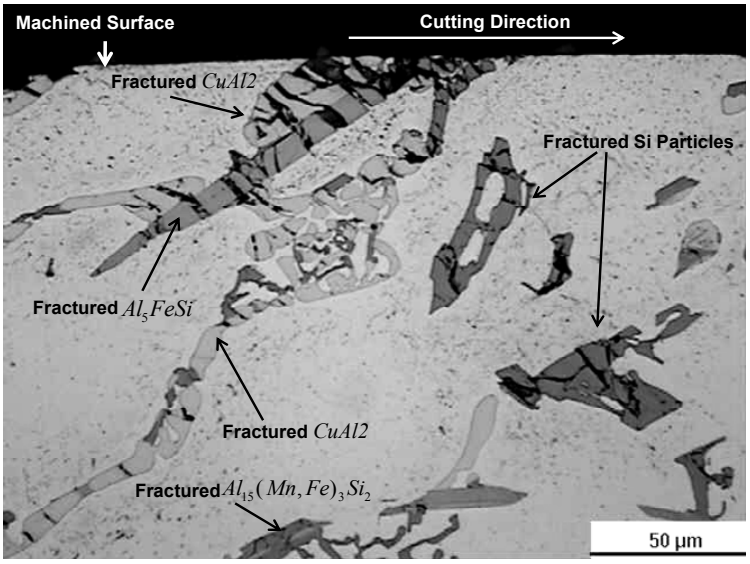

(a)

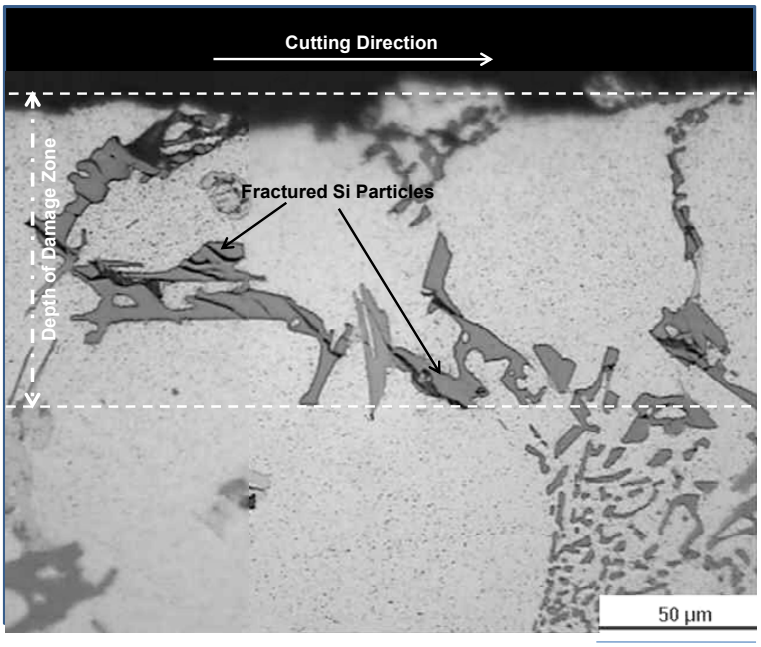

(b)

Fig.5.32 (a) Micrographs showing sub-surface damage to second phase particles in sample machined under cutting speed of 115m/min and feed per revolution of 0.45. (b) Optical micrographs showing variation of depth of zone to which most of the second phase particle damage is confined (damage zone), for cutting speed of 50m/min and feed per revolution 0.45mm.

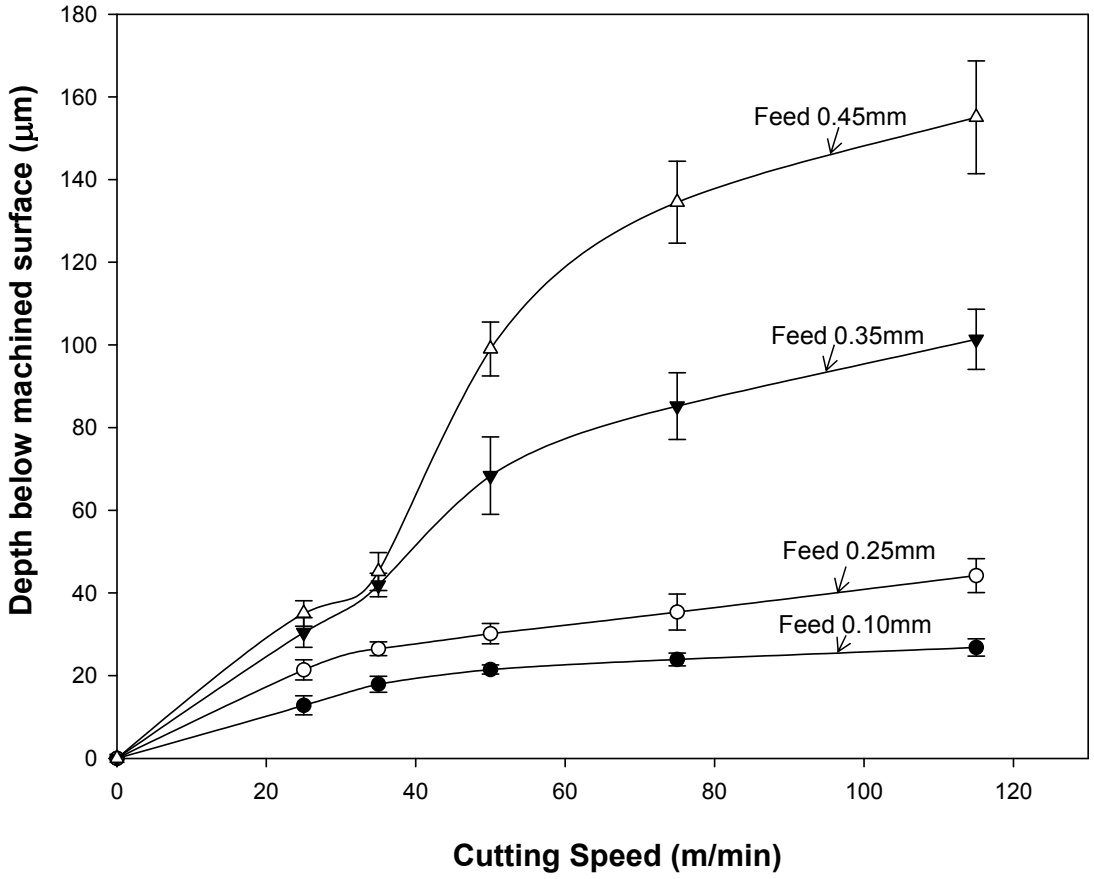

Fig.5.33. Plot showing maximum depth of the damage zones for different cutting conditions. For lower feed rates of 0.10mm and 0.25mm, the depth of the zone shows only a slight increase with an increase in cutting speed from 25m/min to 115m/min. For higher feeds of 0.35mm and 0.45mm per revolution, depth of deformation increases drastically with an increase in cutting speed.

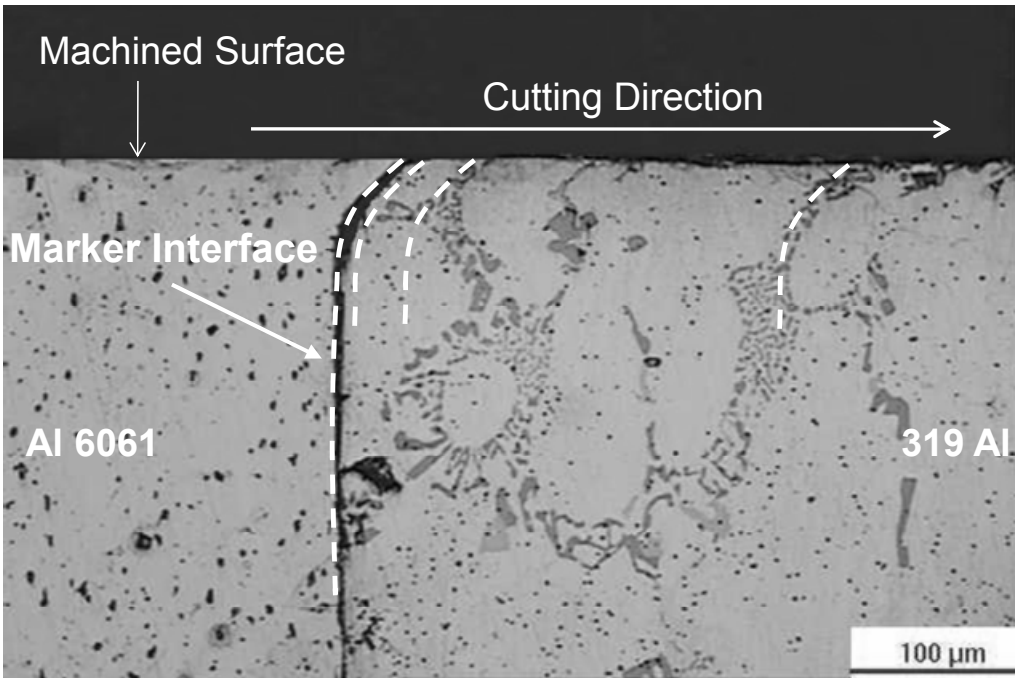

Fig.5.34. Micrograph showing polished and etched cross section an 319 Al sample with 6061 Al marker insert, orthogonally machined under conditions of cutting speed of 50m/min and feed per revolution 0.35mm. It was seen that the marker as well as the machined workpiece material (319 Al) underwent bending in the direction of cutting (shown by dotted lines), and the magnitude of displacement of marker with respect to its original orientation decreased as the distance from machined surface increased.

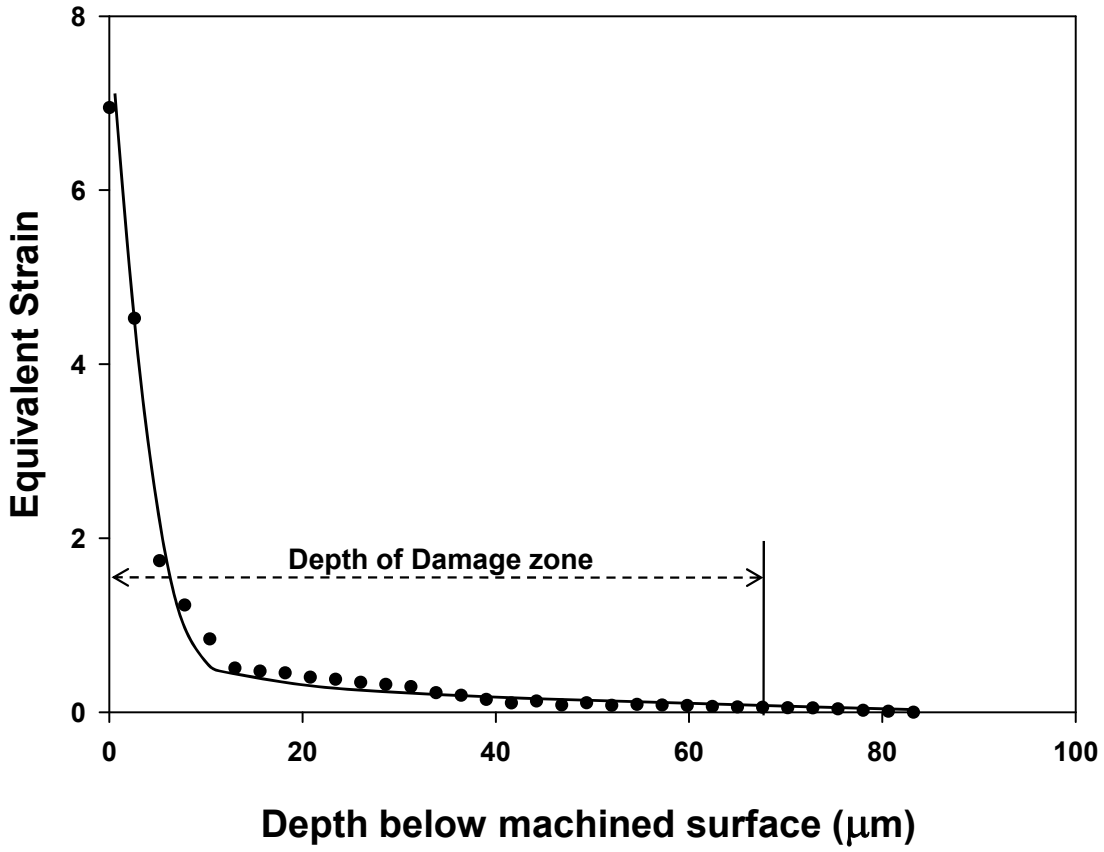

Fig.5.35. Plot showing variation of magnitude of plastic strains, estimated from the displacement of 6061 Al marker with respect to its original orientation, with distance below machined surface. Plot also shows the corresponding depth of damage zone for silicon particle fracture, estimated from maker test (refer to Fig.5.33). Cutting conditions used were cutting speed 50m/min, feed per revolution 0.35mm. High strains were found close to the machined surface, which decreased with increasing depth from machined surface.

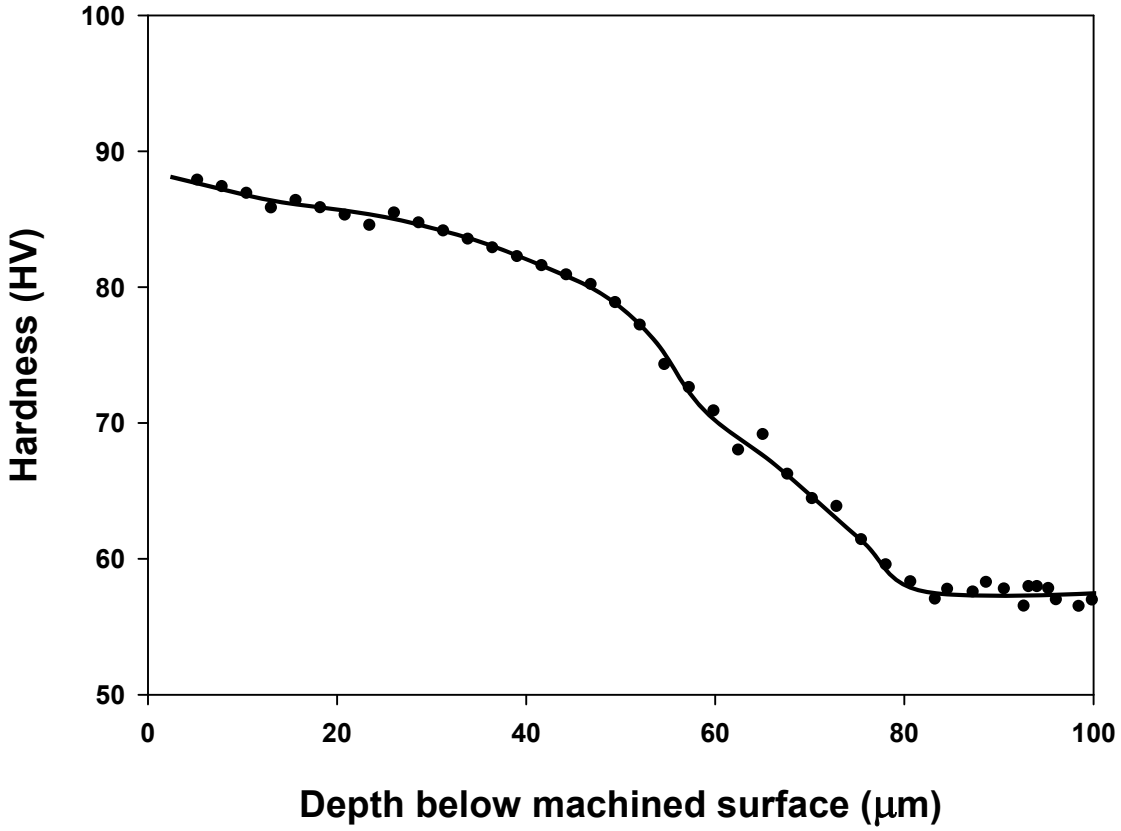

Fig.5.36. Plot showing variation of Vickers hardness of 319 Al with depth below machined surface, estimated along the interface between 6061 Al marker and 319 Al. Load used was 10 grams. Cutting conditions used were cutting speed 50m/min, feed per revolution 0.35mm.

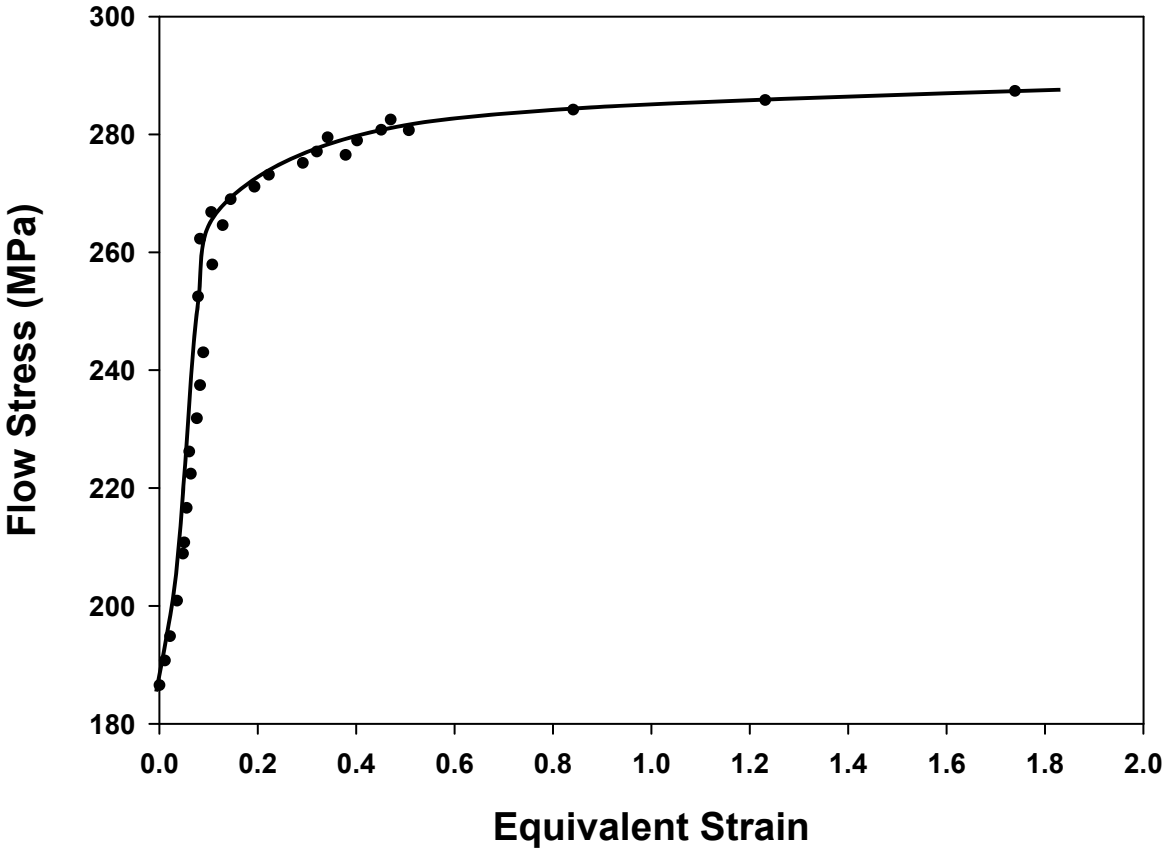

Fig.5.37. Plot showing cumulative stress-strain curve for 319 Al obtained from plastic strains and flow stress estiamtions in the marker specimen (refere to section 4.9 and 5.7). Plot also shows Voce's equation fit for the data. Sample studied was machined under cutting speed of 50m/min and feed per revolution of 0.35mm.

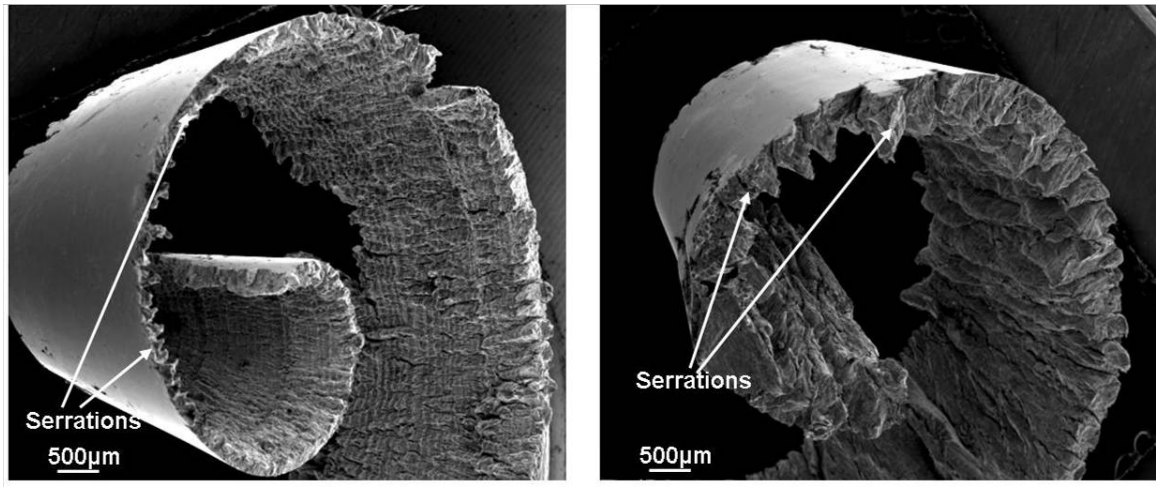

(a) (b)

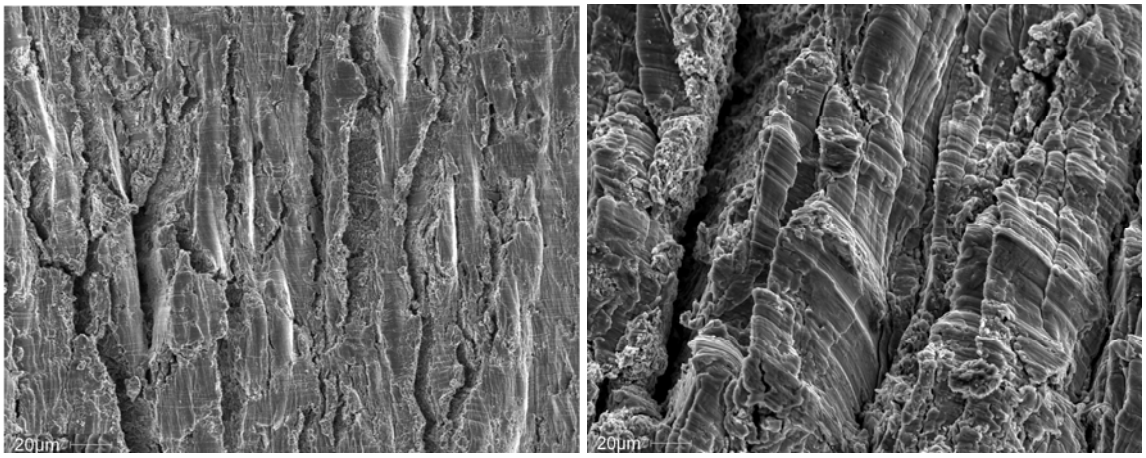

(c) (d)

Fig.5.38. SEM images of chips produced during machining at a constant cutting speed of 75mm/sec with feeds per revolution of (a) 0.25mm, and (b) 0.45mm respectively; free surface of chip produced during (c) 75m/min, 0.25mm, (d) 75m/min, 0.45mm condition. The size and definition of the saw-tooth segments in the chips can be seen to be drastically lager for sample cut under higher feed conditions.

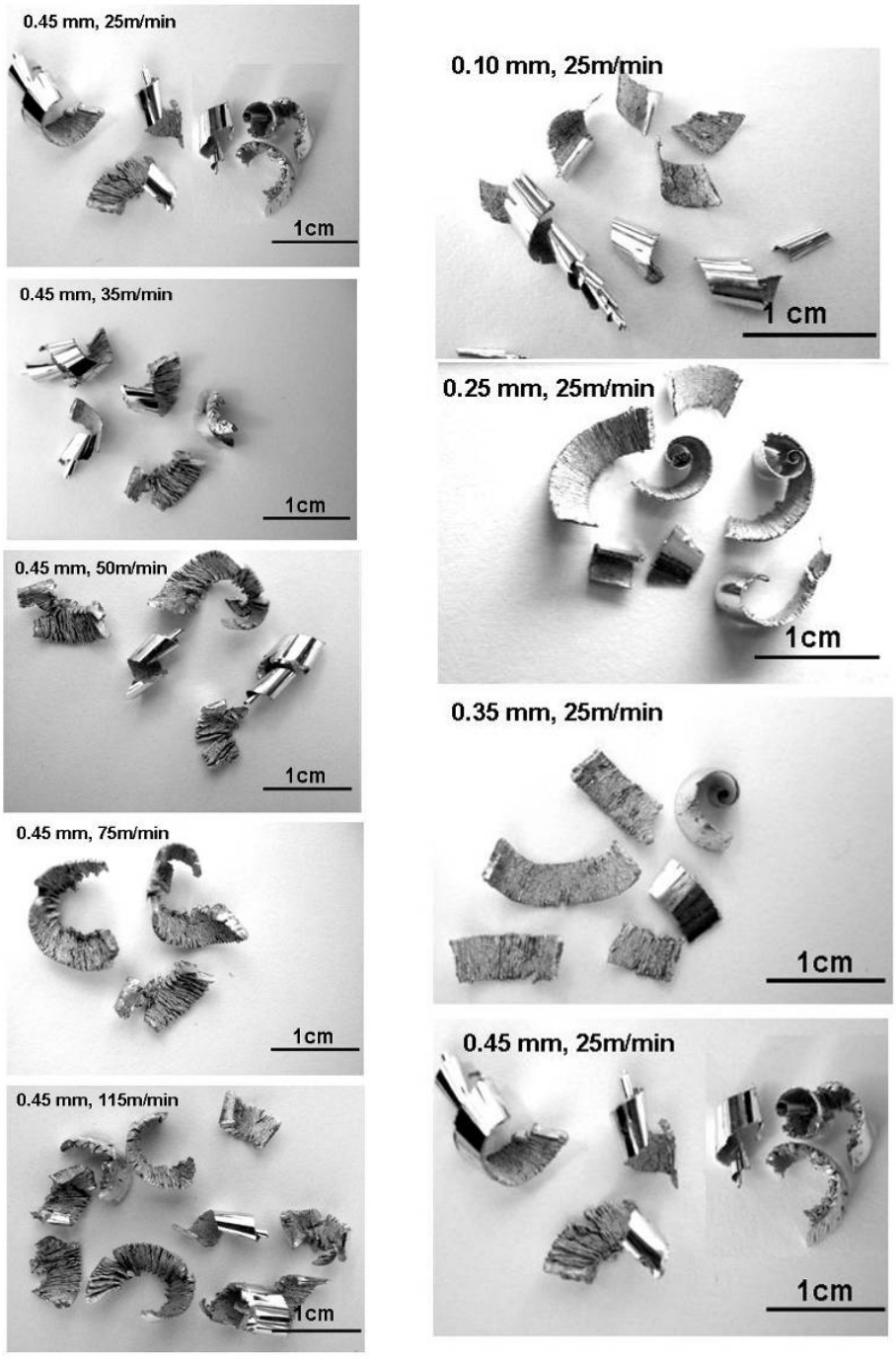

(a) (b)

Fig.5.39. Images of chips produced during orthogonal cutting carried out under conditions of (a) different speeds of cutting with a constant feed rate of 0.45mm, and (b) for different values of feed per revolution with a constant cutting speed of 25m/min respectively. It was seen that the chips become thicker with clearer saw-tooth morphology as the feed rate is increased.

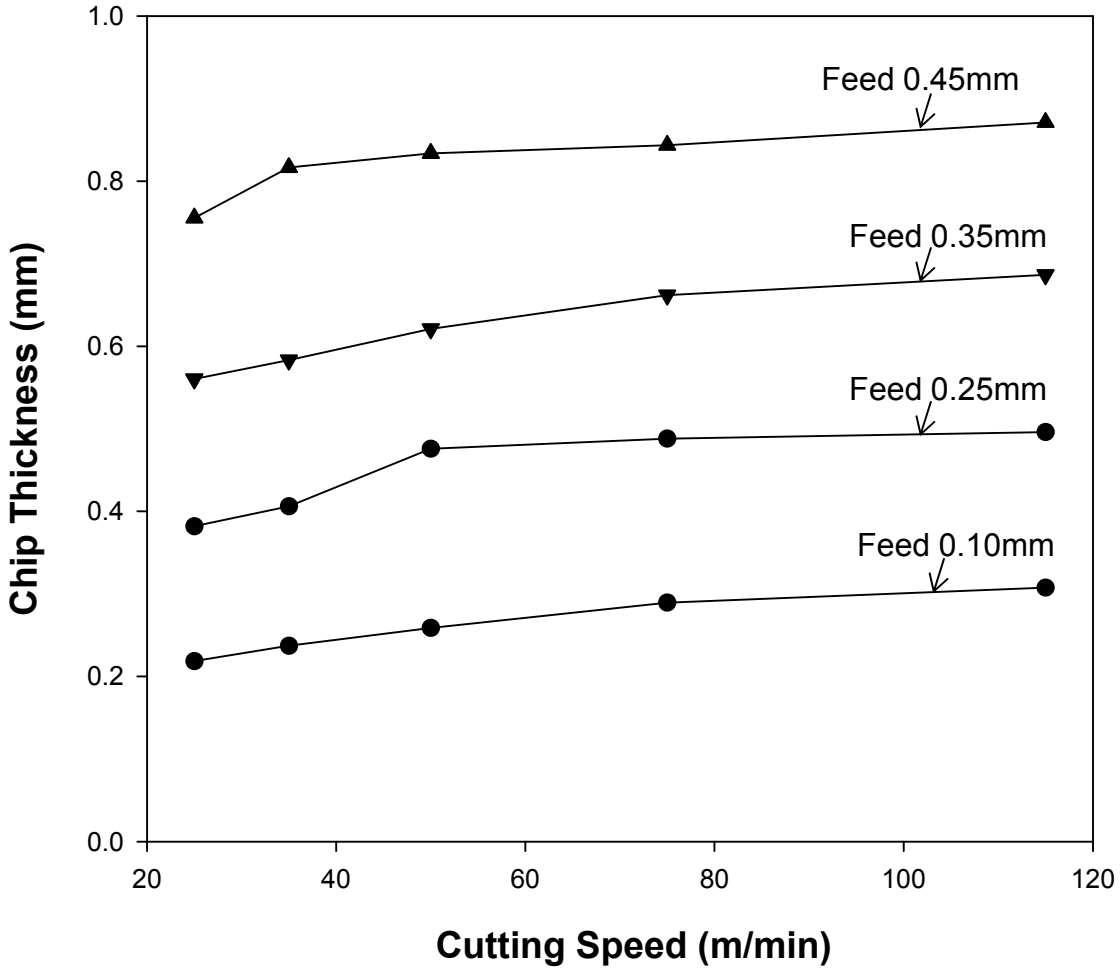

(c)

Fig.5.40. Plot showing variation of chip thickness (measured using optical microscopy studies of mounted and polished samples) with cutting speed for different feed per revolution.

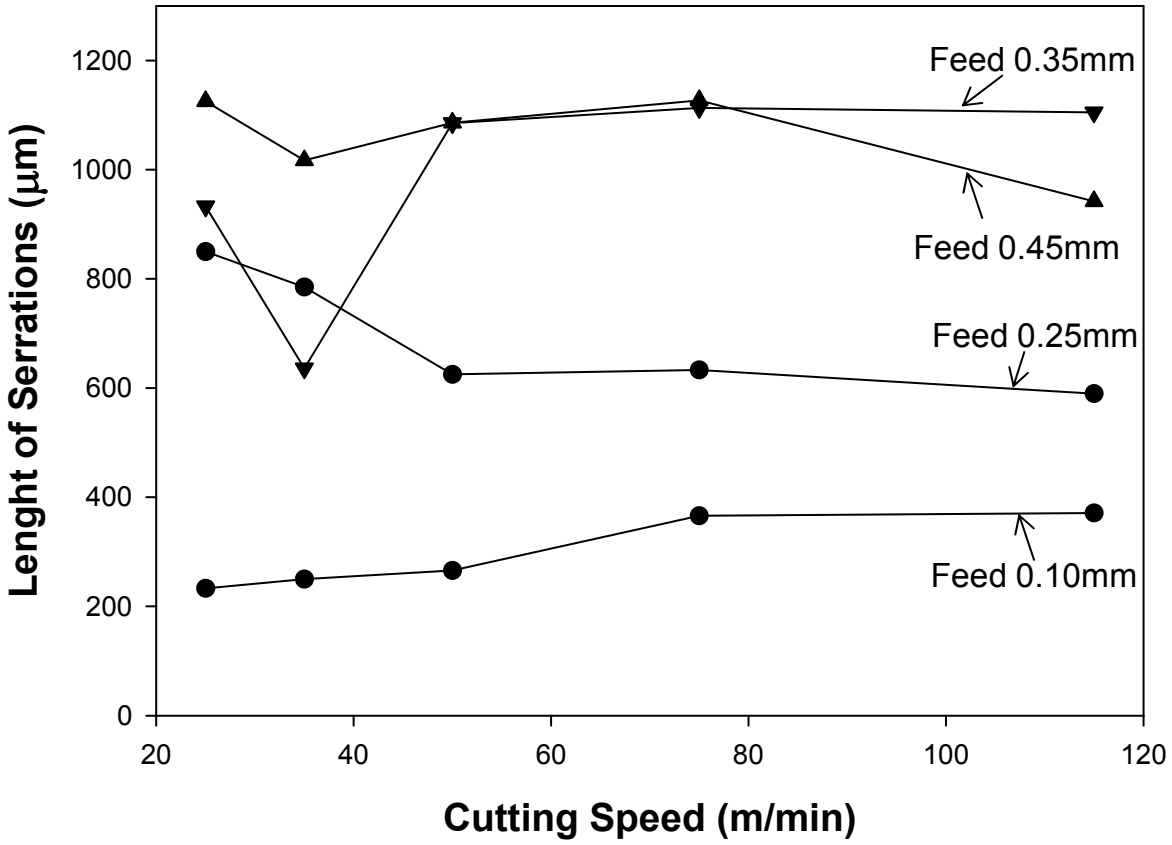

(a)

Fig.5.41 contd.

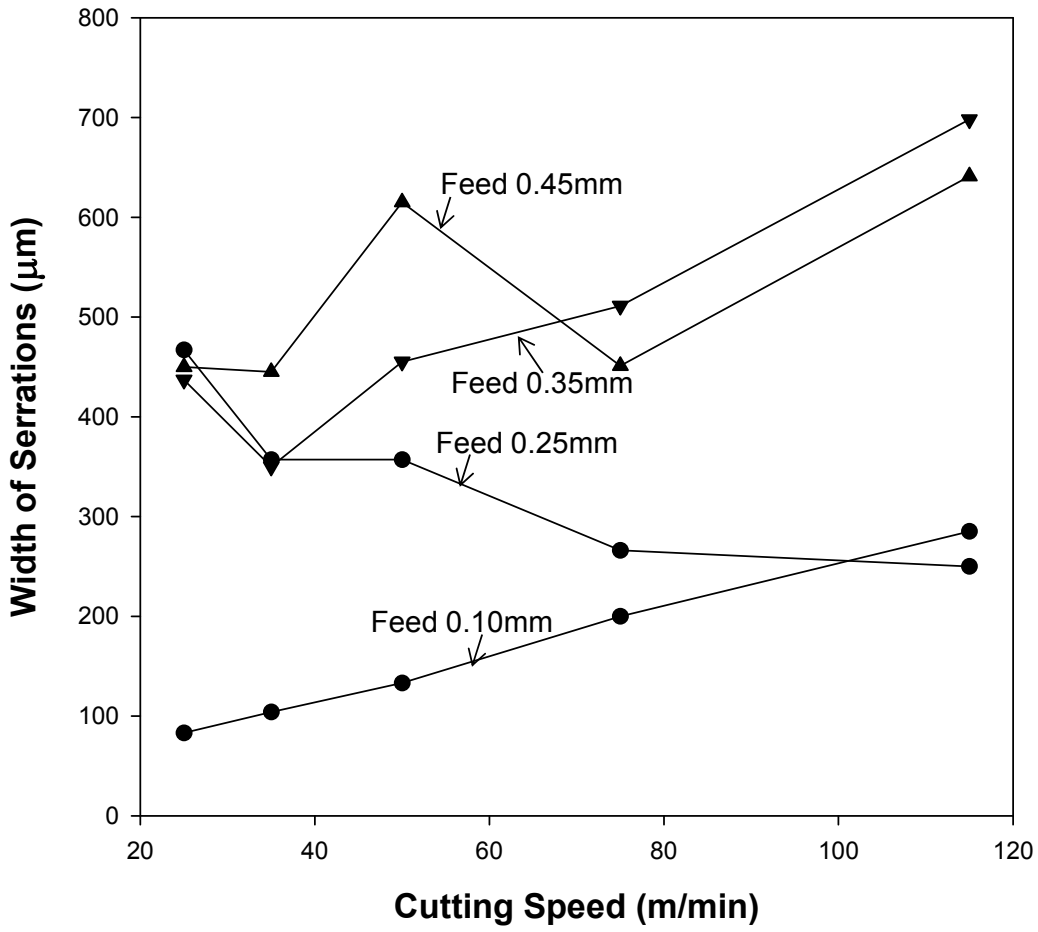

(b)

Fig.5.41. Histograms showing variation of (a) length of serrations, (b) width of serrations, with increase in cutting speed for different feed rates (for 319 Al). The measurements were done for the largest saw-tooth segment obtained under each condition.

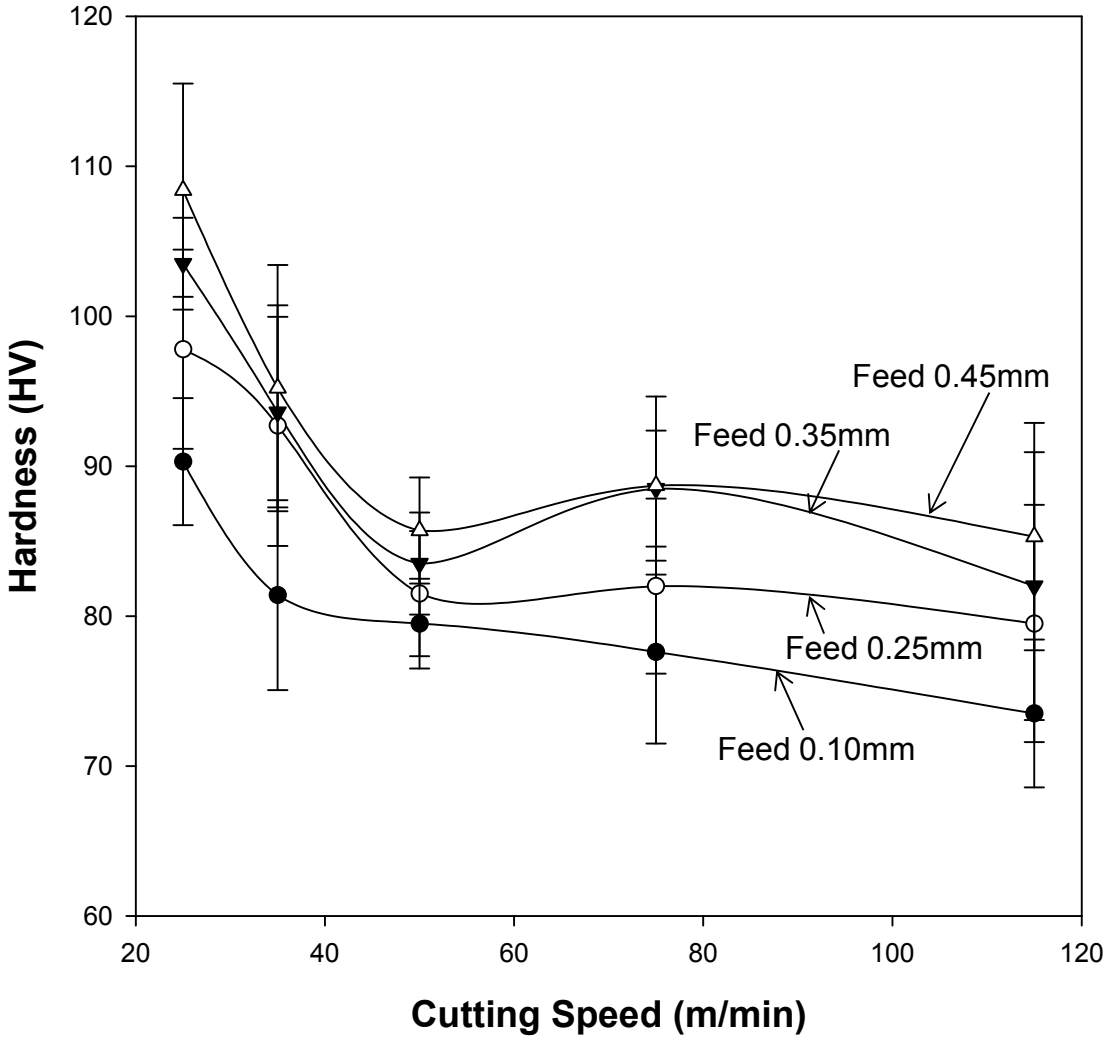

Fig.5.42. Plot showing variation in Vickers hardness values in the chips produced under the different cutting conditions studied. All feed values shown are in units of mm. Loads used for every indentation was 10 grams.

Fig.5.28 contd.

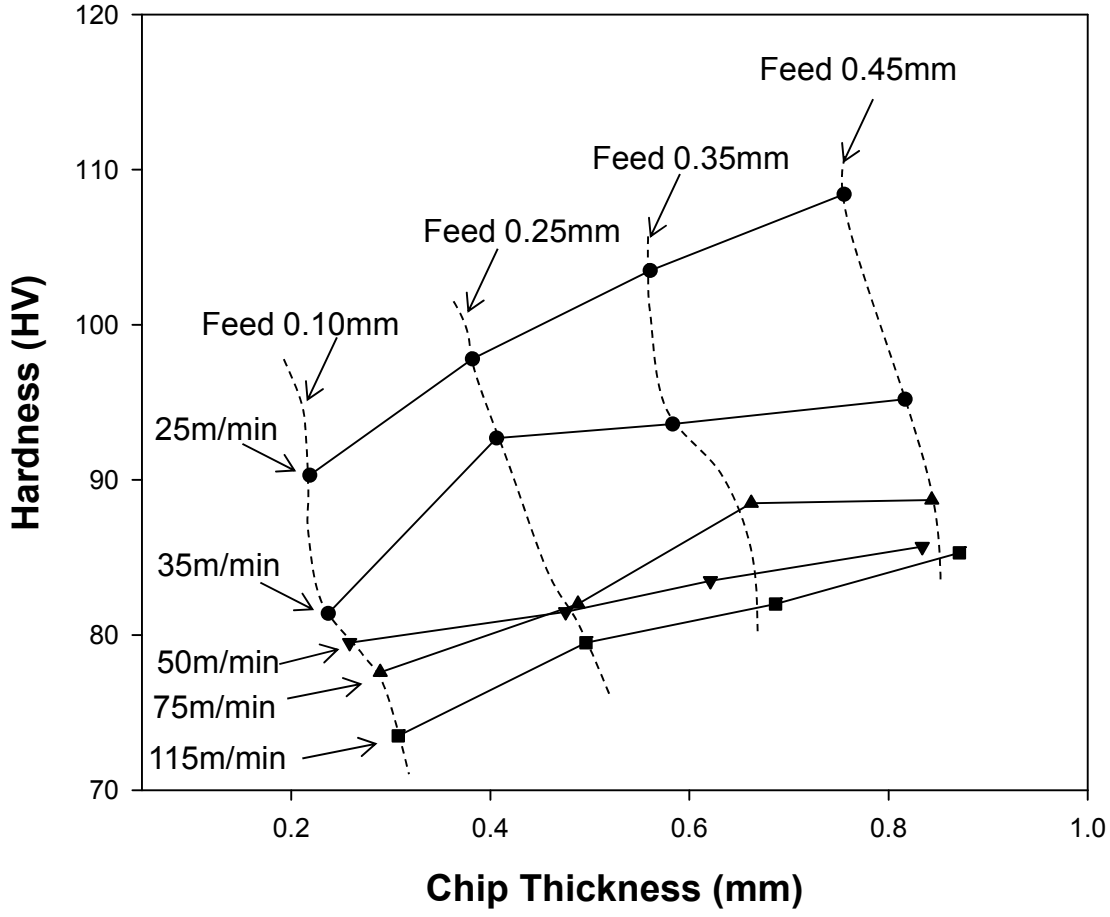

(b)

Fig.5.43. Plot showing variation of chip hardness (HV) as a function of chip thickness (mm). The feed rates considered were 0.10mm, 0.25mm, 0.35mm and 0.45mm. Loads used for every indentation was 10 grams.

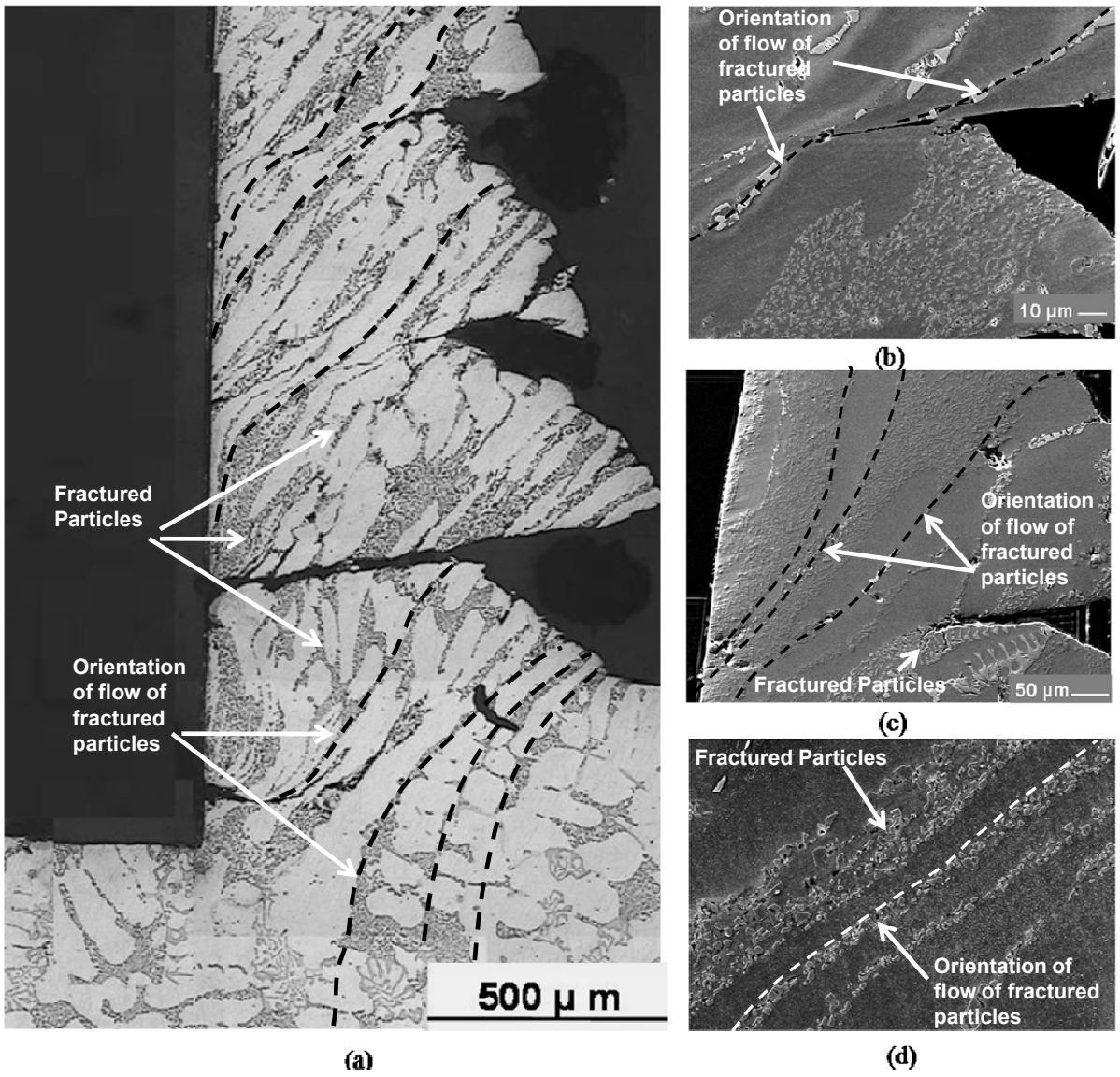

Fig.5.44. (a) Micrographs of Al 319 samples orthogonally machined under cutting conditions of cutting speed of 25m/min, 0.35mm; micrographs of different areas of chips obtained while machining under (b) cutting speed of 75m/min, 0.25mm, (c) cutting speed of 50m/min, 0.35mm, and (d) cutting speed of 35m/min, 0.45mm, showing orientation of alignment of fractured particle in the chip region (shown by dotted lines).

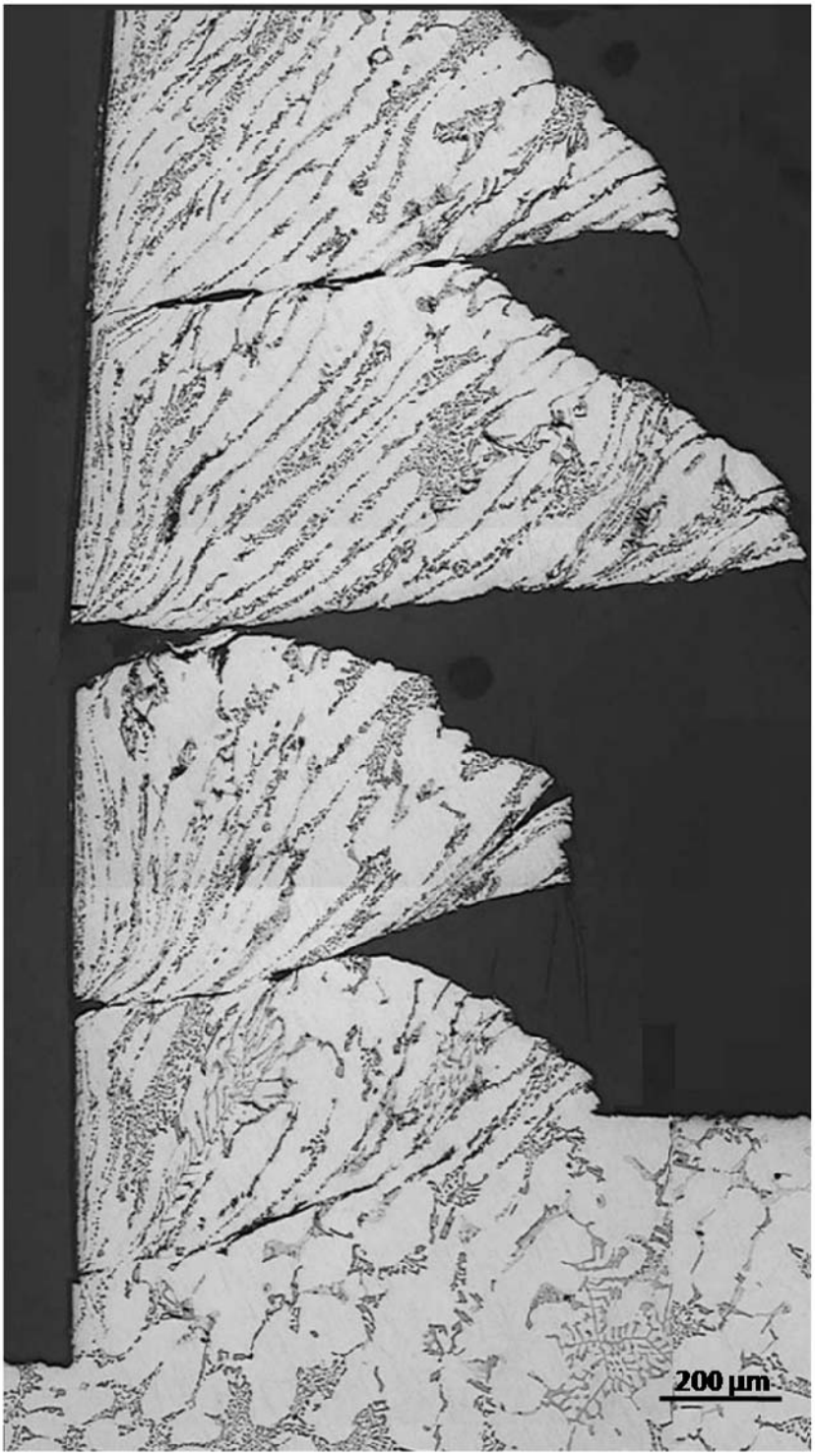

(a)

Fig.5.45 contd.

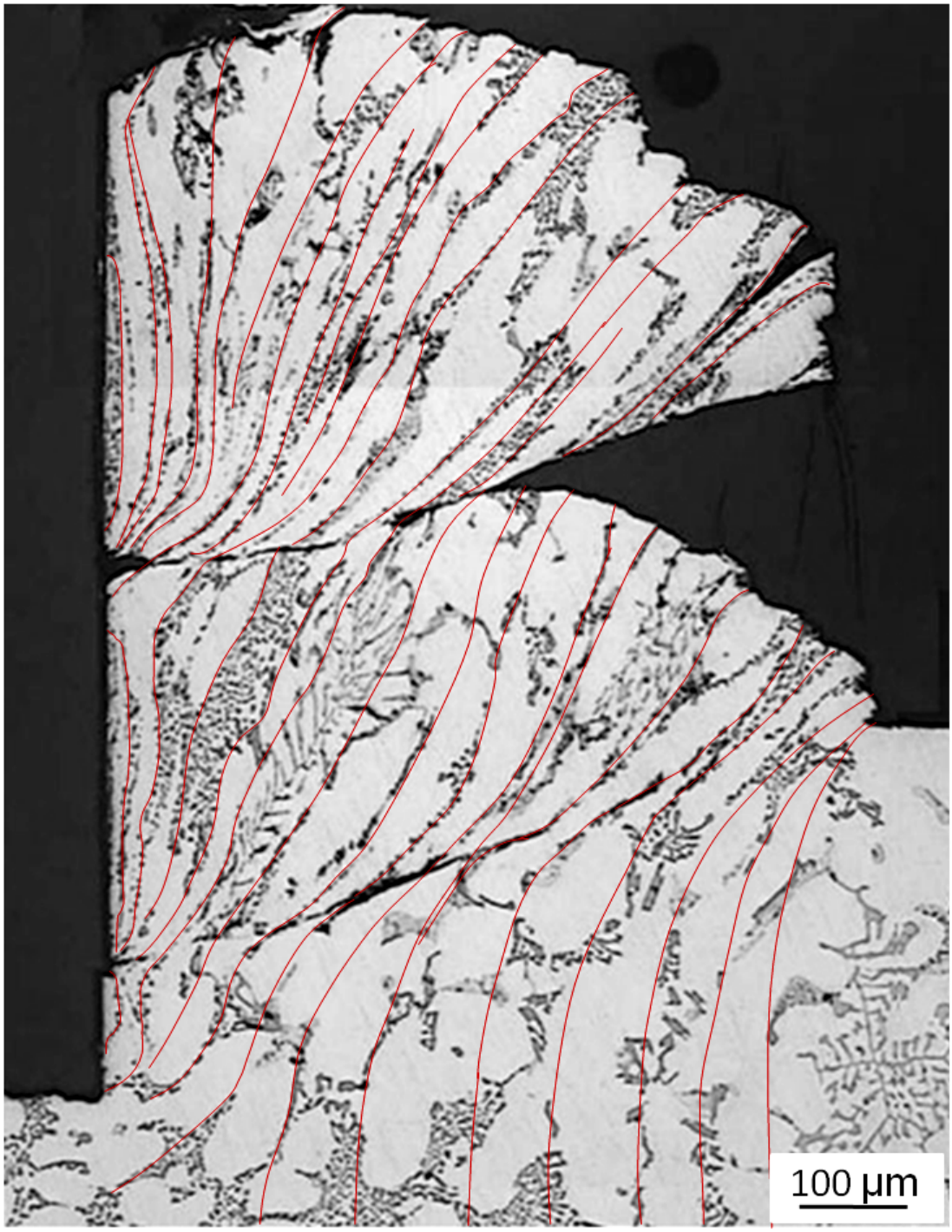

(b)

Fig.5.45. Optical microstructure of cross-section of sample machined under cutting speed of 50m/min and feed per revolution of 0.35mm, showing distinct flowline-like patterns, (b) some of the lines traced out along these patters in order to facilitate the estimation of strains in the workpiece.

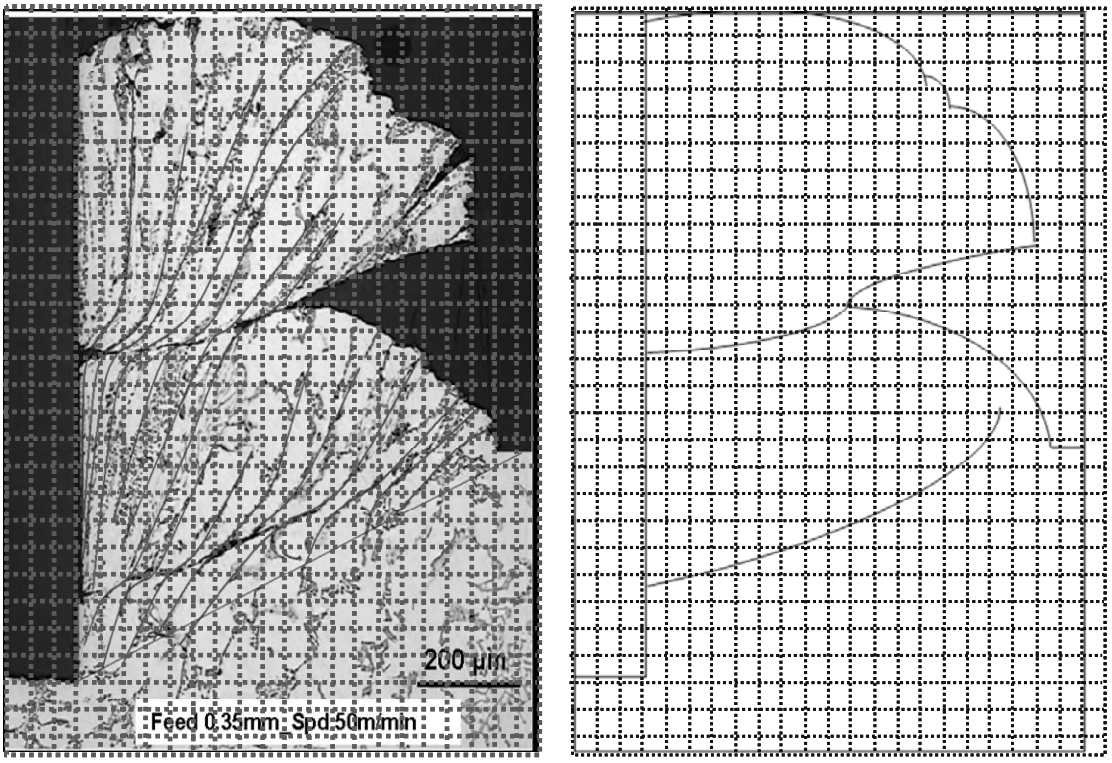

(a) (b)

Fig.5.46. Steps followed for estimating the plastic strains in the sample: (a) flowlines were traced out on the cross-sectional optical-micrograph of the sample following orientation of fractured particle flow, (b) strains were estimated at the points of intersection of a 50µm by 50µm grid placed over the micro-graph, using the value of shear angle at each location.

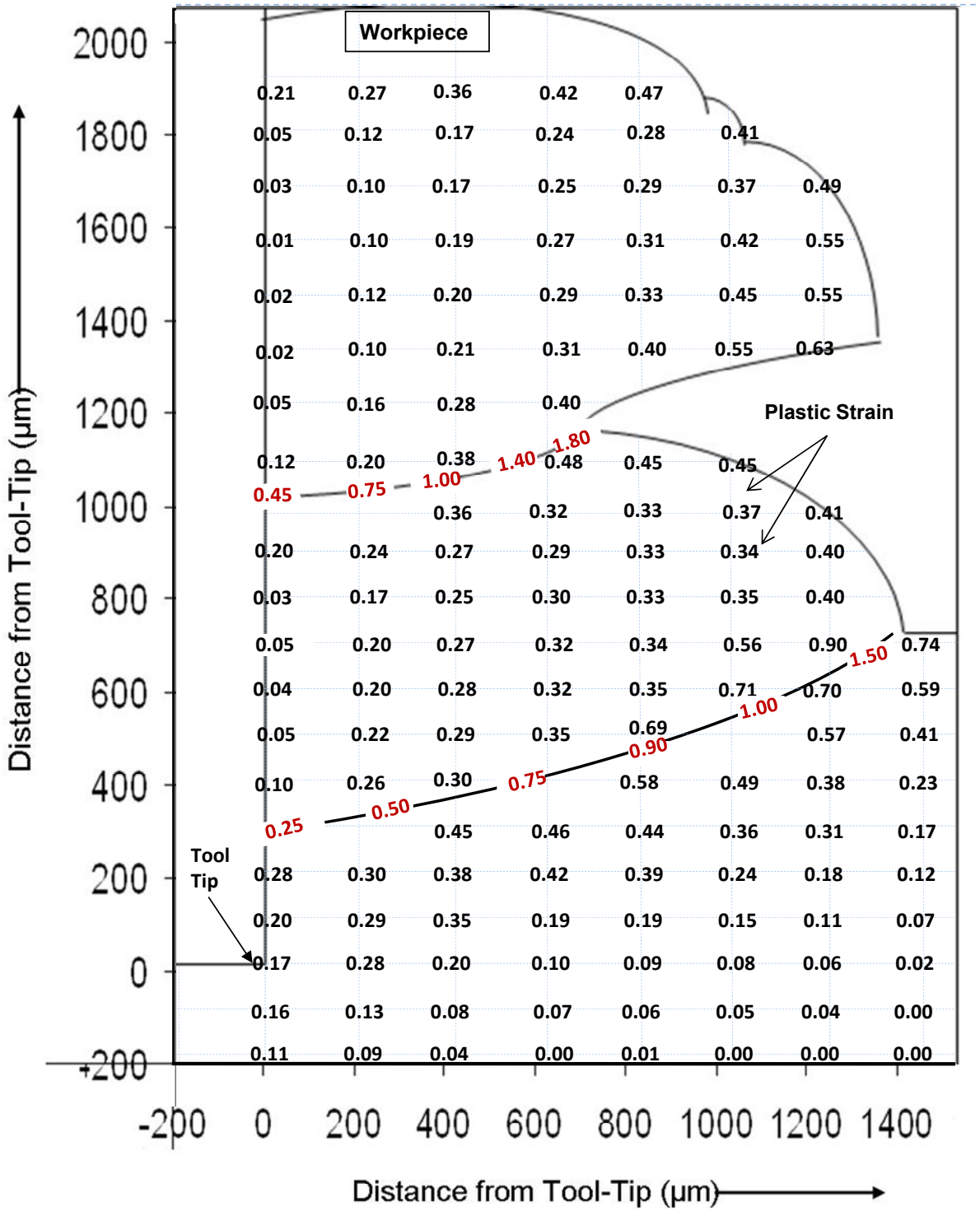

(a)

Fig.5.47 contd.

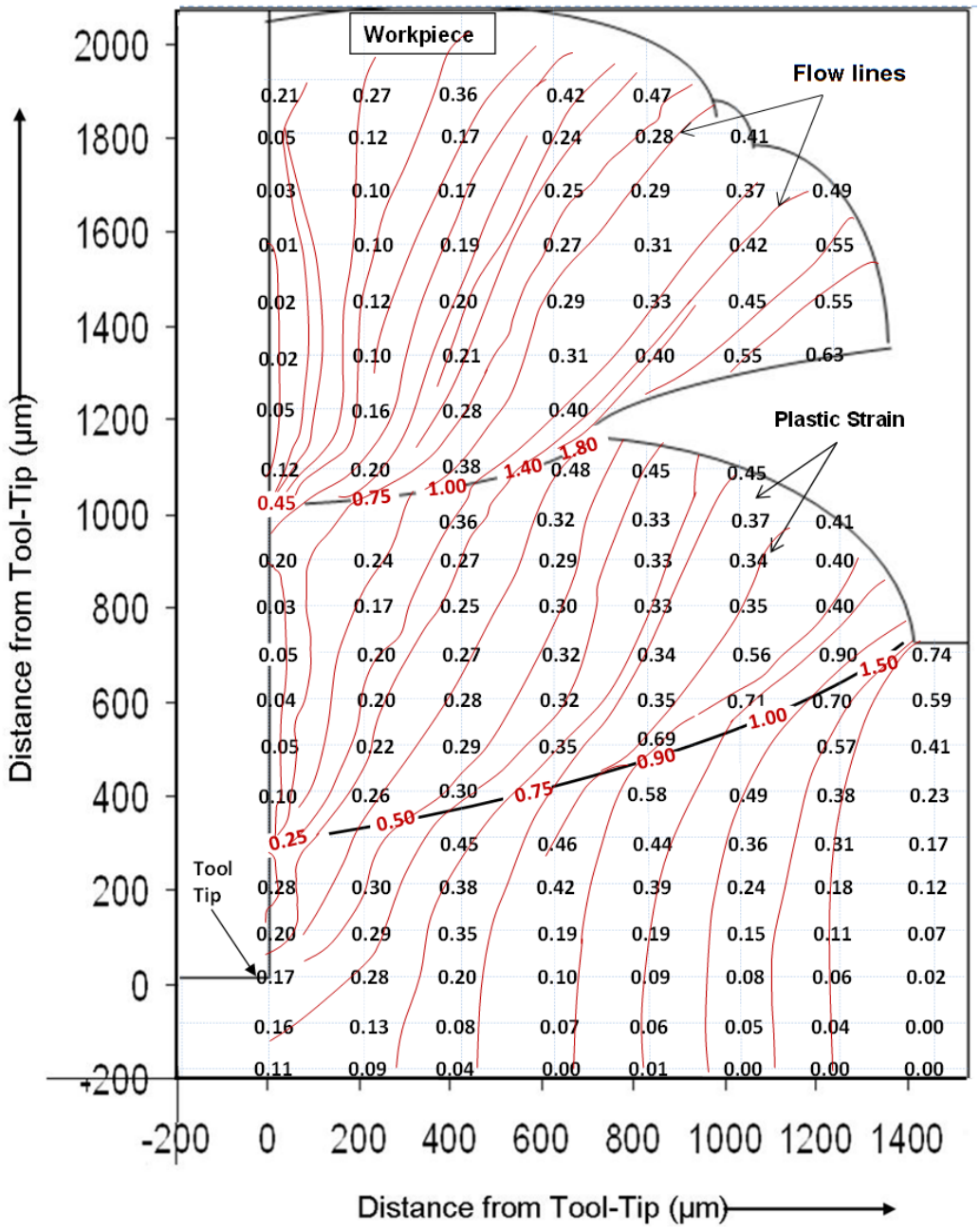

(b)

Fig.5.47. Plastic strain distribution diagram showing (a) strains measured at the points of intersection of a 200X100 imaginary gird in the material ahead of tool tip and in the chip; (b) strains at different locations with flow-lines used for strain estimation. Equivalent strains were estimated using the value of shear angle at each location. Machining conditions were cutting speed of 50m/min and feed per revolution of 0.35mm.

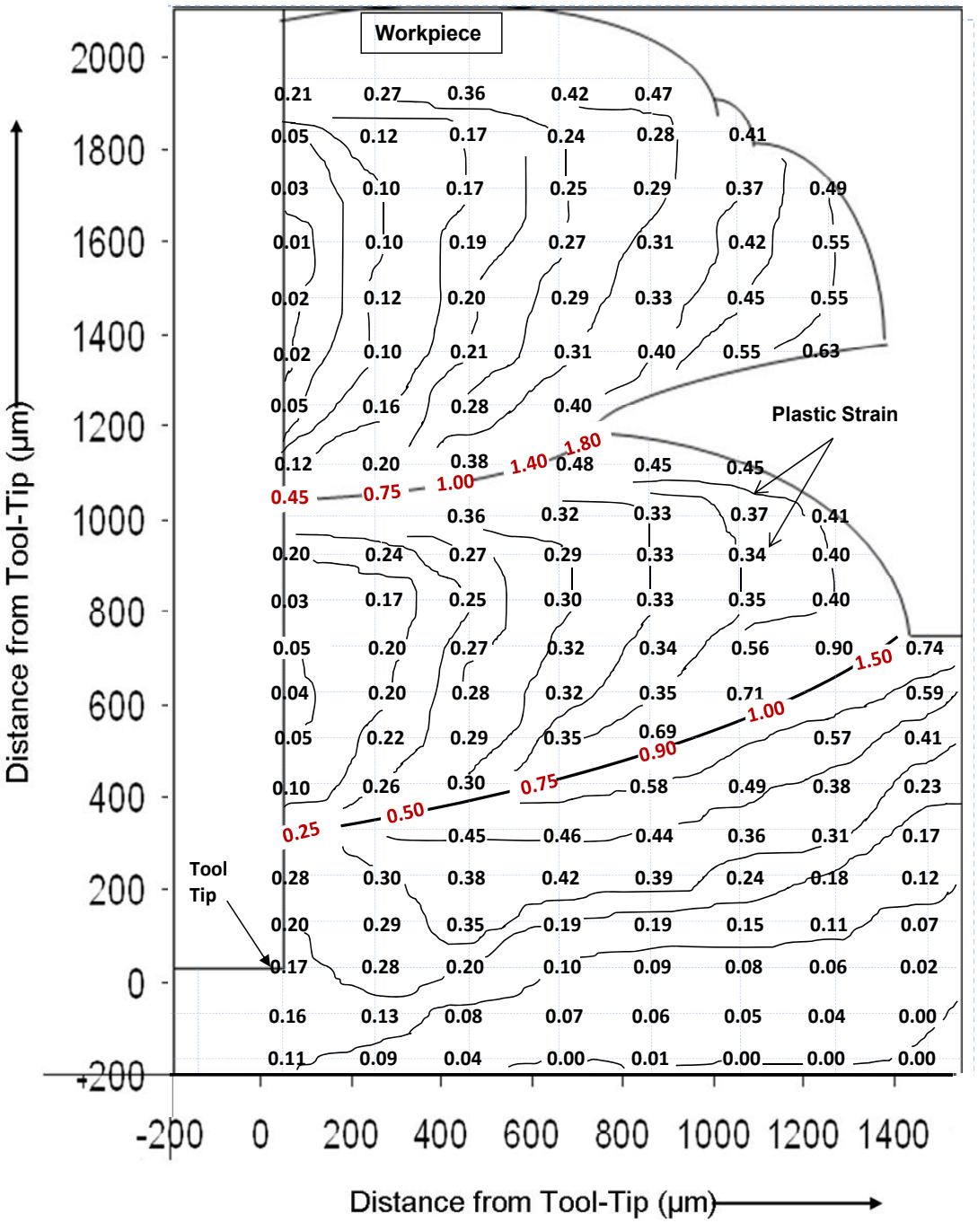

(c)

Fig.5.48. Plastic strain distribution diagram showing iso-strain contours connecting regions having the same values of plastic strains. Equivalent strains were estimated using the value of shear angle at each location. Machining conditions were cutting speed of 50m/min and feed per revolution of 0.35mm.

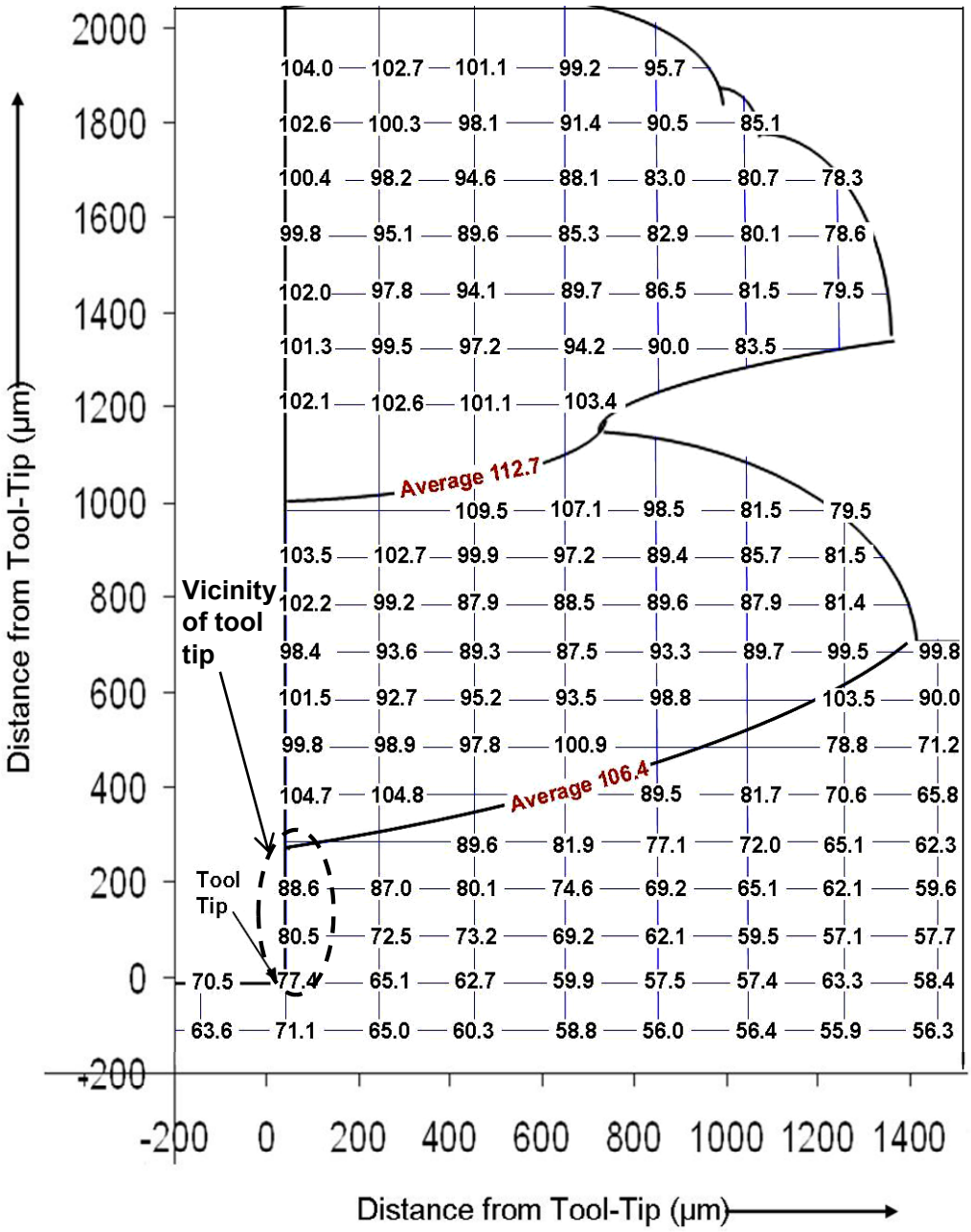

Fig.5.49. Diagram showing the variation in hardness values in the material ahead of the tool tip and in the chip region for sample machined under cutting speed of 50m/min and feed per revolution of 0.35mm. Average hardness value of three indentations, taken on the aluminum matrix, at or around the points of intersection of an imaginary grid of 100µmX75µm, has been used for the diagram. Load used was 10 grams.

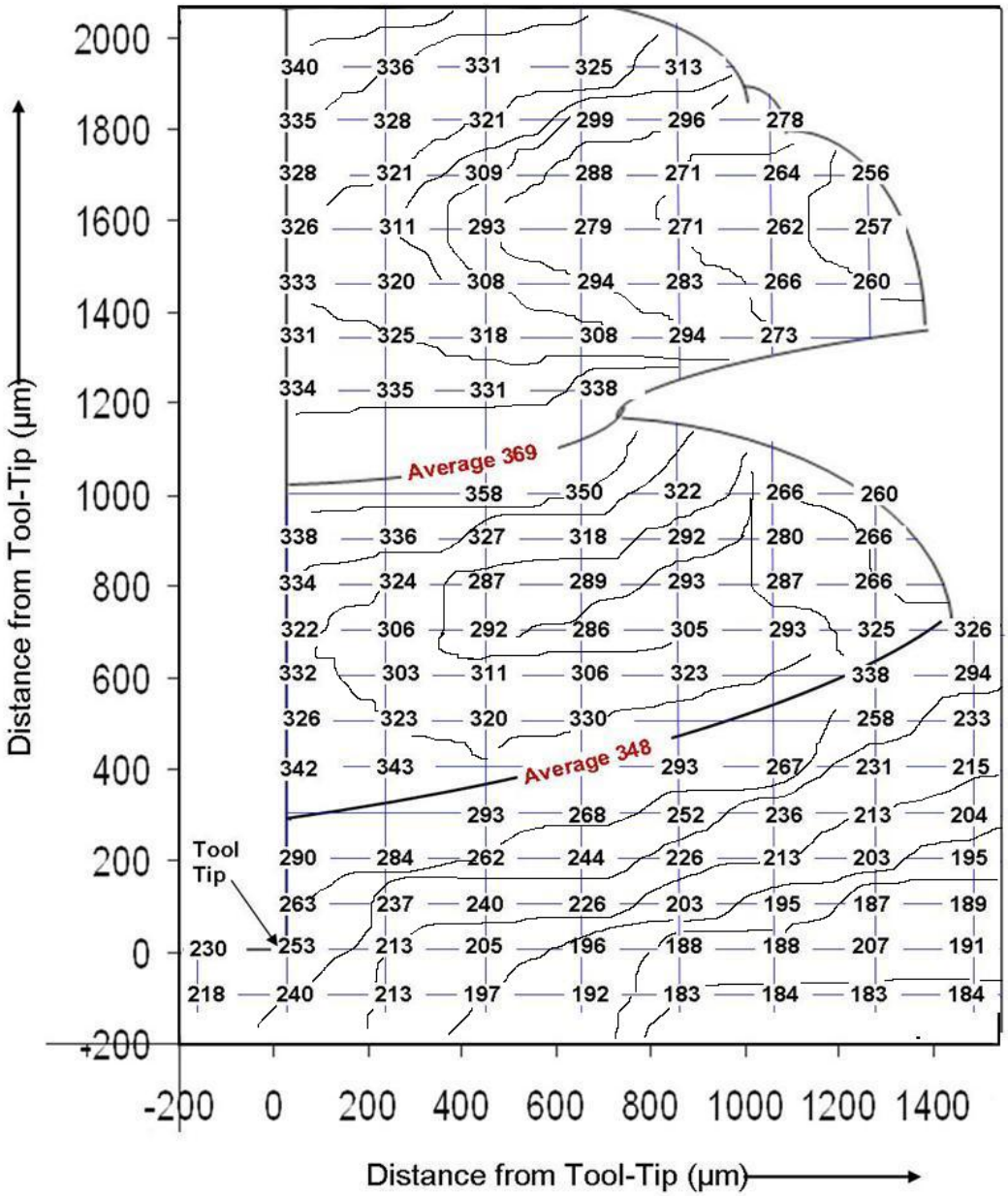

Fig.5.50. Stress distribution diagram showing variation of flow stress (MPa) in the material ahead of the tool tip and in the chip region for sample machined under cutting speed of 50m/min and feed per revolution of 0.35mm. Iso-stress contours have also been shown. Vickers hardness values wee used for estimation of flow stress values.

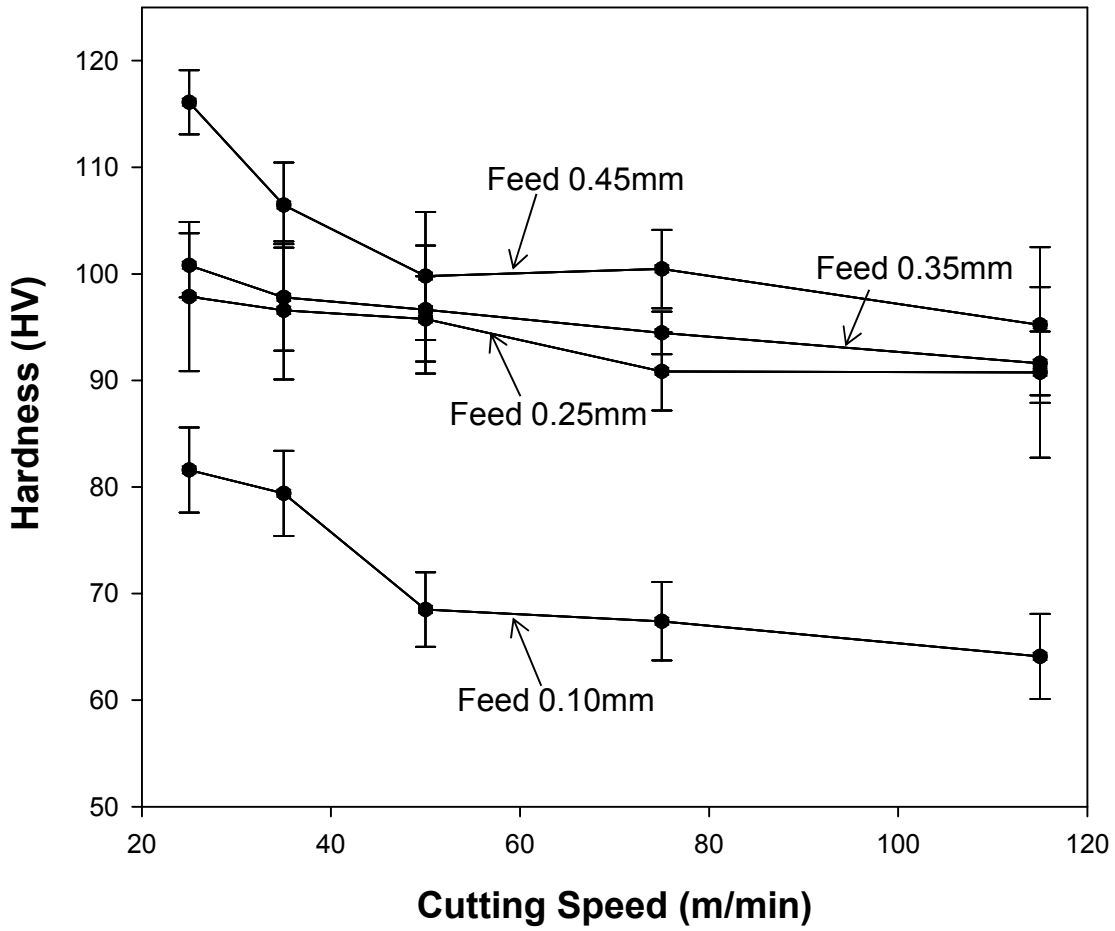

Fig.5.51. Plot showing variation in average hardness values (HV) with cutting speed for chip region in close proximity to tool-tip location (refer to Fig.5.49). Load used was 10 grams. It was seen that hardness values show a tendency to fall in magnitude with an increase in cutting speed and with a decrease in feed per revolution.

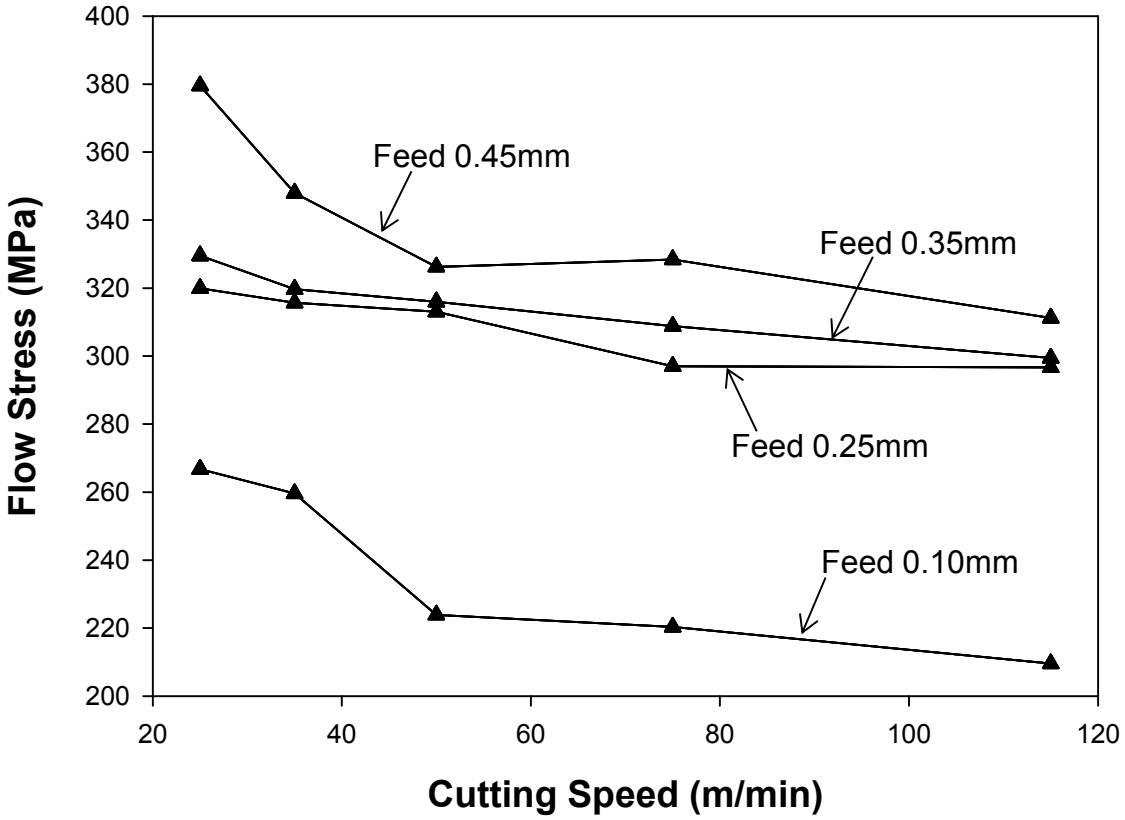

Fig.5.52. Plot showing variation in flow stress values (MPa) with cutting speed for chip region in close proximity to tool-tip location. Vickers hardness values were used for stress estimation. Flow stress values show a tendency to fall in magnitude with an increase in cutting speed and with a decrease in feed per revolution.

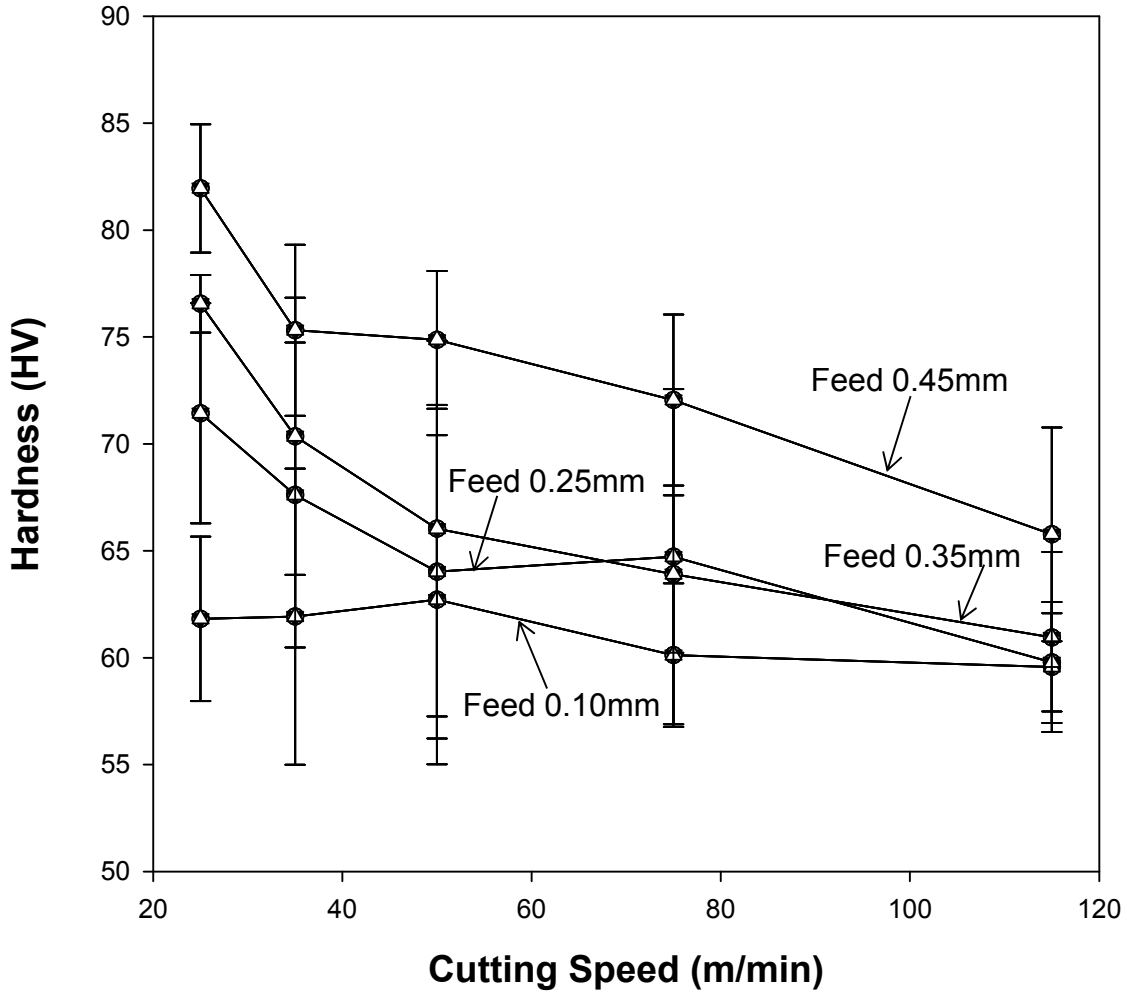

Fig.5.53. Plot showing variation in average hardness values (HV) with cutting speed for region beneath the machined surface (average of 10 indentations placed at approximately 60μm below the machined surface). Load used was 10 grams. It was seen that hardness values show a tendency to fall in magnitude with an increase in cutting speed and with a decrease in feed per revolution.

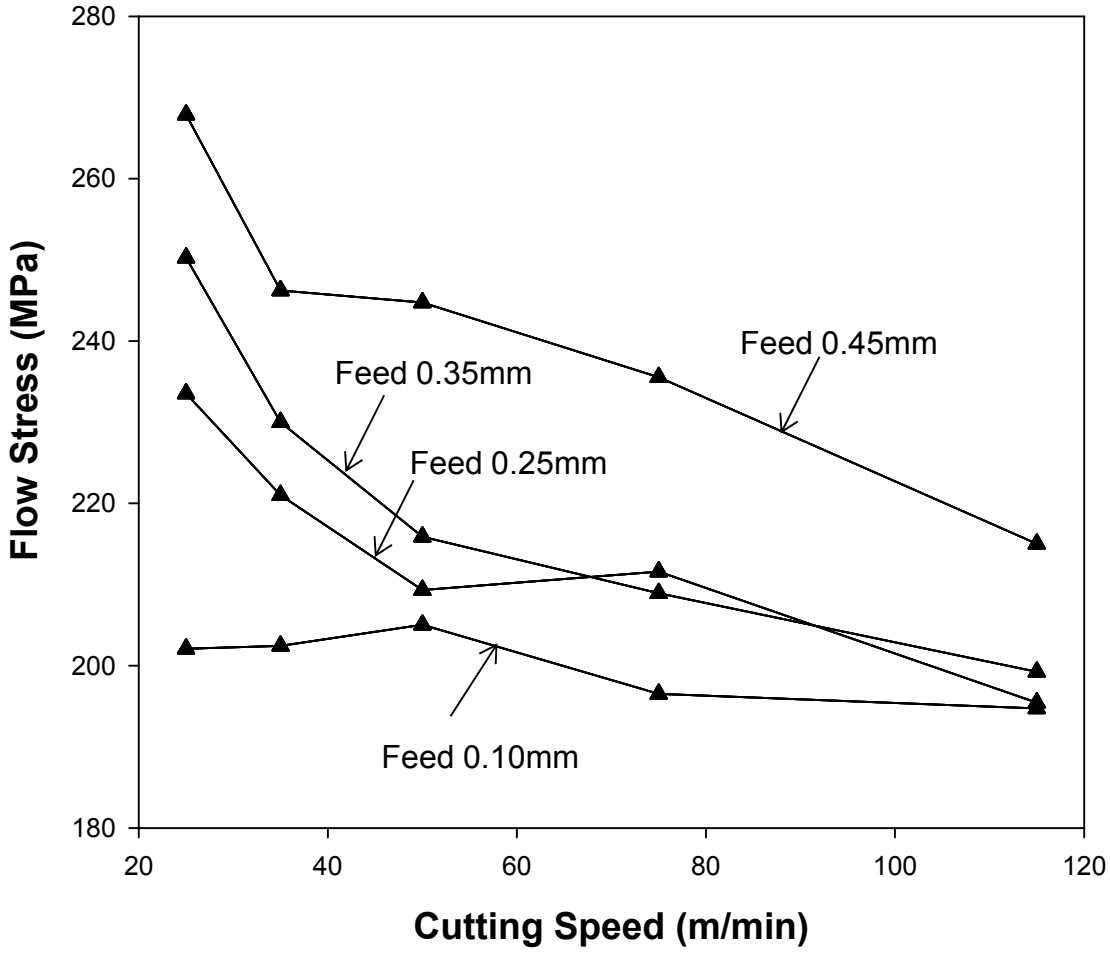

Fig.5.54. Plot showing variation in flow stress values (MPa) with cutting speed for region beneath the machined surface (average of 10 indentations placed at approximately 60μm below the machined surface). Vickers hardness values were used for stress estimation. Flow stress values show a tendency to fall in magnitude with an increase in cutting speed and with a decrease in feed per revolution.

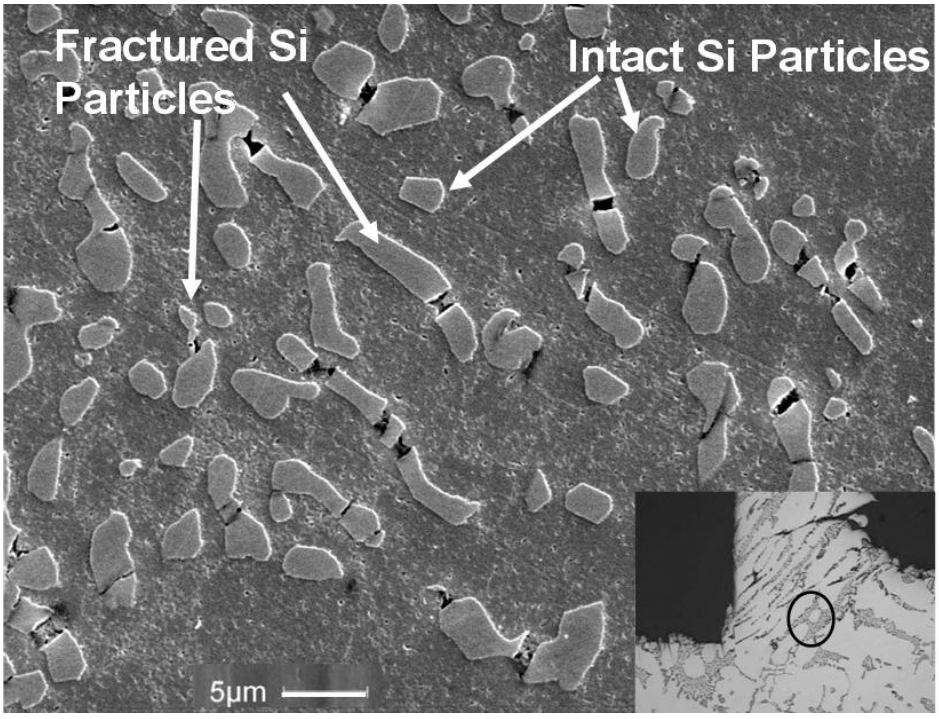

(a)

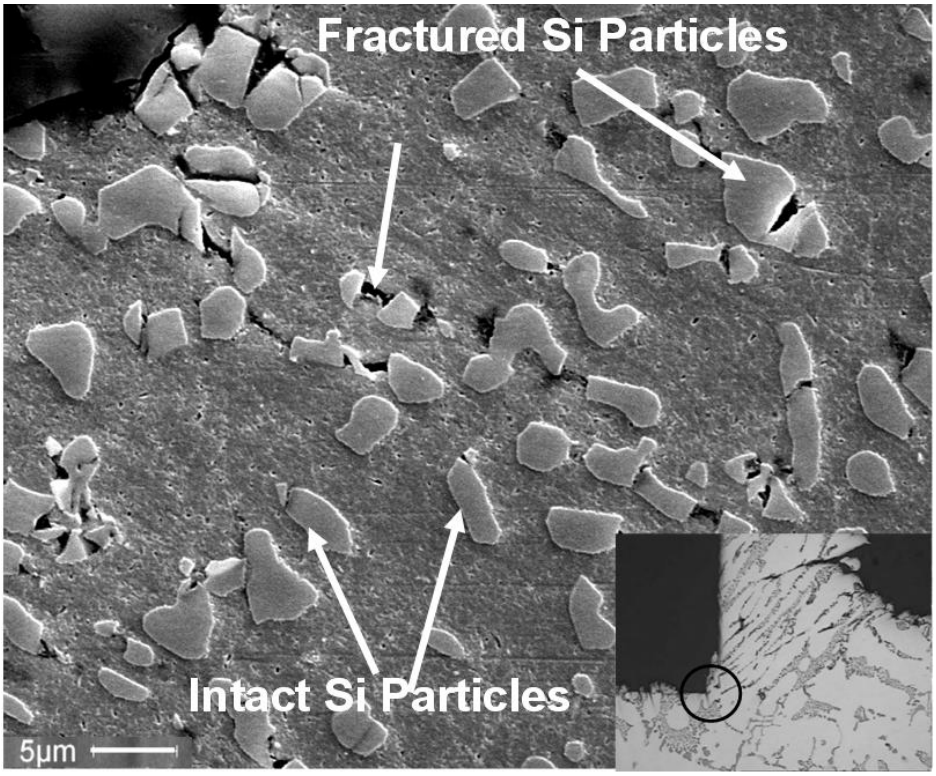

(b)

Fig.5.55 contd.

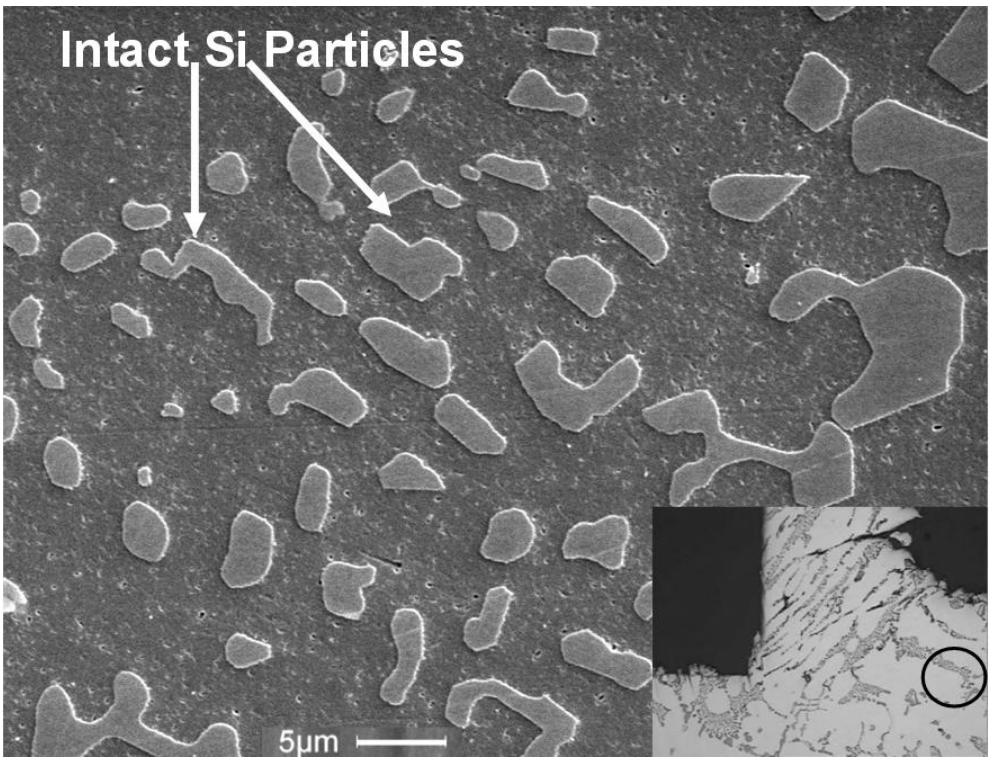

(c)

Fig.5.55. SEM images showing silicon particle fracture (a) near the tool tip location in the Primary Deformation Zone, (b) at a point on the shear plane, away from tool-tip location, and (c) in the undeformed bulk material in the alloy A 319. Small inserts in the micrographs show the locations of the micrograph on the machined section.

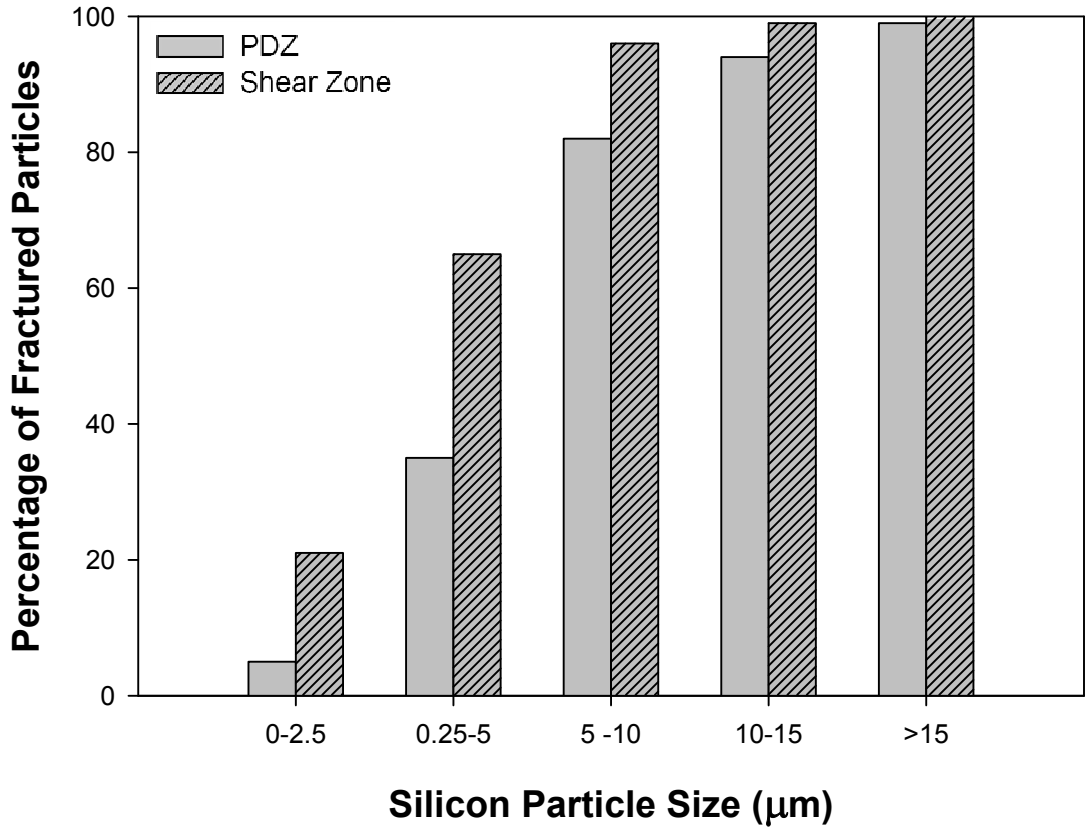

Fig.5.56. Comparison of percentage of silicon particles fractured in Primary Deformation Zone and Shear Zone as a function of particle size. Plastic strains were equal to 0.2 for the zone falling under PDZ and 0.45 for region in Shear zone.

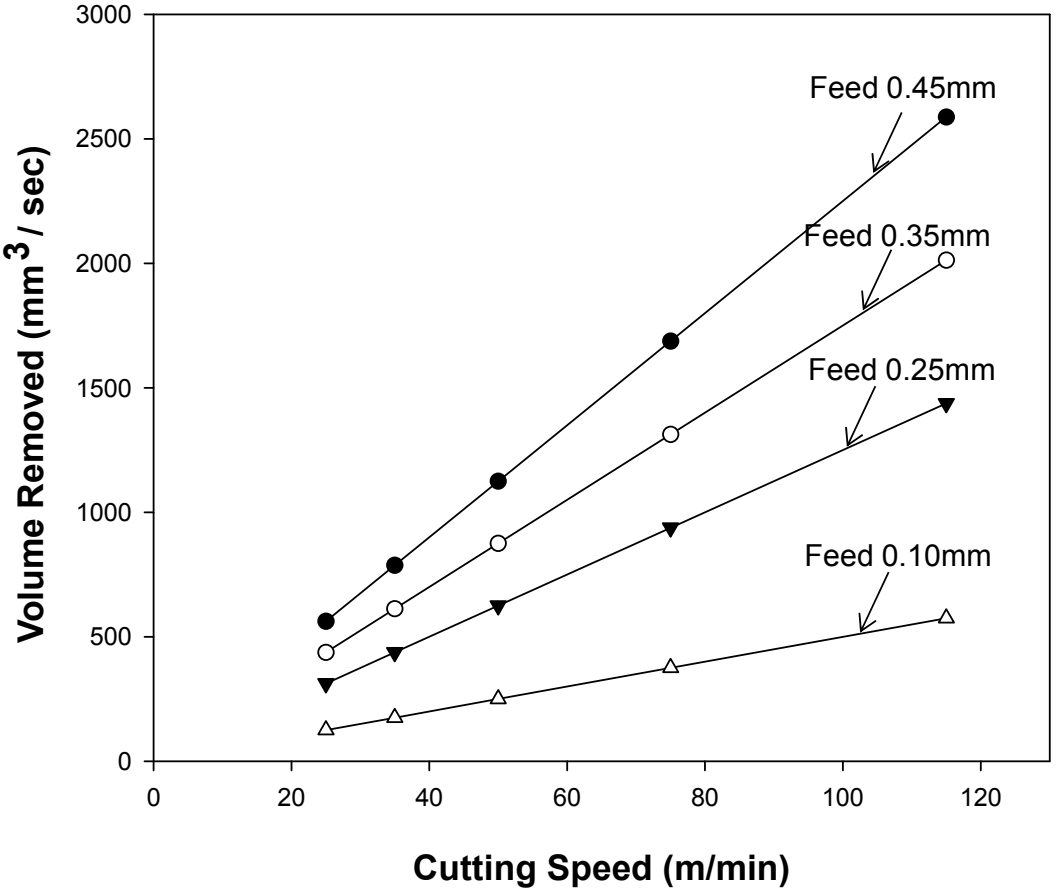

Fig.5.57. Plot showing the volume of material removed during orthogonal cutting under different cutting speed and feed conditions studied for the tube shaped sample with outer radius of 1.5cm and wall thickness of 0.3cm used for the study.

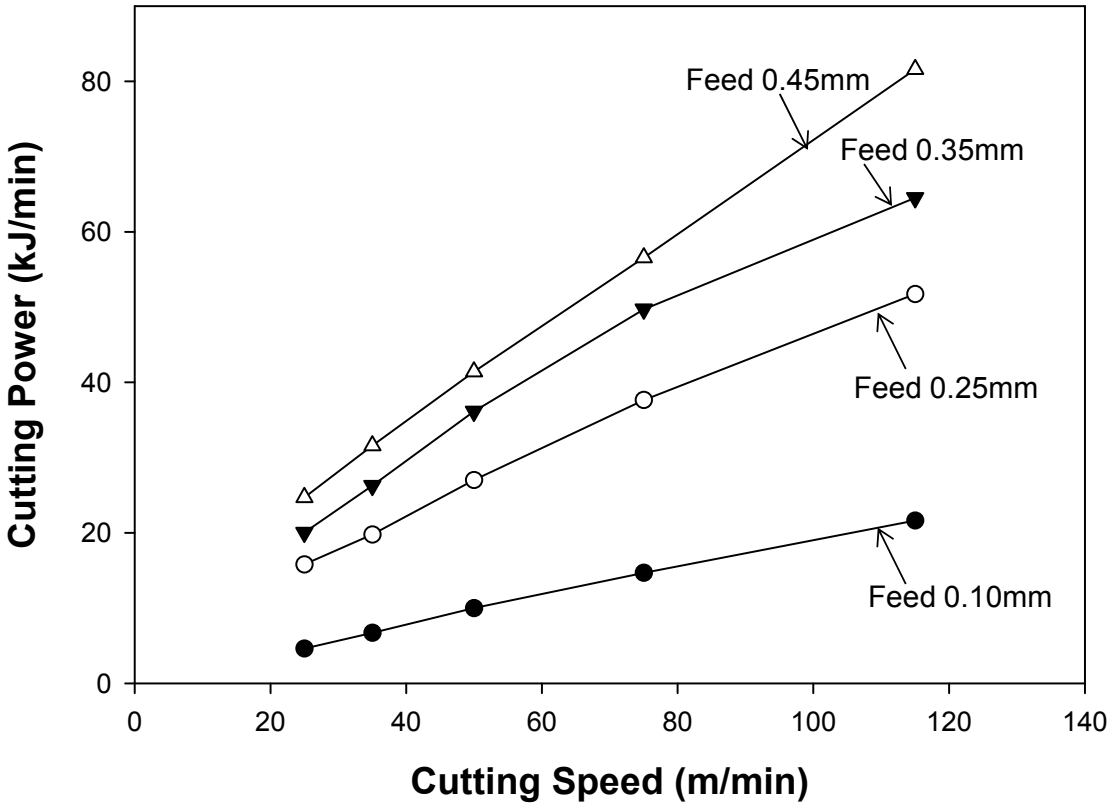

Fig.5.58. Plot showing variation of cutting power (power expended by cutting force) during machining with change in cutting speed for different feed per revolution.

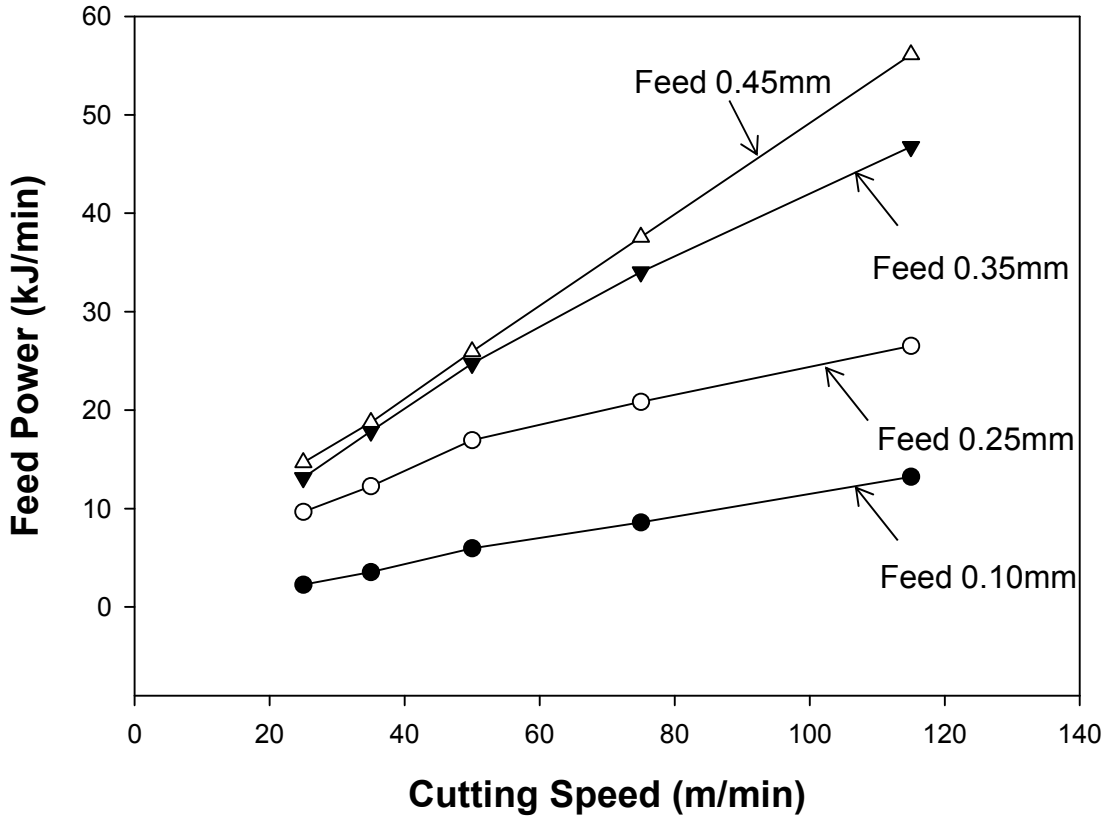

Fig.5.59. Plot showing variation of feed power (power expended by thrust force) during machining with change in cutting speed for different feed per revolution.

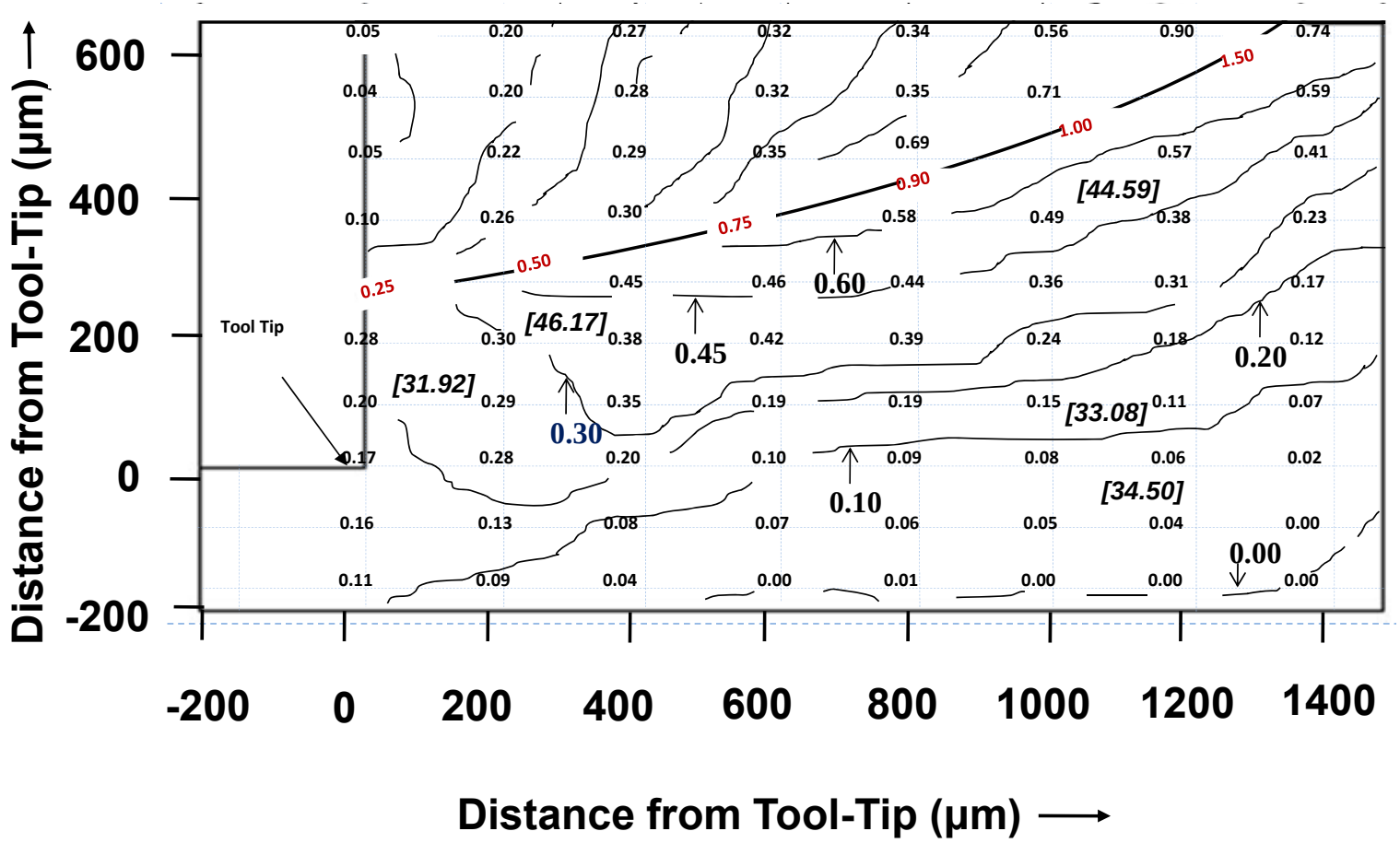

Fig.5.60. Diagram showing distribution of plastic strains at the intersection of an imaginary grid of 200µmX100µm, iso-strain contours (strains along iso-strain lines shown by arrows), and plastic work between iso-strain contours (shown in square brackets) in the material (319 Al) ahead of tool-tip. Machining conditions for sample studied were cutting speed of 50m/min and feed per revolution of 0.35mm.

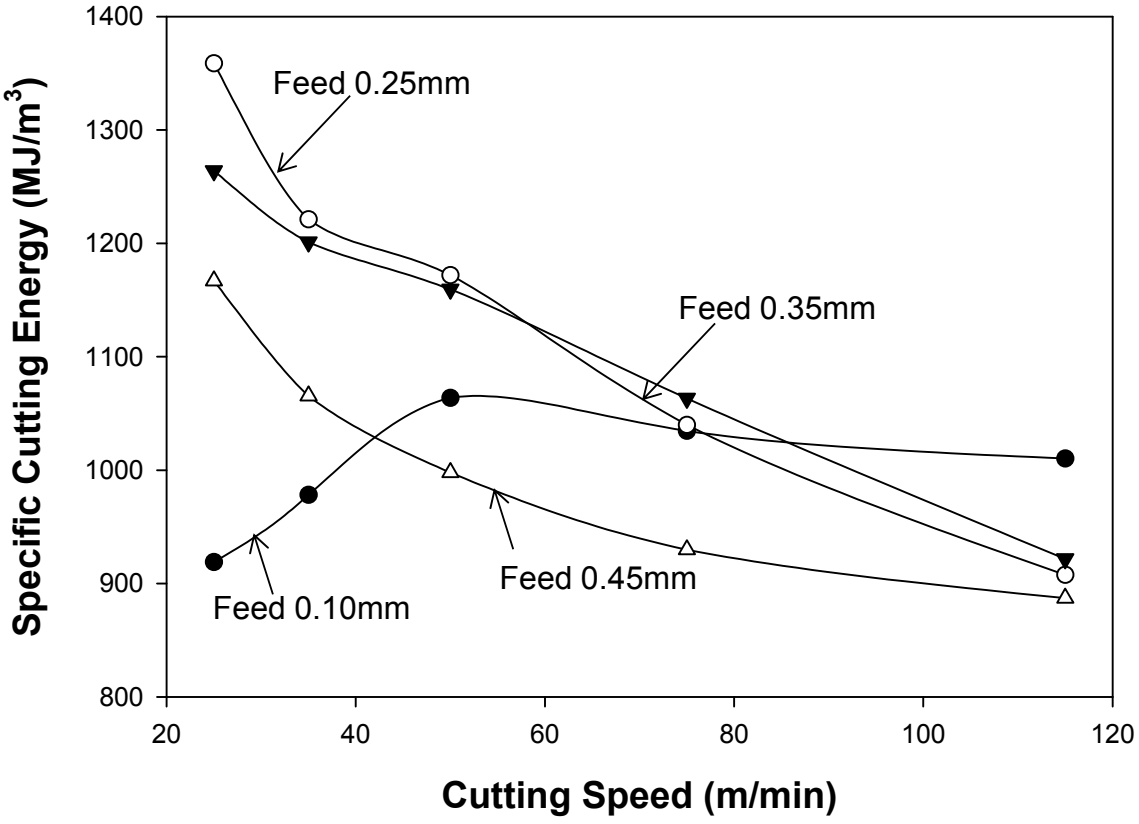

Fig.5.61 Plot showing variation of specific cutting energy for cutting as a function of cutting speed for different feed rates.

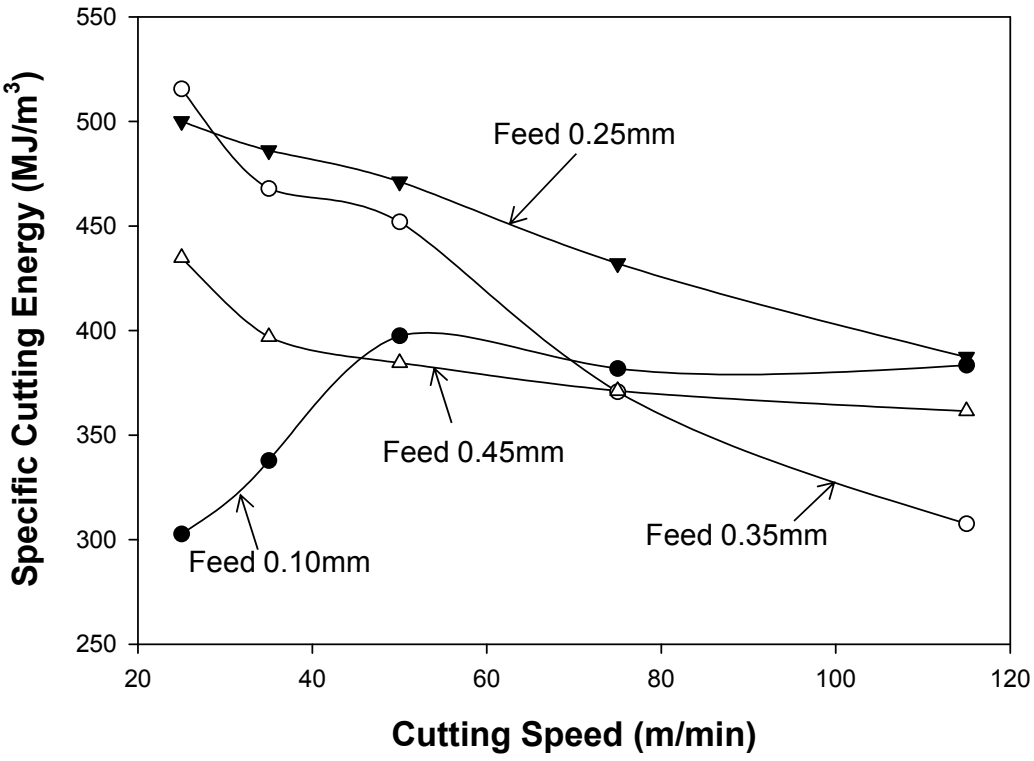

Fig.5.62 Plot showing variation of specific cutting energy due to force of friction between the tool and the workpiece as a function of cutting speed.

CHAPTER 6

DISCUSSION

Dry orthogonal cutting of Aluminum alloy 319 Al, which produced discontinuous chips with saw-tooth like geometry, was studied under this by machining the alloy under twenty different cutting combinations in order to assess the machinability performance and deformation structures produced during the process. The following section discusses the results obtained from the experiments and analyses conducted under this study. It also discusses the application of the experimental results in the construction of numerical models for discontinuous chip formation.

6.1 Chip Geometry and Mechanism of Discontinuous Chip Formation in 319 Al

319 Al produced small to mid-sized chips (Fig.5.39) during machining under the conditions studied. Smaller chips are preferred over larger ribbon-like chips which lead to operational hazards like wrapping around the tool and workpiece and to wastage of energy expended on the process. As discussed in Section 2.7.2.2, aluminum alloys produce different types of chips during machining, which include long ribbon-like chips (for alloys such as 6061-T6, also machined as a part of this study), medium length chips (alloy 2024) and soft and gummy chips (alloys 5052 and 3003) which lead to BUE formation. 319 Al, upon dry machining, produced chips, which are neither long and

ribbon-like, nor soft and gummy, but small to mid-size and easily breakable under most conditions studied, confirming good machinability characteristics under dry orthogonal cutting.

A detailed examination of the microstructure obtained from the chip, primary deformation region and machined surface resulting from dry orthogonal cutting tests conducted on 319 Al under the different cutting conditions, was carried out to understand the flow stress, equivalent strain distribution generated during discontinuous chip formation.

. The model for explaining discontinuous chip generation during machining of several materials that most closely matches the observations in this study has been proposed by Cook et al [23]. According to this theory (Section 2.8, Fig.2.29), formation of a discontinuous segment of chip starts with cracking at a high shear angle, which is followed by the segment sliding up the rake face of the tool. This motion of the segment against rake face leads to an increased friction between the rake and chip, which restricts the motion of the newly formed chip segment and causes it to bulge, with a simultaneous decrease in the shear angle. While the bulging occurs, strain along the shear plane increases constantly until a point where ductile shear fracture occurs in the material leading to formation of a saw-tooth like segment. Trends dictated by this model were corroborated by observations of chip geometry and chip sections showing partial fracture (for example Fig.A1.8, A1.11, A1.12, A1.13, A1.14, A1.15, A1.20 in Appendix I)

observed during this research. Close examination of saw-tooth chip segments in Fig.A1.6, Fig.A1.11 and Fig.A1.13 reveals that material which lies in the region closest to the rake face side of the chip show almost vertical lines traced out by fractured second phase particle flow. This can be attributed to a push by the rake face of tool, acting on the workpiece material directly in front of it, which would be during the time when the chip undergoes restricted movement against the rake face due to higher friction between the two. If noted carefully, it will be seen that the saw-tooth segments show bulging on the chip-face which lies away from the rake face, which can again be attributed to the pushing action of the tool described above and to the fact that as the tool pushes into the material in front of it, the workpiece revolution keeps pushing it upwards against the rake face. The lines traced out by the fractured particles also show an increasing amount of bending (Fig.A1.6, A1.11, A1.13, A1.14) as the distance from rake face increases, which can be attributed to a lesser resistance being faced by the segment still forming as it moves out from the main body of the workpiece (hence the increasing magnitudes of plastic strains in material with increase in distance from rake face (Section 5.9)).

The initiation of the crack that ultimately leads to formation of the saw-tooth geometry, has been reported to form both from the region near tool tip [6, 23], as well as the free surface of the chip [47]. Observation of partially formed cracks on chips made during this study also show crack initiation from both tool-tip side (Fig.A1.11, A1.14, A1.13) as well as at the free surface of chip (Fig.A1.8, A1.12, A1.15, A1.20). During

machining, second phase particles lead to formation of voids which lead to tearing of matrix resulting in crack formation [8, 51, 73] which ultimately result in formation of the saw-tooth segments. The second phase particles may also be deemed responsible for the randomness in the sizes of the saw-tooth segments formed on the chips, as their presence might be influencing the crack formations that ultimately lead to the formation of the segments. High speed photography of the process (2000 frames per second) was done as a part of this study (refer to Appendix III), and the results showed that as the chip is generated, it constantly changes its direction of movement against the rake face of the tool, which leads to a change in the contact angle between the rake face and the chip. This leads to the different morphologies that are seen in a single chip, with some regions showing very well-defined saw-tooth segments while others regions showing wavy or serrated type morphologies.

6.2 Cutting and Thrust Force Measurements

The magnitudes of cutting and thrust forces generated during dry machining of 319 Al was compared with the force data measured for 6061-T6 and it was found that the cutting forces were generally lower for 319 Al as compared to that for 6061-T6. The thrust responses for 319 Al were only slightly higher than those for 6061-T6 for the lower feed per revolution conditions (0.10mm and 0.25mm) studied. This showed that dry

machining of 319 Al generates lower forces and hence power under lower feed conditions when compared to machining of 6061-T6.

As seen in Section 2.7.2.1, the cutting forces for Aluminum alloys (under lubricated conditions) range from approximately 300N to 1200N under the cutting conditions used here [12,56]. All force responses recorded for 319 Al under dry conditions (Fig.5.5) fall well within this range. An alloy 2011-T3 [56], which possesses excellent machinability generates cutting forces of approximately 445N (for a feed rate of approximately 0.25mm) for cutting speeds considered in this study. It is evident from Fig.5.5 that cutting forces generated during dry machining of 319 Al are in the vicinity of 600N. This shows that under dry conditions, force responses of 319 Al fall within the acceptable range for lubricated machining of aluminum alloys.

The force response of 319 Al measured during cutting was found to show fluctuations in magnitude, as has been shown in Fig.5.18. It has been suggested in literature [6,55,56] that periodic or cyclic generation of shear bands in the chips during machining of certain materials leads to saw-tooth morphology in chips which lead to a variation in magnitudes of cutting and feed forces generated during the process. Vibrations in tool and the lath have also been deemed responsible for the fluctuations observed in the data. In order to ascertain whether tool vibrations or chattering was the sole reason for the observed phenomena or whether the morphology of chips produced was also responsible, Aluminum alloy 6061 Al-T6 was machined under the exact same

conditions of cutting speed and feed per revolutions equal to 0.10mm, 0.25mm and 0.35mm) as the ones used for 319 Al and the force response for this alloy was measured and analyzed. When the cutting forces were observed for 6061 Al (T6) (Fig.5.20), it was found that the fluctuations in the forces measured were drastically lower for it than for 319 Al machined under same conditions. However, some small fluctuations in data were found for 6061 Al too and these can be attributed mainly to the tool chatter or unwanted vibrations in the cutting set-up. It was also observed that the amplitude of fluctuation in forces were higher for higher feed per revolution, especially for 319 Al (Fig.5.18), which is in conformance with the fact that the size of the saw-tooth segments rise with an increase in feed as observed from turning tests conducted under this study (Fig.2.5 and Figs.A1.1-A1.20). This is in consistence with trends reported by Stephenson et al [6,8]. Thus, saw-tooth morphology of the chips is one of the factors responsible for the higher degree of fluctuations in cutting and feed forces generated during machining of 319 Al.

6.3 Surface Finish and Silicon Particle Fracture below Machined Surface

The surface finish of the machined samples was studied using SEM and white light optical profilometry. The results showed evidence of fracturing of second phase particles (Fig.5.27 and Fig.5.28). Examination under SEM showed no discernable or quantifiable differences in the surface features for samples machined under different

conditions studied. However, surface roughness measurements done using optical profilometer (Wyko) yielded higher roughness values for areas containing fractures particles for higher feed per revolution values (Fig.5.30). The areas dominant in aluminum or smeared aluminum, which form ploughing like tracks on the machined surface (Fig.5.27), however, showed no significant variation in roughness. The roughness values obtained for feed of 0.10mm were in range for finish turning operations used in the industry [12] and those obtained for feed of 0.25mm, 0.35mm and 0.45mm were found to be in range for a number of applications [12].

Examination of subsurface damage below machined surface (Section 5.6) and in the chip region (Section 5.12) showed that the smaller sized silicon particles undergo fracture to a lesser degree, whereas larger particles show extensive fracturing. Also, as has been reported in literature [42], particles with higher aspect ratio show higher degree of fracturing than spherodized ones. Using marker test, it was found that a plastic strain equal to 0.06 is required for initiation of fracture of silicon particles in the material lying under the machined surface for a sample machined under cutting speed of 50m/min and feed per revolution of 0.35mm.

6.4 Study of Plastic Deformation by Stress-Strain Estimation

Flow stresses and plastic strains developed in an orthogonally machined sample (machining conditions of 50m/min and feed per revolution of 0.35mm) were studied as a

part of this study which lead to an insight into the plastic deformation associated with machining of 319 Al. The plastic strains at different locations on the material in front of the tool tip and in the chip region and the iso-strain lines connecting the points having same values of estimated strains (Fig.5.47 and Fig.5.48) were plotted on an outline of the actual section of the machined sample (as it looked after polishing), which gave an idea about the flow of material as it gets machined. Vickers hardness values, resulting flow stress values and iso-stress contours were similarly plotted on an outline of the machined section (Fig.5.50) to study the variation in hardness of the material in the areas of interest.

The variation of equivalent strain and flow stress below the machined surface, as determined from the marker test (Section 5.7) was used for the estimation of a cumulative flow stress – equivalent strain relationship for 319 Al. It was found that the relationship followed a Voce's type exponential equation (Eqn.2.36), as has been shown in Fig.5.37. These results corresponded with those recorded by researchers [4,5,20] for Al 1100 and Copper respectively. However, they did not hold true for the discontinuous chip region.

The effect of cutting speed on the hardness and flow stress below the machined surface and in the tool tip region was studied by measuring Vickers hardness of the workpiece in the region (shown in Fig.5.51-Fig.5.54). It was found that the hardness and flow stress in the regions decrease with an increase in cutting speed till 50m/min and thereafter there is a only a slight fall in their magnitudes. This can be attributed to the higher heat produced during cutting at higher cutting speeds, and to the fact that with an

increase in speed the amount of time available for dissipation of this heat through the tool is also decreased [12,79], both of which lead to a relative softening of the workpiece as compared to machining at lower cutting speeds. This is also in conformance with the work done related to measuring of residual stresses in aluminum alloys subjected to machining [56,78-80], which showed a decrease in hardness and residual stresses an increase in cutting speed up to 125m/min for Al 2014.

6.5 Power Consumption and Specific Cutting Energy

The power consumed or energy expended during the process was estimated from the average cutting force and thrust forces calculated for the processes and have been shown in Fig.5.58 and Fig.5.59. It was found that the power required for the process increased with an increase in both the feed per revolution and with cutting speed used. The lowest cutting power recorded was below 10kJ/min for cutting speed of 25m/min and feed per revolution of 0.10mm and the highest power recorded was approximately 80kJ/min for cutting speed of 115m/min and lowest feed per revolution of 0.45. Feed power showed similar trends as cutting power, with the lowest and highest feed power recorded being approximately 5kJ/min and 60kJ/min respectively.

Specific cutting energy *(U)* or the energy consumption per unit volume of the material removed was calculated to be equal to $1160\,MJm^{-3}$ for machining conditions of cutting speed equal to 50m/min and feed of 0.35mm (Section 5.15.1). Also, the area

beneath the stress-strain plot found for the material below the machined surface (Section 5.7) was used to estimate the theoretical work or energy consumption per unit volume of the material removed between two iso-strain lines (shown in Fig.5.60).

Energy expended in plastic deformation of material and in overcoming friction between tool and chip (along the region of contact between the two on the rake face) constitutes two of the most important forms of energy dissipation during turning operation [47]. The cumulative work expended between the highest strain (1.8) and lowest strains (0.0) found in the work-material after machining was $504\,MJm^{-3}$ (Section 5.15.2). Also, the specific energy consumed in overcoming friction between the tool and chip in the region of contact between the rake and chip was found to be equal to 515N (Section 5.15.3). Hence, the total specific energy estimated to be consumed in plastically deforming the workpiece and in overcoming friction between tool and chip is equal to $1019\,MJm^{-3}$. Considering the fact that a large fraction of the total work expended during machining is spent on deformation of the work material and in overcoming the friction in rake region [4-6], it can be said that the theoretical work estimated here is in very good agreement with the work calculated from the measured cutting and thrust forces.

6.6 Application of Experimental Results for Numerical Simulation

Numerical modeling of turning operations is a field which has seen a continued effort towards simulating the process [92-109]. An accurate model for orthogonal

machining should be able to predict the magnitudes of cutting forces generated, power requirements, stresses and strains generated in the workpiece and the chip geometry accurately.

The finite element approaches adopted towards modeling of orthogonal machining can be broadly classified on the basis of the mesh used. The first type that has seen extensive use for the purpose is a Lagrangian type finite element mesh. A Lagrangian mesh is made to cover the solid body under consideration with the material points exactly coincident with the mesh [12,92, 94,100-102,106]. When the body deforms, the Lagrangian mesh also deforms with it. However, modeling of a high deformation process like orthogonal machining of ductile alloys, which are subjected to high strains and high strain rates, leads to severe distortion of the Lagrangian mesh elements, thus leading to inaccuracies in the simulation results. In order to overcome the disadvantages associated with mesh distortion, adaptive meshing or continuous remeshing can be used [92,93,100,106]. Failure criteria or chip separation criteria leading to separation of mesh elements along a predefined line, which is generally the cutting line, can also be included in the model for modeling the separation of workpiece material in front of the tool leading to formation of a chip and machined surface [102]. This criterion can be geometrical [102-105], dictating chip separation on the basis of distance between elements lying on the cutting line and the approaching tool, or may be physical [101,102,106], leading to chip separation on the basis of stresses developed, or may be a combination of the two

types [102]. The limitation of this kind of a model, however, is the fact that it uses an approximation of material fracture, which may not very close to the actual material behaviour [20,93,102].

Lagrangian mesh has been used for modeling of orthogonal cutting showing both continuous [93,94] and discontinuous chip formation [92,101,106]. Raczy [94] studied the modeling of continuous chip generation during orthogonal cutting of copper using Lagrangian mesh, with and without adaptivity and reported that without use of adaptivity, elements lying in front of the tool tip undergo sever distortion and lead to erroneous termination of the simulation. Use of adaptivity was found to reduce the mesh distortion. Other studies have shown Lagrangian formulation, with use of a fracture criteria or adaptivity, to yield good results when used for simulating orthogonal cutting process [101,106]. Ceretti et al. [101] reported that use of a Lagrangian model for simulating serrated chip formation during orthogonal machining of mild steel led to effective prediction of chip shapes and cutting forces when compared with experimental results [101]. Calamaz et al. [106] developed a new model for simulating serrated chip formation during machining of Ti6Al4V alloy taking into account the influence of strain, strain rate, strain softening and temperature generated during the process. Based on their results, Calamaz et al. [106] concluded that for effective simulation of discontinuous chip formation, the constitutive model used must include effects of strain softening and temperature rise taking place during the process.

An Eulerian mesh is the second type of mesh that has been used for modeling the workpiece behaviour during orthogonal cutting processes [20,93-95]. Unlike the Lagrangian mesh, an Eulerian mesh has its co-ordinates fixed and it does not change its position as the material deforms. It essentially involves two steps in tracking movement of the modeled material, first one being a step similar to movement of a Lagrangian mesh, the mesh moving with the body as the body deforms, and the second step being an 'advection' step, where the distorted mesh re-maps back to its original position. Absence of mesh distortion and the associated error is the primary advantage of using this mesh for modeling of a high-deformation process like the one considered here. This also eliminates the need for failure criteria to be introduced in the model. Raczy et al [93,94] and Akarca et al [95] have used an Eulerian mesh for modeling the workpiece during a finite element study of orthogonal machining of commercially pure copper and 1100 Al respectively, both of which generated continuous chips during machining. Raczy [94] compared the performance of Lagrangian (with adaptivity), Eulerian and Arbitrary Lagrangian-Eulerian (ALE – discussed below) mesh formulations for modeling orthogonal cutting of copper. It was found during the study that, despite use of adaptivity, Lagrangian mesh was still highly susceptible to errors in results and termination of simulation due to excessive mesh distortion [94]. An ALE mesh with smoothing introduced was found to be more capable of handling element distortion near the tool tip as compared to the Lagrangian mesh, however, even the ALE mesh led to erroneous terminations due to mesh distortion and

loss of initial constraints placed on the workpiece [94]. Use of an Eulerian mesh showed good correspondence between simulation and experimental results [94]. Caroll and Strenkowski [107] also compared the performances of an updated Lagrangian and an Eulerian formulation for metal cutting of 2024-T361 Al alloy to conclude that an Eulerian model is computationally less intensive than the Lagrangian model. Another noteworthy advantage of using an Eulerian formulation is that, unlike a Lagrangian mesh element, an single Eulerian mesh element can be assigned to more than one material [93,94].

An Arbitrary Lagrangian-Eulerian (ALE) mesh uses a combination the advantages of both Lagrangian and Eulerian type formulations, with the difference between an ALE mesh and an Eulerian mesh lying in the degree of advection. This mesh has been shown to offer an efficient way to model high deformation processes like metal cutting by Movaheddy and Altintas [96], who modeled the orthogonal cutting behaviour of low carbon free cutting steel using this formulation [96] and found it to yield good results in terms of chip geometry generated during cutting without running into excessive element distortion. However, the shortcoming of this study was that no comparisons were made between experimental and simulation results. Attempts by Raczy [97] to model orthogonal machining of commercial copper using an ALE formulation, however, met with limited success (discussed above) due to loss of original constraints during smoothing and due to erroneous termination of code due to element distortions.

Construction of an accurate FE model to simulate a process requires exact information about the material behaviour during the process. An elastic plastic hydrodynamic (EPH) material model, also available in one of the most popular nonlinear FE codes, LS-DYNA, can be used for defining the material properties during orthogonal machining process. This model requires definition of stress strain relationship applicable during the process being modeled, and has been successfully used by Raczy [93,94] for simulating orthogonal machining of copper using stress-strain relationship determined experimentally for the process. The shortcoming of this material model, however, is the fact that it does not incorporate the influence of temperature on the properties of material being studied. Johnson-Cook material model [97,111], one of the most common constitutive equation used for modeling strain and temperature sensitive plastic [111] behaviour of materials subjected to large strains, high strain rates and high temperatures and is frequently used for modeling of orthogonal machining process [20, 93-95, 98, 99, 106]. According to the Johnson-Cook (JC) constitutive equation, flow stress (σ) of a material can be expressed as:

$$\sigma = [A + B\varepsilon^{n}][1 + C\ln\dot{\varepsilon}^{*}][1 - T^{*m}] \tag{6.1}$$

where ε is the equivalent plastic strain, $\dot{\varepsilon}^{*} = \dot{\varepsilon}/\dot{\varepsilon}_0$ is the dimensionless plastic strain rate for $\dot{\varepsilon}_0 = 1.0s^{-1}$, T^{*} and is the homologous temperature. *A, B, n, C* and *m* are five material constants. Johnson and Cook [97] conducted uniaxial tensile tests, torsion tests and

dynamic Hopkinson bar tensile tests on a number of materials to define this constitutive equation for these materials.

It is important to use a material constitutive equation that closely follows material behaviour during the process being modeled, and hence, the most accurate results would be expected from a model simulating orthogonal machining if the constitutive material model was defined using experimental results gathered during actual machining process. Although most modeling efforts trying to simulate orthogonal machining of materials use data from split Hopkinson pressure bar (SHPB) tests for defining the material properties [98, 99], some researchers have used the stresses and strains obtained during study of plastic deformation of machined samples to define this constitutive equation partially [95]. However, an accurate definition of the variables associated with the Johnson-Cook constitutive equation require detailed information to be recorded about the strain rates associated with the test. The temperature rise during the process also needs to be studied and its effect needs to be incorporated in the equation to effectively define the constitutive equation for modeling the process. Studies into modeling of segmental chip formation using Johnson Cook material model have shown good correspondence between experimental results and modeling results [110]. As the present study focuses in on orthogonal machining of 319 Al, noteworthy here is the development of a modified Johnson-Cook type model for orthogonal machining of 319 Al proposed by Hu et al [98,99], who modified the model to incorporate the effects of secondary dendritic arm

spacing in 319 Al on the machining process. The modified equation and the values of the related parameters are as follows:

$$\sigma = [A + B\varepsilon^{n}][1 + C\ln\dot{\varepsilon}^{*}][1 - T^{*m}][D + Ed^{-k}] \tag{6.2}$$

where σ is the flow stress in units of MPa, ε is the equivalent plastic strain, $\dot{\varepsilon}^{*} = \dot{\varepsilon}/\dot{\varepsilon}_{0}$ is the dimensionless plastic strain rate for $\dot{\varepsilon}_{0} = 1.0s^{-1}$, $T^{*} = \dfrac{T - T_{amb}}{T_{melt} - T_{amb}}$ is the homologous temperature and d is the secondary dendritic arm spacing. Values of the material constants *A, B, n, C*, *m* and *h* are as follows [99]:

A=56.7783MPa, *B*=91.1038MPa, *C*=0.0213, *D*=3.323, *E*=6.534, *h*=0.41, *m*=0.72 and *n*=0.136.

The performance of this model for predicting orthogonal machining of 319 Al was evaluated by comparison of cutting forces predictions with experimentally measured forces during actual disc turning experiments on the alloy [99], which were reported to show good correspondence with each other.

In order to effectively simulate orthogonal cutting process with discontinuous chip generation, failure and erosion of elements which undergo extreme distortion and very high stresses and strains need to be incorporated into the model. This is necessary as the elements lying the areas which undergo shear band formation and shear cracking leading to formation of discontinuous saw-tooth segments, experience extreme distortion and need to be deleted from the code for accurate modeling of the saw-tooth geometry and for

successful simulation of the process. Most of the constitutive models in LS-DYNA do not incorporate this effect. As such, MAT_ADD_EROSION option can be used for incorporating material failure in the above models. This option can be successfully used with codes having other material constitutive equations which may or may not have other failure criteria included in them. Whenever any of the failure conditions, which can be defined in terms of maximum or minimum pressure, strain or stress in the element, specified in the code are met for a given element, either from the constitutive equation used, or from the MAT_ADD_EROSION option definition, the element is deleted from the mesh and is excluded for all subsequent calculation purposes [111].

Apart from the deformation behaviour of the material in terms of the stresses and strains generated during the process, it is important to incorporate the effect of microstructural features in the model in order to accurately predict the machining response of the work material. Since 319 Al is a cast alloy of aluminum with 6% silicon present in it, an effective simulation of orthogonal cutting of this material would require information about the behaviour of the silicon particles during the process. As this work carried out an extensive analysis of machining of 319 Al, including force measurement, and study of fracture behaviour of silicon particles present in the alloy in the region below the machined surface, in the PDZ and in the shear zone of the machined section, the work done in this study can be very useful for development and verification of accuracy and effectiveness of a model constructed for simulating orthogonal cutting process. The

investigation of local stresses and strains in the machined material, undertaken during the study, also provide useful information for modeling discontinuous chip formation process. The following section summarizes the results of this study with a focus on their use for modeling of the process.

From analysis of silicon particle fracture below machined surface, it was observed that the depth of damage zone (zone where silicon particles suffered damage in the form of cracking and fracturing during machining) was dependent on the machining conditions used (Section 5.6.1). The depth of this damage zone increased with an increase in feed rate used, with the maximum depth being 150μm for feed rate of 0.45mm and cutting speed of 115m/min. For cutting condition of cutting speed 50m/min and feed rate of 0.35mm, the depth of zone of silicon particle damage was found to be equal to 64μm (Section 5.7). Estimation of equivalent strains and flow stresses for this cutting condition was done using a modified specimen with a marker insert placed in it. Equivalent strain measured at the depth of 64μm (depth of deformation zone for this sample) was equal to 0.06 and the flow stress estimated at this depth was 222MPa. From these observations, it can be said that an equivalent strain of 0.06 and flow stress of 222MPa are the conditions for initiation of fracture in silicon particles in the region below machined surface.

Study of silicon particle fracture in the PDZ (equivalent strain 0.20) and in the shear band area (equivalent strain 0.45) showed that the size of silicon particles have an effect on their fracture behaviour (Section 5.12.1). Fraction of fractured silicon particles

increased with particle size in both of these regions, with larger particles (> 10μm) showing almost 100 % fracture. It was seen that most particles measuring above 5μm (longer side) show cracking and fracturing in the regions analyzed. It was also noted that silicon particles with size below 2μm do not show any evidence of cracking and fracturing.

Study of the distribution of equivalent strains and flow stresses in the region ahead of tool tip and in the chip (Section 5.9), including the shear bands, showed localization of high strains and high stresses in the shear zones. The highest strains estimated in the two shear zones studied were equal to 1.8 and 1.5 respectively. The flow stresses in the above shear zones were estimated at 369MPa and 348MPa respectively. Another noteworthy feature of this analysis was the fact that equivalent strain increased as one approached the free surface of the chip. Also, it was noted that the optical examination of chips generated showed evidence of shear cracks, which ultimately lead to discontinuous segments of the chip breaking off the main body of the chip, initiating at the free surface of the chips, which exhibit higher strains (Section 6.2,). By correlating the two observations, it can be said that equivalent strains equal to 1.5 and flow stress equal to 348 MPa constitute conditions that lead to fracturing of the 319 Al alloy, which ultimately leads to formation of saw-tooth morphology and hence discontinuous chip geometry during dry machining of 319 Al.

For effectively simulating the contact behaviour or interaction between the tool and the chip during orthogonal machining, information about the frictional interaction between the two surfaces also needs to be included in the model. Friction characteristics at the tool-chip interface greatly influence the predictions of finite element models simulating orthogonal cutting model process [109] as it influences the geometry and flow direction of the chips generated. Temperature at the tool-chip contact surface is also dependent on the type of frictional interaction between the two surfaces [106]. This study investigated the COF for dynamic friction present between the two surfaces from the force measurements (Section 5.4). The lowest and the highest magnitudes of COF found during the dry machining of 319 Al were 0.60 and 0.87 respectively. The trends outlined by the study showed that magnitudes of COF were higher for the higher feed rates studied. As has been confirmed by Ozel [109], models with constant coefficient of friction along tool-chip interface predict orthogonal machining results with reasonable accuracy, the COF results generated experimentally during this work can be effectively utilized for defining the contact behaviour between the tool and workpiece.

Beside the above information, the study also investigated the variation of cutting and thrust forces with cutting speed and with feed rate. It provides the magnitudes of the two forces for twenty different cutting conditions, which can be used as input for modeling the process to simulate the process for a wide range of conditions. Comparison of power consumption predicted by a numerical model for the process with the power

estimated from the measured cutting and thrust force results is a widely used way to judge the efficiency of the model [20, 93-95, 98,99, 108].

This work also presents a very detailed analysis of the geometry and thicknesses of the chips produced during this process, which is one of the easiest and most widely used ways of comparing the performance of a numerical model simulating orthogonal machining with the experimental results [20, 93-95, 98,99, 108]. The flow stress and equivalent strain distribution profiles plotted for material in front of the tool tip and the chip region are also useful in determining the accuracy of the model in predicting the deformation of the material during the process [20, 93-95, 98, 99, 108]. Studies have also shown that FEA simulations for segmental chip formation show fluctuations in the force results obtained from the models [110]. This study also carried out an investigation into the oscillations in the force responses recorded during the study, and the resulting data can be used to compare the force responses obtained from the modeling efforts for the alloy.

In the light of the above discussion, future work in the direction of modeling the process of orthogonal machining of 319 Al should incorporate effects of material behaviour obtained from investigation of the microstructural features of the alloy into the model. An ideal model for predicting discontinuous chip formation in 319 Al alloy would have a workpiece which includes second phase particles in the aluminum matrix. A basic model on this line would be one that contains silicon particles embedded in an aluminum

matrix. The silicon particle fracture analysis done in this study included study of the cracking and fracturing of these particles as a function of particle size (discussed above). The information derived from this study about the equivalent strain (0.06) and flow stress (222 MPa) at which silicon particle fracture is seen to start and about the relation of silicon particle size with fracture (no fracturing observed for silicon particle size below 2μm and almost 100 percent particle fracture for sizes above 10 μm) can be used for defining the damage conditions for silicon particles incorporated in the model. The Voce's type flow stress/equivalent strain relationship found for the material under the machined surface can also be used for defining the material behaviour, as, even though this relationship was found to not hold true for the area in front of the tool tip, it was obtained from analysis of the an area which had been subjected to orthogonal machining, unlike the standard tests like SHPB tests normally used for obtaining material information used in orthogonal machining modeling efforts. Also, the COF results, flow stresses and strains in shear bands (348MPa and 1.5 respectively) and force measurement results (for twenty different cutting conditions), as discussed above, can be incorporated in the model. An Eulerian mesh may be used for modeling the workpiece as unlike a Lagrangian mesh, an Eulerian mesh formulation is not susceptible to severe distortion of the elements, which would be encountered not only at the tool tip location, but at the workpiece-silicon particle interfaces. Also, as the workpiece containing aluminum and silicon would contain two different materials, an Eulerian mesh which allows a single

mesh to be assigned to two materials would be better suited to modeling of such workpiece. Since the mesh density of the workpiece will have to be very high in order to capture the interactions of not only the tool and the workpiece, but also of the second phase particles modeled into the workpiece, use of an Eulerian mesh, which has been shown to be computationally less intensive than a Lagrangian mesh [94], would be suitable. Another advantage associated with an Eulerian mesh would be the elimination of chip separation criteria. An incipient chip shape can be modeled using the extensive analysis of chip geometries undertaken during this work.

CHAPTER 7

SUMMARY AND CONCLUSIONS

7.1 Summary and Conclusions

The present work focused on assessing the machinability performance of 319 Al during dry orthogonal cutting tests. Investigating plastic deformation of the alloy and optically studying the facture of silicon particles during the machining process has provided rationale for discontinuous chip formation. The main conclusions drawn from this study are:

1. The 319 Al alloy generated medium length, discontinuous chips showing saw-tooth morphology when machined under the conditions studied. The chip breakability was good (except for highest feed rate of 0.45mm), which is an advantage over 6061-T6 which when machined under conditions identical conditions produced long and ribbon-like chips.
2. On the basis of general chip morphology, orientation of fractured silicon particle flow and the hardness values at different locations in the material ahead of the tool tip and in the chip, it was concluded that the mechanism leading to formation of saw-tooth segments during dry machining of 319 Al closely resembles the mechanism dictated by Cook [23]. This mechanism proposes that formation of a discontinuous segment of chip initiates at a high shear angle, which then

undergoes subsequent sliding up the rake face, its motion being continually deterred due to increasing magnitudes of friction force experienced by it. This resistance to sliding leads to bulging out of the segment in directions away from the rake face. Strain along the shear plane continues to increase till fracture occurs, with this segment breaking free from the main body of the workpiece.

3. Force measurements showed an increase in magnitude of the cutting force with an increase in feed rate. Additionally a decrease in the cutting force was found when increasing the cutting speed. The lowest cutting force measured was approximately 200N for a feed of 0.10mm, irrespective of cutting speed used. The highest cutting forces were approximately 1000N, measured for machining under condition of lowest cutting speed (25m/min) and highest feed (0.45mm).
4. The thrust force increased with an increase in feed rate. A decrease in the thrust force was found when increasing the cutting speed. The lowest thrust forces measured were approximately 100N for a feed of 0.10mm (for all cutting speeds) and the highest magnitudes were found to be approximately 600N for the combination of lowest cutting speed (25m/min) and highest feed (0.45mm). Thus, it can be concluded that higher cutting speed and low feed per revolution conditions should be used for decreasing the power requirements of the machining process for the 319 Al alloy.

5. Comparisons carried out between average cutting force and average thrust force responses of 319 Al and 6061-T6 alloy, measured as a part of the study, showed that 319 Al led to lower cutting forces than those produced by 6061-T6. Also, the thrust forces generated by 319 Al while using lower feed rates of 0.10mm and 0.25mm were very close to those generated by 6061-T6. Thus it can be concluded that dry machining of 319 Al is more efficient than that of 6061-T6 in terms of forces generated during the process.
6. Average surface roughness values measured for machined surface were found to be approximately 0.6 microns for machining at the lowest feed rate (0.10mm/rev) and approximately 0.9 microns for the combination of highest cutting speed and feed rate (115m/min and 0.45mm), which falls within the range commonly observed for aluminum alloys (up to 3 microns). Hence, it can be concluded that surface roughness values obtained by dry machining of 319 Al under conditions studied fall within the range expected of finish turning operations (Ra 0.75 – 1.5) [6].
7. Damage and fracture of silicon particles and iron rich phases in the 319 Al material lying below the machined surface showed that the extent of damage increased with an increase in feed rate. Maximum depth of zone to which fracture of silicon particle fracture was observed was measured to be equal to 150 microns. It was also found that at lower speeds of cutting, subsurface damage was limited

to a relatively narrow zone beneath the machined surface. It was thus concluded that in order to avoid extensive damage to the second phase particles, and hence maintain the strength and good surface finish of the alloy, lower feed rates should be used during its machining.

8. Marker test results led to the estimation that an equivalent plastic strain equal to 0.06 is required for initiation of fracture of silicon particles in the material lying under the machined surface for a sample machined under cutting speed of 50m/min and feed per revolution of 0.35mm. Equivalent strain estimation in the primary deformation zone and chip region showed evidence of very high strains in the regions of the shear bands, with relatively lower strains in the region lying between them. The highest strain measured in the shear zone was 1.8.
9. Hardness measurements in the material lying ahead of tool tip showed higher hardness values in regions close to the shear zones and rake face of tool. Hardness values were found to be relatively lower in regions lying towards the centre of the chip segments. Stress estimations from hardness values showed stresses as high as 369 MPa in the shear zones.
10. The flow stress effective plastic strain relationship for the 319 Al material was determined using observations from flow stress and plastic strain estimations in material below machined surface. A regression analysis of the data showed that the relationship between the flow stress and plastic strain followed a Voce's type

relation with saturation stress for the material ($\bar{\sigma}_s$) equal to 287 MPa, flow stress of the material ($\bar{\sigma}_0$) equal to 186 MPa and constant $\bar{\varepsilon}_c$ equal to 0.12. The flow stress and equivalent strain distribution in the chip, however, did not follow this relationship.

11. Estimation of the specific work from the force of friction (515MJm^{-3}) in the contact region between the tool and rake face showed that nearly half of the total energy required in the process is spent on overcoming the friction between the rake-face and the chip as the total specific work calculated from average force measurements was 1160MJ·$^{m-3}$
12. Good agreement was found between specific cutting energy or the energy consumption per unit volume of the material removed calculated using machining forces measured (1160MJm^{-3}) and that estimated theoretically from area under the stress-strain curve plot for the material and specific energy consumed by friction forces (1019MJm^{-3}).
13. An investigation into fracture of silicon particles in PDZ and shear zone with respect to size of the particles (prior to any interaction with tool) led to the conclusion that percentage of silicon particles fractured increased with an increase in particle size. Also, a higher percentage of silicon particle fracture was seen in shear zone than in PDZ.

14. For the conditions considered in this stududy, the optimized cutting condition for dry machining of 319 Al is obtained by using a cutting speed of 50m/min and feed of 0.35mm. The main criteria used in arriving at this result were the power expended for machining at this condition which was 61kJ/min (cutting power 36kJ/min and feed power 25kJ/min) and the volume removed which was equal to 875mm3/second.

7.2 Final Comments

This work led to exploring and recording of the key aspect of dry machining of 319 Al alloy. The alloy generated medium length chips with good breakability (under most conditions) and saw-tooth morphology. Microstructural studies were carried out to understand the mechanism associated with discontinuous chip generation. It was observed that the formation of discontinuous chips closely followed the mechanism proposed by Cook [23] which dictates initiation of a discontinuous chip segment formation at a high shear angle, followed by subsequent sliding up the rake face of tool. The friction present between the rake face of tool and newly generated chip segment resists the sliding of chip segment against the rake face, thus leading to bulging out of the segment in directions away from the rake face which leads to raising of strain along the shear plane which finally leads to fracturing and separation of the segment from the main body of the chip or workpiece (described in details in Section 6.1).

Using a force measurement system constructed and calibrated as a part of this work, cutting and thrust forces generated during machining under different cutting conditions were measured for 319 Al (a cast aluminum alloy) and 6061-T6 (a wrought aluminum alloy). For all cases studies, both cutting and thrust forces increased with an increase in feed rate and with a decrease in cutting speed. Comparison of force responses of the two alloys showed that 319 Al generated lower cutting forces and higher oscillations in the force response among the two alloys. It was also observed that dry cutting of 319 Al generated magnitudes of forces which are comparable with forces generated by other aluminum alloys during wet-cutting (refer to Section 2.7.2.1). Forces measured for 319 Al were further used for estimation of cutting and feed power which showed that power required for cutting increases with increase in cutting speed and feed rate used.

Surface roughness of machined material also was very well within acceptable limits, reaching up to a maximum of 1μm. Optical microscopy investigations into silicon particle fracture behaviour below machined surface showed that depth or thickness of zone where silicon particle is mainly confined to, increased with an increase in feed rate.

Analysis of distribution of plastic strains and local flow strength values in 319 Al showed high strains and stresses to be concentrated in the shear zones, with relatively lower stresses and strains present in the region lying between shear zones. Estimation

of specific energy theoretically by considering the energy expended for plastic deformation and in overcoming friction (estimated from COF calculated from cutting and thrust force results) and comparison of the same with the specific energy obtained from force results showed excellent match, thus emphasizing the role of plastic deformation and friction force as the two most important factors leading to energy consumption during the process. Thus, it was concluded that 319 Al exhibits very good machinability under dry turning conditions.

7.3 Suggestions for Future Work

Future work that may be done to carry this work forward would include:

- Use of coolant in the cutting of 319 Al alloy with force measurements carried out under the conditions studied in the work. A comparison of forces generated and power expended under dry machining conditions and flooded conditions would lead to important information about the effects of cutting fluids on the process, which may be utilized for finding ways to reduce and ultimately do away with the use of lubricants and coolants. Effect of cutting fluids on the chip morphology should also be investigated to understand the effect of heat generated on the chip morphology.
- Temperature generated during the process should be measured to find out the relation between different cutting conditions and temperature rise during

machining. It would also lead to an understanding of the way temperature rise affects the morphology of chips formed during cutting.

- TEM investigations should be carried out to investigate the shear zone region further and to find out if there is any phase transformation taking place in the area. This would lead to an explanation for the very high stresses found in the region.
- It was found that smaller silicon particles undergo fracture to a lesser extent. As such, subjecting the alloy to a heat treatment process that would lead to a reduction in the silicon particle size would lead to less fracturing and hence a lower degree of damage to the alloy during dry machining.
- Study of tool wear and adhesion of workpiece material to cutting insert is another aspect of judging the machinability of a material. An investigation into adhesion of 319 Al to the tool's cutting edge and the corresponding tool wear during dry machining of the alloy should be carried out to analyze an additional aspect of machinability of the material.
- One of the most important ways to take this study further is to develop a numerical model to simulate the process of orthogonal turning of alloys which have microstructures similar to 319 Al. The data found in this study can be used as input for such a model and can also be used for verifying the efficiency of the same. The construction of an accurate model would lead to prediction of results of a cutting test on the material under consideration without the need to procure

material, or to set-up the tools and machinery and would contribute in a great way to advancement of the machining of materials.

REFERENCES

[1] ME Merchant, Mechanics of the metal cutting process, I, Orthogonal cutting and a type 2 chip, Journal of Applied Physics 16 (1945) 267-275.

[2] ME Merchant, Mechanics of the metal cutting process, II, Plasticity conditions in orthogonal cutting, Journal of Applied Physics 16 (1945) 318-324.

[3] V Piispanen, Theory of formation of metal chips, Journal of Applied Physics 19 (1948) 876-881.

[4] M Elmadagli, AT Alpas, Metallographic analysis of the deformation microstructure of copper subjected to orthogonal cutting, Materials Science and Engineering A, 355 (2003) 249-259.

[5] M Elmadagli, H Ni, AT Alpas, Mechanical properties and microstructures of 1100 aluminum subjected to dry machining, Materials Science and Engineering A, 385 (2004) 267-278.

[6] MC Shaw, Metal Cutting Principles, 2nd ed,, Oxford University Press (2004),9-38,432-572.

[7] JT Black, Modern Manufacturing and Products Techniques, Prentice Hall PTR (1993),50-178.

[8] DAA Stephenson, JS Agapiou, Metal Cutting Theory and Practice, Second Edition ed,, CRC Press, Florida, (2006),17-20,371-416,459-478,551-697.

[9] CZ Duan, MJ Wang, Characteristics of adiabatic shear bands in the orthogonal, cutting of 30CrNi3MoV steel, Journal of Material Processing Technology 168 (2005) 102-106.

[10] H Ernst, ME Merchant, Chip formation, friction, and high quality machined surfaces, Surface Treatment of Metals, 29 (1941) 299-378.

[11] S Ramalingam, JT Black, On the metal physical considerations in the machining of metals, Journal of Engineering for Industry, Transactions ASME, 94 (1972) 1215-1224.

[12] ASM Handbook: Machining, ASM, Metals Park, Ohio, 1989,439-445.

[13] K Okushima, K Iwata, Study of machinability of metals, Japan Society of Mechanical Engineers Transactions, 28 (1962) 1034-1043.

[14] EH Lee, BW Shaffer, Theory of plasticity applied to problem of machining, American Society of Mechanical Engineers, Journal of Applied Mechanics ASME Transactions 19 (1952) 234-239.

[15] EH Lee, BW Shaffer, Theory of plasticity applied to problem of machining, Journal of Applied Mechanics, ASME Transactions, 19 (1952) 234-239.

[16] PLB Oxley, MJM Welsh, Calculating shear angle in orthogonal metal cutting from fundamental stress-strain-strain rate properties of work material, (1963) 73-86.

[17] P Dewhurst, On The Non-Uniqueness of The Machining Process, Proceeding of Royal Society of London Ser A, 360 (1978) 587-610.

[18] CE Campbell, LA Bendersky, WJ Boettinger, R Ivester, Microstructural characterization of Al-7075-T651 chips and work pieces produced by high-speed machining, Materials Science and Engineering A, 430 (2006) 15-26.

[19] H Ni, M Elmadagli, AT Alpas, Mechanical properties and microstructures of 1100 aluminum subjected to dry machining, Materials Science and Engineering A, 385 (2004) 267-278.

[20] X Song, Experimental studies and numerical simulations of continuous and discontinuous chip formation during orthogonal cutting, MASc Thesis, University of Windsor, Windsor, ON, Canada (2005).

[21] H Zhang, AT Alpas, Quantitative evaluation of plastic strain gradients generated during orthogonal cutting of an aluminum alloy, Materials Science and Engineering A, 332 (2002) 249-254.

[22] B Venkataraman, G Sundararajan, Sliding wear behaviour of Al-SiC particulate composites - II, The characterization of subsurface deformation and correlation with wear behaviour, Acta Materialia, 44 (1996) 461-473.

[23] NH Cook, I Finnie, MC Shaw, Discontinuous chip formation, Transactions of the American Society of Mechanical Engineers, 76 (1954) 153.

[24] DC Drucker, An analysis of the mechanics of metal cutting, Journal of Applied Physics, 20 (1949) 1013-1021.

[25] R Komanduri, T Schroeder, J Hazra, DG Flom, BF von Turkovich, On the catastrophic shear instability in high-speed machining of an AISI 4340 steel, Journal of Engineering for Industry, ASME Transaction, 104 (1982) 121-131.

[26] TZ Blazynski, Materials at high strain rates, Elsevier Publishing Company,Essex 1987.

[27] JA Hines, KS Vecchio, Recrystallization kinetics within adiabatic shear bands, Acta Materialia, 45 (1997) 635-649.

[28] EM Trent, Metal cutting and the tribology of seizure: III, Temperatures in metal cutting, Wear, 128 (1988) 65-81.

[29] SP Timothy, Structure of adiabatic shear bands in metals: a critical review, Acta Metallurgica, 35 (1987) 301-306.

[30] AJ Bedford, AL Wingrove, KRL Thompson, Phenomena of Adiabatic Shear Deformation, Journal of the Australian Institute of Metals, 19 (1974) 61-73.

[31] JC Lemaire, WA Backofen, Adiabatic instability in the orthogonal cutting of steel, Metallurgical Transaction, 3 (1972) 477-481.

[32] RF Recht, Catastrophic Thermoplastic Shear, Transactions ASME, Series E-Journal of Applied Mechanics, 86 (1964) 189-193.

[33] GK Boothroyd WA Knight, Fundamentals of machining and machine tools, Marcel Dekker Inc, Florida,1989.

[34] R Komanduri, Z Hou, On thermoplastic shear instability in the machining of a titanium alloy (Ti-6Al-4V), Metallurgical and Materials Transactions; A: Physical Metallurgy and Materials Science, 33 (2002) 2995-3010.

[35] BFV Turkovich, Shear stress in metal cutting, Journal of Engineering for Industry, Transactions ASME, 92 Ser B (1970) 151-157.

[36] R Nakkalil, Formation of adiabatic shear bands in eutectoid steels in high strain rate compression, Acta Metallurgica et Materialia, 39 (1991) 2553-2563.

[37] ASM Metals Handbook, 8th edition, American Society of Metals, v 8, 1967.

[38] Y Fujii, Proposal for a step response evaluation method for force transducers, Measurement Science and Technology, 14 (2003) 1741-1746.

[39] Y Fujii, A method for calibrating force transducers against oscillation force, Measurement Science and Technology, 14 (2003) 1259-1264.

[40] A Gangulee, J Gurland, On the fracture of silicon particles in aluminum-silicon alloys, Transactions of the Metallurgical Society of AIME, 239 (1967) 269-272.

[41] E Rincon, HF Lopez, MM Cisneros, H Mancha, Temperature effects on the tensile properties of cast and heat treated aluminum alloy A319, Materials Science and Engineering A, 519 (2009) 128-140.

[42] CH Caceres, JR Griffiths, Damage by the cracking of silicon particles in an Al-7Si-0,4Mg casting alloy, Acta Materialia, 44 (1996) 25-33.

[43] VP Ashtakhov, Metal Cutting Mechanics, CRC Press 1998.

[44] JA Hines, KS Vecchio, S Ahzi, A model for microstructure evolution in adiabatic shear bands, Metallurgical and Materials Transactions A: Physical Metallurgy and Materials Science, 29 (1998) 191-203.

[45] CA Brown, BF von Turkovich, A Practical Method for Estimating Machining Forces from Tool-Chip Contact Area, CIRP Ann, Manufacturing Technology, 32 (1983) 91-95.

[46] JG Cowie, FR Tuler, Flow localization models-a review, Material Science and Engineering, 95 (1987) 93-99.

[47] A Vyas, MC Shaw, Mechanics of saw-tooth chip formation in metal cutting, Journal of Manufacturing Science and Engineering, Transactions ASME, 121 (1999) 163-172.

[48] R Komanduri, BF Von Turkovich, New observations on the mechanism of chip formation when machining titanium alloys, Wear, 69 (1981) 179-188.

[49] J Hua, R Shivpuri, Prediction of chip morphology and segmentation during the machining of titanium alloys, Journal of Materials Processing Technology, 150 (2004) 124-133.

[50] MT Pérez-Prado, JA Hines, KS Vecchio, Microstructural evolution in adiabatic shear bands in Ta and Ta-W alloys, Acta Materialia, 49 (2001) 2905-2917.

[51] BFV Turkovich, DR Durham, Machining of Titanium and its alloys, (1982) 257-274.

[52] R Kountanya, I Al-Zkeri, T Altan, Effect of tool edge geometry and cutting conditions on experimental and simulated chip morphology in orthogonal hard turning of 100Cr6 steel, Journal of Materials Processing Technology, 209 (2009) 5068-5076.

[53] R Komanduri, T Schroeder, J Hazra, DG Flom, BF von Turkovich, On the catastrophic shear instability in high-speed machining of an AISI 4340 steel, Journal of Engineering for Industry, Transactions ASME, 104 (1982) 121-131.

[54] TJ Burns, MA Davies, On repeated adiabatic shear band formation during high-speed machining, International Journal of Plasticity, 18 (2002) 487-506.

[55] MA Davies, TJ Burns, CJ Evans, On the dynamics of chip formation in machining hard metals, CIRP Annals Manufacturing Technology, 46 (1997) 25-30.

[56] GE Totten, GE, DS Mackenzie, Handbook of Aluminum: Physical metallurgy and processes, CRC Press (2003),1063-1103.

[57] S Ramalingam, ED Doyle, DM Turley, On chip curl in orthogonal machining, Journal of Engineering for Industry, Transactions ASME, 102 (1980) 177-183.

[58] DM Turley, ED Doyle, S Ramalingam, Calculation of shear strains in chip formation in Titanium, Materials Science and Engineering, 55 (1982) 45-48.

[59] M Kronenberg, Machining science and application, Pergamon Press, Oxford, New York, 1966.

[60] DM Turley, ED Doyle, Microstructural behaviour – its influence on machining On the Art of Culling Metals - 75 Years Later, a Tribute to FW Taylor, (1982) 99-118.

[61] E Voce, The relationship between stress and strain for homogeneous deformation, Journal of the Institute of Metals, 74 (1948) 536-562.

[62] SL Semiatin, SB Rao, Shear localization during metal cutting, Material Science and Engineering, 61 (1983) 185-192.

[63] GE Dieter, Mechanical Metallurgy, McGraw-Hill, New York, (1988) 524.

[64] GW Rowe, PT Spick, A new approach to determination of shear-plane angle in machining, Journal of Engineering for Industry, Transactions ASME, 89 (1967) 530-538.

[65] DM Turley, Dislocation substructures and strain distributions beneath machined surfaces of 70/30 brass, Journal of the Institute of Metals, 99 (1971) 271-276.

[66] PK Wright, Predicting the shear plane angle in machining from work material strain-hardening characteristics, (1982) ASME, New York, NY, USA,285-292.

[67] S Raman, A Basu, DS Kilic, Analysis of fractal frictional contact in machining, Proceedings of the Institution of Mechanical Engineers, Part B (Journal of Engineering Manufacture), 221 (2007) 1119-1128.

[68] S Raman, DS Kilic, Observations of the tool-chip boundary conditions in turning of aluminum alloys, Wear, 262 (2007) 889-904.

[69] NN Zorev, Interrelationship between shear processes occurring along tool face and on shear plane in metal cutting, Proceedings of the International Production Engineering Research Conference, (1963) 42-49.

[70] EM Trent, Metal cutting and the tribology of seizure: II, Movement of work material over the tool in metal cutting, Wear, 128 (1988) 47-64.

[71] EM Trent, Metal cutting and the tribology of seizure: I, Seizure in metal cutting, Wear, 128 (1988) 29-45.

[72] S Bhowmick, AT Alpas, The performance of hydrogenated and non-hydrogenated diamond-like carbon tool coatings during the dry drilling of 319 Al, International Journal of Machining,Tools Manufacturing, 48 (2008) 802-814.

[73] H Zhang, Plastic Deformation and chip formation mechanisms during machining of Copper, Aluminum and an Aluminum matrix composite, PhD Thesis, University of Windsor, Windsor, ON, Canada (2000).

[74] N Fang, Q Wu, The effects of chamfered and honed tool edge geometry in machining of three aluminum alloys, International Journal of Machine Tools and Manufacture, 45 (2005) 1178-1187.

[75] M Ravi Shankar, S Chandrasekar, WD Compton, AH King, Characteristics of aluminum 6061-T6 deformed to large plastic strains by machining, Materials Science and Engineering A, 410-411 (2005) 364-368.

[76] I Shareef, M Natarajan, OO Ajayi, Dry machinability of aluminum alloys, (2005) 831-832.

[77] EM Trent, PK Wright, Metal Cutting, IV ed,, Elesevier 2000.

[78] R Natarajan, S Biswas, S Jeelani, Residual stress distribution in 2024T351 Aluminum alloy due to machining, Computers in Engineering, Proceedings of the International Computers in Engineering Conference 2, (1985) 59-63.

[79] S Jeelani, S Biswas, R Natarajan, Effect of cutting speed and tool rake angle on residual stress distribution in machining 2024-T351 Aluminum alloy-unlubricated conditions, Journal of Materials Science, 21 (1986) 2705-2710.

[80] R Natarajan, S Biswas, S Jeelani, Determination of residual stresses in a ring due to machining, Computers in Engineering, Proceedings of the International Computers in Engineering Conference 2, (1984) 773-777.

[81] A Mallock, The action of cutting tools, Proceedings of Royal Society of London, 33 (1881) 127–139.

[82] AK Balaji, IS Jawahir, A machining performance study in dry contour turning of aluminum alloys with flat-faced and grooved diamond tools, Machining Science and Technology, 5 (2001) 269-289.

[83] MM Elkhabeery, JA Bailey, Surface integrity in machining solution-treated and aged 2024-Aluminum alloy, using natural and controlled contact length tools: Part I: Unlubricated conditions Part II: Lubricated conditions, Journal of Engineering Materials and Technology, 106 (1984) 152-166.

[84] JA Bailey, Friction in metal machining - Mechanical Aspects, Wear, 31 (1975) 243.

[85] AR Riahi, AT Alpas, Fracture of silicon-rich particles during sliding contact of Al-Si alloys Materials Science and Engineering A, 441, (2006) 326-330.

[86] AR Riahi, T Perry, AT Alpas, Scuffing resistances of Al-Si alloys: effects of etching condition, surface roughness and particle morphology, Materials Science and Engineering A, v A343, (2003)76-81.

[87] C Perrin, WM Rainforth, Work hardening behaviour at the worn surface of Al-Cu and Al-Si alloys, Wear, v 203-204,(1997)171-9.

[88] AT Alpas, H Hu, J Zhang, Plastic deformation and damage accumulation below the worn surfaces, Wear, v 162-64, (1993)188-195.

[89] MA Moore, RM Douthwaite, Plastic deformation below worn surfaces, Metallurgical Transactions A (Physical Metallurgy and Materials Science), v 7 A,(1976) 1833-1839.

[90] JH Dautzenberg, JH Zaat, Qunantitative determination of deformation by sliding wear, Wear, v 23, (1973) 9-19.

[91] R Hill, The mathematical theory of plasticity, Clarendon Press, Oxford, 1950, P29.

[92] TD Marusich, M Ortiz, Simulation of chip formation in high-speed machining American Society of Mechanical Engineers, Machining of Advanced Materials-Applied Mechanics Division, v 208, (1995) 127-139.

[93] A Raczy, M Elmadagli, WJ Altenhof, AT Alpas, An Eulerian finite-element model for determination of deformation state of a copper subjected to orthogonal cutting, Metallurgical and Materials Transactions A: Physical Metallurgy and Materials Science, v 35 A, (2004) 2393-2400.

[94] A Raczy, An eulerian finite element for determination of deformation state of a copper subjected to orthogonal cutting, MASc Thesis, University of Windsor, Windsor, ON, Canada (2004).

[95] SS Akarca, X Song, WJ Altenhof, AT Alpas, Deformation behaviour of aluminium during machining: Modelling by Eulerian and smoothed-particle hydrodynamics methods Proceedings of the Institution of Mechanical Engineers, Part L: Journal of Materials: Design and Applications, v 222, (2008) 209-221.

[96] M Movaheddy, MS Gadala, Y Altintas, Simulation of the orthogonal metal cutting process using an arbitrary Lagrangian-Eulerian finite element method, Journal of Materials Processing Technology, v 103, (2000) 267-275.

[97] GR Johnson, WH Cook, A constitutive model for metals subjected to large strains, high strain rates and high temperatures, Proceedings of the 7th International Symposium on Ballistics, The Hague (1983) 541-547.

[98] X Hu, JW Sutherland, JM Boileau, Characterizing the effect of 319 aluminum microstructure on Machinability, Part 1 : Model development American Society of Mechanical Engineers, Manufacturing Engineering Division, MED, v 16-2 (2005) 1071-1080.

[99] X Hu, JW Sutherland, JM Boileau, Characterizing the effect of 319 aluminum microstructure on machinability, part 2: Model validation, American Society of Mechanical Engineers, Manufacturing Engineering Division, v 16-2, (2005) 1081-1090.

[100] E Cerreti, P Fallbohmer, WT Wu, TR Altan, Application of 2D FEM to chip formation in orthogonal cutting, Journal of Materials Processing Technology, v 59, (1996) 169-180.

[101] E Cerreti, M Lucchi, T Altan, FEM simulation of orthogonal cutting: serrated chip formation, Journal of Materials Processing Technology, v 95, (1999) 17-26.

[102] JM Huang, JT Black, Evaluation of chip separation criteria for the FEM simulation of machining, Journal of Manufacturing Science and Engineering, ASME Transactions, v 118, (1996) 545-554.

[103] SP Lo, YY Lin, An investigation of sticking behaviour on the chip-tool interface using thermo-elastic-plastic finite element method, Journal of Materials Processing Technology, v 121, (2002) 285-292.

[104] ZC Lin, SP Lo, Ultra-precision orthogonal cutting simulation for oxygen-free high-conductivity copper, Journal of Materials Processing Technology, v 65, (1997) 281-291.

[105] AG Mamalis, M Horváth, AS Branis, DE Manolakos, Finite element simulation of chip formation in orthogonal metal cutting, Journal of Materials Processing Technology, v 110, (2001) 19-27.

[106] M Calamaz, D Coupard, F Girot, A new material model for 2D numerical simulation of serrated chip formation when machining titanium alloy Ti-6Al-4V, International Journal of Machine Tools and Manufacture, v 48, (2008), 275-88.

[107] JS Strenkowski, JT III Caroll, Finite element model of orthogonal metal cutting, American Society of Mechanical Engineers, Production Engineering Division (Publication) PED, v 12, (1984) 157-166.

[108] Y Zheng, X Hu; JW Sutherland, Application of finite deformation theory to the development of an orthogonal cutting Model-part II: experimental investigation and model validation, Journal of Manufacturing Science and Engineering, ASME Transactions, v 128, (2006) 767-74.

[109] T Ozel, The influence of friction models on finite element simulations of machining, International Journal of Machine Tools and Manufacture, v 46, (2006) 518-530.

[110] YB Guo, DW Yen, A FEM study on mechanisms of discontinuous chip formation in hard machining, Journal of Materials Processing Technology, v 155, (2004) 1350-1356.

[111] LS-DYNA keyword user's manual, Livermore software technology corporation, volume 1, version 971, (2007) 18 (MAT) -58 (MAT).

[112] M Baker, J Rosler, C Siemers, The influence of thermal conductivity on segmented chip formation, Computational Materials Science, v 26, (2003) 175-182.

APPENDIX I

AN ATLAS OF CHIP MICROSTRUCTURES OF 319 AL SAMPLES MACHINED AT DIFFERENT CUTTING CONDITIONS

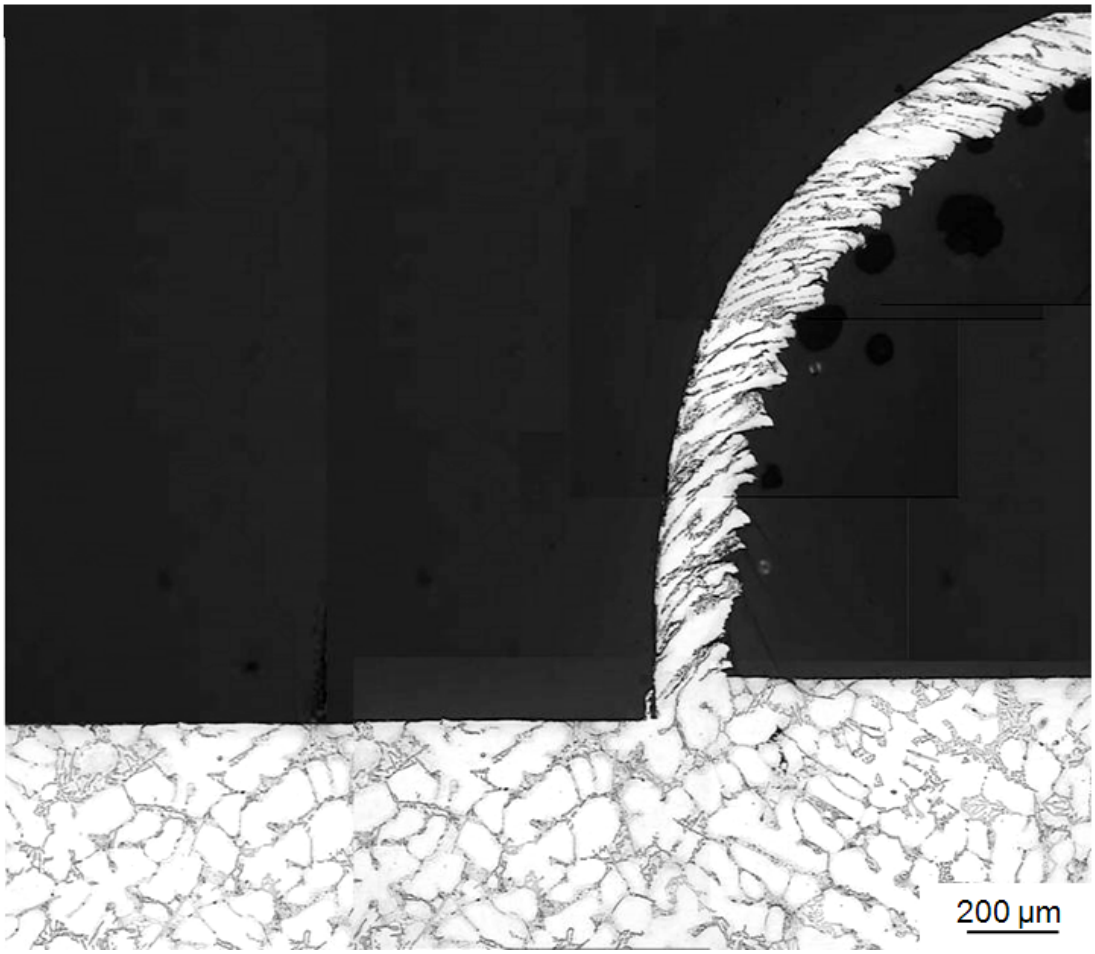

Fig.A1.1. Cutting Speed 25m/min, Feed 0.10mm

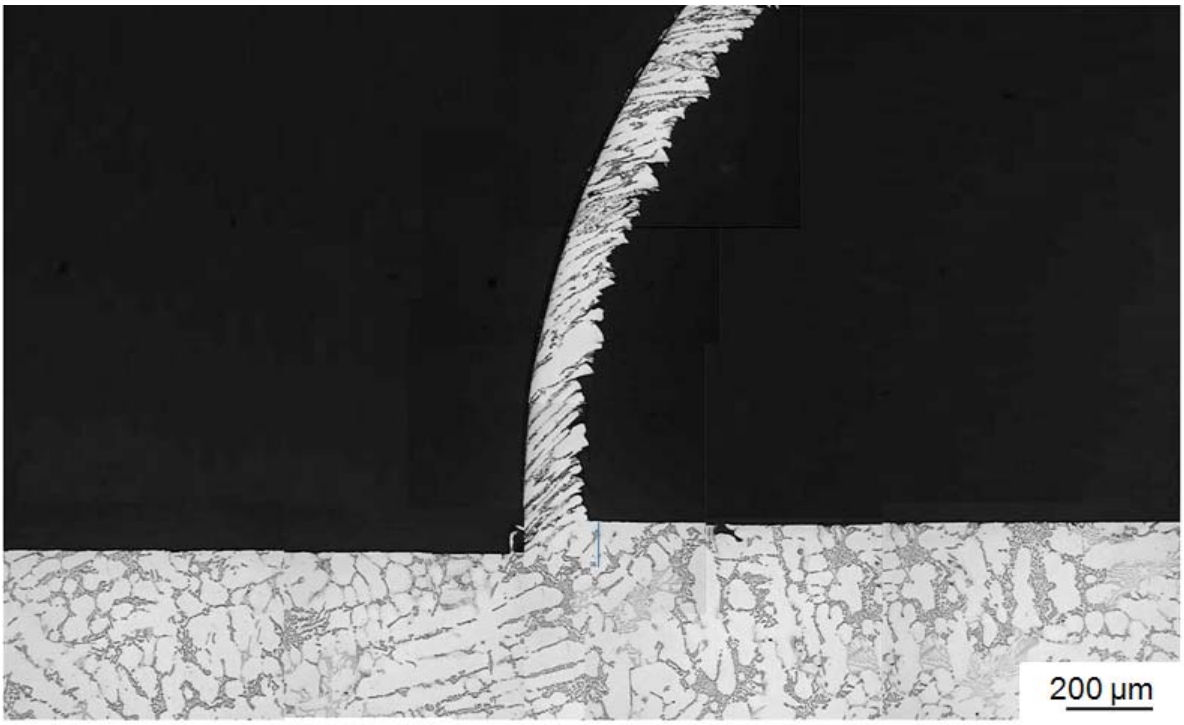

Fig.A1.2 Cutting Speed 35m/min, Feed 0.10mm

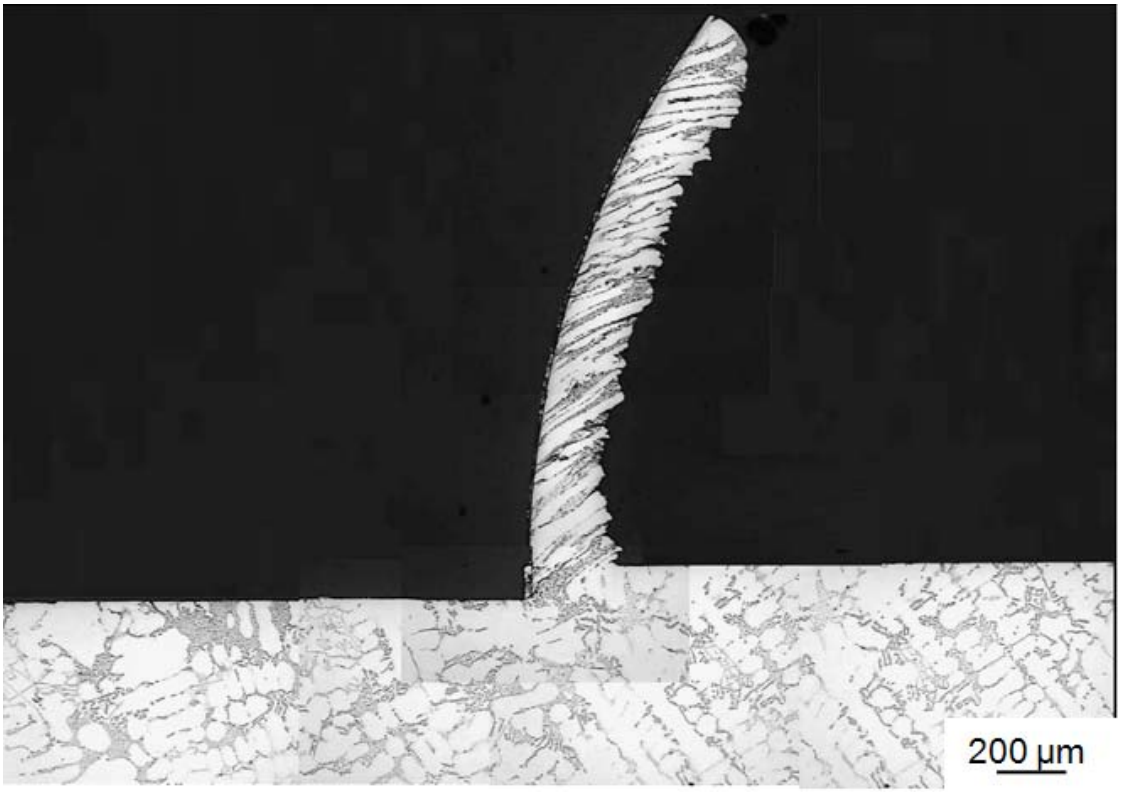

Fig.A1.3. Cutting Speed 50m/min, Feed 0.10mm

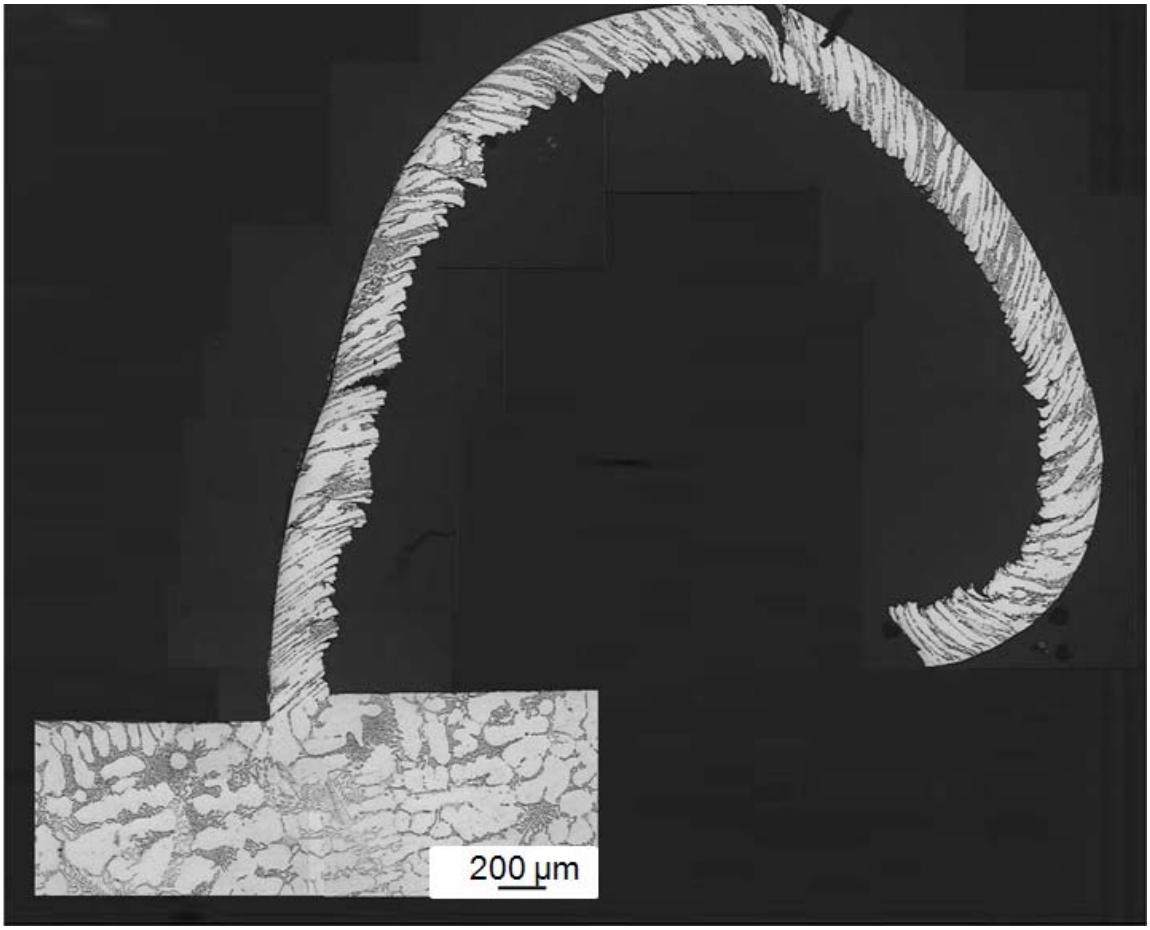

Fig.A1.4 Cutting Speed 75m/min, Feed 0.10mm

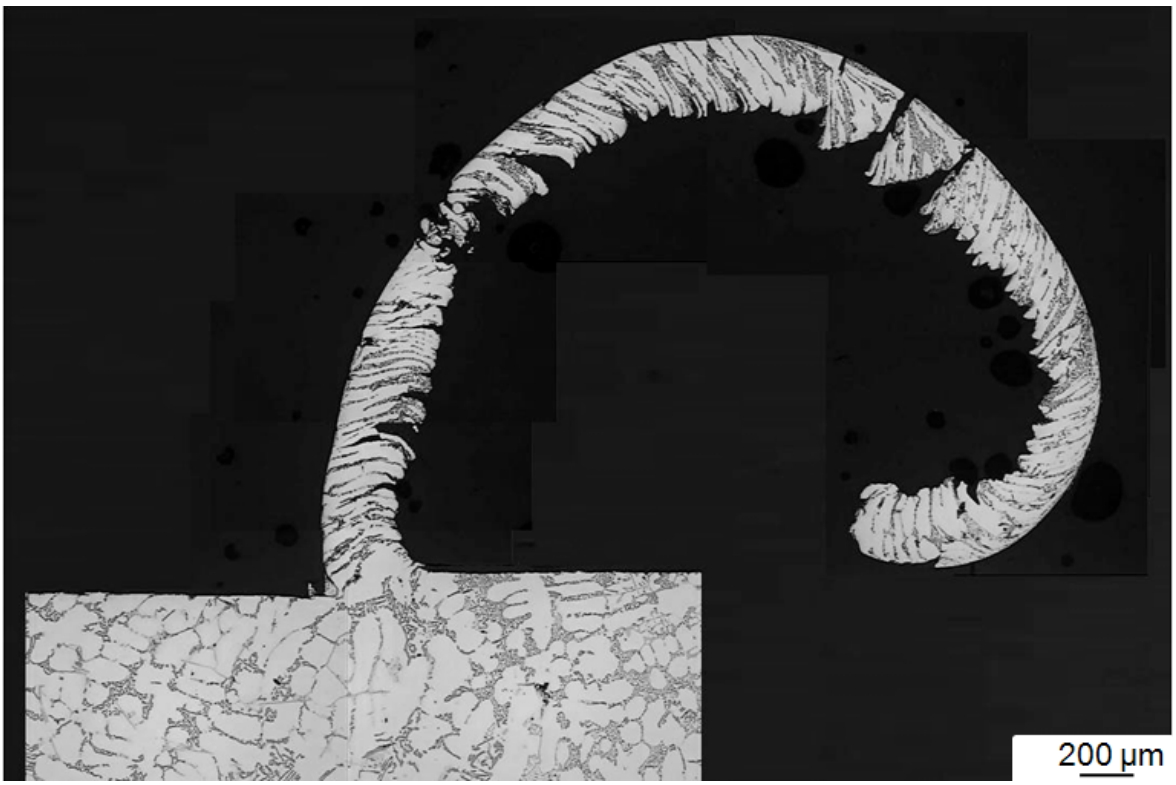

Fig.A1.5 Cutting Speed 115m/min, Feed 0.10mm

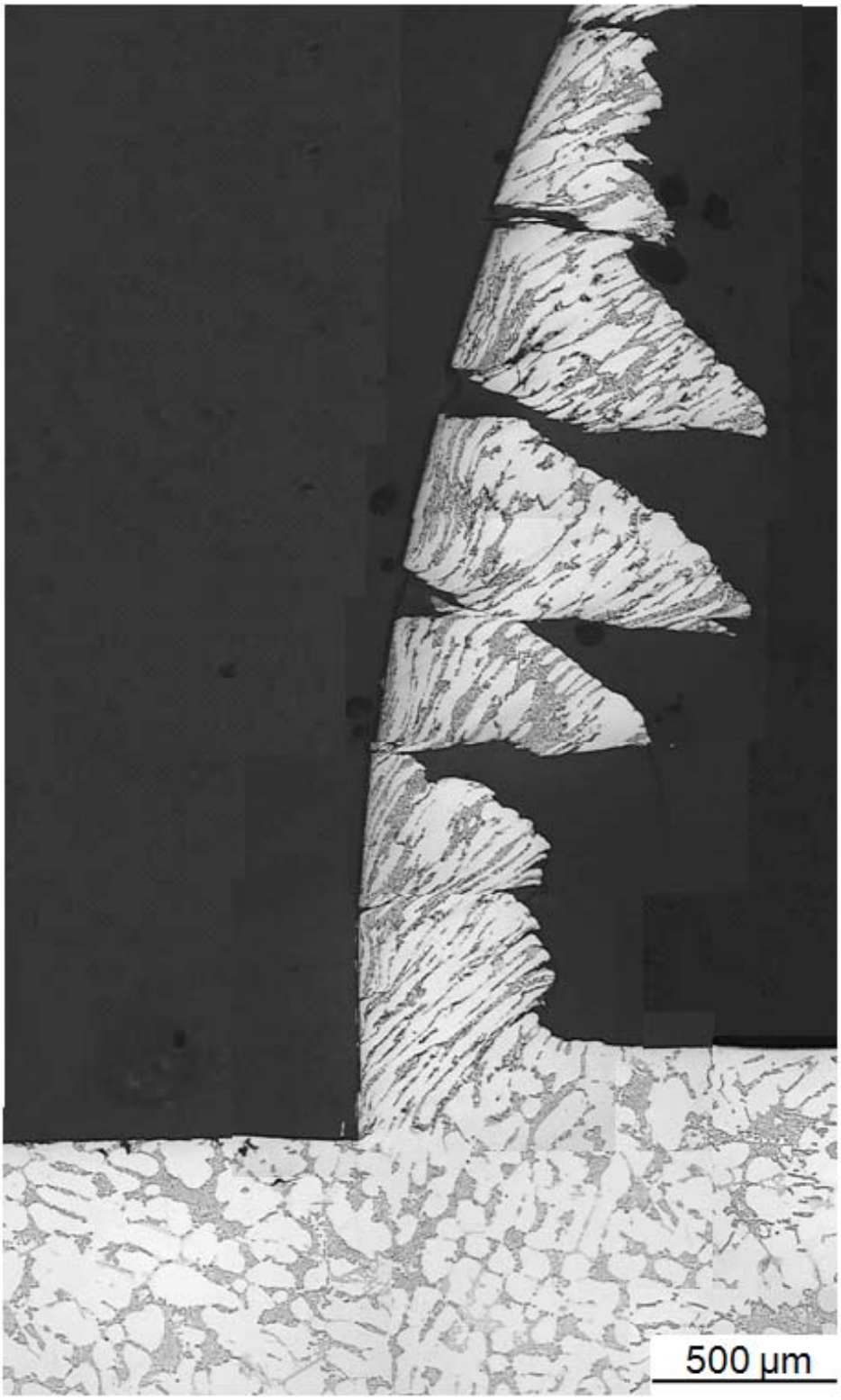

Fig.A1.6 Cutting Speed 25m/min, Feed 0.25mm,

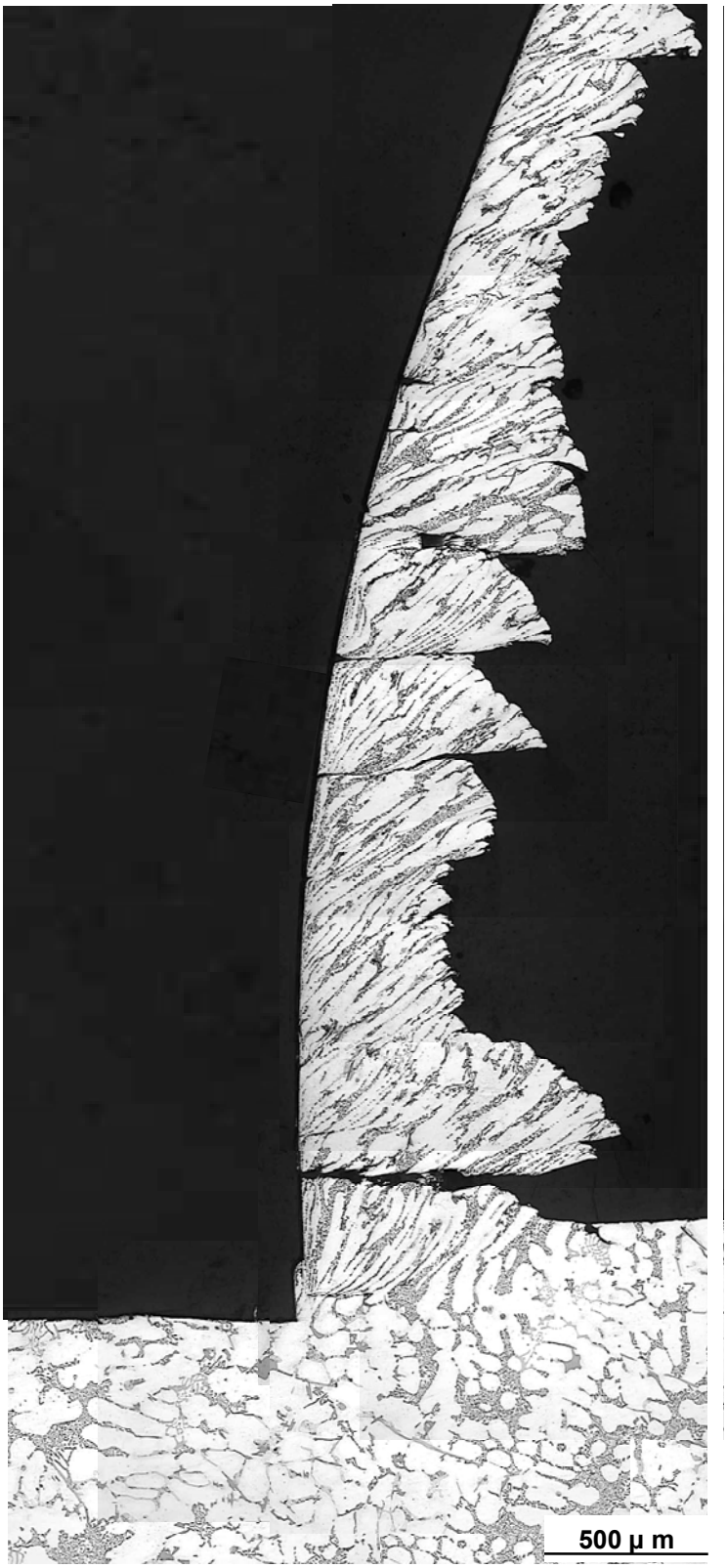

Fig.A1.7 Cutting Speed 35m/min, Feed 0.25mm

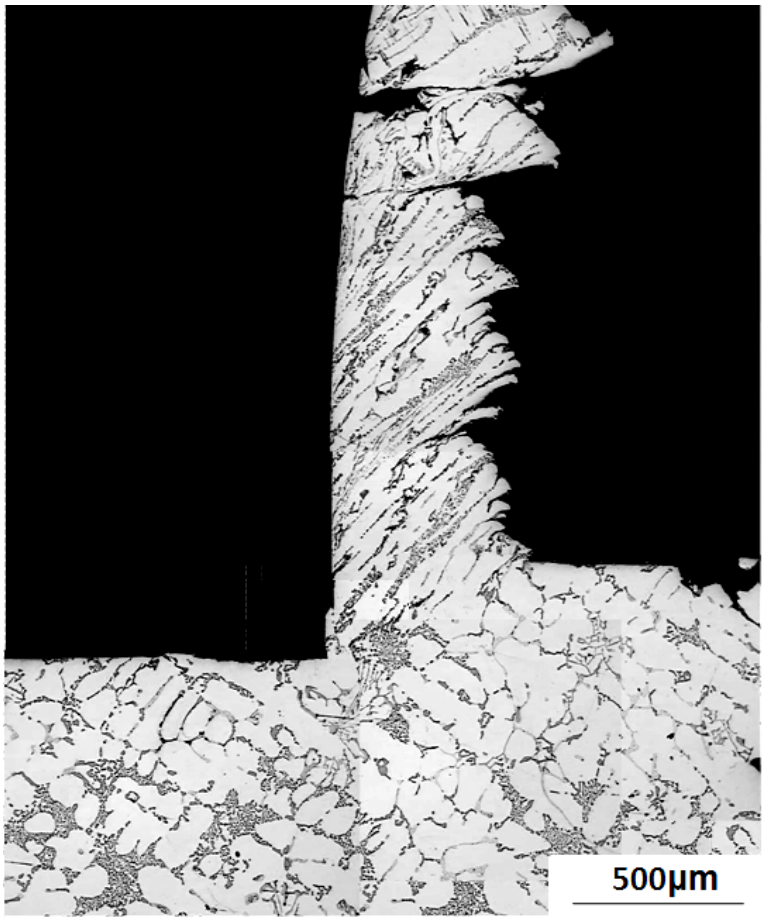

Fig.A1.8 Cutting Speed 50m/min, Feed 0.25mm

Fig.A1.9 Cutting Speed 75m/min, Feed 0.25mm

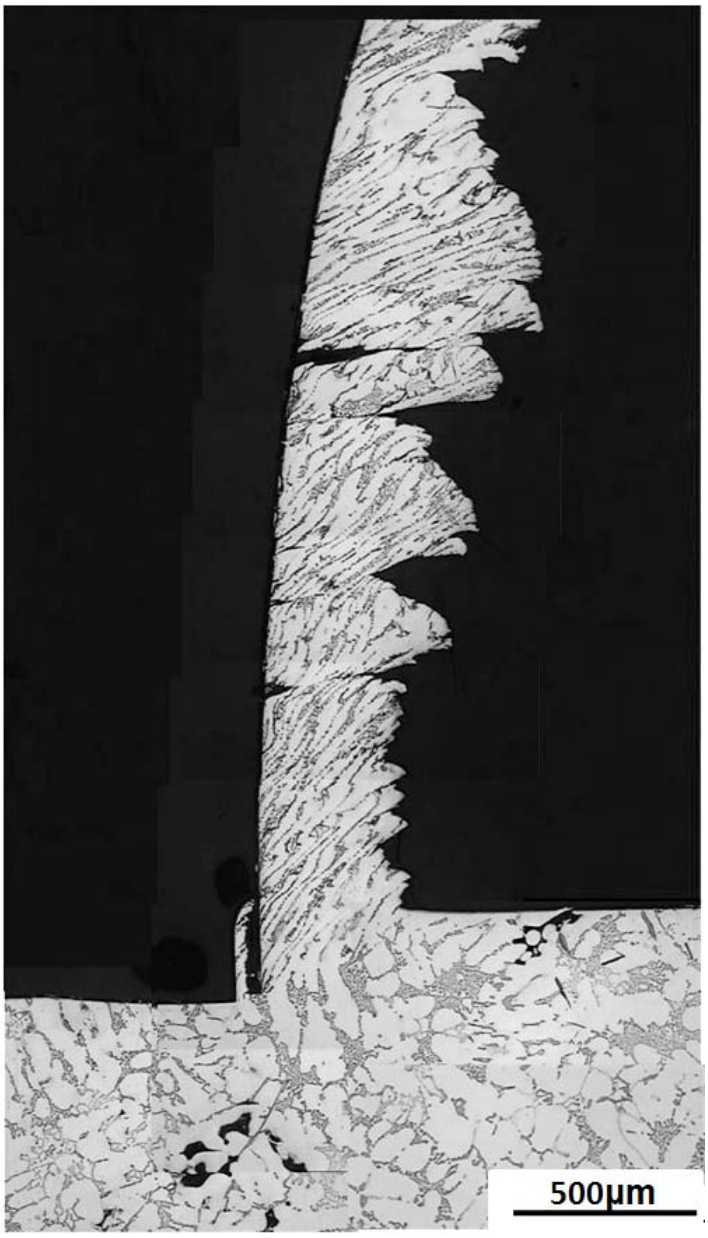

Fig.A1.10 Cutting Speed 115m/min, Feed 0.25mm

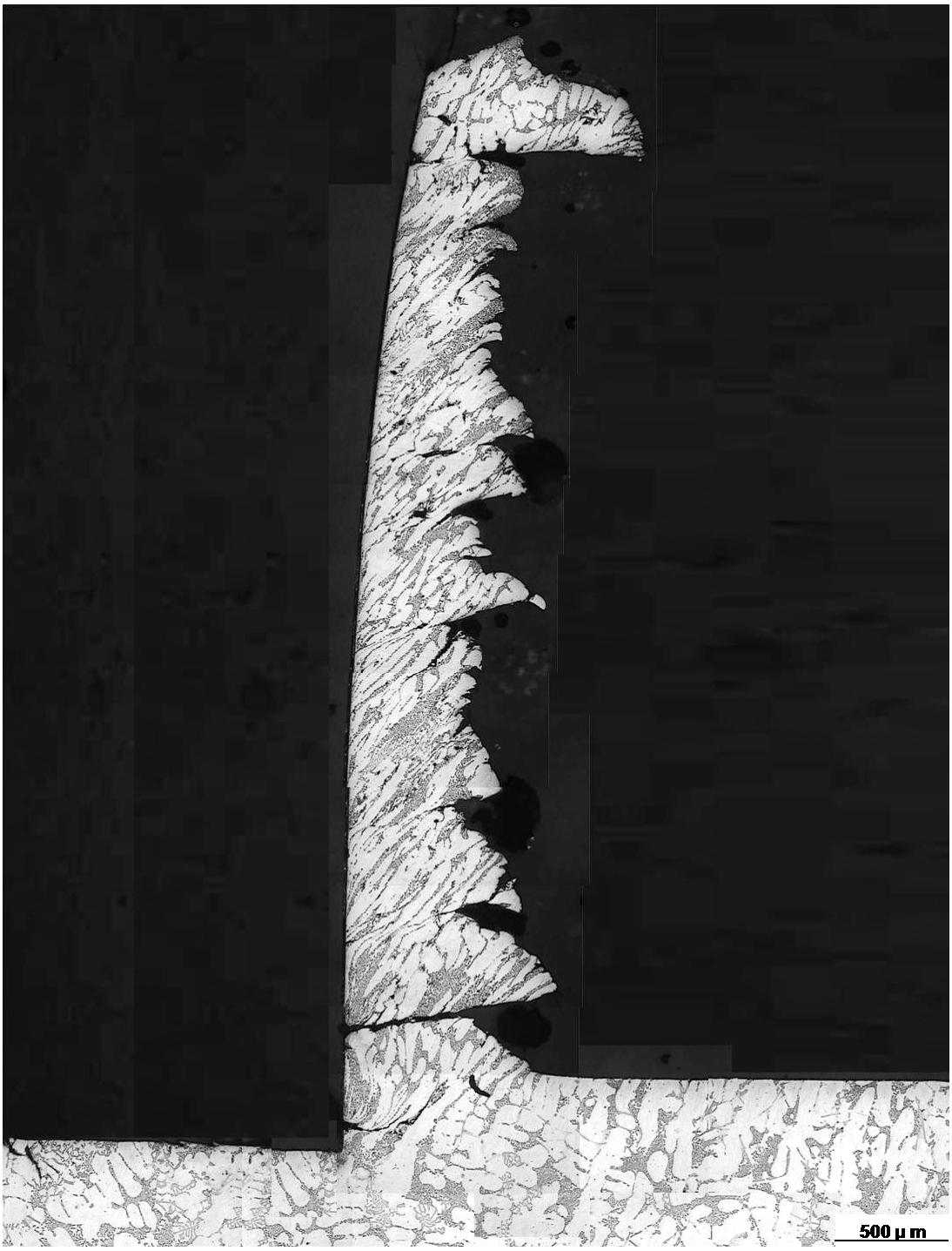

Fig.A1.11 Cutting Speed 25m/min, Feed 0.35mm

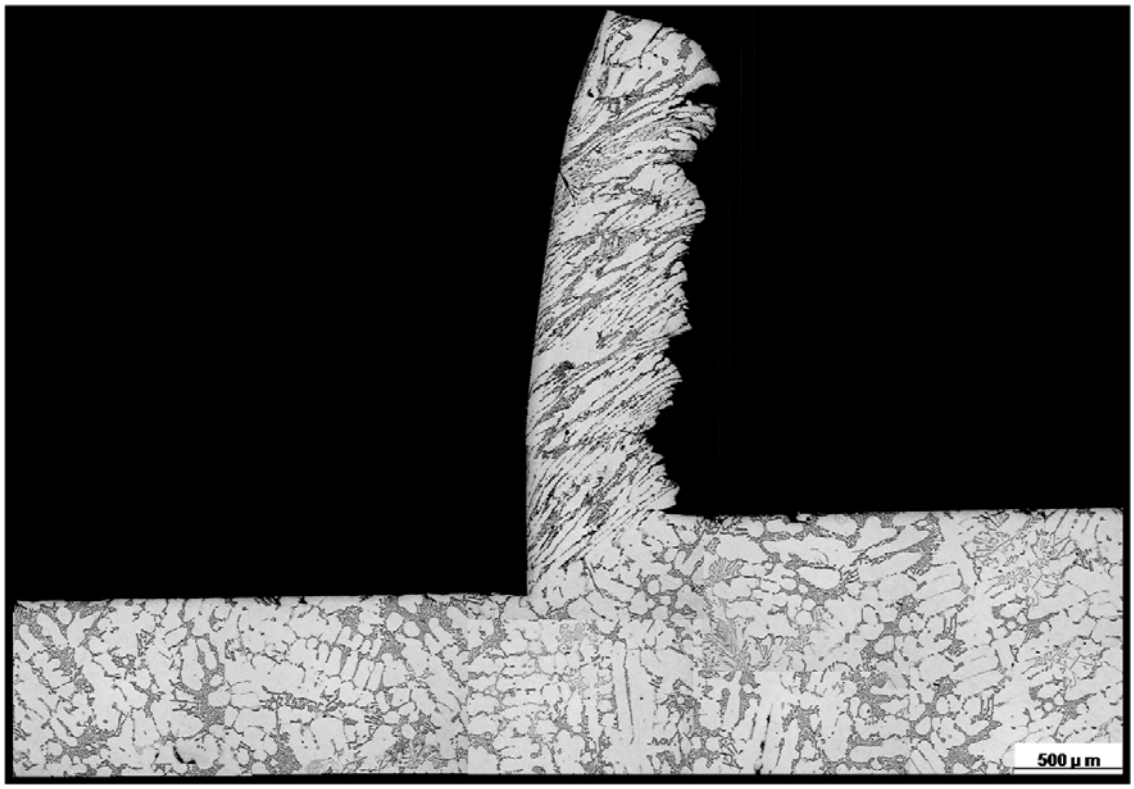

Fig.A1.12 Cutting Speed 35m/min, Feed 0.35mm

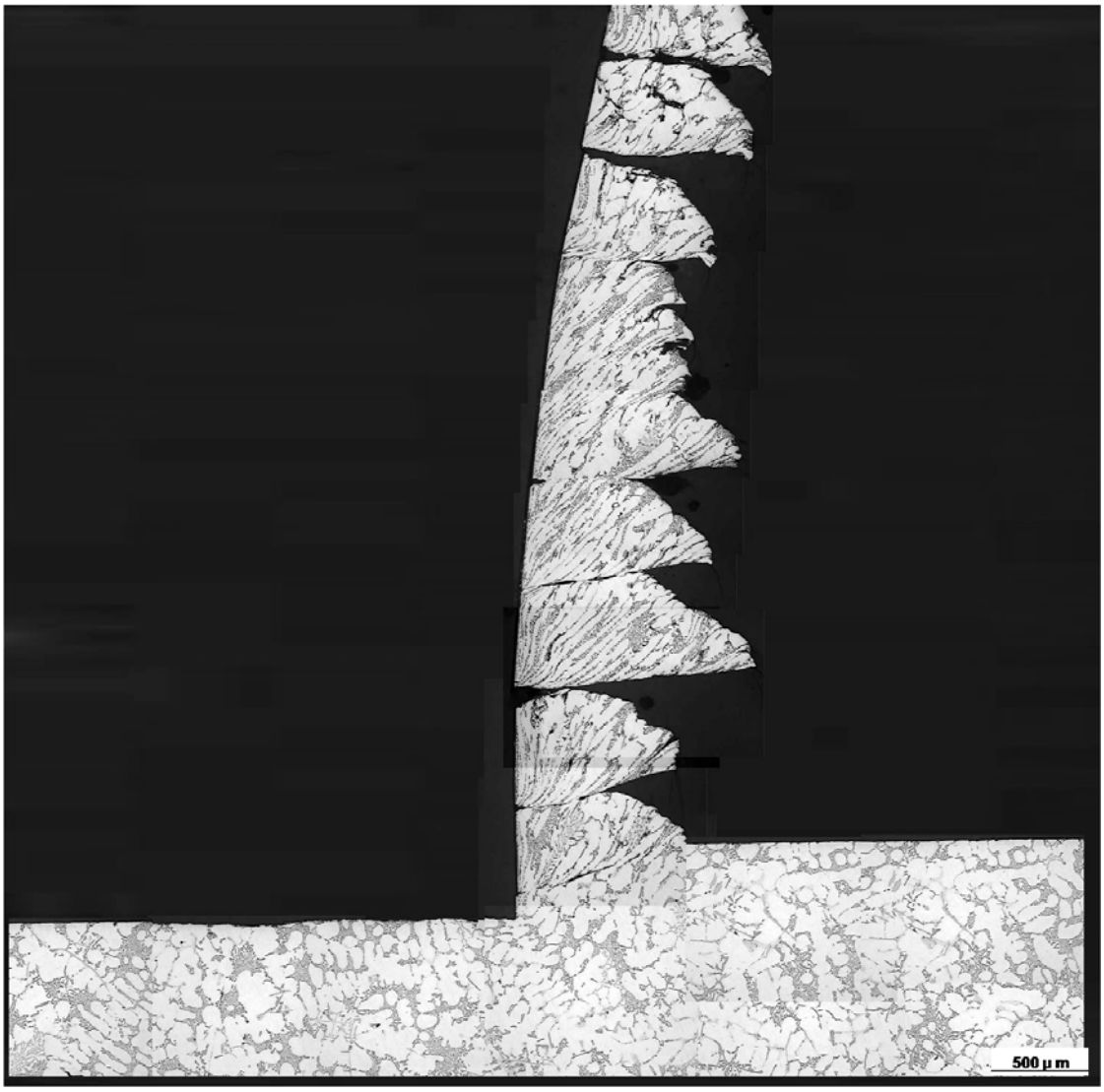

Fig.A1.13 Cutting Speed 50m/min, Feed 0.35mm

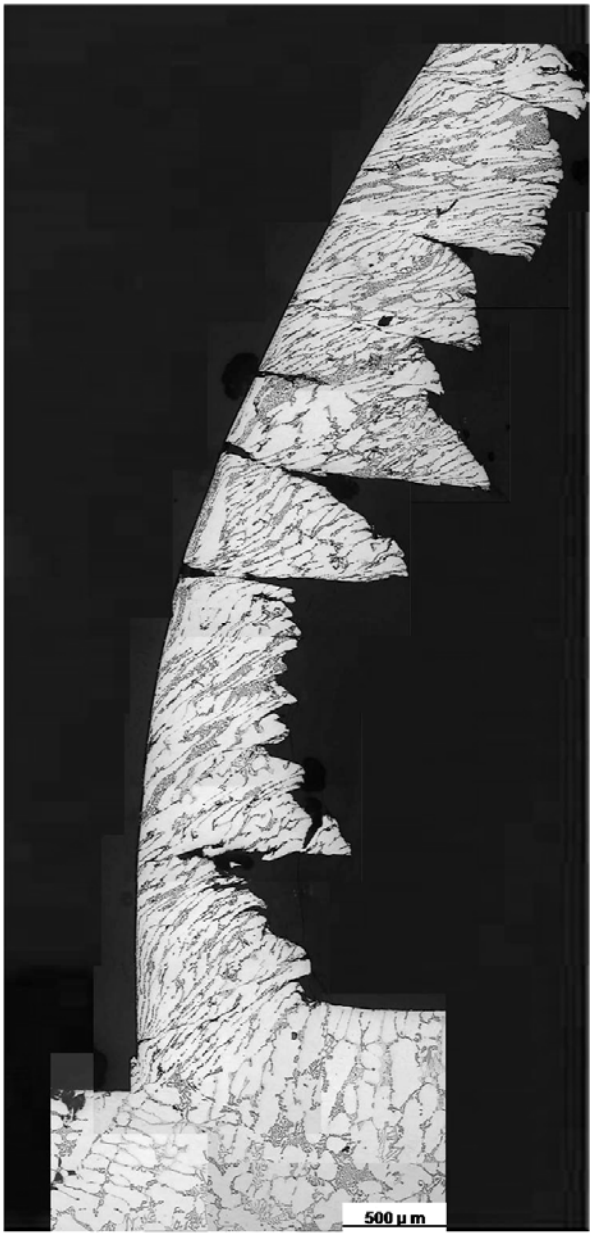

Fig.A1.14 Cutting Speed 75m/min, Feed 0.35mm

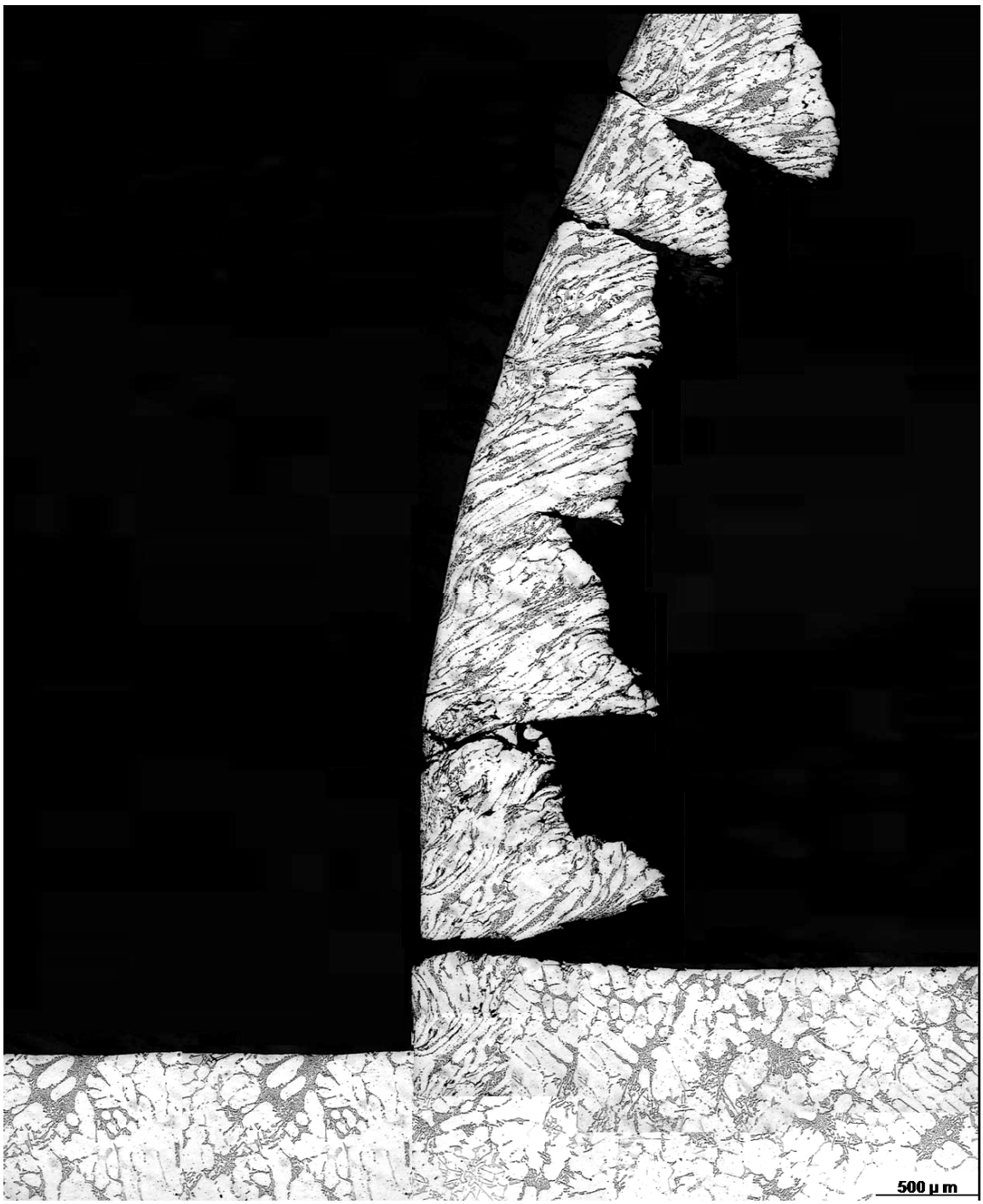

Fig.A1.15 Cutting Speed 115m/min, Feed 0.35mm

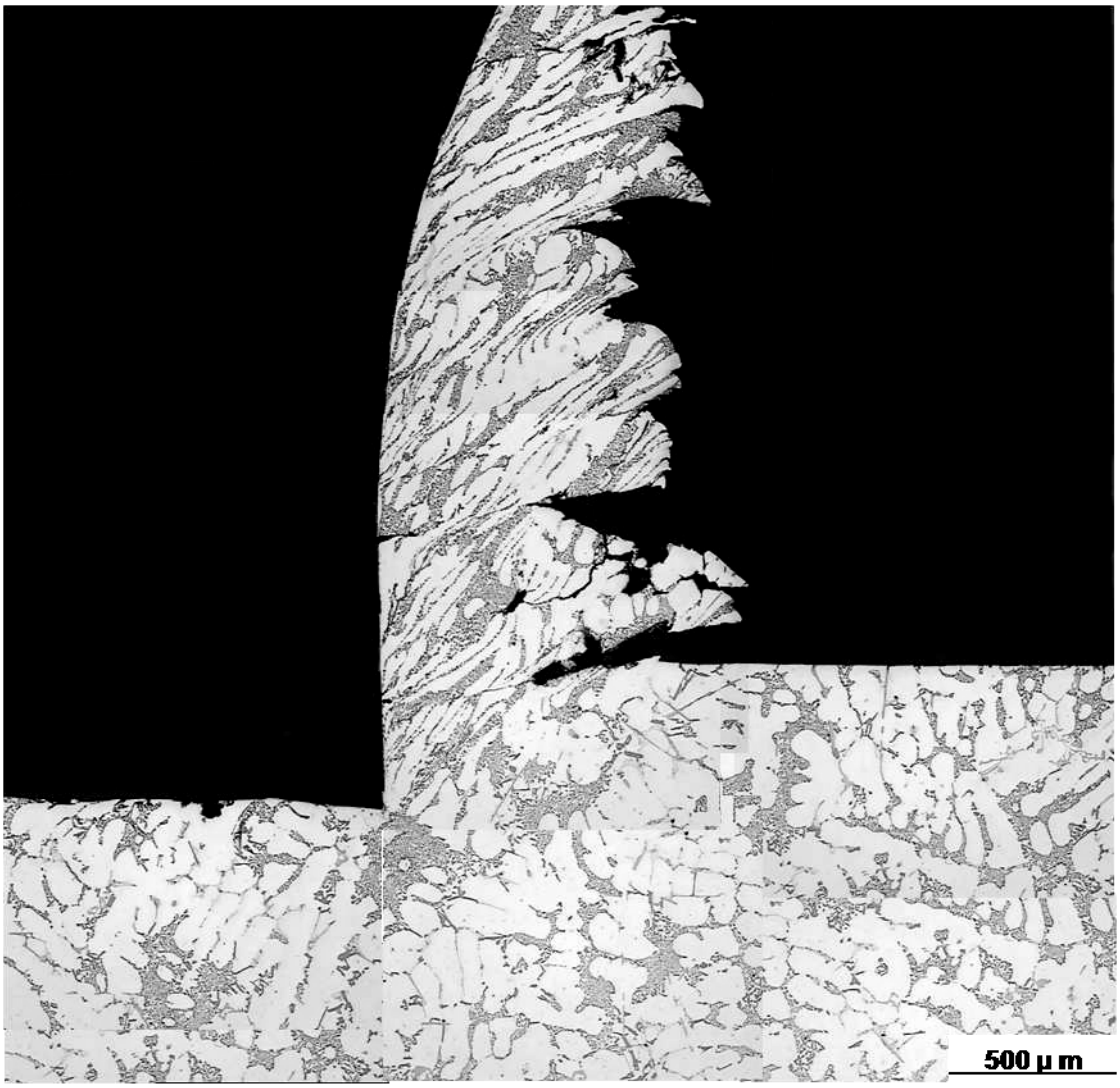

Fig.A1.16 Cutting Speed 25m/min, Feed 0.45mm

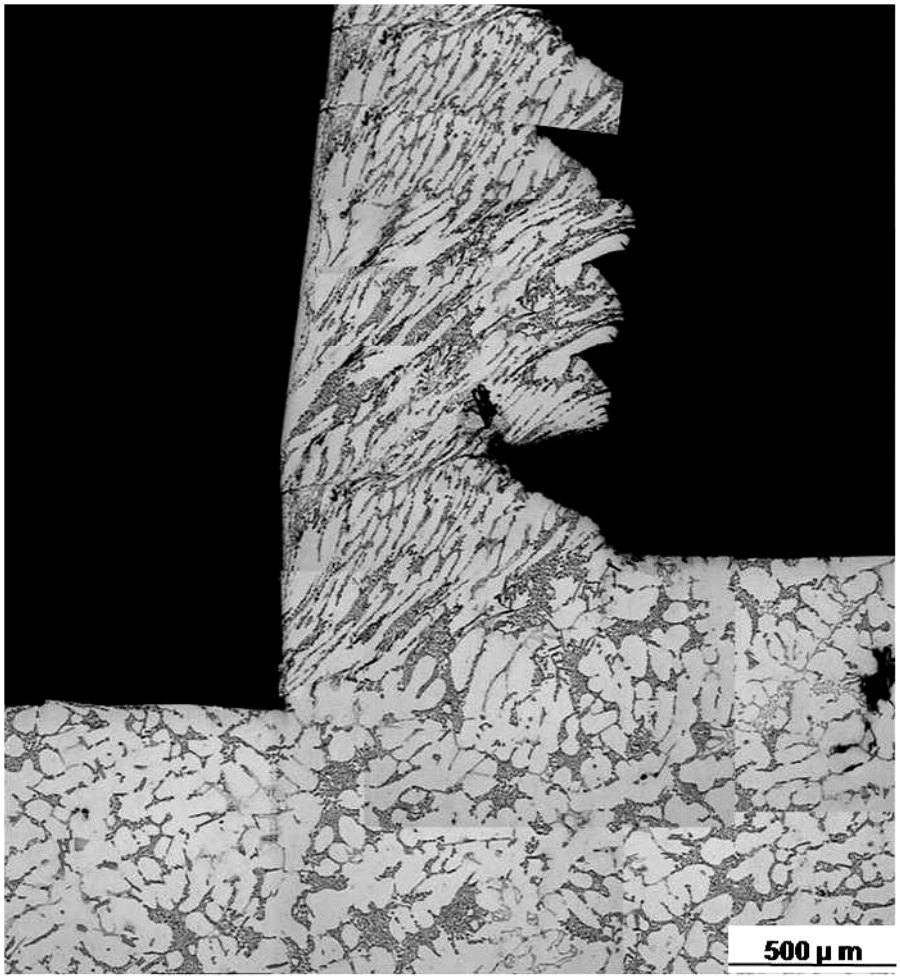

Fig.A1.17 Cutting Speed 35m/min, Feed 0.45mm

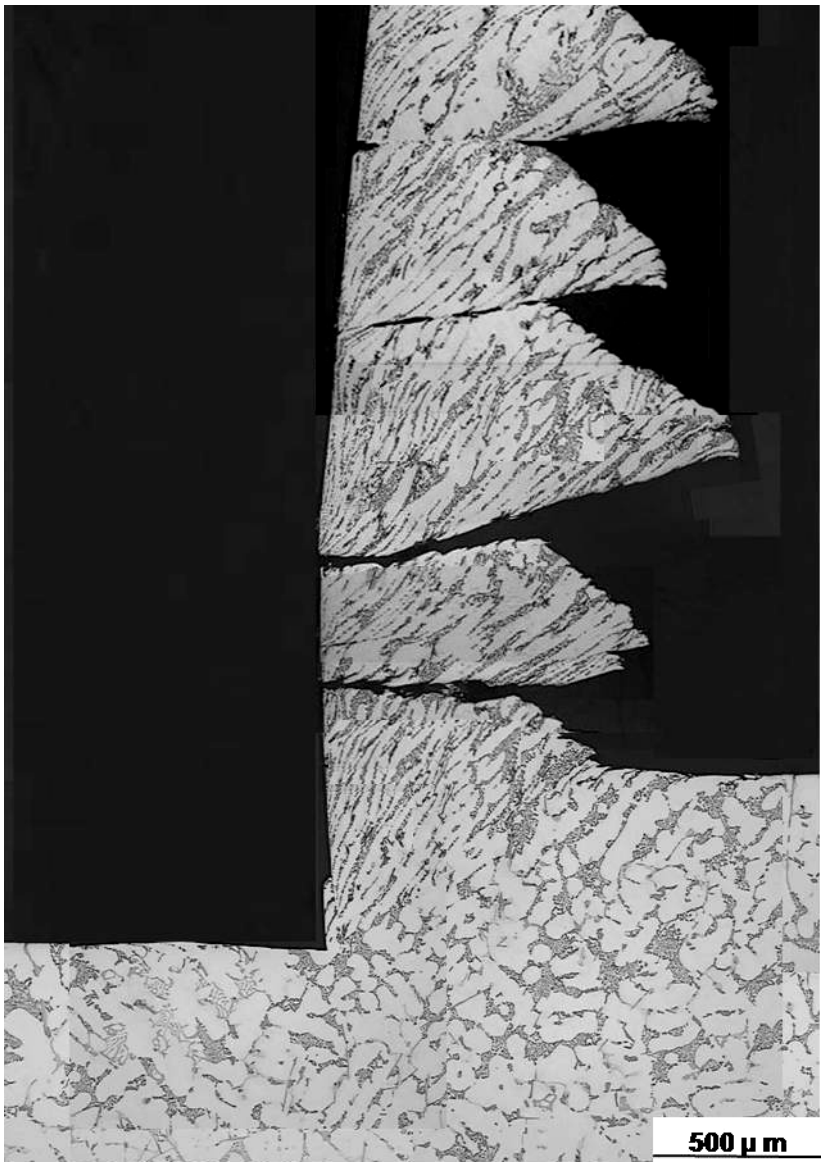

Fig.A1.18 Cutting Speed 50m/min, Feed 0.45mm

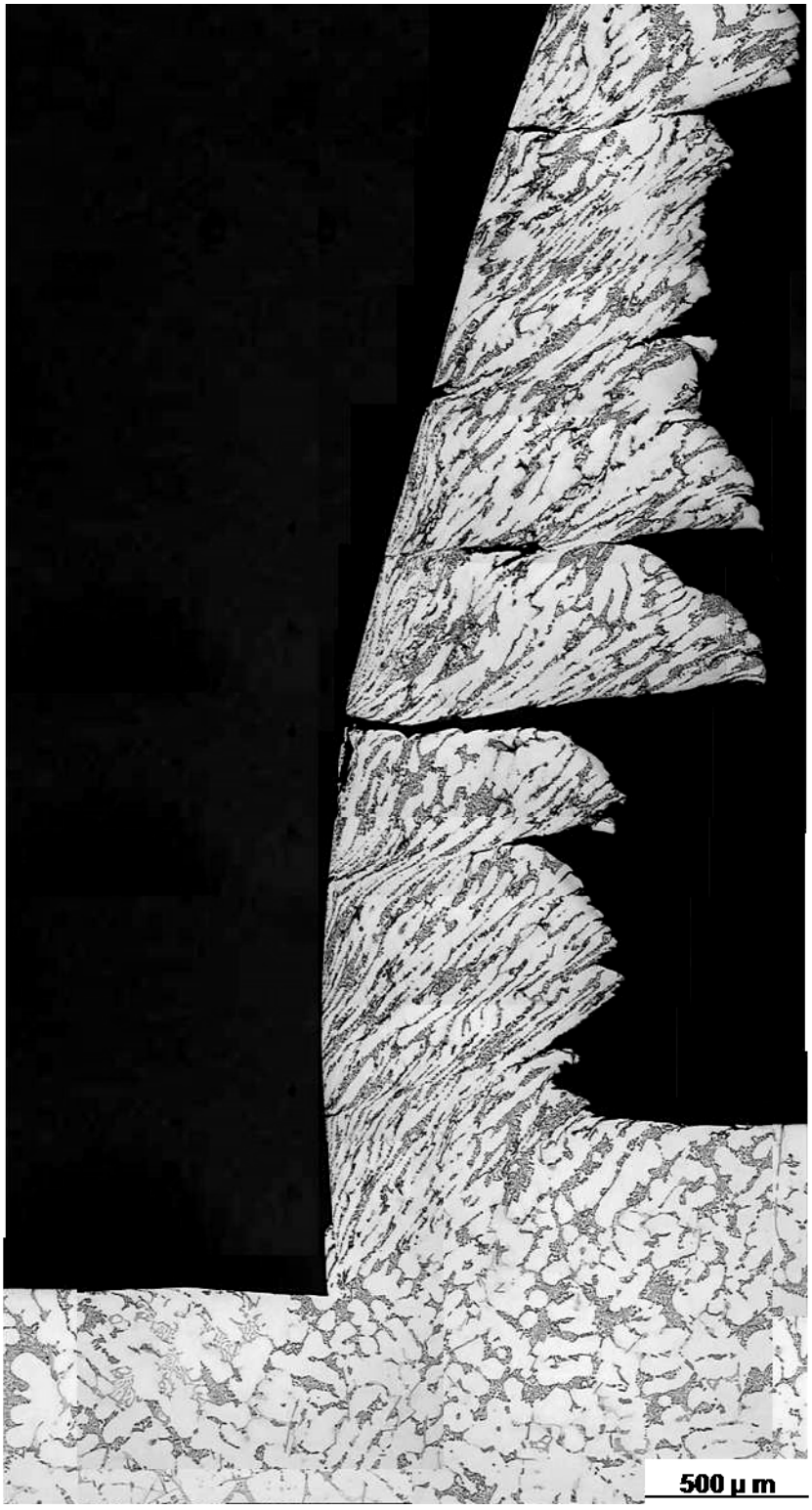

Fig.A1.19 Cutting Speed 75m/min, Feed 0.45mm

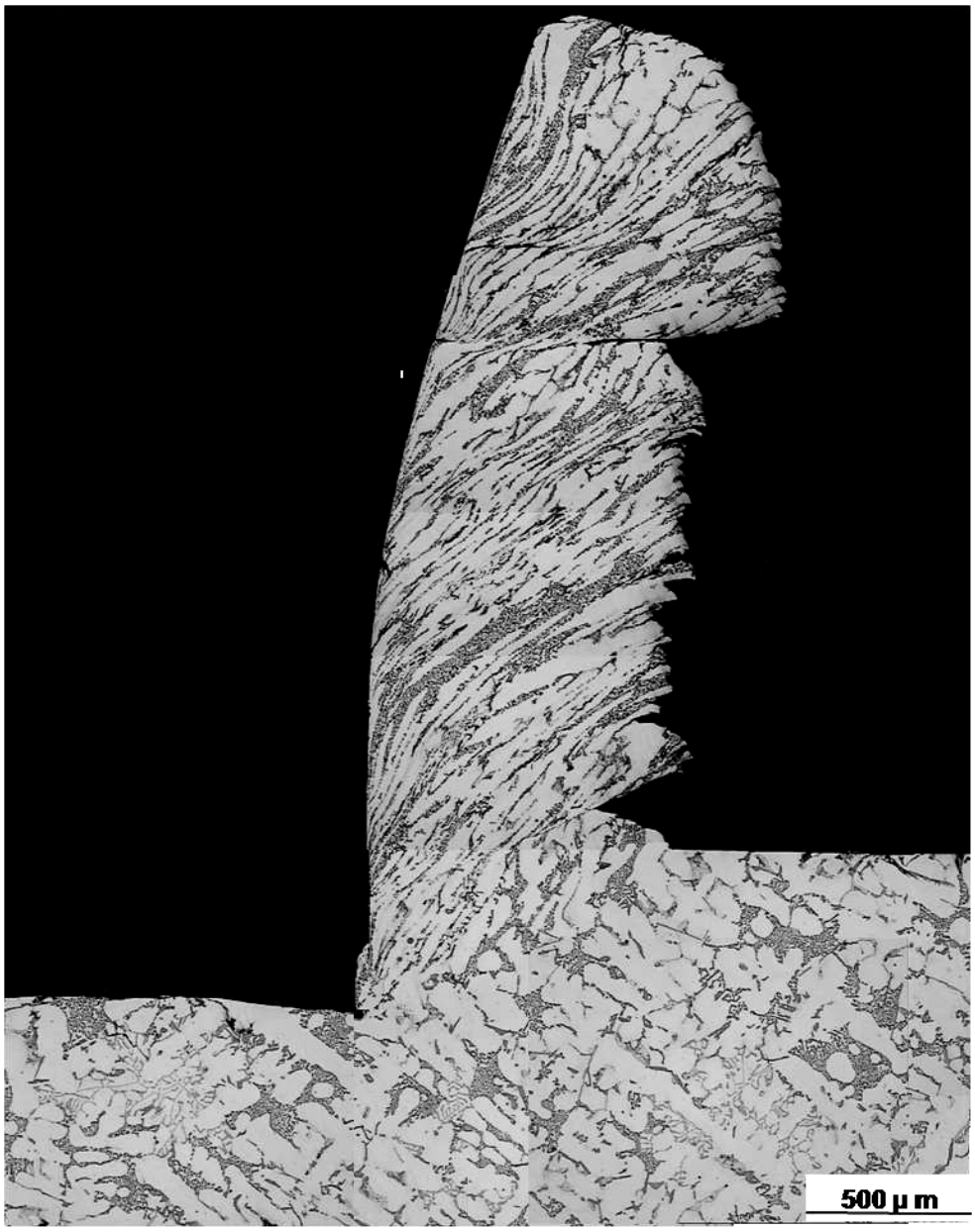

Fig.A1.20 Cutting Speed 115m/min, Feed 0.45mm

APPENDIX II

MACHINABILITY RATINGS OF AL ALLOYS

Table AII - I: Machinability ratings of cast aluminum alloys [8,12].

Alloy designation	Temper	Casting form	Hardness, BH (500 kg load, 10 mm ball)	Machinability rating(a)
208	F	Sand	55	B
213	F	Permanent mold	85	. . .
222	T52	Permanent mold	100	. . .
	T551	Permanent mold	115	. . .
	T65	Permanent mold	140	. . .
238	F	Permanent mold	100	B
A240	F	Sand	90	A
242	F	Sand	. . .	. . .
	T21	Sand	70	B
	T571	Sand	85	B
	T571	Permanent mold	105	B
	T61	Permanent mold	110	B
	T77	Sand	75	B
A242	T77	Sand	70	. . .
295	T4	Sand	60	B
	T6	Sand	75	B
	T62	Sand	90	B
B295	T4	Permanent mold	75	B
	T6	Permanent mold	90	B
	T7	Permanent mold	80	B
308	F	Permanent mold	70	B
319	F	Sand, permanent mold	70	C
	T5	Sand	80	B
	T6	Sand	80	B
	T6	Permanent mold	95	B

Note: Ratings A, B, C, D and E are relative ratings in increasing order of chip length an decreasing order of quality of finish obtained under standard or wet machining (A: very small broken chips, excellent finish; B: curled or easily broken chips, good-to-excellent finish; C: continuous chips, good finish; D: continuous chips, satisfactory finish; E: optimum tool design, machine setting required to obtain satisfactory control of chip and finish) [8,12].

APPENDIX III

HIGH SPEED IMAGES OF CHIP GENERATION DURING ORTHOGONAL CUTTING PROCESS

High speed images (2000fps) of the workpiece and tool tip were taken during orthogonal machining of 319 Al and 6061-T6 alloy for investigating the chip generation process. The following section presents the images from the high speed photography showing the tool, workpiece being machined and the newly formed chip as recorded during the process. The time interval between each image is 0.05sec. Fig.A3.1 shows the configuration of the tool and workpiece in detail and highlights the area that has been shown for all the high speed imagery shown in this section. Fig.A3.2 show one frame from the high speed photos to further illustrate the elements present in them.

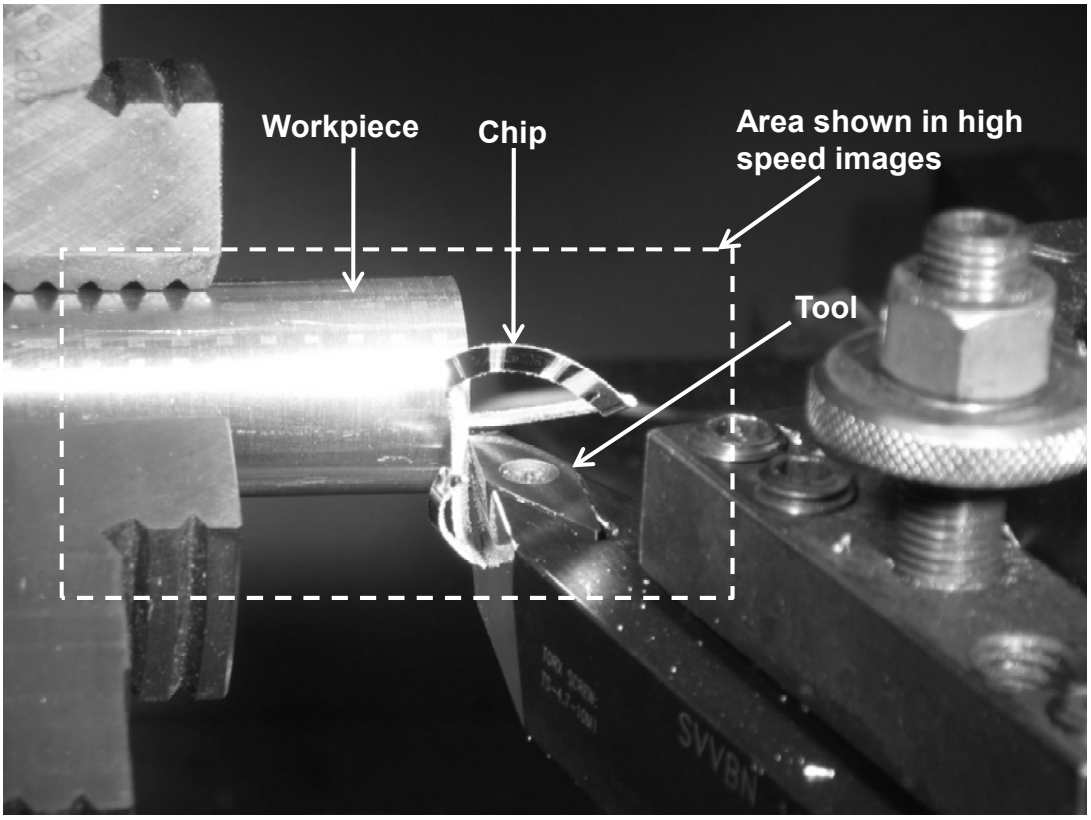

Fig.A3.1. The configuration of the tool and workpiece during orthogonal cutting process.

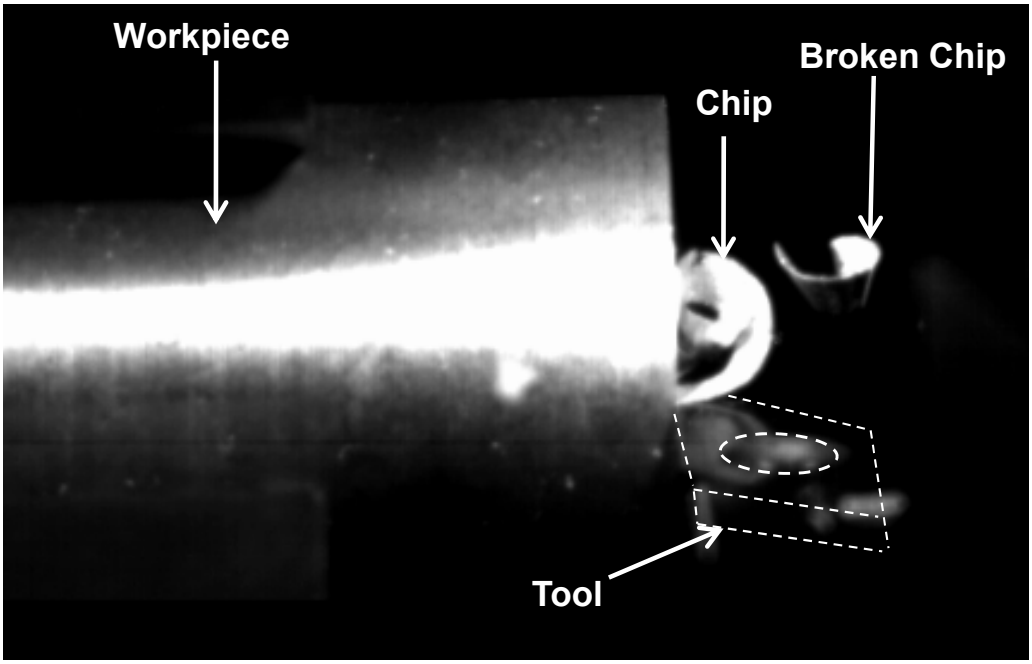

Fig.A3.2. Tool, workpiece, newly formed chip and a broken chip as seen in the high speed images taken during orthogonal cutting. The image has the tool highlighted using dotted line for enhanced visibility.

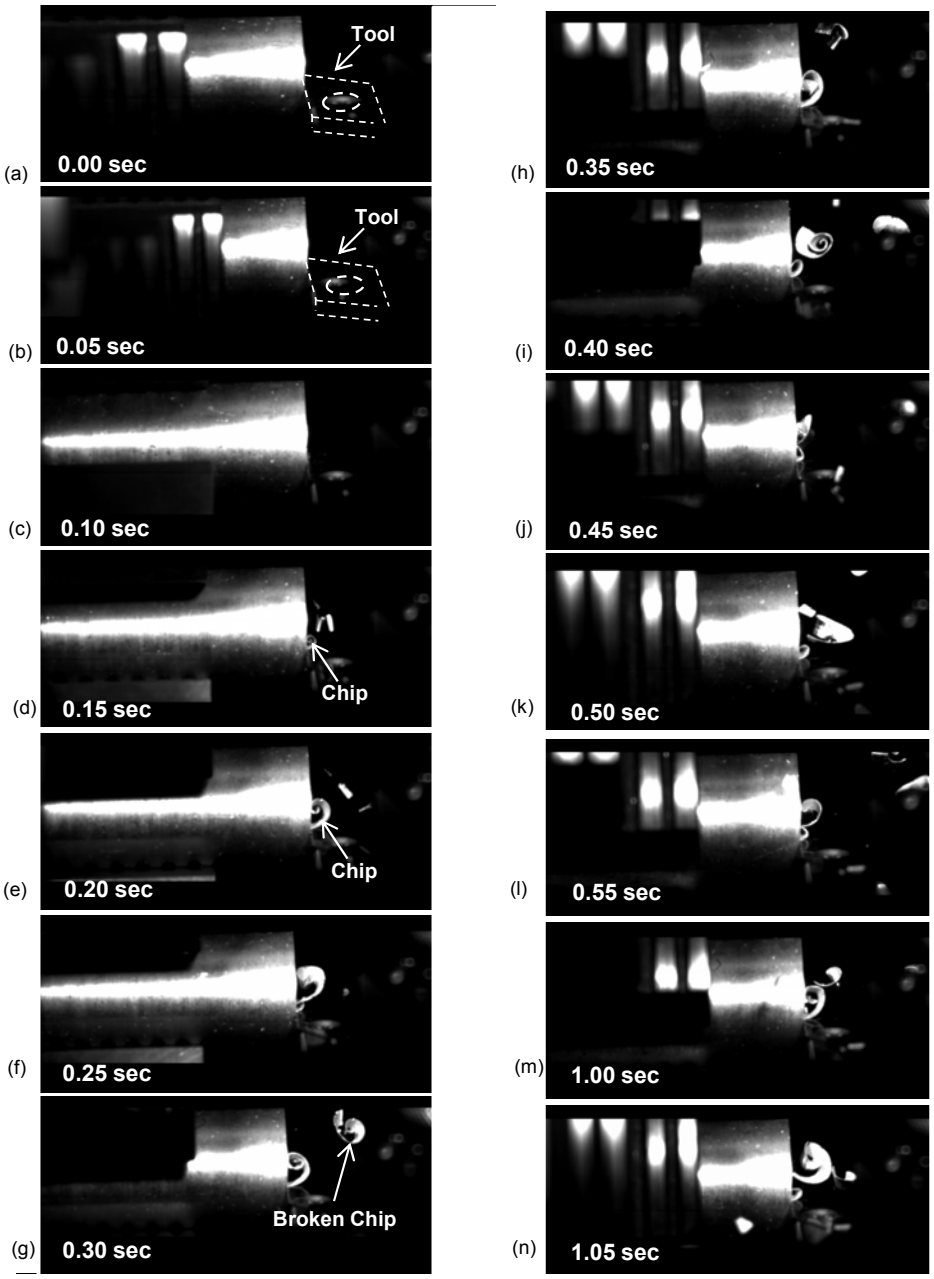

Fig.A3.3. (a-n) Images showing sequential generation of chips at 0.05 sec intervals for the first 1.05 seconds during orthogonal machining of 319 Al under cutting conditions of feed per revolution of 0.10mm and cutting speed of 75m/min. The time when each of the above images was taken has also been indicated. The tool has been highlighted in image (a) and (b) for enhanced visibility. Newly formed chip has also been indicated (d) and broken or fragmented chip has been highlighted in 'g'. It is evident from above that during chip generation, the contact angle between the tool and the chip constantly changes as the newly formed chip starts to elongate and curl.

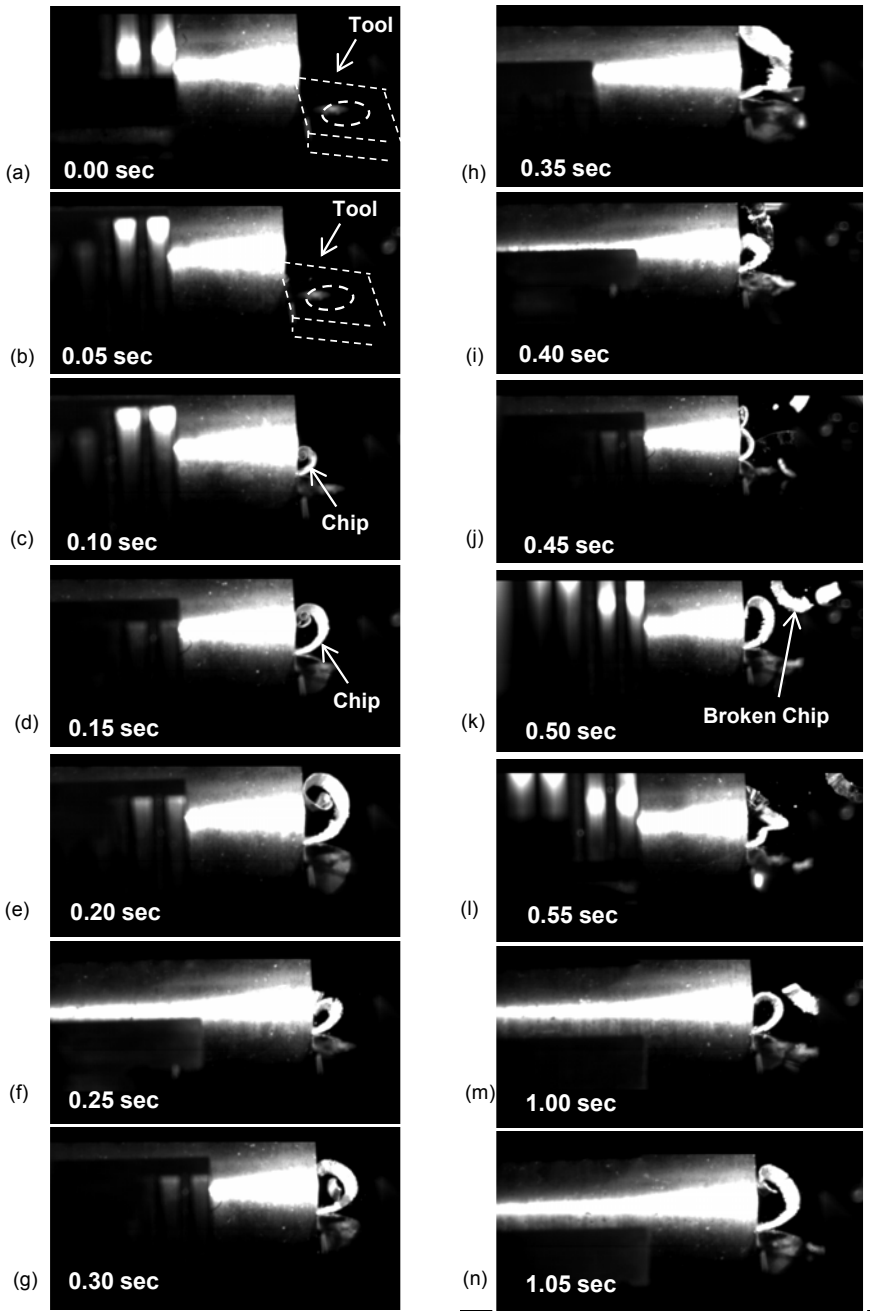

Fig.A3.4. (a-n) Images showing sequential generation of chips at 0.05 sec intervals for the first 1.05 seconds during orthogonal machining of 319 Al under cutting conditions of feed per revolution of 0.25mm and cutting speed of 75m/min. The time when each of the above images was taken has also been indicated. The tool has been highlighted in image (a) and (b) for enhanced visibility. Newly formed chip has also been indicated (c and d) and broken or fragmented chip has been highlighted in 'k'. It is evident from above that during chip generation, the contact angle between the tool and the chip constantly changes as the newly formed chip starts to elongate and curl.

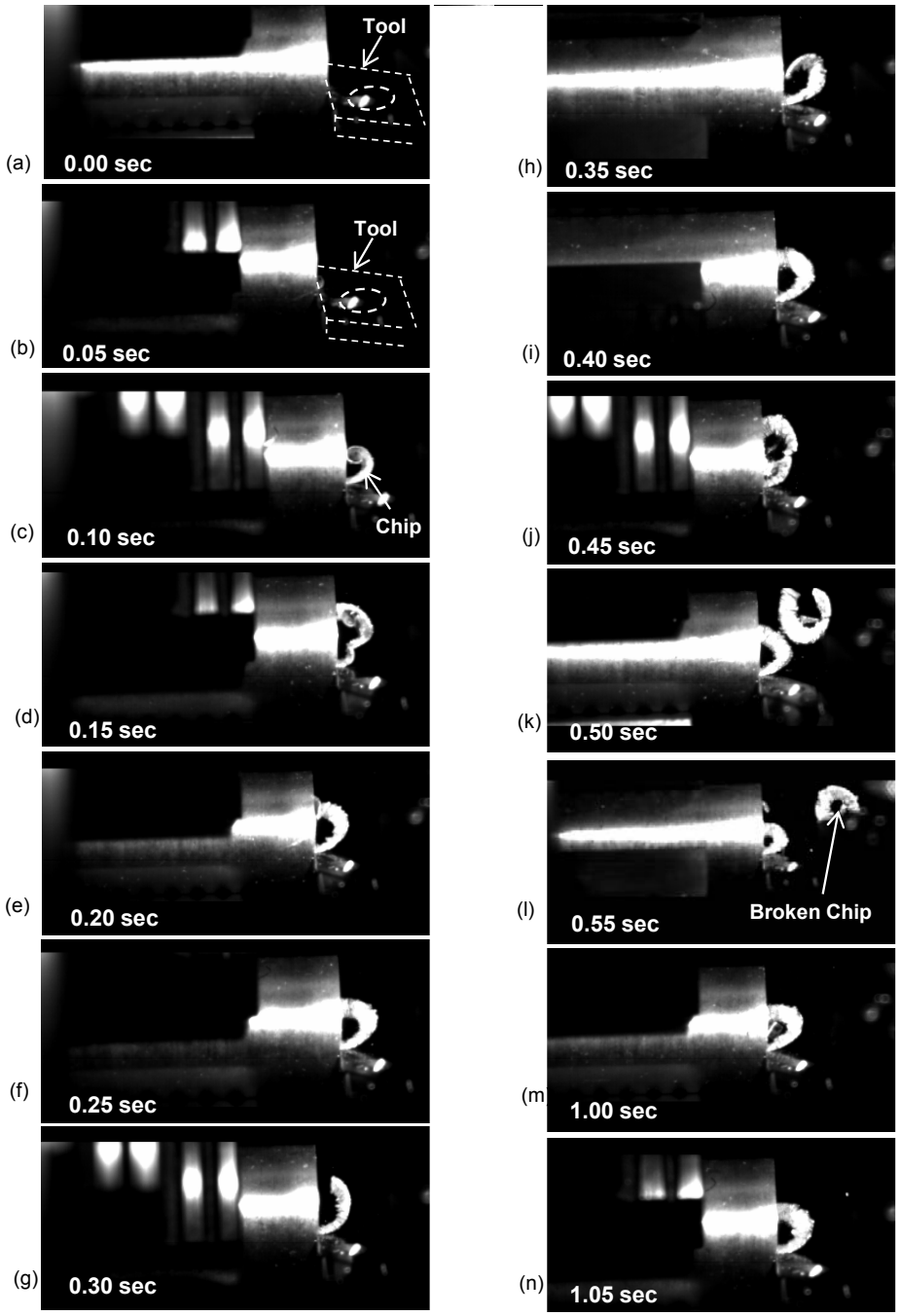

Fig.A3.5. (a-n) Images showing sequential generation of chips at 0.05 sec intervals for the first 1.05 seconds during orthogonal machining of 319 Al under cutting conditions of feed per revolution of 0.35mm and cutting speed of 75m/min. The time when each of the above images was taken has also been indicated. The tool has been highlighted in image (a) and (b) for enhanced visibility. Newly formed chip has also been indicated (c) and broken or fragmented chip has been highlighted in 'l'. It is evident from above that during chip generation, the contact angle between the tool and the chip constantly changes as the newly formed chip starts to elongate and curl.

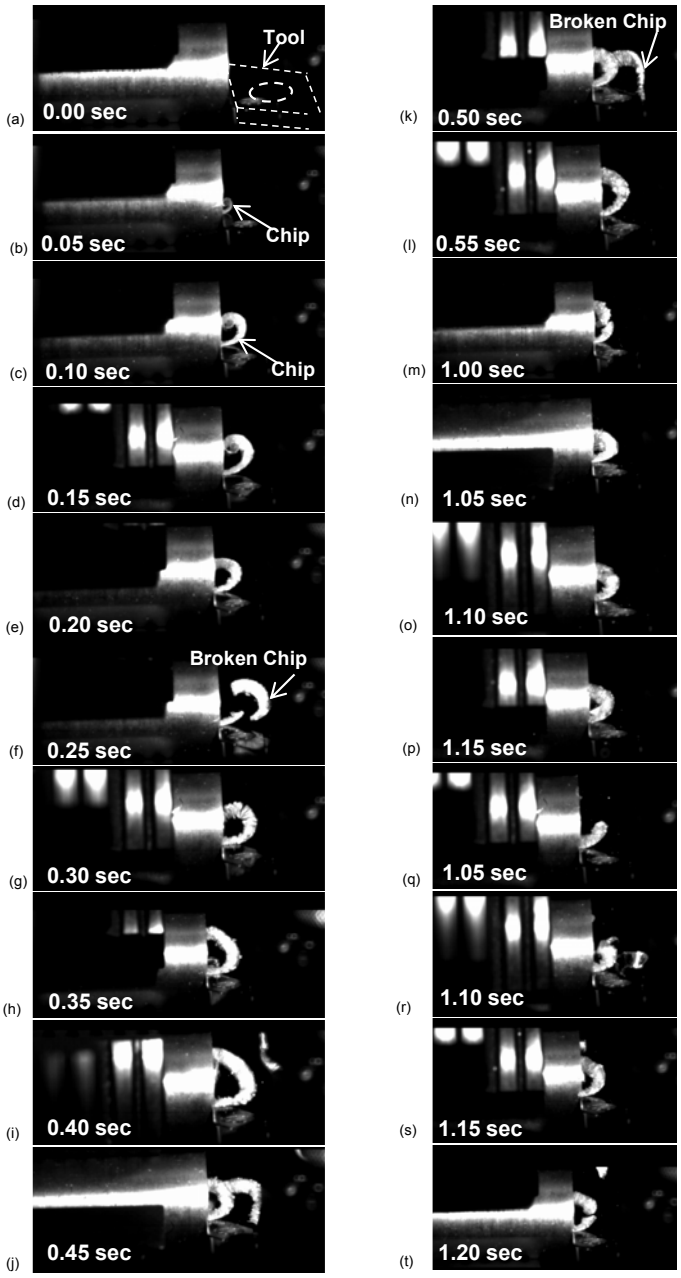

Fig.A3.6. (a-t) Images showing sequential generation of chips at 0.05 sec intervals for the first 1.20 seconds during orthogonal machining of 319 Al under cutting conditions of feed per revolution of 0.45mm and cutting speed of 75m/min. The time when each of the above images was taken has also been indicated. The tool has been highlighted in image (a) for enhanced visibility. Newly formed chip has also been indicated (b and c) and broken or fragmented chip has been highlighted in 'f'. It is evident from above that during chip generation, the contact angle between the tool and the chip constantly changes as the newly formed chip starts to elongate and curl.

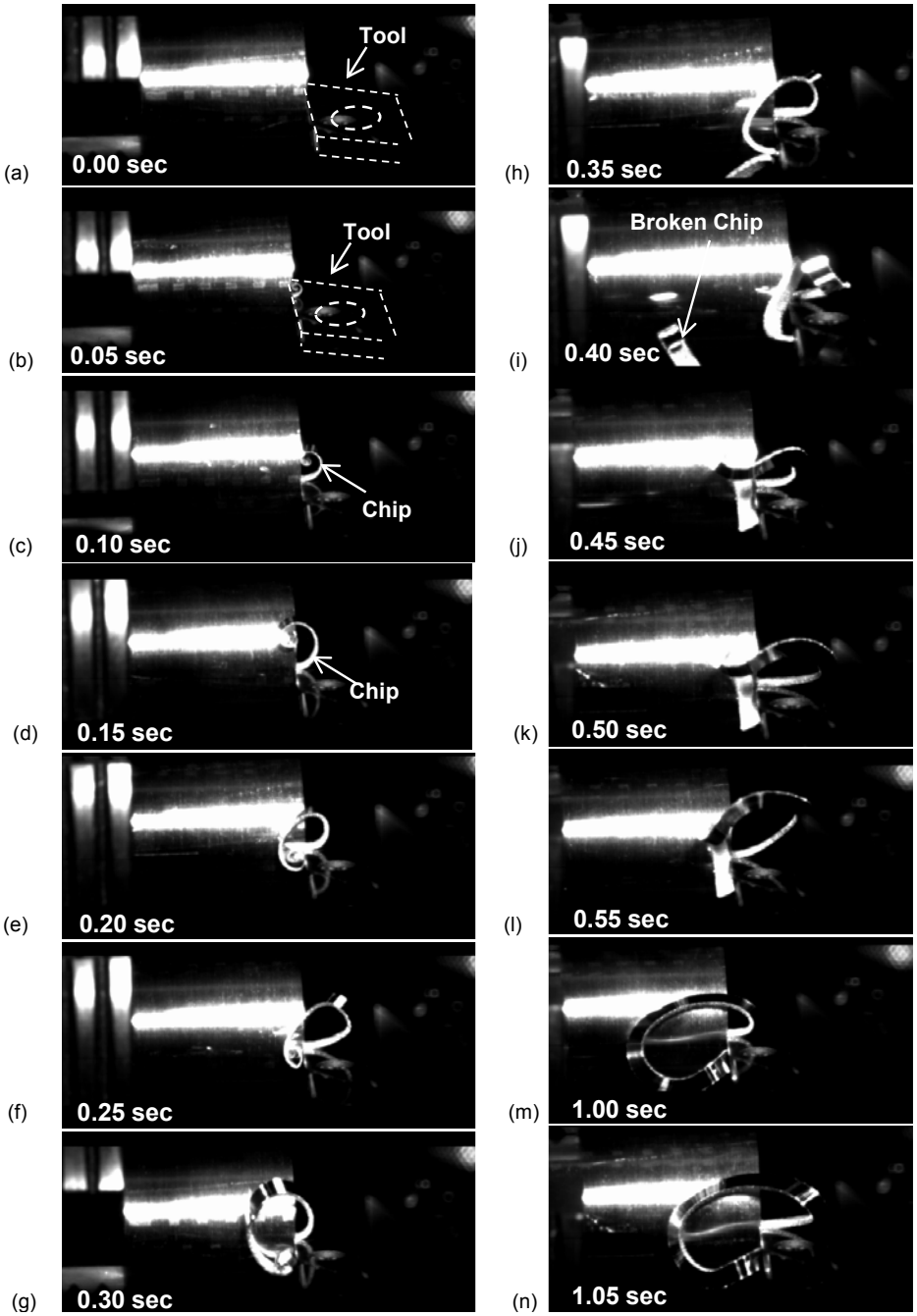

Fig.A3.7. (a-n) Images showing sequential generation of chips at 0.05 sec intervals for the first 1.05 seconds during orthogonal machining of 6061-T6 under cutting conditions of feed per revolution of 0.25mm and cutting speed of 75m/min. The time when each of the above images was taken has also been indicated. The tool has been highlighted in image (a) and (b) for enhanced visibility. Newly formed chip has also been indicated (c) and broken or fragmented chip has been highlighted in 'i'. It is evident from above that during chip generation, the contact angle between the tool and the chip constantly changes as the newly formed chip starts to elongate and curl.

VITA AUCTORIS

Shilpi Pratibha was born in 1982 in Jamtara, Jharkhand, India. She obtained her Bachelor of Engineering in Metallurgy and Materials Engineering at the Bengal Engineering and Science University, Shibpur, Howrah, India in 2005. She is currently an MASc candidate in the Engineering Materials Graduate Program at the University of Windsor and hopes to graduate in Fall 2009.